On the Distribution of Luminous and Dark Matter in Strong Lensing Galaxies

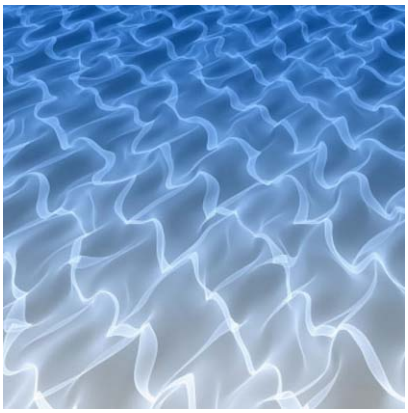

Dominik Leier
Astronomisches Rechen-Institut
Zentrum für Astronomie der Universität Heidelberg

Heidelberg 2011

Cover picture: "Caustic I" – A random lens refracting light.
Courtesy of Prof. Eric J. Heller (Harvard University, Cambridge, USA)

Dissertation
submitted to the
Combined Faculties for the Natural Sciences and for Mathematics
of the Ruperto-Carola University of Heidelberg, Germany
for the degree of
Doctor of Natural Sciences

Put forward by

Dipl.-Phys. Dominik Leier
Born in: Dortmund

Oral examination: November 23rd, 2011

On the Distribution of Luminous and Dark Matter in Strong Lensing Galaxies

Referees: Prof. Dr. Joachim K. Wambsganß
Dr. Prasenjit Saha

On the Distribution of Luminous and Dark Matter in Strong Lensing Galaxies

Abstract: The interplay between luminous and dark matter is essential to the formation of galaxies. It is thought to take place in a multistage process, starting with the gravitational collapse of dark matter, followed by baryonic gas falling into the potential wells. As baryons cool down, they form stars, resulting in the first galaxies. The formation process is still poorly understood, but observations provide empirical relations between galaxy characteristics, such as the "fundamental plane" of elliptical galaxies, which correlates brightness, size and velocity dispersion. This work explores aspects of galaxy formation trough two techniques. Non-parametric modeling of gravitational lenses constrains their total mass content. Stellar mass can be estimated via population synthesis. Both techniques are applied to a sample of 21 lenses, using archival HST data. In a first step the fundamental plane is recovered. The lensing galaxies are shown to be close to virial equilibrium. We extract radial mass profiles (spatially resolved $\lesssim 1$ kpc) and find a common radial range, where the transition from baryonic to dark matter dominated regions occurs. For different radii R, we study the enclosed stellar ($M_s(< R)$) to total mass ($M_L(< R)$) plane, which can be viewed as a projection of the fundamental plane. Extrapolating dark matter profiles, we find an extension of the concentration to virial mass relation to unprecedented low masses. Finally we examine possible diagnostics of the baryonic cooling process and test common prescriptions used in simulations.

Über die Verteilung leuchtender und dunkler Materie in starken Gravitationslinsen

Zusammenfassung: Das Zusammenspiel von leuchtender und dunkler Materie ist von grundlegender Bedeutung für die Entstehung von Galaxien. Diese wird als mehrstufiger Prozess angenommen, der mit dem gravitativen Kollaps dunkler Materie beginnt und das Einfallen baryonischen Gases in entstandene Potentialtöpfe nach sich zieht. So wie Baryonen kälter werden, bilden sich Sterne, was die Entstehung der ersten Galaxien zur Folge hat. Der Entstehungsprozess ist bis heute wenig verstanden, jedoch geben Beobachtungen Aufschluss über empirische Beziehungen zwischen charakteristischen Galaxiemerkmalen, wie z.B. die Fundamentalebene elliptischer Galaxien, die eine Korrelation zwischen Helligkeit, Größe und Geschwindigkeitsdispersion darstellt. In dieser Arbeit werden Aspekte der Galaxienentstehung durch zwei Verfahren erkundet. Nichtparametrisches modellieren von Gravitationslinsen ermöglicht es, die in ihnen enthaltene Gesamtmasse einzuschränken. Die stellare Masse kann mittels Populationssynthese abgeschätzt werden. Beide Methoden werden auf eine Auswahl von 21 Gravitationslinsen, für die HST Daten zur Verfügung steht, angewendet. Damit wird in einem ersten Schritt die Fundamentalebene reproduziert. Wie gezeigt wird befinden sich Gravitationslinsengalaxien nahe am virialen Gleichgewicht. Wir extrahieren radiale Massenprofile (räumlich aufgelöst $\lesssim 1$ kpc) und finden einen gemeinsamen radialen Bereich, in dem der Übergang vom baryonen-dominierten Gebiet zum dunkle-materie-dominierten Gebiet stattfindet. Für unterschiedliche Radien R untersuchen wir die durch eingeschlossene stellare Masse ($M_s(< R)$) und Gesamtmasse ($M_L(< R)$) aufgespannte Ebene, die als Projektion der Fundamentalebene betrachtet werden kann. Durch Extrapolation der Dunkle-Materie-Profile, finden wir eine Erweiterung der Relation zwischen Konzentration und Virialmasse hin zu beispiellos kleinen Massen. Schließlich untersuchen wir mögliche Diagnoseverfahren für die Kühlung von Baryonen und testen deren Realisierung innerhalb von Simulationen.

Contents

Acronyms used in this work

AC	Adiabatic Contraction
ACS	Advanced Camera for Surveys
CASTLES	CfA-Arizona Space Telescope LEns Survey
CDM	Cold Dark Matter
COSMOS	Cosmic Evolution Survey
DM	Dark Matter
FP	Fundamental Plane
GOODS	The Great Observatories Origins Deep Survey
HST	Hubble Space Telescope
IMF	Initial Mass Function
IRAF	Image Reduction and Analysis Facility
MCMC	Markov Chain Monte Carlo
NDF	Number of Degrees of Freedom
NFW	Navarro Frenk White (profile)
NICMOS	Near Infrared Camera and Multi-Object Spectrometer
PA	Position Angle
PSF	Point Spread Function
RMS	Root Mean Square
RMSD	Root Mean Square Deviation
SDSS	Sloan Digital Sky Survey
SFH	Star Formation History
SIE	Singular Isothermal Ellipsoid
SIS	Singular Isothermal Sphere
SIS+γ	Singular Isothermal Sphere plus Shear
SLACS	Sloan Lens ACS Survey
SPIDER	Spheroids Panchromatic Investigation in Different Environmental Regions
SPS	Stellar Population Synthesis
WFPC2	Wide Field Planetary Camera 2
WMAP	Wilkinson Microwave Anisotropy Probe

— The vastness of the heavens stretches my imagination – stuck on this carousel my little eye can catch one-million-year-old light.
— A vast pattern – of which I am part . . .

Richard Feynman,
The Feynman Lectures on Physics

1 Introduction

Nature provides a rich variety of light patterns caused by curved space time similar to those well-known and understood in geometrical optics. Although the reason for the deflection of photons is totally different - a change in material properties leading to a rotation of a wave front in classic optics, while the underlying medium, space, through which light propagates is distorted in general relativity - the governing theories can be expressed in one common formalism, Fermat's principle. It states that the time light takes to cover the distance from one fixed point to another is an extremum. In this mathematical framework, optics and gravitational lensing are represented by the minimal and the maximal solution of a calculus of variations problem. Knowing this, the light patterns can be used to constrain the properties of the lens. For astrophysical lenses the distribution of its matter constituents can be explored.

Gravitational lensing - the early years

Gravitational lensing is part of Einstein's theory of general relativity, which explains the interaction of matter and space-time. In the aftermath of the solar eclipse in 1919 and the observation of the shift of a background star close to the solar disc, which supported Einstein's theory, other manifestations of light deflection were considered. In 1924 Orest Chwolson published an article on the possibility of a luminous circle caused by a deflector, e.g. a foreground star in perfect alignment with a light source, a background star (Chwolson 1924). History gave initially little credit to his idea. A few years later Einstein discussed the very same *lens-like action* in a brief note, published only at request of the Czech engineer Rudi W. Mandl (Einstein 1936) and considered its direct observation "*hopeless*". Despite Einstein's doubts about Chwolson's luminous circles they are nowadays most commonly known as Einstein-Rings. Certainly, at that time Einstein was thinking not of galaxies but of stellar sized objects acting as lenses, although extragalactic nebulae were known since Hubble's distance measurement of M33 (Hubble 1926).

It was Fritz Zwicky who first came up with the idea of clusters of galaxies acting as giant lenses (Zwicky 1937). His visionary idea was rooted in efforts to explain the kinematics of the Coma galaxy cluster or, more precisely, the mismatch between the cluster mass deduced from the virial theorem and the mass inferred from the stars of the cluster members. This resulted in the postulation of a hidden mass component, dark matter. Zwicky figured that the masses of galaxies could be directly measured by lensing. Moreover, he pointed out that lensing could be used as a tool to test general relativity. Observations of galaxy clusters were not the first evidence of a hidden mass component in galaxies. Earlier in the 30's Jan Hendrik Oort had claimed that the kinematics of stars in

the solar neighbourhood cannot be explained by the visible mass only (Oort 1932). The notion was further strengthened through observations by Volders (1959) using rotation curve measurements of spiral galaxies.

Luminous and missing mass

Little progress in either field, the "missing mass" in clusters or galaxies and the unverified existence of lenses, was achieved until the 1970's. Using the then-newest generation of spectrographs, Vera Rubin was able to determine the radial motion of very faint hydrogen emission regions at large projected distances from the centre of their host galaxies (Rubin & Ford 1970). With their then-unprecedented radial extent many rotation curves speak in favour of a dark matter component (Bosma 1978). Gravitational lenses as suggested by Zwicky or Chwolson were not found until the rather accidental discovery of the lens system $Q0957+561$ by (Walsh et al. 1979). Soon after its discovery first attempts on measuring the mass using the lens effect were made (see e.g Young et al. 1981, Falco et al. 1985*a*). With the arrival of better photometric data and the discovery of new lens systems mass estimates became increasingly precise. Rix et al. (1992) were the first to determine the mass of the Huchra-lens $Q2237+0305$ assuming a fixed conversion factor between mass and light.

Since then the combination of gravitational lensing and photometric observations – combined with the study of stellar dynamics – have been very effective at constraining the total mass responsible for the lens effect and the total mass-to-light ratio Υ. However, dynamical studies are not ideal for a direct decomposition of dark and stellar mass components. As galaxies emit the combined light of billions of unresolved stars, assumptions on the light distribution are necessary in order to estimate their stellar content. The total mass-to-light ratio is mostly much different from the stellar mass-to-light ratio depending on the galaxy type. If an average Υ similar to that of the Milky Way is assumed one can estimate the stellar mass distribution of an observed galaxy by applying this simplistic conversion factor. Doing so, however, neglects the complex build-up of galaxies consisting of different stellar populations and morphological components, such as bulge and disk, as well as evolutionary trends of Υ.

During the 1950's and 60's the understanding of stellar chemistry and evolution improved. Ground-breaking studies, e.g. of Eggen et al. (1962), showed for disjunct stellar populations correlations between angular momentum and UV-excess as an indicator of age, which was suggestive for an evolutionary sequence of events. The first studies designed to directly express the observed galaxy light in terms of stellar mass were conducted by Spinrad & Taylor (1971) and Faber (1972). They attempted to assemble the integrated spectrum of a galaxy by a linear combination of individual stellar spectra. Due to the large number of free parameters, such as the number of stars of a certain spectral type, this approach was abandoned. More sophisticated techniques – known as stellar population synthesis – reduce the problem to few main parameters, such as the initial mass function (IMF), the star formation rate (SFR) and the chemical enrichment, that can be used to compute the integrated spectral evolution (e.g. Tinsley 1978, Bruzual 1983).

The dark matter paradigm

From both the study of gravitational lenses and the study of stellar populations one can hope to gain insights about structure formation and evolution within our multi-component universe consisting of baryons, dark matter and dark energy. It must be emphasized that despite the focus of this thesis on the dark matter paradigm, alternative explanations for plateaued rotation curves, mass profiles of galaxy clusters and gravitational lensing are available. Most of them attempt to modify Newtonian gravity (by amending the Poisson equation) or general relativity (by amending the action integral) without invoking dark matter. There are two particularly important arguments in favour of dark matter. Firstly, weak lensing maps of cluster mergers compared with X-ray data show that the gravitational potential does not trace the plasma component, which is the dominant baryonic mass component rather than the stellar content (Clowe et al. 2006, Bradač et al. 2008). Secondly, micro-lensing studies reveal anomalous flux ratios of lensed images that indicate a ratio of smooth (dark matter) to clumpy matter (stars) which exceed 50%, for some lenses even 90% (Schechter & Wambsganss 2002, Pooley et al. 2009, Bate et al. 2011). Neither effect can be explained by modified theories of gravity alone. Nevertheless, at present incontrovertible proofs of dark matter remain elusive.

The formation of galaxies can be largely explained by means of N-body simulations, that model the motion of gravitationally interacting particles. Originally intended to simulate star clusters (von Hoerner 1960) they are used today on large scales to verify cosmological models (e.g. Springel et al. 2005). Due to limited computation time most cosmological simulations only take into account one collisionless matter component, dark matter. However, in these models structure formation occurs in an expanding universe that drives matter apart. This so-called Hubble flow acts against the gravitational collapse. In cold dark matter (CDM) simulations structures form hierarchically, i.e., smaller masses collapse earlier than larger masses and are on average denser. Navarro, Frenk & White (1996) found that the density distribution of simulated dark matter halos follows a characteristic power law (henceforth called NFW profile). The baryonic counterpart however is commonly added to the dark matter halos only after the simulations are completed. The gravitational interactions between baryons and dark matter are then modeled by means of semi-analytic prescriptions. In contrast to the purely numerical method semi-analytics enrich the picture of hierarchical structure formation by including physical processes such as angular momentum transport, dynamical friction and adiabatic contraction. Considering baryon-dark matter interactions and adiabatic contraction might also help to find better agreement between simulations and observations, as they are thought to affect the matter distribution in particular in the centre of massive galaxies.

Observations versus simulations

Comparisons between simulations and observations yield a variety of inconsistencies, which are often attributed to model shortcomings. CDM simulations, for example seem to indicate that cuspy matter distributions are favoured in dense halo centres (Flores & Primack 1994). Observations, however, tend to belie this notion (e.g. de Blok 2010). Nevertheless, the occurrence of multiple lensed images requires the surface mass density to be large (i.e. a central convergence larger unity), a condition always fulfilled for cuspy density profiles, like NFW, but not necessarily for cored profiles, as κ_c is inversely proportional to the

core radius. Lensing statistics on the contrary seem to give evidence against a dominant cuspy class of elliptical galaxies (e.g. Chen 2003, Li & Chen 2009). Modifying the dark matter properties (e.g., self-interacting or warm dark matter) or including interactions between baryons and dark matter to dissolve the cusps are commonly invoked solutions to this problem (see e.g. Romano-Díaz et al. 2008, Peirani et al. 2008). The problem can, however, be addressed by gravitational lens modeling in a unique way. If baryons change the mass profiles in the central region of dark matter halos, lens models considering the presence of baryons appear to be well suited to reproduce the mass distribution in the poorly constrained central region of the lens system.

Lens modeling - conventional or free form

There is one critical caveat in conventional analytic models of gravitational lenses. Using mass models and model-based prescriptions for gravitational lens modeling introduces hard-to-quantify deviations from real mass distributions. Assuming a mass model for a lensing system excludes mass distributions, which are not accessible in the parameter-space of the model and introduces the problem of model non-uniqueness. This holds also for the modeling of the light distribution of a galaxy. Such fits are based on analytic formulas whose reliability to recover the actual light or mass distribution is not always given, as will be shown in this thesis.

Saha & Williams (1997) introduced a novel technique of free form modeling, which permits the mass-reconstruction of lenses in a pixelated manner, without making use of conventional pre-defined mass models, like isothermal ellipsoid, King or De Vaucouleurs model (see e.g. Keeton 2001*a*). With an increasing number of observational constraints and improved precision single-galaxy parametric models have become unacceptable (Schechter et al. 1997). One explanation can be found for example in the impact of nearby galaxies, which perturb the lens morphology. In view of the hard to quantify number of perturbers a multi-component extension of the parametric modeling approach seems difficult, while the free form models offer a viable alternative. Ferreras, Saha & Williams (2005) first combined free form mass reconstruction of lenses with stellar population synthesis in a pixel-based manner to get insights in the distribution of luminous and dark matter in lensing galaxies. Directly analyzing resolved pixelated stellar and total mass maps is a promising way of addressing problems in astronomy related to the internal structure of galaxies.

1.1 Key problems

Due to the aforementioned shortcomings of parametric models, for which further evidence is given in Chapter 3, extensive use is made of pixel-based mass reconstruction (Saha & Williams 1997, 2004) throughout this dissertation to address the following key problems.

- *The fundamental plane and the degree of virialization of gravitational lenses:* Early-type galaxies follow the fundamental plane, a well-known scaling relation between effective radius, kinematic velocity dispersion and surface brightness. Theoretical predictions of this relation based on the virial theorem, however, show a significant deviation ('tilt') from observations. The reason for the fundamental plane tilt is still to be found. Commonly offered explanations invoke variation of the stellar

mass-to-light ratio with luminosity, varying DM content and non-homologies, such as structural and orbital anisotropies. All these solutions address different aspects of the interplay between the stellar and dark matter. In this framework we give answers to the following questions, which help to narrow down the variety of explanations: Is the lensing inferred velocity dispersion from non-parametric mass reconstruction equal to the kinematic velocity dispersion? Is this applicable to cluster scale lensing objects? Are the computed lens mass and the virial mass consistent with the fundamental plane? Does the fundamental plane relation extend to galaxy clusters?

- *Resolving baryonic and dark matter distributions:* The combination of stellar population synthesis (SPS) and pixel-based mass reconstruction can be used to visualize the dark matter. The SPS process requires photometric modeling of lens galaxies in as many spectral bands as possible in order to constrain population synthesis models. We produce these models and use the stellar mass profiles output by the SPS routine described in Ferreras et al. (2008) to analyze the radial dependence of stellar versus total mass profiles for a sample of 21 lenses as well as their baryon fractions. First intriguing insights in the set-up of lens galaxies can be given in terms of enclosed mass ratios and novel concentration indices for stellar and total mass profiles. In particular we investigate stellar baryon fractions and their impact on dark matter halos on scales below 10 kpc.

- *Concentration-to-virial mass relation and testing adiabatic contraction:* Previous studies have found evidence for an inverse proportionality between concentration and virial mass that is a natural consequence of CDM cosmologies (e.g. Bullock et al. 2001). We deduce the concentration to virial mass relation for unprecedentedly low virial masses for a sample of 18 lenses. Moreover, by comparing stellar baryon fractions, baryonic length scales and concentration parameters with predictions from synthetic, adiabatically contracted halo profiles, we test the quality of standard prescriptions for baryonic cooling.

The questions raised and investigated in this work are directly connected with a variety of current research topics, all of which aim to enrich our picture of structure formation and evolution of galaxies. Results of this study may serve as benchmarks for large scale simulations, studies of the initial mass function, baryon-dark matter interactions and the modeling of strong gravitational lenses.

1.2 Outline

This thesis is structured as follows. A brief introduction to the theoretical framework and basic concepts is given in Chapter 2. The methodology chapter provides the concepts of parametric and non-parametric lens modeling and stellar population synthesis (Chapter 3). It is followed by three chapters addressing the key problems of the fundamental plane and the degree of virialization of gravitational lenses (Chapter 5), resolving baryonic and dark matter distributions (Chapter 6) and the concentration-to-virial mass relation and testing adiabatic contraction (Chapter 7). We summarize the results and give an outlook for future work in Chapter 8.

2
Fundamental Concepts

The studies carried out in this thesis are closely connected to different topics in astrophysics, such as lens modeling, galaxy scaling relations and galaxy evolution, just to mention few. Strong lensing, as a tool to investigate the mass distribution in centres of lens galaxies, is introduced in Section 2.1. We continue by giving a brief overview of the diversity of lens systems in Section 2.2. The distance measures commonly used in the framework of cosmology are explained in Section 2.3. In Section 2.4 the big picture of hierarchical structure formation is given. Galaxies, the products of structure formation, are briefly classified in Section 2.5. The distribution of masses of stellar populations in galaxies is governed by the theoretical initial mass function. It is a key ingredient in the stellar population synthesis and therefore introduced in Section 2.8. As galaxies evolve they change not only their stellar composition but also their mass distribution. We discuss the most important processes likely to change stellar and dark matter distributions in galaxy centres in Section 2.7. Since galaxies obey a number of underlying regularities, so-called scaling relations, we discuss a selection important to this work in Section 2.6. Finally, analytic functions used to parameterize light, stellar mass or dark matter distributions are given in Section 2.9.

2.1 Gravitational lensing

The research field of gravitational lensing can be structured into several sub categories with respect to its phenomenology. *Strong lensing* produces multiple images of the same background object, if its light passes close enough to a dense region in space. In the case of a pointlike background object, e.g. a quasar, which is lensed by a foreground galaxy, two or more quasar images can be produced with typical angular separations of order one arcsecond. If the background source is a resolved object a strong lens produces extended distorted images of the same, so-called arcs or Einstein rings. Image distortions occur also if the density of the region crossed by light is not sufficient to produce several images. Latter regime is generally referred to as *weak lensing*. *Microlensing* refers to an angular regime of the order of microarcseconds, where several lensed images with a separation below the resolution limit are produced by stellar-sized objects. Uncorrelated brightness variations in the lightcurves of different strongly lensed images are a consequence of this effect. For more details on the different classes of gravitational lensing see Schneider et al. (2006).

A more mathematically motivated distinction between strong and weak lensing will be shown in the following. Gravitational lensing has equivalent representations in different physical and mathematical disciplines. In the following three equivalent formulations of

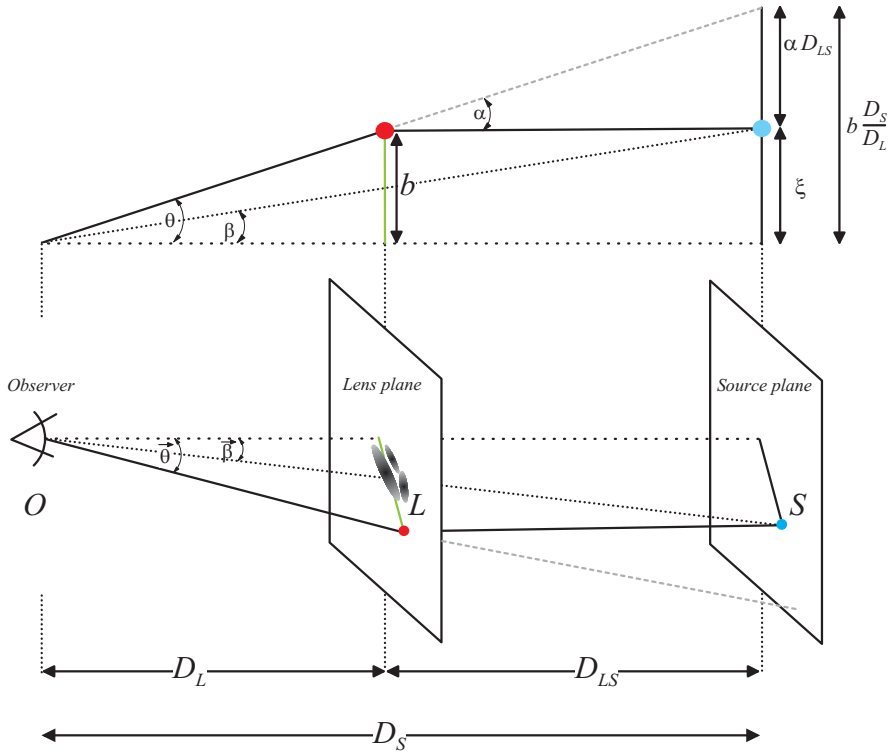

***Figure 2.1*:** Schematic illustration of a gravitational lens in the approximation for thin lenses and small angles. The lower part shows the scheme in a three-dimensional side view. The upper part is a projection. The cyan dot marks the source position, the red dot the lensed image position. The green line highlights the distance, described by the impact parameter b. All symbols are explained in the text.

gravitational lensing shall be introduced to clarify the phenomenology of strong gravitational lensing. All of which give useful insights in different aspects of the one lens effect.

2.1.1 The lens equation - a vectorial approach

From the schematic illustration (Fig. 2.1) one can deduce the following relation for the distance vector $\vec{\xi}$ depending on the impact vector $\vec{b}$, the deflection angle α, and the angular diameter distances D_L, D_s and D_{LS}.

$$\vec{\xi} = \frac{D_S}{D_L}\vec{b} - D_{LS}\ \vec{\alpha}(\vec{b}) \tag{2.1}$$

Note that the upper scheme in Fig. 2.1 represents the two-dimensional projection of the three-dimensional lower scheme, which explains the henceforth used vectorial notation. Switching to purely angular coordinates, this becomes the *lens equation*:

$$\vec{\beta} = \vec{\theta} - \frac{D_{LS}}{D_s}\vec{\alpha}(D_L\vec{\theta}), \tag{2.2}$$

which is a linear mapping from the lens to the source plane. Introducing a two-dimensional potential ψ whose gradient is the deflection angle, Eq. 2.2 can be written as

$$\vec{\beta} - \vec{\theta} = \frac{D_{LS}}{D_s}\vec{\alpha}(D_L\vec{\theta}) = \nabla\psi(\vec{\theta}). \tag{2.3}$$

With the enclosed surface mass density $\Sigma(\vec{b}) = \int \rho(\vec{b}, z)dz$, written as the density integrated along the line of sight, the deflection angle ($\alpha = 4GM/bc^2$, with gravitational constant G, lens mass M, impact parameter b and speed of light c) in the approximation for thin lenses, i.e. their spatial extent is negligible against its distance to the observer, can be written as

$$\vec{\alpha} = \frac{4G}{c^2} \int \frac{(\vec{b} - \vec{b}')\Sigma(\vec{b}')}{|\vec{b} - \vec{b}'|} d^2b'^2. \tag{2.4}$$

Using this expression in the derivative of Eq. 2.3 yields the Poisson-Equation

$$\nabla^2\psi(\vec{\theta}) = \frac{D_L D_{LS}}{D_s} \frac{8\pi G}{c^2} \Sigma(\vec{\theta}) = 2\frac{\Sigma(\vec{\theta})}{\Sigma_c} = 2\kappa(\vec{\theta}), \tag{2.5}$$

where κ is the convergence, conveniently chosen to be a dimensionless quantity, which serves as a source field and $\Sigma_c = c^2 D_s / 4\pi G D_L D_{LS}$ is the critical surface density. The latter can be regarded as a boundary between strong and weak lensing. For a mean enclosed surface density larger than the critical one, i.e. $\Sigma > \Sigma_c$ ($\kappa > 1$) multiple images are produced. This does not hold for the weak lensing regime, equivalently described by $\Sigma < \Sigma_c$ ($\kappa < 1$).

2.1.2 Wavefront picture - a geometrical method

A gravitational lens can be approximated as a slit diffraction set-up. Huygens' principle states that each point of a wavefront can be considered as the starting point of a spherical wavelet, which is constituent of a new wavefront. The latter can be regarded as a superposition of all wavelets. Kayser & Refsdal (1983) elaborated the difference in light travel time between gravitational lens images in this framework, which comes in helpful for the understanding of critical lines and caustics. The left hand scheme of Fig. 2.2 shows a two-dimensional illustration of the light path. One wavefront propagates from the source (S) to the the lens (L), which, depending on the shape of the gravitational potential, inflicts a distortion upon the wavefront. For the given example, this can be approximated by different wavefronts emerging from L at three different positions (A, A', B) and time-stamps. Their superposition results in the typical caustic-like structure. An image of S will be seen by an observer (O) for a line-of-sight perpendicular to each wavefront. Thus for any position between the dashed envelopes (critical curve), which connects the locations of crossing wavefronts, three images of S are seen. Outside this region the number of observed images is reduced. As one can see in Fig. 2.2 a signal originating from S will be seen first in image B, then in A and eventually in A'. The time delay between the signal seen in two different images corresponds to the distance of wavefronts, which depends on the difference in the length of the respective light paths. This difference is larger than the purely geometrical difference of light paths, as the lens potential – speaking in terms of general relativity – warps the space. As a three-dimensional counterpart, the right hand panel of Fig. 2.2 shows five spherical wavefronts with time delays, four of which are directly visible. In superposition a diamond shaped window is produced through which an observer will see all five images.

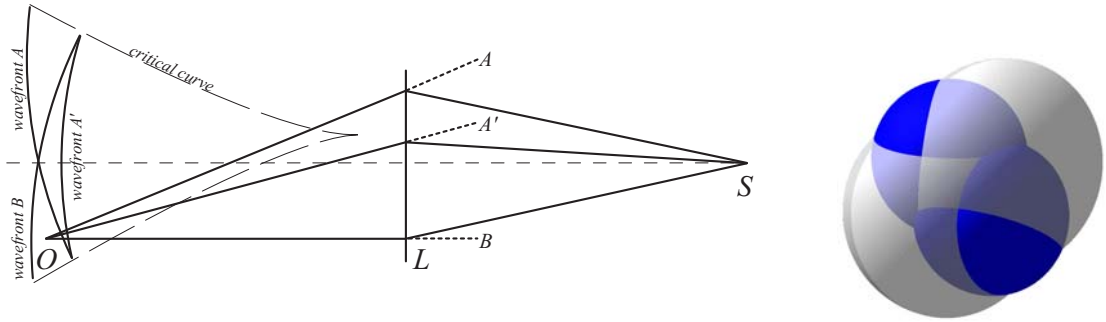

***Figure 2.2*:** Left: Schematic illustration of an extended deflector in the wavefront picture according to Kayser & Refsdal (1983). Here a non-symmetric case is shown, i.e. the upper and lower critical curves are not symmetric with respect to the central line. Three images will be observed from any location between the critical curves. The difference in light travel time corresponds to the distance between wavefronts. Right: Three-dimensional analogue to left hand scheme. Instead of three positions there are five from which spherical wavefronts emerge. The one produced by the central image (counterpart to A') is not visible in this illustration. The colours indicate wavefronts with comparable time-delay.

2.1.3 The arrival time surface - using Fermat's principle

The time delay can be written conveniently as a sum of a geometrical t_{geom} and a gravitational t_{grav} contribution, as shown below by means of light path integration. Cooke & Kantowski (1975) showed the same in a wavefront picture. The equivalence of light path integration and wavefront method was shown by Borgeest (1983). However, the following equations are an approximation for small angles and are given in the observer frame, which explains the additional factor of $(1 + z_L)$, where z_L denotes the redshift of the lens.

$$t_{geom}(\vec{\theta}, \vec{\beta}) = \frac{1}{2c}(1 + z_L)\frac{D_L D_S}{D_{LS}}(\vec{\theta} - \vec{\beta})^2 \tag{2.6}$$

$$t_{grav}(\vec{\theta}) = -2(1 + z_L)\int \varphi(\vec{\theta})\, ds \tag{2.7}$$

In Equation 2.7, $\varphi(\vec{\theta})$ denotes the Newtonian potential, which is integrated along the line of sight. This yields the two-dimensional potential ψ known from Eq. 2.3, which satisfies the Poisson Eq. 2.5. Adding up Eq. 2.6 and 2.7 gives the total time delay. Using

$$\tau = \frac{D_{LS}}{(1 + z_L)D_L D_S}t \tag{2.8}$$

this can be more conveniently written as

$$\tau(\vec{\theta}, \vec{\beta}) = \frac{1}{2}(\vec{\theta} - \vec{\beta})^2 - \psi(\vec{\theta}), \tag{2.9}$$

which is called the arrival-time surface. Judging by its quality to visualize time differences, it can be regarded as a relative of the wavefront. If we assume for a moment the potential ψ to be negligible – which means that effectively there is no lens mass – τ is fully represented by the quadratic term. In that case the arrival-time surface looks like a paraboloid as shown in the right hand panel of Fig. 2.3. Its rotation axis indicates the time delay, the surface contours are isochrones. One should emphasize that the arrival time surface cannot be directly observed, except as a relative time-delay between images. However,

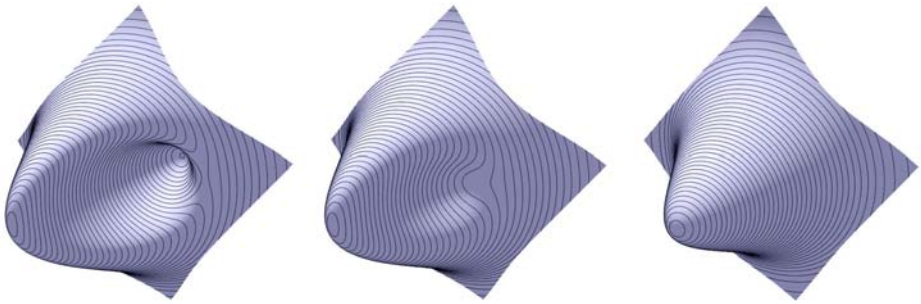

***Figure 2.3*:** Illustration of the arrival time surface for large (left panel), small (middle panel) and negligible (right panel) contributions from the gravitational potential. The rotation axis indicates the time-delay, the contours are isochrones. Images occur where the surface has a minimum, a maximum or a saddle-point.

as we gradually increase the lens mass, i.e. $\psi < 0$, the arrival-time surface will get distorted, as shown in middle panel of Fig. 2.3, until eventually new extrema form (left panel).

Fermat's principle states that the time light takes to cover the distance between two fixed points is an extremum. As a consequence, images of a lensed background source will be located at stationary points in the arrival time surface, meaning

$$\vec{\nabla}\tau(\vec{\theta}) = 0. \tag{2.10}$$

This is certainly fulfilled for the simple case of negligible lens mass, where we get only one image located at the minimum of the paraboloid. Increasing the potential creates additional extrema and saddle points which become visible for the distorted arrival time surface. Isochrone contours passing through saddle points are of special significance as they build figuratively the skeleton of the arrival time surface. We will come back to this in the next section. The partial derivative of Eq. 2.9 becomes

$$\vec{\theta} = \vec{\beta} + \nabla\psi(\vec{\theta}) \tag{2.11}$$

The gradient of the two-dimensional scalar potential points into the direction of the maximum increase, that is towards the apparent source position and its modulus is the angular offset between apparent and actual source position. The latter can be expressed as $\alpha D_{LS}/D_S$, as shown in Fig. 2.1, and Eq. 2.11 turns into the familiar lens equation 2.2.

Since mass reconstruction is a tool essential to this work the following re-writing of the lens equation comes in handy. As the Poisson Eq. 2.5 must be solved to infer the projected mass density Σ the arrival time surface can be written as

$$\tau(\vec{\theta}) = \frac{1}{2}(\vec{\theta} - \vec{\beta})^2 - 2\nabla^{-2}\kappa(\vec{\theta}). \tag{2.12}$$

Hence it is shown that Fermat's principle and the scalar description of the arrival time surface is an analogue to the previously introduced vector notation (Blandford & Narayan 1986).

Apart from the stationary points on the arrival time surface, there is additional information included in the curvature (second derivative) of $\tau(\vec{\theta})$. Looking at the simple

parabola it becomes clear that sharp peak-like features in the surface correspond to less photons per projected area, which defines the demagnification case. Magnification instead occurs for broad valleys on the surface. As the second derivative of Equations 2.9 and 2.11 we get

$$\vec{\nabla}\vec{\nabla}\tau(\vec{\theta}) = \mathbf{1} - \vec{\nabla}\vec{\nabla}\psi(\vec{\theta}) = \vec{\nabla}\vec{\beta}. \tag{2.13}$$

As an aside, transformations like $\kappa \to 1-\lambda(1-\kappa)$ and $\beta \to \lambda\beta$ with an arbitrary constant λ will produce the same image configuration, as they just scale the arrival-time surface. In other words rescaling the lens mass and adding/subtracting a constant mass-sheet will not change any observed quantity. This effect known as the 'mass-sheet-degeneracy' is discussed amongst other lensing degeneracies in Gorenstein et al. (1988) and Saha (2000*a*).

However, from Eq. 2.13 we see already that the curvature of τ is equal to a change in source-position causing the image to shift. Latter image displacement is the inverse of the magnification. Thus we can define the magnification tensor $\mathbf{M}$ to satisfy the equation

$$\mathbf{M}^{-1} = \vec{\nabla}\vec{\nabla}\tau(\vec{\theta}). \tag{2.14}$$

Like any symmetric 2×2 matrix $\mathbf{M}^{-1}$ can be re-written in the form

$$\mathbf{M}^{-1} = (1-\kappa)\begin{pmatrix} 1 & 0 \\ 0 & 1 \end{pmatrix} - \gamma \begin{pmatrix} \cos 2\phi & \sin 2\phi \\ \sin 2\phi & -\cos 2\phi \end{pmatrix} \tag{2.15}$$

By comparison with 2.12 and 2.13 one finds that not coincidentally κ is indeed the convergence introduced in Eq. 2.5, where γ is a traceless component of $\mathbf{M}^{-1}$ called shear, originating mostly from external masses influencing the shape of the lens potential and thus ψ. It changes the shape of an image but not the size. The scalar magnification, the determinant of $\mathbf{M}^{-1}$, brings an interesting feature of the mathematical description of lensing to light, the case of infinite magnification. We have

$$det(\mathbf{M}) = ((1-\kappa)^2 - \gamma^2)^{-1}, \tag{2.16}$$

which shows a singular behaviour for $\gamma = |1-\kappa|$. All points in the lens plane that satisfy this relation lie on critical lines, which – formally speaking – separate regions with same algebraic sign of the tensor's eigenvalues (λ_1,λ_2), i.e. both positive, both negative or one positive and one negative. They consequently frame regions in which $\tau(\vec{\theta})$ is allowed to have maxima, minima or saddle-points. The lens equation is a mapping from the lens to the source plane. If critical lines are mapped to the source plane we obtain caustic curves. Caustics separate regions in the source plane that determine the number of lens images. The phenomenology of lenses will be discussed in the following section on basis of the caustics, critical lines and saddle-point contours.

2.2 On the phenomenology of gravitational lenses

The arrival time surface comes along in a variety of shapes, corresponding to different lens image configurations. All of which exhibit elementary contours which have the interesting property to be self-crossing, which consequently means that they pass through a saddle-point. Those saddle-point contours can be classified depending on their morphology as lemniscates and limaçons shown in the top and bottom row of Fig. 2.4 respectively. From an initial paraboloid (circular contour) with one minimum (L) the contours can evolve to form an outer or an inner loop. The latter case is known from Fig. 2.3 and as one can see the inner loop encompasses a maximum in arrival-time.

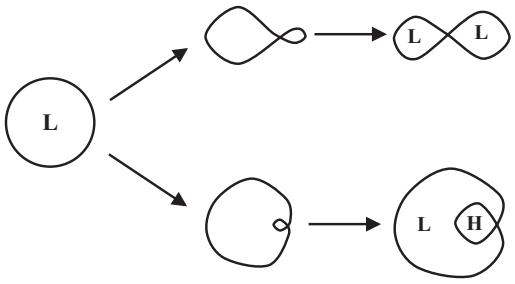

***Figure 2.4*:** Self-crossing contours. Top (bottom) row shows formation of lemniscates (limaçons). Maxima (minima) are marked with an H (L) for high (low) time-delay. According to Figure by H. M. AbdelSalam in Saha & Williams (2003).

The former case forms instead two minima. Either way one saddle-point is produced. Eventually saddle-point contours can form nested structures, even more complex than the one shown in Fig. 2.5. Critical curves, as introduced in the last section separate regions in which maxima, minima and saddle-points may occur (Fig. 2.6). As gradually as saddle-point contours can form inner and outer loops new images are created. Since they emerge in pairs of saddle-point and minimum or maximum, the point of their closest approach must lie on a critical curve. This points us to another equivalent interpretation of the critical lines where images merge under theoretically infinite magnification. Magnified or demagnified images are indicated by larger or smaller red dots in Fig. 2.5. As the critical curves are mapped to the source-plane via Eq. 2.3 they become the caustical curves shown in Fig. 2.7. It should be noted that the inner diamond-shaped (asteroid) caustic maps onto the outer critical line and vice versa, indicated by the line colour. Shifting the source closer to these lines affects the image positions. If the source lies at the centre of the diamond shaped caustic (asteroid caustic), a cross-configuration of four images can be seen (Einstein-cross). Note that a number of distinct images are produced. Einstein-rings cannot be reproduced as we consider point-sources (unresolved background objects) and elliptical potentials only. However, the closer the source gets to a caustical line the less symmetric becomes the image configuration. From Fig. 2.6 and 2.7 it becomes clear as the source crosses a caustic in outward direction from the centre images merge and vanish eventually.

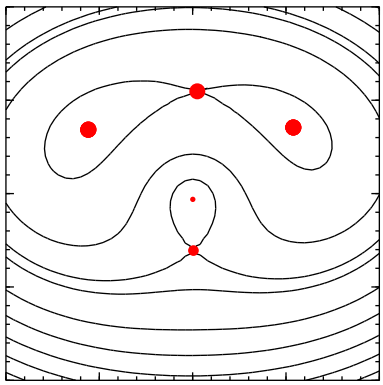

***Figure 2.5*:** Isochrone contours of the arrival-time surface. Size of red dots indicates (de-)magnification. The lower saddle-point is about the original source size.

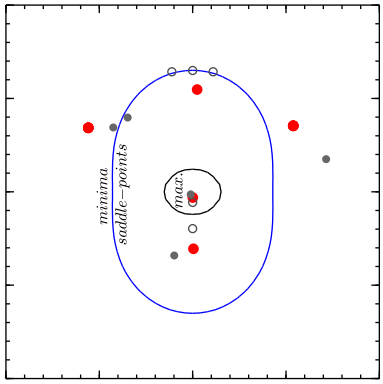

***Figure 2.6*:** Critical lines in lens-plane. Filled and open circles indicate image positions corresponding to the source positions in Fig. 2.7.

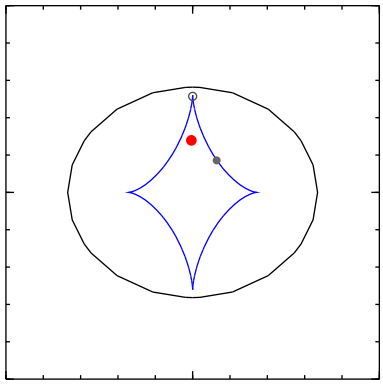

***Figure 2.7*:** Caustical lines in source-plane with different source positions.

So-called fold caustics define the edges of asteroid caustics which, when crossed by the source, lead to a two-image merger (black filled circles in Fig. 2.6 and 2.7), whereas cusp caustics, i.e. the sharply peaked caustics, lead to three-image mergers (open circles). A source situated between asteroid and circular cusp produces still three images. Depending on the properties of the projected potential of the lens mass and possible convergence and shear contributions from the lens environment the caustic lines can diverge from the simple case discussed so far. The asteroid and circular caustics may vary in size and shape. The inner caustic might even extend beyond the circular caustic, which means that for source positions inside asteroid but outside circular caustic two images merge and vanish on the inner critical line, but three remain to produce a naked cusp configuration. This is speaking in terms of saddle-point contours the rare case of a lemniscate not encompassed by a limaçon (top row Fig. 2.4). However, more detailed studies on interesting lens morphologies can be reviewed in Saha & Williams (2003). So far we have seen predictions for lens systems that involve an odd number of images. Dyer & Roeder (1980) demonstrated that non-pointlike lens masses produce always an odd number of lensed quasar images. This odd-number theorem is a consequence of a general theorem for non-singular lenses, which is commonly stated in the form

$$\langle maxima \rangle + \langle minima \rangle = \langle saddle \rangle + 1.$$

This can be easily verified for the lensed image systems in Fig. 2.6. Consequently the sum over extrema and saddle points must be an odd number. Observations, however, seem to contradict the theorem as mostly doubly or quadruply imaged quasars are found (see Fig. 4.1). Evans & Wilkinson (1998) investigate under which conditions one of the previously odd number of images can be lost and find that models with sufficiently steep density cusps, i.e. $\rho \propto R^{-\gamma}$ and $1 < \gamma < 2$ do not possess radial caustics. Thus the maximum in Fig. 2.6 vanishes. The rather few exceptions with an odd number of images could be explained by a potential fourth image being too faint to be detected or by external perturbations causing one image to split (Schechter & Wambsganss 2002) or by the naked-cusp case as explained above. All cases are discussed in Oguri et al. (2008) for a cluster lens, however it is widely believed that for standard lensing galaxies the reason for a missing image is that the central image, as it should be produced in the maximum of a limaçon (see Fig. 2.5), is strongly demagnified by the commonly steep surface density profile of the lens (Narasimha et al. 1986).

Up today there are about 250[1] lens systems known. The amount of available lenses can be divided in resolved and unresolved lensed images of the background source. Resolved objects, like background galaxies, cover extended regions in Fig. 2.6. Consequently distorted images (arcs) are produced, which may span across the critical lines. However, lensing of quasars, which are unresolved background objects that serve as point-sources, offers the advantage of precise determination of image positions. The large range of lens morphologies imaginable from Figures 2.5 to 2.7 is reflected by the sample of strong lenses provided in Fig. 4.1, Section 4.2.

[1]This is a rough sum over the number of quasar (point source) lenses in the compilation of the CfA-Arizona Space Telescope LEns Survey (CASTLES) and the two galaxy lensing surveys, the Sloan Lens ACS Survey (SLACS) and the Cosmological Evolution Survey (COSMOS).

2.3 Basic concepts in cosmology

The theoretical basics given in this section can be found in Hogg (1999) and references therein. The standard world model consistently used throughout this thesis is defined by the Friedmann equation

$$H(a) = H_0 \left(\Omega_m a^{-3} + \Omega_k a^{-2} + \Omega_\Lambda\right)^{1/2}, \tag{2.17}$$

where $H(a) = \dot{a}/a$ defines the change of the scale factor a depending on a set of cosmological parameters, the present-day Hubble constant H_0 in units of (km s^{-1} Mpc^{-1}) and the energy densities Ω_i for matter ($i = m$), vacuum energy or dark energy ($i = \Lambda$) and curvature ($i = k$). The energy densities are defined in terms of the critical density $\rho_c = 3H^2/8\pi G$. With this the total energy density is defined as $\Omega_0 \equiv \rho/\rho_c$. The critical density was introduced to distinguish possible geometries of the universe. For an 'open' universe Ω_0 is larger than unity, that is, the universe will stop expanding and eventually collapse. For a 'closed' universe Ω_0 is less than unity, which means that the universe expands forever. The case of Ω_0 being exactly unity corresponds to a 'flat' universe with Euclidean geometry.

The Friedmann equation is the solution for the field equations of General Relativity in case of an isotropic homogeneous universe, defined by the Friedmann-Robertson-Walker metric

$$ds^2 = c^2dt^2 - a(t)^2 \left(\frac{dr^2}{1-kr^2} + r^2 d\theta^2 + r^2 sin^2\theta d\phi^2\right). \tag{2.18}$$

The aforementioned scale factor is defined by the redshift z to be $a \equiv (1+z)^{-1}$. In agreement with results from the Wilkinson Microwave Anisotropy Probe (WMAP) (Komatsu et al. 2011) we make consistently use of

$$(H_0, \Omega_m, \Omega_\Lambda, \Omega_k) = (72, 0.3, 0.7, 0.0). \tag{2.19}$$

Computing the dimensionless deceleration parameter q_0 defined by

$$q_0 = -\frac{\ddot{a}(t_0)a(t_0)}{\dot{a}(t_0)^2} = \frac{\Omega_m}{2} - \Omega_\Lambda \tag{2.20}$$

for the given set of cosmological parameters yields $q_0 = -0.55$. This determines the currently accelerating state of the universe.

For a proper treatment of cosmological length scales the following distance quantities must be known. The proper distance is the distance light covers from source to observer considering the expanding universe (Hubble drag), i.e.

$$D_p = \int c\ dt = c \int \frac{da}{aH(a)} = \frac{c}{H_0} \int_0^{z^*} (1+z)^{-1} \mathcal{I}(z)\ dz, \tag{2.21}$$

with

$$\mathcal{I}(z) = \frac{1}{\sqrt{(1+z)^2 \cdot (1+\Omega_m \cdot z) - (\Omega_\Lambda \cdot z(2+z))}} \tag{2.22}$$

The time-span $\tau = D_p/c$ is called the *look-back time.*

The comoving distance is a distance measure, which is independent of the Hubble drag. It is determined in the following way. As light trajectories are null geodesics ($ds^2 = 0$) the radial coordinate of Eq. 2.18 becomes

$$c^2 dt^2 = a(t)^2 \frac{dr^2}{1 - kr^2}, \tag{2.23}$$

which transforms to

$$D_{comov} = c \int_{t_0}^{t_1} \frac{dt}{a(t)} = \int_0^r \frac{dr'}{\sqrt{1 - kr^2}} = \begin{cases} sin^{-1} r & (k = 1) \\ r & (k = 0) \\ sinh^{-1} r & (k = -1) \end{cases} \tag{2.24}$$

The *luminosity distance* is defined by the ratio of luminosity L and flux F through the surface of a unit sphere, that is

$$d_L = \sqrt{\frac{L}{4\pi F}}. \tag{2.25}$$

The *angular diameter distance* is defined by the ratio of the proper size of an object and the angle it subtends. It is linked to the luminosity distance by

$$d_A = d_L/(1 + z)^2. \tag{2.26}$$

The integrand $\mathcal{I}(z)$ of Equation 2.22 can be used to re-write d_L as a function of z. Similar to the calculation of D_{comov} one finds for $\Omega_k \gtrless 0$

$$d_L(z_1, z_2) = \frac{(1 + z_2)}{H_0 |\Omega_k|^{1/2}} \ \text{sinn} \left\{ |\Omega_k|^{1/2} \int_{z_1}^{z_2} dz \ \mathcal{I}(z) \right\}, \tag{2.27}$$

where *sinn* is a placeholder for *sinh* in case of a hyperspherical universe ($\Omega_k > 0$) and for *sin* in case of a hyperbolic one ($\Omega_k < 0$). For a flat universe ($\Omega_k = 0$) we have

$$d_L(z_1, z_2) = \frac{(1 + z)}{H_0} \int_{z_1}^{z_2} dz \ \mathcal{I}(z). \tag{2.28}$$

Note that $D_{comov} = d_a$ holds only for the zero-curvature case.

2.4 Structure formation

In the previous sections, it was shown how massive objects produce a system of lensed images, but not how lensing galaxies themselves form in the first place. The basic ideas of structure formation will be given in the following.

Gaussian fluctuations in the matter distribution of the early universe provide a primordial power spectrum, which describes the density fluctuations after initial inflation. These fluctuations may be subject to dissipation, pressure and amplification due to gravitational instabilities. In the standard cosmological model the history of the universe is structured into distinct epochs dominated by different energy densities Ω_i. In the radiation dominated epoch $z \gtrsim 1000$ the expansion rate of the universe is too large to permit any clumping of matter. Structure formation cannot begin prior to the matter dominated epoch. After last scattering of cosmic microwave background (CMB) photons, at $z \sim 1000$,

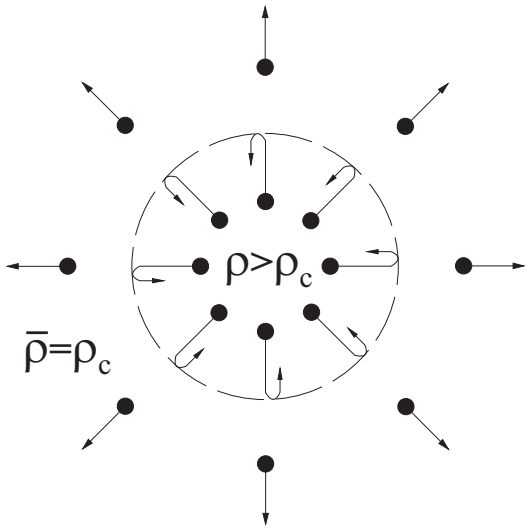

***Figure 2.8*:** Illustration of a spherical collapse. In an universe with $(\Omega_m, \Omega_\Lambda) = (0.3, 0.7)$ an initially expanding overdense region with $\rho > \rho_c$ reaches its maximal extent (dashed line), detaches from $Hubble - flow$ as it contracts to form gravitationally bound object. Figure according to Rich (2001).

structures formed in a star-less dark universe. It was not until $z \sim 10$ that the first stars formed in the collapse of molecular hydrogen clouds, as the discovery of the oldest yet known galaxy seems to suggest (Bouwens et al. 2011). Structure formation, however, continues to $z \approx (\Omega_\Lambda/\Omega_m)^{1/3} - 1 \approx 0.3$ which defines the end of the matter dominated epoch in a Friedmann world model including dark energy Λ. This applies for matter density $\Omega_m = 0.3$ and dark energy density $\Omega_\Lambda = 0.7$ which is in agreement with WMAP[2] findings (Komatsu et al. 2011). In this context the spherical collapse of an overdense region in the early universe can be illustrated as in Fig. 2.8. In this simple scheme gravity and universal expansion (Hubble flow) compete. Is the gravitational drag large enough a region determined by the turn-around radius of particles decouples from the Hubble flow and contracts.

This affects naturally all matter within the collapsing sphere, which should thus have the same baryon-to-dark matter composition as the surrounding universe. The seven years release of WMAP (Komatsu et al. 2011) shows that the global baryon fraction, the ratio of baryonic and total matter in the universe is ~ 0.17. Since dark matter particles are collisionless the Jeans' instability will not be opposed by other forces such as radiation pressure. Certainly, the Jeans' instability applies to dark matter, since the velocity dispersion of the particles can be understood as a source of pressure. Nevertheless, galaxies will eventually form in the potential wells, which are getting steeper as mass concentrates in their centre.

The physics driving the evolution from the collapse of gas and dark matter halos to the formation of galaxies remains one of the open questions in astrophysics, which will be reviewed in Section 2.7.

[2]Wilkinson Microwave Anisotropy Probe

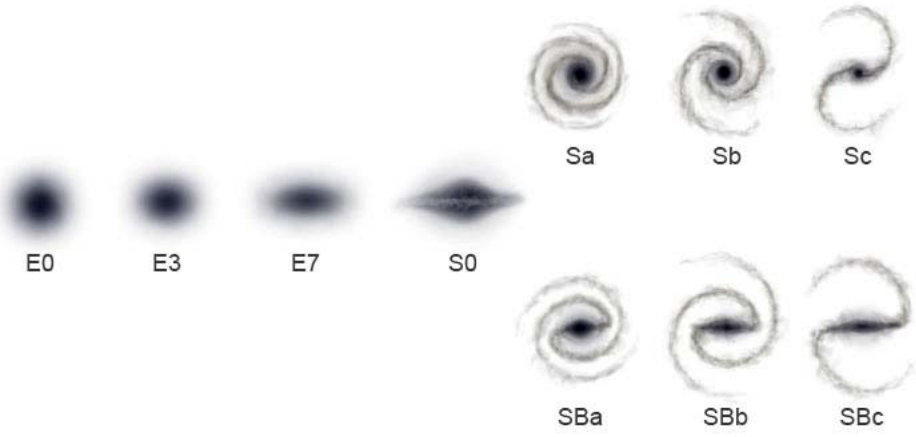

***Figure 2.9*:** The Hubble Sequence serves as a morphological classification scheme for galaxies. Elliptical galaxies are labelled En with the number n indicating the ellipticity. Spirals (S) are classified according to tightness of their arms in sub-categories a to c. A capital B in the morphological type indicates the presence of a bar. $S0$ at the junction of the barred and non-barred spirals refers to lenticular galaxies, which exhibit, unlike ellipticals, a prominent disk and bulge component. Image from Ville Koistinen.

2.5 Galaxies

In 1936, Edwin Hubble introduced the first morphological classification scheme of galaxies based on his observations over many years. He arranged the galaxies according to their appearance in optical light in a sequence, which he believed was an evolutionary scheme from early to late-type galaxies, as seen in Fig. 2.9, with the galaxy age decreasing to the right. At its beginning he placed an almost spherical galaxy, he considered oldest, that becomes gradually flattened. This is expressed by the nomenclature En for ellipticals with n being about ten times the ellipticity $\epsilon = 1 - b/a$, where b and a denote minor and major axes of the ellipse. Defined values for n range from 0 to 7. In the middle the morphological type of lenticular galaxies (S0) marks the branch point of two sub-categories, the spiral galaxies (S) and the barred spiral galaxy (SB). Depending on the ratio of bulge to disk size and the tightness of the spiral arms, lower case letters a to d (the original Hubble sequence ended with c) are added to the morphological type. Due to their in average lower masses ($< 10^{12} M_{\odot}$), late-type galaxies are underrepresented among the lensing galaxies, which is why we continue with a closer look on early-type galaxies.

2.5.1 Early-type galaxies

Although galaxy formation turned out to be more complex than Hubble's evolutionary scheme, it is still used for classification to the present day. Same applies to the anachronism 'early-type galaxies', which is based on Hubble's interpretation of the sequence. In a recent study, the evolution of the Hubble sequence was shown by comparing the local abundance of galaxy morphologies with the one at $z = 0.65$ (Delgado-Serrano et al. 2010). The fraction of early-types was shown to remain almost unchanged at $3 - 4\%$ of the total amount of galaxies. For more general studies on the morphological evolution of galaxies, see e.g. Ilbert et al. (2006). Early-type galaxies span a stellar mass range from 10^7 $M_{\odot}$ (Dwarf elliptical galaxies, see Ferguson & Binggeli (1994)) to 10^{12} (central dominant /

compact diffuse (cD) galaxies, see e.g. Hughes (1989), Lewis et al. (2003)). Early-type galaxies at the high mass end of this range constitute the majority of lensing galaxies. They are furthermore attractive as studies of their centres allow for addressing yet unanswered questions directly linked to structure formation, such as the cusp-core problem, discussed in the following section.

2.5.2 Cusp-core problem

Numerical simulations in the ΛCDM concordance model were found to reproduce the large scale structures in the universe very well. On galaxy scales, however, studies of stellar kinematics (rotation curves) tend to disagree with predictions from simulations (e.g. Gilmore et al. 2008, Primack 2009). Among other discrepancies (missing satellite and angular momentum problem) the cusp-core problem is one of the long-lived problems in astrophysics. It arises from observationally inferred DM density profiles $\rho \sim r^{\alpha}$ that are found to be much flatter than expected by simulations. The latter tend to predict cuspy profiles with inner slopes slightly steeper than $\alpha = -1$ (NFW). There is strong evidence, especially for low-mass disk galaxies, that the central dark matter density is nearly constant (Kuzio de Naray et al. 2009). Discrepancies between observations and simulations, which are found even for galaxies with low stellar mass content, speak for a flawed dark matter model. However, interactions between baryons and cold dark matter might be able to impede inner density cusps by feedback mechanisms (described in Section 2.7) and give thus an explanation for the problem especially for galaxy types dominated by stars, such as giant ellipticals.

2.6 Scaling relations

Understanding scaling relations means to understand structure formation. The following sections introduce the most important scaling relations that govern the dynamics and distribution of matter in galaxies. They are essential for the following analysis, as they will be addressed several times throughout this thesis (see Chapters 5 and 6).

2.6.1 The fundamental plane of early-type galaxies

The fundamental plane (FP) for early-type galaxies is a well-known scaling relation between the effective radius (or half-light radius) $R_{\rm e}$, the kinematic velocity dispersion $\sigma_{\rm obs}$ and the surface brightness $I_{<R_{\rm e}}$ in logarithmic space found by Djorgovski & Davis (1987) and Dressler et al. (1987). Not so well understood is the mismatch between theoretical predictions for the FP on one hand and observations on the other. A simple theoretical deduction starts with the virial theorem

$$2\langle T\rangle = -\langle V\rangle, \tag{2.29}$$

which relates the time average of the kinetic energy per unit mass $\langle T\rangle = \sigma^2/2$ and potential energy $\langle V\rangle = -GM/r$. This can be transformed into

$$M \propto R_{\rm e}\sigma^2. \tag{2.30}$$

Combining the virial theorem and the universality of light profiles $L \propto R_{\rm e}^2 I$ while assuming a constant mass-to-light ratio yields the deliberately simple-minded version of the

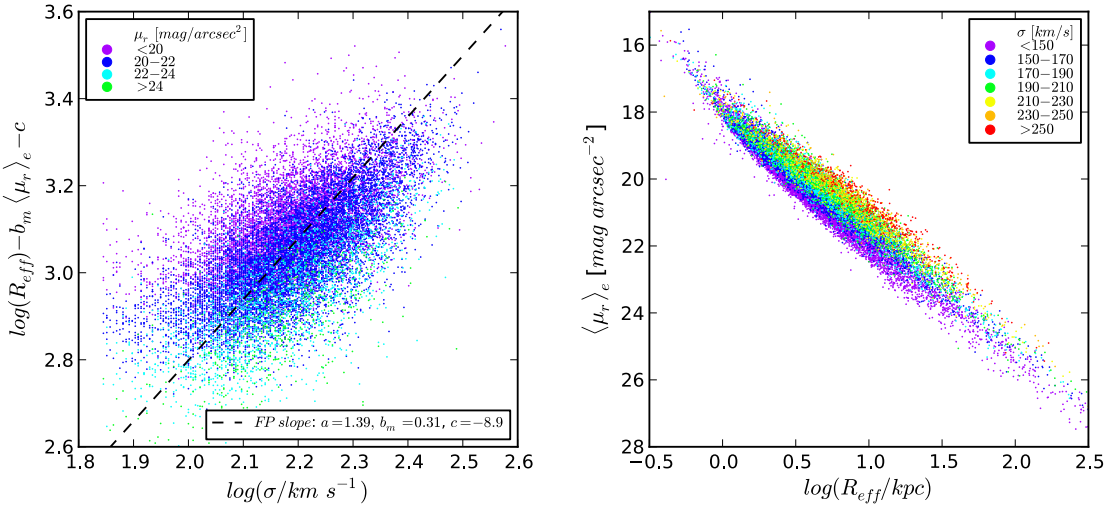

***Figure 2.10*:** Left: Projection of the fundamental plane, showing the photometric quantities R_e and $\langle\mu_r\rangle$ plotted against the spectroscopic quantity σ. Surface brightness bins are indicated by colour. The dashed line indicates the best fit to the combined sample. Right: Kormendy relation. The colour indicates different central velocity dispersion bins. The data set comprises 40,356 early-type galaxies from the *Spheroids Panchromatic Investigation in Different Environmental Regions* (SPIDER) sample (La Barbera et al. 2010). The given r-band data comes from the *Sloan Digital Sky Survey* (SDSS) sample of early-type galaxies.

fundamental plane relation

$$R_\mathrm{e} \propto \sigma^2 I^{-1}. \tag{2.31}$$

In contrast observations show a relation with slightly different power indices a and b, as in

$$R_\mathrm{e} \propto \sigma^a I^b, \tag{2.32}$$

with $a \approx 1.2$ and $b \approx -0.8$ (e.g., Jørgensen et al. 1996). The power indices are thus not in agreement with above values $(a, b) = (2, -1)$ for constant M/L, which is suggestive of an underlying regularity beyond the above formulas. This deviating slope is often referred to as the fundamental plane *tilt*.

In the left panel of Fig. 2.10, a projection of the three-dimensional FP parameter space is shown. The ordinate includes all photometric quantities. Note the change in nomenclature for the surface brightness quantity $\langle\mu\rangle$. It is equal to I_{R_e}, but given in magnitudes, which is already a logarithmic quantity. Thus the coefficient b_m in the Figure translates to b from Eq. 2.32 with $b_m = b/-2.5$. The constant c denotes an offset due to the definition of the zero point. The dashed line shows the best fit to the data. The FP parameters for this particular sample of SDSS r-band selected early-type galaxies are given in the plot. In Table 2.1 we provide an incomplete overview of FP studies.

The different explanations proposed for the tilt of the fundamental plane affect different aspects of galaxy formation as a consequence of the interplay between baryonic and dark matter. The main explanatory approaches can be summarized as follows.

- *Structural non-homologies*, first addressed by Hjorth & Madsen (1995), refer in particular to a scatter in the steepness of the light profiles of early-type galaxies, which is correlated with R_e, meaning that the light profile of early-type galaxies varies systematically with their size, i.e. large galaxies are more centrally concentrated than small ones (see also Busarello et al. (1997)). Comparing non-homologous light profiles for Virgo early-type galaxies with estimates based on universal de Vaucouleurs profiles produced no significant difference in the fundamental plane (Graham & Colless 1997*a*).

- *Orbital anisotropies*, as discussed in detail by Nipoti et al. (2002), address the underlying assumption of early-type galaxies being in a relaxed state. This may contribute only marginally to the FP tilt if early-types with one matter component and initial anisotropies are simulated. The latter lead to instabilities that cause the elliptical galaxies to fall back to a given FP. However, if a two component model is assumed, in particular massive and more concentrated DM halos can lead to unstable (non-virial) galaxies well-outside the FP. This however cannot account for the whole tilt.

- *Variation of the stellar mass-to-light ratio* (M/L) with luminosity, addresses the assumption of a common formation history of early-type galaxies, in particular dependencies of M/L on the initial mass function (IMF) or star formation (SF) (e.g. Jørgensen 1999). If a dependency between the SF history and mass content is established the FP tilt could be explained (Chiosi & Carraro 2002). A systematic variation of the IMF is disfavoured, as the lower stellar mass limit of the IMF is forced to be unreasonably high (Renzini & Ciotti 1993).

- *Variation of the DM content*, refers to possibly flawed assumptions on the total mass-to-light ratio on scales $\lesssim R_e$. To keep objects on the FP baryonic matter has to be the dominant mass component in the centre of early-type galaxies. This speaks however against cuspy dark matter profiles as expected from ΛCDM simulations. Indeed ΛCDM with its typical NFW DM profiles predicts – in disagreement with observations – a curved fundamental surface rather than a plane (Borriello et al. 2003). Assuming cored DM profiles and an additional stellar mass profile permits to recover the FP tilt. In contrast to latter authors who express the slope mismatch in terms of $M/L \sim L^{\alpha}$, Ferreras & Silk (2000) emphasize that the *only plausible way* to solve the FP tilt is by "imposing a non-linear correlation between the total mass (including dark matter) and the stellar mass" classification.

Reference	a	b
(Dressler et al. 1987)	1.33 ± 0.05	-0.83 ± 0.03
(Djorgovski & Davis 1987)	1.39 ± 0.14	-0.90 ± 0.09
(Lucey et al. 1991)	1.27 ± 0.07	-0.78 ± 0.09
(Guzman et al. 1993)	1.14	−0.79
(Jørgensen et al. 1996)	1.24 ± 0.07	-0.82 ± 0.02
(Hudson et al. 1997)	1.38 ± 0.04	-0.82 ± 0.03
(Scodeggio et al. 1997)	1.25 ± 0.02	-0.79 ± 0.03
(Pahre et al. 1998)	1.53 ± 0.08	-0.79 ± 0.03
(Müller et al. 1998)	1.25	−0.87
(Gibbons et al. 2000)	1.39 ± 0.04	-0.84 ± 0.01
(Colless et al. 2001)	1.22 ± 0.09	-0.84 ± 0.03
(Bernardi et al. 2003)	1.49 ± 0.05	-0.75 ± 0.01

***Table 2.1*:** List of previously found fundamental plane parameters.

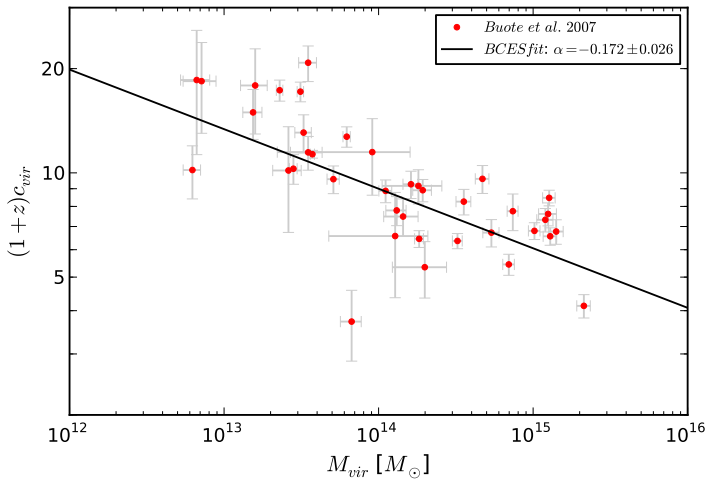

Figure 2.11: Concentration to virial mass relation. The data from Buote et al. (2007) comprises galaxy systems ranging in mass from individual early-type galaxies to galaxy clusters. Their best fit is found with a BCES method (Bivariate Correlated Erros and intrinsic Scatter), see Akritas & Bershady (1996).

2.6.2 The Kormendy relation

The correlation between the logarithm of the effective radius and the mean surface brightness μ enclosed at R_e, is known as the Kormendy relation (Kormendy 1977):

$$\langle\mu\rangle_e = \gamma_1 + \gamma_2 \log(R_e). \tag{2.33}$$

The Kormendy relation, shown in the right hand panel of Fig. 2.10, comes along with a high intrinsic dispersion of ~ 0.4 mag in $\langle\mu\rangle_{<R_e}$ (e.g. Hamabe & Kormendy 1987, Hoessel et al. 1987, La Barbera et al. 2010), which can be attributed to the missing third parameter of the FP (Ziegler et al. 1999) and corrections introduced for different biases, such as K-correction and reddening (Nigoche-Netro et al. 2008).

2.6.3 The concentration to virial mass relation

The concentration to virial mass relation ($c - M_{vir}$), unlike previous scaling relations, does not directly depend on any light-related quantity. It states that less massive halos are more concentrated than more massive halos. Figure 2.11 shows the $c - M_{vir}$ relation based on studies of X-ray clusters, according to Buote et al. (2007). The relation arises naturally in a universe with hierarchical structure formation. For measurements on X-ray clusters, constraints on the mass-profile are inferred by temperature and gas density profiles assuming hydrostatic equilibrium (e.g. Sarazin 1988, Buote 2004). Numerical ΛCDM simulations determine the concentration c and the virial mass M_{vir} directly from fits to their dark matter halos. Moreover, simulations find a considerable intrinsic scatter, independent of the virial mass (e.g. Bullock et al. 2001).

The correlation is commonly expressed by a simple power-law

$$c = \frac{c_0}{1+z}\left(\frac{M}{M_0}\right)^{\alpha}, \tag{2.34}$$

where c_0 and M_0 are reference masses. The slope is inferred to be negative, i.e. $\alpha < 0$. Studies based on observations mostly determine slopes in the range from -0.15 to -0.17 (see e.g. Comerford & Natarajan 2007, Buote et al. 2007, Johnston et al. 2007). Simulated mass profiles however appear to differ from observationally inferred profiles. The former yield consistently shallower slopes, i.e. $\alpha \sim -0.09$ (see e.g. Duffy et al. 2008, Macciò et al. 2008). The mismatch between observations and simulations might be due a mass dependence of the slope. Also, a number of uncertainties enter the definition of the c-M-relation. The concentration is commonly defined as the ratio of the virial radius $R_{\rm vir}$ and the scale radius of the NFW profile

$$c_{vir} = \frac{R_{\rm vir}}{r_s}. \tag{2.35}$$

The virial radius is defined as the radius for which the mean enclosed density is equal to a multiple Δ_c of the critical density

$$\rho_c(z) = 3H(z)^2/(8\pi G), \tag{2.36}$$

i.e. $\langle \rho(R_{\rm vir}) \rangle = \Delta_c \rho_c(z)$. The values for the overdensity Δ_c are determined by

$$\Delta_c = 18\pi^2 + 82x - 39x^2 \tag{2.37}$$

with $x = (\Omega_m(1+z)^3/E(z)^2) - 1$ and $E(z)^2 = \Omega_m(1+z)^3 + \Omega_\Lambda$, according to Bryan & Norman (1998). This relation fits the solution to the collapse of spherical perturbation in the "top-hat" scenario[3] (Peebles 1980). In some studies however $R_{\rm vir}$ is approximated by r_{200}, which is defined with a characteristic overdensity $\Delta_c = 200$. Since $R_{\rm vir}$ is defined with respect to a certain overdensity Δ the notation r_Δ is used equivalently. This approximation is not taking proper account of the spherical collapse. The scale radius r_s in Eq. 2.35 is often referred to as r_{-2}, the radius at which $\rho \propto r^{-2}$. For an NFW profile r_s and r_{-2} are indeed equal. The sought-after virial mass can thus be calculated as the mass enclosed in a sphere with radius $R_{\rm vir}$

$$M_{vir} = \Delta_c \rho_c(z) \times \frac{4}{3}\pi r_\Delta^3. \tag{2.38}$$

Since the $c - M$-relation depends on the definition of the overdensity Δ_c, redshift and cosmological parameters comparisons between different studies must be put on the same standard.

2.7 Galaxy evolution

Fully understanding the evolution from an initial collapse of gas and dark matter to the formation of galaxies is a yet unreached aim of astrophysics. Star formation can also be interpreted in terms of the stellar to total mass fraction within the virial radius of a halo. It is highest for galaxies similar to the Milky Way and decreasing towards higher and lower masses (Moster et al. 2010). In the process of galaxy evolution following feedback processes are important, as they directly affect the star formation efficiency.

[3] In this simple scenario, a spherical overdensity of radius R is replaced by a smaller one of radius $R - \Delta R$ with same enclosed mass. The annulus of ΔR would be, figuratively speaking, the brim of the top-hat, which explains the name-giving. In a slightly different explanation of the name-giving, the one-dimensional cut of the initial model of the perturbation shows a constant central region (flat-crown), and a "low" background farther away (broad brim).

- *Stellar Feedback*: The lower escape velocities in less massive galaxies allow the gas to be ejected by stellar feedback (Larson 1974, Dekel & Silk 1986). Supernova-induced winds are energetic enough to significantly impede galaxy formation at baryonic masses below $10^{11}\mathrm{M}_{\odot}$ (Brooks et al. 2007). Such feedback regulates the star formation efficiency, which is responsible for the mass-metallicity relation (Tremonti et al. 2004).

- *AGN-Feedback*: For more massive galaxies, an Active Galactic Nucleus (AGN) is believed to account for the decreasing star formation efficiency (see e.g. Di Matteo et al. 2005). This feedback mechanism explains the exponential cut-off in the luminosity function, either by the thermal coupling of AGN outflows with gas (e.g. Tabor & Binney 1993, Croton et al. 2006, Bower et al. 2006) or by mechanical feedback that prevents gas cooling (Sijacki et al. 2007).

Evolution of galaxies and their properties such as mass distribution and kinematics depends furthermore on the following.

- Mergers: A major merger is a collision between two galaxies of comparable masses. Major mergers may play a key role in the growth of galaxies (see e.g. Toomre & Toomre 1972). Especially gas-rich ("wet") mergers can boost rapid star formation (starbursts) as they can trigger gaseous inflows due to strong variations of the potential (e.g. Schweizer & Seitzer 2007). Moreover the angular momentum may be conserved in gas rich mergers to form galactic disks (Robertson et al. 2004). Merged galaxies show long-lived imprints of their history in non-axial symmetric mass distributions (Jog & Maybhate 2006). About 70% of all galaxies with present-day stellar masses above $5 \times 10^{10} M_{\odot}$ have undergone a major merger since $z = 1$ (Bell et al. 2006). See Sanders & Mirabel (1996) for a review.

- Dynamical friction: As a massive object propagates through a cloud of smaller particles, a gravitational wake is produced behind the massive object which imposes a force opposite to its velocity vector. This effect was first investigated by Chandrasekhar (1943). Dynamical friction is important in the context of mergers, as it increases significantly the merging time and delays subsequent relaxation (Boylan-Kolchin et al. 2008).

- Adiabatic contraction: As baryonic gas cools down to form stars, considerable dissipation of gravitational energy occurs. Thus the distribution of baryons gets gradually more concentrated causing the dark matter to follow its lead and steepen its inner density profile. This process is called adiabatic contraction (AC), since angular momentum conservation is imposed, as $rM(< r)$ (radius times total mass enclosed in a sphere with radius r) is treated as an adiabatic invariant. Eggen et al. (1962) were first to use adiabatic invariants in calculations of stellar motions. In context of the interplay between dark matter and baryons Blumenthal et al. (1984) introduced the today most commonly used AC model, which assumes spherical symmetry, conservation of angular momentum, circular particle orbits and homologous contraction, meaning that the mass distribution can be understood as a number of nested radially contracting spheres which do not cross each other. Orbital anisotropies were taken account of in a later AC prescription introduced by Gnedin et al. (2004). Recent studies by (Abadi et al. 2010) gives rise to doubts about the meaning of AC in galaxy

formation. Gao et al. (2004) argued that dissipationless evolution can even erase the AC effect on the density distribution.

In the following section we focus on elliptical galaxies (also called early-type galaxies) as the most common galaxy type among strong lenses, which is thought to be affected by aforementioned evolutionary processes.

2.8 Initial mass function

The initial mass function (IMF) defines the distribution of stellar masses in a new population of stars

$$\frac{dN}{d\log m} \propto m^{-\Gamma}, \tag{2.39}$$

i.e. the number of stars per unit volume with a mass between M and $M + dM$. It is an important link between stellar and galactic evolution and provides insights on theories of star formation. It affects both the chemical enrichment and the stellar mass content of galaxies. The IMF comes in useful while trying to model the evolution of stellar populations starting from an initial state. Edwin Salpeter determined first in his seminal work a single power-law relation for the solar neighbourhood with a power index of $\Gamma = 1.35$ in a stellar mass range between 0.4 and $10M_\odot$ (Salpeter 1955*a*). Many recent studies address its shape and possible universality (e.g. Kroupa 2001, Larson 2006, Kroupa 2008, Bastian et al. 2010). Especially the slope of the IMF below $1M_\odot$ is matter of ongoing debate, as it appears to become negative below a peak at few tenths of the solar mass. The physical significance of such a peak can be understood as a preferred scale of fragmentation during the formation phase of stars (e.g. Li et al. 2003). For its determination knowledge about the present day luminosity function, the stellar mass-to-light relation and the star formation history is required. The latter is based on model assumptions.

Constraining the IMF for other galaxies however is even more challenging, as only the integrated flux of a composition of stellar populations is observed, which are degenerate with respect to age, metallicity and dust. Figure 2.12 gives an overview on some commonly used IMFs (Salpeter 1955*a*, Kroupa 2001, Chabrier 2003).

In this work we use the Chabrier (2003) IMF, given as

$$\frac{dN}{d\log m} \propto \begin{cases} \exp\left[-\frac{(\log m - \log m_c)^2}{2\sigma^2}\right] & (m \leq 1M_\odot) \\ m^{-1.3} & (m > 1M_\odot) \end{cases} \tag{2.40}$$

where m_c denotes the mass at the turn-over and σ is the standard deviation. It should be noted that most of the frequently used choices of the IMF have similar declining distributions at the low mass end (see also Miller & Scalo 1979, Scalo 1986). It is only the traditional single-power law of the Salpeter (1955*b*) IMF that gives significantly different stellar mass predictions. Previous detailed work on the kinematics of nearby early-type galaxies (Cappellari et al. 2006) or strong lenses (Ferreras et al. 2008, 2010) shows that the low-mass end of the Salpeter IMF is ruled out as it predicts stellar mass surface densities higher than the dynamical or lensing estimates.

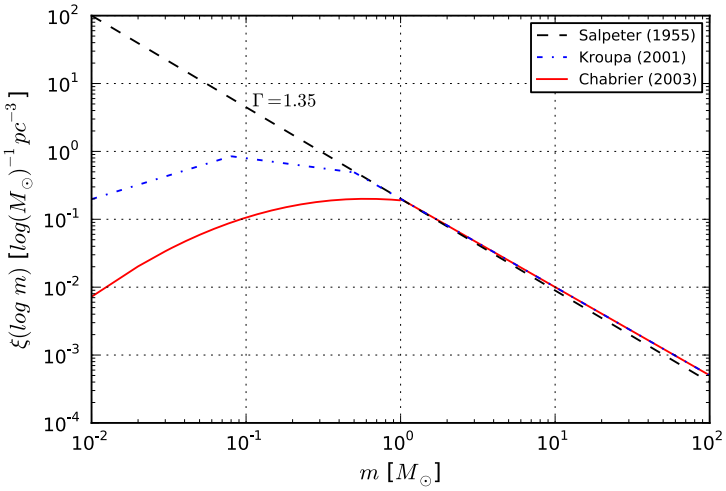

***Figure 2.12*:** Initial mass functions with a single power-law (Salpeter 1955*a*), a broken power law with turning points at 0.08 $M_\odot$ and 0.5 $M_\odot$ (Kroupa 2001) and an exponential decline below 1 $M_\odot$ according to Eq. 2.40 (Chabrier 2003).

2.9 Light and mass profiles

A couple of parameterizations of light and matter distributions are basic to this work and will be briefly discussed in the following. See Keeton (2001*a*) and Coe (2010) for further information on mass models used in gravitational lensing.

2.9.1 The Sérsic profile

A versatile fitting function for surface brightness profiles $I(r)$ of early-type galaxies, bulges, bars and discs to mention only a few is given by Sérsic (1963). The function

$$I(r) = I_e \exp\left\{-b_n\left[\left(\frac{r}{r_e}\right)^{1/n} - 1\right]\right\} \tag{2.41}$$

is normalized to the core brightness I_e and contains a scale length which is expressed in Eq. 2.41 in terms of the effective radius R_e and a conversion factor b_n. It goes furthermore with the inverse power index n. A profile with $n = 4$ corresponds to a de Vaucouleurs profile, for which b_n becomes ~ 7.67, as can be derived numerically (see Prugniel & Simien 1997).

2.9.2 The Hernquist profile

A surface mass density distribution which closely approximates the de Vaucouleurs $R^{1/4}$ surface brightness profile for elliptical galaxies is given by Hernquist (1990)

$$\rho(r) = \frac{M}{2\pi}\frac{a}{r}\frac{1}{(r+a)^3}. \tag{2.42}$$

Integrating along the line of sight and once more over the area within r yields

$$M_{cyl}^{hern}(< r) = \frac{M}{\Upsilon}\left(\frac{r}{r_h}\right)^2 \frac{\mathcal{X}(r, r_h) - 1}{1 - \frac{r}{r_h}}, \tag{2.43}$$

with

$$\mathcal{X}(r, r_h) = \begin{cases} \frac{1}{\sqrt{1-(r/r_h)^2}} \operatorname{sech}^{-1}(r/r_h) & r \leq r_h \\ \frac{1}{\sqrt{(r/r_h)^2-1}} \sec^{-1}(r/r_h) & r \geq r_h. \end{cases} \tag{2.44}$$

2.9.3 The Singular Isothermal Sphere

The singular isothermal sphere is one solution for the hydrostatic equilibrium maintained by a spherically symmetric gas cloud with the same temperature everywhere. It is

$$\rho(r) = \frac{\sigma^2}{2\pi G r^2} \tag{2.45}$$

with the velocity dispersion σ and the gravitational constant G. Its projection onto the lens plane is then given by

$$\Sigma(b) = \frac{\sigma_{los}^2}{2Gb}, \tag{2.46}$$

where σ_{los} is the velocity dispersion along the line of sight and b is the physical distance to its centre in the lens plane, as shown in Fig. 2.1.

2.9.4 The Singular Isothermal Ellipsoid

The generalization of an isothermal sphere to elliptical lenses can be obtained by replacing b in Eq. 2.46 with $b \equiv \sqrt{b_1^2 + f^2 b_2^2}$

$$\Sigma(b) = \frac{\sqrt{f}\sigma_{los}}{2G} \frac{1}{\sqrt{b_1^2 + f^2 b_2^2}}, \tag{2.47}$$

where the normalization is conveniently chosen to give enclosed masses inside an elliptical iso-density contour independent of f for fixed Σ (Kormann et al. 1994).

2.9.5 The NFW profile

Navarro et al. (1996) found that simulated CDM halos are well-approximated by

$$\rho(r) = \frac{\rho_s}{(r/r_s)(1 + r/r_s)^2}. \tag{2.48}$$

The scale parameters ρ_s and r_s are degenerate with one another as will be shown. Both depend on the halo mass. By integration over the radius one finds the mass enclosed in a sphere of radius r, i.e.

$$M_{sph}(< r) = 4\pi\rho_s r_s^3 \left\{ \ln\left(1 + \frac{r}{r_s}\right) - \frac{\frac{r}{r_s}}{1 + \frac{r}{r_s}} \right\}. \tag{2.49}$$

By projecting and subsequent integration over the area within the projected radius R we obtain the total mass enclosed in a cylinder

$$M_{cyl}^{NFW}(< R) = 4\pi\rho_s r_s^3 \times \mathcal{F}(R, r_s), \tag{2.50}$$

with

$$\mathcal{F}(R, r_s) = \ln \frac{R}{2r_s} + \begin{cases} \frac{1}{\sqrt{1-(\frac{R}{r_s})^2}} \cosh^{-1} \frac{r_s}{R} & (R < r_s) \\ 1 & (R = r_s) \\ \frac{1}{\sqrt{(\frac{R}{r_s})^2-1}} \cos^{-1} \frac{r_s}{R} & (R > r_s) \end{cases} . \tag{2.51}$$

3 Methodology

After the theoretical foundations are given, we will introduce the mass reconstruction methods and procedures carried out in this work. The motivation for non-parametric mass reconstruction or free-form modeling, as an alternative to solution besides analytic modeling is motivated in Section 3.1. The tools to create pixelated total and stellar surface mass maps are presented in Section 3.2. Total lens mass reconstruction is basic to the studies presented in the Chapters 5 and 6. Stellar mass reconstruction by means of population synthesis will be employed for the analyses in Chapter 6.

3.1 Parametric and non-parametric modeling

Expressing the light and matter distribution in galaxies in terms of more or less simple analytic parameterizations is an enticing way to study gross features of galaxy samples with respect to their formation and evolution. However, in order to properly model different types of galaxies, a template function has to account for distinct features of their build-up, such as a stellar bulge and disk. Its quality to give a proper description of an object depends to some extent on the accuracy and size of the data sample. Mass models motivated by numerical simulations, such as the NFW profile (Section 2.9.5), invoke assumptions on the nature of the particles which are simulated. Together with the increasing complexity of models – considering different matter components and a variety of physical processes – uncertainties may pile up and introduce hard to quantify departures from real matter distributions. Stacking several parametric models opens a door to the problem of *non-uniqueness* of the solution, as multicomponent fitting is inherently prone to some degree of degeneracy.

Up to now there are not many studies which help to unravel such degeneracies. Witt & Mao (1997) found that for general elliptical potentials external shear is necessary even to simply reproduce the observed galaxy and image positions. They also show that the lens models are degenerate with respect to the ellipticity and the magnitude of the shear. The larger the amounts of observational constraints the less acceptable become one-component lens models. In many cases parametric models which take account of a single galaxy profile only fail to reproduce time-delays (see e.g. Schechter et al. 1997, Keeton & Kochanek 1997). In view of the growing number of model-parameters necessary to satisfy the increased number of observational constraints and possibly connected degeneracies it appears advisable to take parametric models with a pinch of salt. Using them as a basis for extrapolations may lead to significant deviations from studies which resolve the centre of the lens galaxy as will be shown in the following.

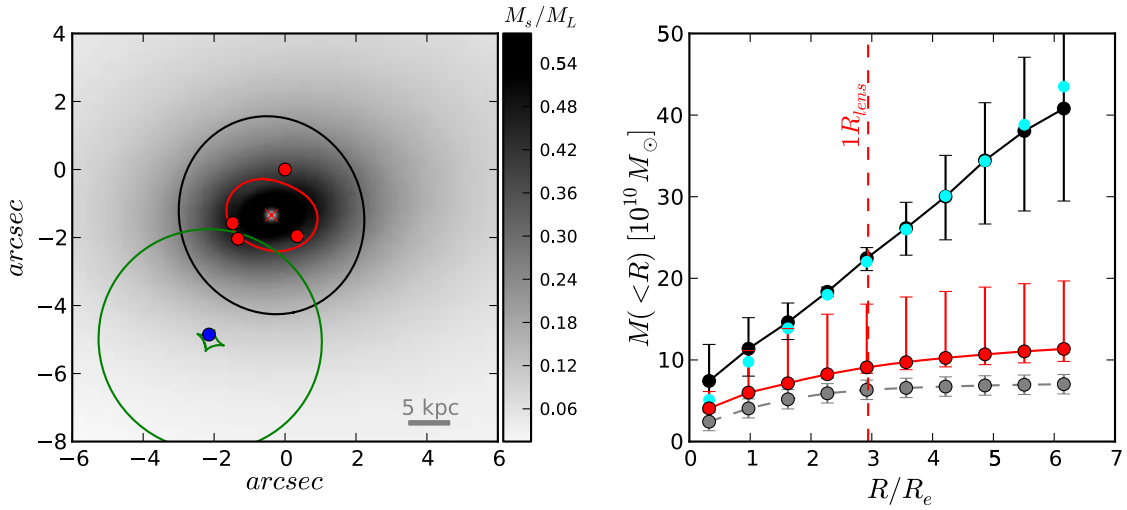

Figure 3.1: Comparison of two different modeling strategies on the lens PG1115+080. Left: A fit to a three-component lens model (stellar, dark matter, and external group) without population synthesis. Red dots mark the image positions and the red curve is the model critical curve. The blue dot is the model source position and the green curves show the model caustics. The greyscale indicates stellar-mass fraction, while the black ellipse indicates the ellipticity and position angle of the stellar component. The length of the semi-major axis of the latter is set here to $2R_{\rm lens}$. Right: The red and cyan dots show the stellar and total enclosed mass respectively from the model in the left panel. The red error bars enclosing the red dots correspond to a 1σ region around the best χ^2. The black and grey dots with error bars are the stellar mass and total enclosed mass from pixelated lens models and population synthesis.

In Fig. 3.1 we contrast enclosed stellar and total mass profiles from a parametric and non-parametric analysis of the lens PG1115+080 (henceforth called PG1115). Using `GRAVLENS`,a program by Keeton (2001*b*) we model this complex lens system with an NFW profile for the dark matter component, a de Vaucouleurs profile for the light and an SIS+γ which takes account of a nearby group. The observationally determined effective radius $R_{\rm e} = (0.85 \pm 0.07)''$ (Treu & Koopmans 2002), positions, ellipticities and position angle are allowed to vary within small uncertainties. Multiple component models introduce degeneracies which are usually minimized but never fully broken by observational constraints. A Markov Chain Monte Carlo (MCMC) search for best parameters yields best χ^2 NFW and de Vaucouleurs profiles. The ratio of stellar to total mass is shown in the left hand panel of Figure 3.1 together with the critical (red) and caustic lines (green). Azimuthal averaging along the elliptical contour of the stellar component and subsequent summation along the major semi-axis yields cumulative mass profiles of both stellar mass and combined total mass as shown in the right hand panel of Figure 3.1. As one can see, the total mass profile of the analytic (cyan dots) and the non-parametric (black dots) models are in good agreement. The enclosed stellar mass profiles (red circles for analytic and grey circles for pixelated profiles, however, show considerable disagreement even within the error range here chosen to be the 1σ region around the best model. Note that the red dots do not represent the median of the distribution but the best χ^2 model in the MCMC search. One also needs to think about the consequences for studies which make extensive use of two-component models without having a direct resolved view on the stellar mass distribution, but rather constrain surface brightness profiles via kinematic velocity dispersions.

3.2 Disentangling matter

Strong lensing permits to constrain the total mass within the central region of the lens situated crudely speaking between the quasar images. Apart from the degeneracies mentioned in Chapter 2.1.3, model-based assumptions contribute to attempts of mass reconstruction with considerable uncertainties. Statistical approaches must be chosen to properly address the issue of different mass distributions creating the same lens configuration, the problem of *non-uniqueness*. To avoid this, free-form methods are necessary. In the following analysis we make extensive use of the `PIXELENS` program[1] (Saha & Williams 2004, Coles 2008) to reconstruct the surface mass density of a sample of lens galaxies.

As the combined mass content of a lens system can be accessed by the above tool, the stellar part can be deduced using population synthesis. The stellar mass estimates as used in Chapters 6 and 7 are based on a comparison of surface brightness profiles with stellar mass-to-light ratios (Υ) determined by population synthesis models for each pixel in the photometry (Ferreras, Saha & Williams 2005, Ferreras et al. 2008). The code used for this procedure was written by Ignacio Ferreras and relies on synthesis models and stellar spectral libraries from Bruzual & Charlot (2003*a*). In a preparatory step surface brightness profiles are carefully modeled on basis of given photometry using the code `GALFIT` by Peng et al. (2002).

The following sections describe in detail how lensing and stellar population synthesis are used to address the key problems elucidated in Chapter 1.

3.2.1 Total mass content

`PIXELENS` reconstructs the projected mass in a pixelated manner by solving a set of linear constraint lensing equations, according to Eq. 2.3, using the image positions, the redshifts of lens and source, the Hubble time (herein $h = 0.72$ is always assumed) and optionally the time delays between the lensed images. Multiple-image systems with the observed positions must arise as solutions of the lens equation. The images are considered to be unresolved; for extended images, the peak of their surface brightness distribution is located and considered as an unresolved image. For lenses with measured time delays, the model is required to reproduce them. For each lens, the projected total-mass distribution is reconstructed on a circular field made up of n square tiles or pixels, where n is either 350 or 750 for a map radius of 10 or 15 pixel, respectively. Each pixel consists of a uniform mass distribution with a mass density of a few times the critical density. Figure 3.2 shows an example for a surface mass map reconstructed with `PIXELENS`. Following prior conditions are imposed on the mass distribution: It has to be non-negative,

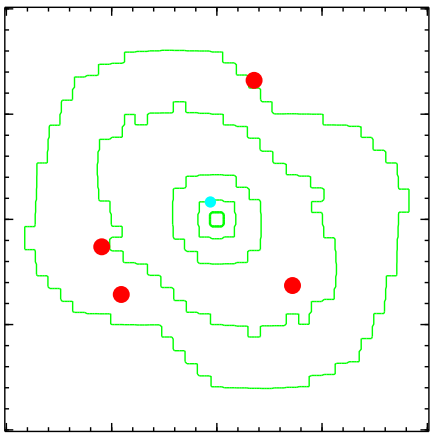

***Figure 3.2*:** Typical surface mass map, here shown for the lens PG1115. The box size is 3×3 arcsec^2. The red dots mark the image positions, the cyan dot indicates the source position.

[1] Available from www.qgd.uzh.ch/projects/pixelens/

centrally concentrated, with a local density gradient pointing no more than 45° away from the centre of brightness. Since the central regions of galaxies are expected to be dominated by stars, it seems safe to assume that the mass and light peaks coincide. Also, for few lenses this was shown to be correct by Yoo et al. (2006). Pixels having more than twice the mean of their neighbours are prohibited, except for the central pixel, which can be arbitrarily high to mimic central density cusps. The circularly averaged projected density (around the centre) is required to be $R^{-0.5}$ or steeper. The three-dimensional mass profiles of galaxies are thought to be invariably steeper than $r^{-1.5}$, so again this appears to be a safe prior assumption. Unless the lens shows signs of asymmetry, the mass distribution is required to be symmetric under a 180° rotation around the centre. The above constraints (observational or prior) can be conveniently formulated as a set of linear equations or inequalities. As a consequence of underdeterminacy, solutions of the lens equation are highly non-unique (Falco et al. 1985*b*, Saha 2000*b*, Liesenborgs et al. 2008), i.e. there are infinitely many mass models that satisfy all the above conditions. Thus an MCMC technique, used to sample the model space and produce an ensemble of models per lens, seems well-suited. The algorithm defining the search strategy in model space introduces an additional prior whose physical significance is not easily accessible. However, to obtain a largely unbiased result the algorithm has to be insensitive to changes of dimensionality and rescaling of units. Only then any weighted mean of ensemble members can be considered an admissible model. Coles (2008) shows that this is indeed the case for the algorithm used in `PIXELENS`. Hence, we can conveniently use the ensemble mean to represent a typical model. The uncertainties on any parameter can readily be derived from the model ensemble.

`PIXELENS` has been extensively tested in other work:

1. for tests of the recovery of simulated galaxy lenses, see Read et al. (2007),

2. for the recovery of gross features of even extended lens structures from the information encoded in the image positions of lensed objects, see Saha & Williams (2001), Ferreras et al. (2008).

3. In Leier (2009) we analyze the sensitivity of $\sigma_{\rm lens}$ on the size of the ensemble by calculating the absolute deviation between the average formal velocity dispersion of an ensemble of 100 models and one with about 10000 models, which we take as a close to exact representation of the lens model.

4. In Chapter 5 we show how additional source-image systems alter the mass reconstruction.

3.2.2 Light profiles

To translate pixelwise the photon counts into stellar mass we need to make sure that no nearby objects such as lensed quasar images or intervening stars contribute to the light profile of the lens galaxy. Separating the light which originates from the lens galaxy from possible contaminating sources is a difficult procedure, which will be elucidated in the following. In Fig. 3.3 the lens system PG1115 is shown consisting of an early-type galaxy surrounded by four point sources, the lensed quasar images. Since the response of an imaging system to a point source is the Fourier transform of the very same delta-function,

a so-called point-spread function (PSF) is found in the image at any point source position. Its wings, the typical four-spike shape, extend even in regions far from the actual position of the point source. In the given example (Fig. 3.3) light from the PSF wings clearly contaminates the central region of the system where the lensing galaxy is located. Therefore a light (or surface brightness) profile, the Sérsic profile as introduced in Section 2.9.1, is fitted to the available photometry to account for the light profile of early-type galaxies. At the same time PSFs are fitted to the quasar images and subtracted off (point-source reduction). As an aside, the given photometry is always a convolution of the real light source with the instrument's response. As a consequence, the given photometry must be deconvolved in whole with a PSF template. The whole fitting procedure – consisting of galaxy profile fit, quasar image fits and deconvolution) is carried out using `GALFIT`, a code written by Peng et al. (2002). This way we obtain best-fitting surface brightness profiles, freed from interfering light, for the given multiband data. The output, i.e. the lens galaxy model, is used to constrain stellar populations and to estimate pixel-by-pixel the stellar mass, which will be explained in the following section.

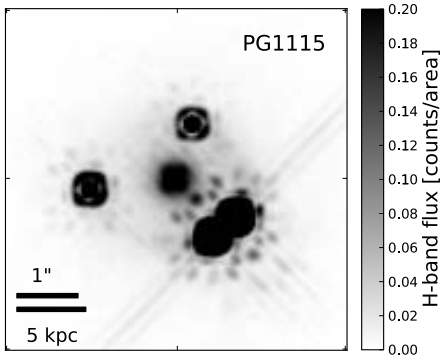

***Figure 3.3*:** H-band photometry of the lens PG1115. The elliptical lens galaxy in the centre is surrounded by four lensed quasar images.

As for now we want to focus on the problems arising during this procedure. They can be assigned to one of the following categories:

(a) finding an appropriate PSF for deconvolution and point-source reduction, or

(b) removing perturbing light sources that negatively affect the fitting procedure.

Since we will use photometric data in different filters, one of the following PSF-picking procedures has to be suitably chosen for each case and spectral band.

1. *Star-picking method*: Sufficiently isolated stars from the same or a contemporaneous (as nearly as possible) image recorded by the same instrument provide already a high quality PSF. A star can be considered as isolated if its sky background shows no gradient. Extracting the star together with a part of the surrounding region large enough to include the PSF wings and small enough to avoid light pollution by other sources is a matter of trial and error.

2. *Iteration method*: Select the image of a lensed quasar that is most distant from the rest of the lens system and use it for quasar image fitting. While the lens galaxy and

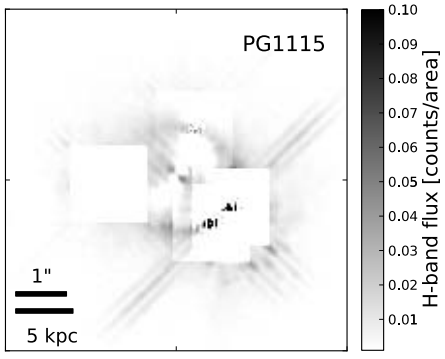

***Figure 3.4*:** H-band photometry of the lens PG1115 after lens and PSF reduction (residual map) via iteration method.

the other quasar images are fitted with GALFIT (Peng et al. 2002), the residual image, showing only the previously chosen outermost image without any contaminating light, can then be taken as a qualitatively refined PSF. This step can be repeated until we reach the desired level of enhancement. After two to four iterations the procedure converges and yields a flat residual. In some cases, when the picked quasar image is sufficiently isolated, iteration brought no further improvement. Figure 3.4 shows the residual image after PSF reduction with the iteration method. The leftmost quasar image (compare with Fig. 3.3) is used for the reduction. Also the other three quasar images show except for some central pixels good reduction.

3. *Synthetic PSF reduction:* The program *TinyTim* is capable of simulating PSFs for all Hubble Space Telescope cameras (Krist 1993). The quality of its synthetic PSFs depends on the instrument for which it is created. Better reduction can be achieved with PSFs simulating the response of the Wide Field Planetary Camera 2 (WFPC2) rather than with the Near Infrared Camera and Multi-Object Spectrometer (NICMOS) PSFs. This is presumably due to the higher stability of WFPC2 PSFs. In Fig. 3.5 we show this by a comparison of a quasar image in NICMOS H-band photometry reduced by a star and a synthetic PSF. The top panels show stellar (left) and synthetic PSF (right) and the bottom panels corresponding weighted residual maps. The weighted residual map is computed from the original photometry and the best fit model by $(original - model)/(original)$. The comparison shows that the synthetic PSF produces a non-flat residual map, i.e. it leaves structures behind that might disturb the fit of the surface brightness profile to the lens galaxy.

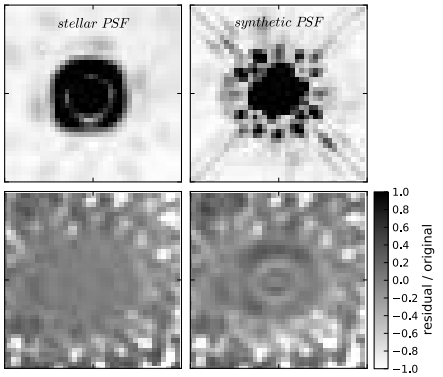

***Figure 3.5*:** Comparison of stellar and synthetic PSFs (top row). The bottom row shows the ratio of residual and original map.

Methods (1) to (3) can also be combined with other methods to remove luminous structures (such as PSF wings or foreground galaxies) interfering with the fit. Light sources which clearly do not belong to the lens (e.g., when found to be at different redshift) can be removed by fitting and consequent reduction of additional light profiles. *Masking* is another method to avoid interfering light sources. Masked out regions are simply ignored during the fit. Such a technique comes in helpful for example if the surface brightness profile fit to the lens galaxy converges to a position other than the brightness peak of the lens. This happens for instance in the case of nearby bright objects, such as stars and quasar images. On the contrary the method can always be applied to objects with a sufficient angular separation. Certainly, if an object's light profile is clearly distinct from the light profile of the lens, i.e. the photon counts per pixel between the two drops to the level of the background noise, the fitting will hardly be affected by its presence. In Fig. 3.6 we show the lens system B2045+265 for which extensive use of masking is made. Masked out regions are highlighted by a bluish hue. The radius of the masked regions depends on the surface brightness profile and is defined as the radius in which 95% of the total light (above background) of the object is enclosed.

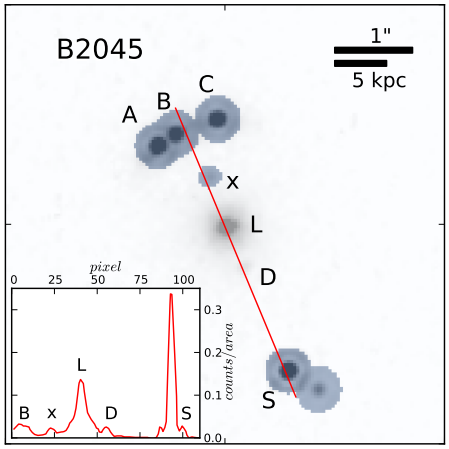

***Figure 3.6*:** Masking of quasar images, stars and other light sources which might affect the quality of the surface brightness profile of the lens on the example of the lens system B2045. The blue shaded regions are masked out. The inset plot shows the section of the surface brightness profile along the red line.

The lensed quasar images A, B and C as well as the two stars (S) are masked out, as they meet the above criterion of sufficient separation. The inset plot shows the section of the photometry along the red line, which crosses the quasar image C, an object of unknown origin labelled x, the lens galaxy (L), the quasar image D and finally one of two stars (S). The object x and the image D have roughly the same angular distance to the centre of the lens galaxy. However, since D is known to be a very dim image, i.e. point source for which only the first maximum of the PSF is visible, we choose PSF reduction instead of masking. Object x is masked as an additional profile fit and subsequent reduction was no valid option due to interference with the lens profile. Other examples for masks used in this work are shown in Fig. A.1 of the appendix. To prevent the fit from diverging, further constraints can be imposed via `GALFIT` on all free parameters of the profiles introduced in Section 2.9, i.e. the Sérsic index n, the effective radius R_e, the magnitude, as well as the position (x, y), the axis-ratio b/a, i.e. minor over major axis, and the position angle PA, which is the angle between the major axis of the ellipse and the y-axis increasing counterclockwise. In particular we make use of

- *fixing the sky*, i.e. the background noise level to a value determined with SExtractor (Bertin & Arnouts 1996), since estimating the background is essential to extract a meaningful profile of the lens (Häussler et al. 2007), (low signal-to-noise objects are thus neglected, increasing the goodness of the fit for the generally bright lens galaxy),
- *fixing the position* (x, y) of the surface brightness profiles to previously determined light centroid positions,
- *constraining light profile*, refers to constraining R_e and/or the Sérsic index n, since both parameters are degenerate, being basically inversely related, i.e. constraining R_e to a low value causes n to diverge and vice versa,
- *constraining projected shape*, by means of the position angle PA and the axis ratio b/a, to a physically appropriate range of values (e.g. $b/a > 0.1$ (Odewahn et al. 1997)), and finally
- *constraining peak brightness*, restricting the range of magnitudes of the point sources, e.g., constraining image A to be at least 0.5 magnitudes brighter than image B.

Except for the first two constraints, which are necessary for only a few lensing systems, we try to keep the number of degrees of freedom of the fit as high as possible and fix the parameters only if there is no alternative. In cases where the best-fit PA in one band was found to differ significantly from the PA in another band e.g. due to intervening quasar

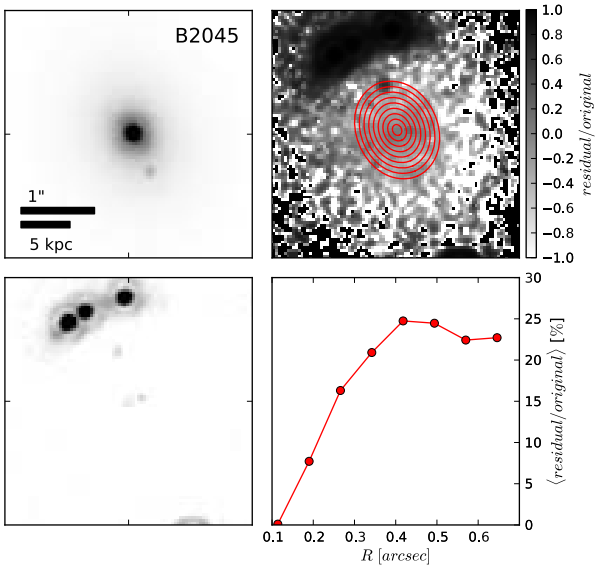

***Figure 3.7*:** Upper left panel: model for lens galaxy and image D in NICMOS H-band photometry for lens system B2045. North is left and East is down. Best fits for the lens galaxy could be obtained by masking out images A, B, C, the stellar objects east of the lens and a "blob" west of the lens galaxy, as shown in Fig. 3.6. Lower left panel: Residual map, i.e. original reduced by the model. Upper right panel: Residual map (*original* − *model*) over original map. The red ellipses are centred on the brightness peak of the lens and have the same ellipticity and position angle. Their major axes range from 2 to 18 pixels. Lower right panel: azimuthally averaged annuli of the upper right panel versus major axis of the ellipses taken as radial distance.

light, it was necessary to constrain PA to the less biased value. The same applies to the axis ratio b/a. If a highly eccentric ellipse is fitted to an actual round lens galaxy due to interfering PSF wings, the parameter space must be constrained to exclude less likely b/a values. Since both the lensing galaxies and quasar images are in some cases too bright to be distinguishable in H-band, but too faint in V-band, we use the shape parameters PA or b/a from I-band as a proxy for the fits in other bands. This approach is legitimized by the fact that different stellar populations visible in different bands do not change their relative positions and orientations considerably. All other fitting parameters apart from the boxiness, which is set to zero throughout the process are free. The boxiness as well as all other parameters are defined in Peng et al. (2002). The determination of the light centroid and the size of masked regions, as well as checks for fulfilled masking criteria are conducted via `IRAF` (Image Reduction and Analysis Facility).

To minimize χ^2 and test the stability of the fit, the fitting procedure was repeated with slight changes to the initial parameters. For lenses with photometric data in more than one band the I or V-band parameters for R_e and n were taken as a prior to the H-band parameters if necessary. However, χ^2 is not the only criterion to assess the quality of a fit. We focus on the goodness of the fit in regions most important to our analysis, i.e. in the central region of the lens galaxy. The ratio of the residual image and the original image yields a percentage map of the lens systems showing pixel-by-pixel the quality of the model, as illustrated in Fig. 3.7 (upper right panel). Note that the Figure shows the central region enlarged by a factor of two compared to Fig. 3.6. As the original image

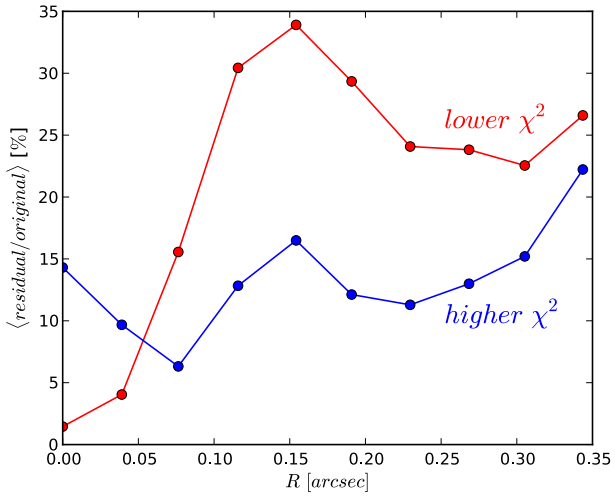

***Figure 3.8*:** As in the lower right panel of Fig. 3.7, but for two different photometric models of the lens galaxy B1422. The model with the lower χ^2 according to GALFIT produces a residual map that exceeds the high-χ^2 model over a wide radial range.

of the lens system drops quickly to small pixel values, the *residual/original* ratio can become extremely large. At pixel positions where the model overestimates the original photometry the values can become negative. We note that in some cases, better χ^2 fits were rejected in favour of the flatness of the residual in central regions $\lesssim 1R_e$ of the lens. This occurs in particular for lenses for which the short distance to a lensed quasar image makes constraints mandatory. An example is given in Fig. 3.8 for two different models of the lens system B1422. The lower χ^2 is due to better agreement between model and photometry in regions not important for the lens model. In general regions more distant from the centre of the light profile affect the χ^2 value stronger, as the amount of pixel with same distance to the centre increases with distance. At the same time the pixel values decline, which should countervail the impact of the increasing amount of pixels. The quasar images leave however an imprint in the residual map, as their wings extend mostly beyond the reduced box as one can see in Fig. 3.4. That is why the χ^2 assessment of the goodness of the fit needs to be verified by consideration of the *residual/original* map. It should be noted that even though GALFIT does a parametric search to get the best fit, for this analysis we are just interested in the 2D distribution that minimizes the residuals, regardless of the parameters themselves, i.e. we are less sensitive to the inherent degeneracies associated with parametric fits. After creating photometric models for all available band-passes, we proceed with the stellar population synthesis process.

3.2.3 Stellar mass component

The baryonic matter component in form of stars can be inferred using the previously modeled photometry. In early-type galaxies the baryon budget is dominated by the stellar mass content. We estimate stellar masses using population synthesis models to set constraints on the history of star formation. In this procedure an initial mass function

$\phi(m) = dN/d\log m$ (see Section 2.8) as a starting point for a single stellar population is assumed. A spectrum Λ, or spectral energy distribution, can be synthesized from a spectral library, such as the one of Bruzual & Charlot (2003*a*), depending on the metallicity Z, the mass and the stellar age t. So a single stellar population is defined by

$$S(t, Z) = \int \phi(m)\Lambda(m, t, Z)\ dm. \tag{3.1}$$

To obtain an evolved stellar population the single stellar population needs to be convolved with the star formation rate. The star formation rate $\psi(t - t_{FOR}) \propto \exp -(t - t_{FOR})/\tau$ describes the transformation of gas into stars over a typical formation timescale τ, starting at the formation epoch t_{FOR}. The rate decreases exponentially with time as the galaxies get depleted of gas and recycle the gas ejected by stellar remnants. Its exponential shape is a consequence of a simple power law found to relate the density of interstellar gas to the rate of star formation (*Schmidt (1959) law*).
The integrated spectrum of a stellar population in spectral band λ can then be written as

$$F_\lambda(t_{FOR}, \tau, Z) = \int_{t_{FOR}}^{t_{OBS}} \psi(t - t_{FOR}) \times S_\lambda(t, Z)\ dt. \tag{3.2}$$

Knowing the integrated spectrum F_λ (left hand side of Eq. 3.2) for two different spectral bands, allows computing the colour, i.e. the difference in magnitude, by $-2.5\log(F_{\lambda_1}/F_{\lambda_2})$. Note that even if spatially resolved photometric data is available in one band only, the colour can still be computed using the integrated flux (i.e. the total light output) of the lens galaxy known in I-band for the whole sample. In some population synthesis models the evolution of dust is taken into account by an additional exponential term in the integrand of Eq. 3.2. Since most of the lens galaxies are dust-poor early types, we just consider a single constant dust screen (see also Section 3.2.4). However, we now have a direct connection between observations and a stellar population synthesis model consisting of the initial mass function, the spectral library, the star formation history, dust attenuation and metallicity. This means also that one can directly relate colour and stellar mass, since the spectrum Λ as used in Eq. 3.1 depends on the latter. As an aside, the problem of age and metallicity of lens galaxies being degenerate cannot be solved by broadband photometry alone. But as it turns out stellar masses are less sensitiv to the degeneracy, when estimated via 'red' M/L ratios (see e.g. Ferreras et al. 2008).

Fixing the IMF to the one given in Eq. 2.40 (Chabrier 2003) the total amount of free parameters in the colour-mass relation breaks down to three: the formation epoch t_{FOR}, which – when expressed in terms of redshift – lies in the range $2 < z_{FOR} < 10$, the exponential timescale τ, broadly estimated to be in the range $-1 < \log(\tau/\mathrm{Gyr}) < 1$ and the metallicity Z, which is assumed to range from 0.1 to $2Z_\odot$, corresponding to the relative abundance range of $-1 < [\mathrm{m/H}] < +0.3$. The range of values for formation epoch and exponential timescale is as large as possible, i.e. the star formation can happen between the redshift of the oldest yet known stars $z = 10$ and the observed star formation cut-off at $z = 2$ below which it drops by one order of magnitude (Hopkins & Beacom 2006). As for the metallicity, early-type galaxies are known to be in general of solar or slightly super-solar metallicity (Trager et al. 2000). For robustness we include here an even wider range.

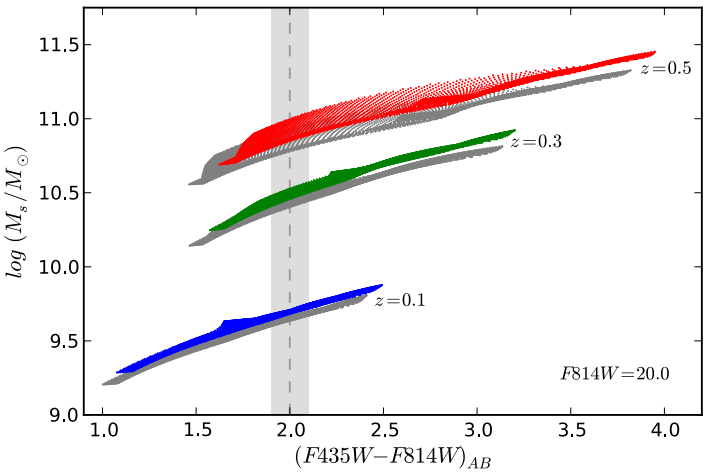

Figure 3.9: Colour-mass relation for a galaxy at $z = 0.1$ (blue), $z = 0.3$ (green), $z = 0.5$ (red) with a formation redshift $z_{FOR} = 5$, corresponding grey regions represent $z_{FOR} = 2$. Assuming an observed colour of $B - i = 2.0 \pm 0.1$ (dashed line) gives a ~ 0.2 dex uncertainty in stellar mass. Data from Ferreras et al. (2008).

For each lens we ran a grid of $32 \times 32 \times 32$ models in this three dimensional parameter space. For each choice of the parameters, a composite population is obtained, transformed to the redshift of the lens, and folded with the passband response to compare with the observed colours and to extract a mass-to-light ratio in the observer-frame H-band. The colours are furthermore corrected for Galactic extinction using the dust maps of Schlegel et al. (1998).

Even though photometry is a poor way to determine stellar ages and metallicities, it can give good estimates of the stellar mass for a given Initial Mass Function, as shown in Fig. 3.9. Therein a galaxy assumed to be at redshift $z = 0.5$ (red); 0.3 (green) or 0.1 (blue) is observed through the B and i passbands and compared with a large grid of exponentially decaying SFHs using the models of Bruzual & Charlot (2003*a*). If for this galaxy a colour of $B-i = 2.0\pm0.1$ is observed, the stellar mass can be constrained with an uncertainty of about 0.2 dex. The coloured regions in Fig. 3.9 correspond to two formation epoch of $z_{FOR} = 5$, whereas the underlying grey counterparts correspond to $z_{FOR} = 2$.

In that way the modeled profiles are used to constrain stellar population synthesis models and to estimate pixel-by-pixel the stellar mass via the colour-to-mass relation. Figure 3.10 shows the end-product of the stellar population synthesis pipeline, a stellar surface mass map (Σ_{M_s}) in a logarithmic scale. The contours enclose pixels with stellar masses equal to or greater than the value stated in the contour labels. Knowing the total reconstructed lens mass (shown in Section 3.2.1) and the stellar mass by means of the photometric models (shown in Section 3.2.2) one can compute stellar mass fractions as well as dark matter surface maps in the style of Fig. 3.10.

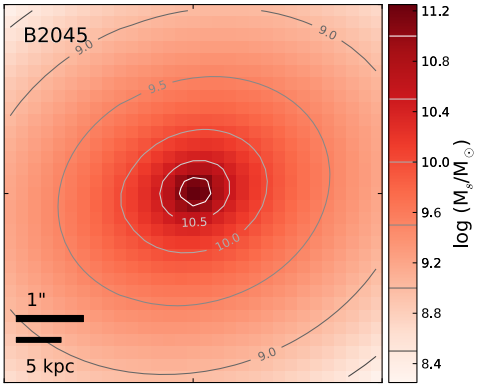

Figure 3.10: Projected stellar surface mass map for the lens B2045. Note that the contours enclose pixels of same or higher stellar mass. They do not refer to the total stellar mass enclosed. The box size is 31×31 pixels.

3.2.4 Dark matter component and stellar baryon fractions

The difference between total mass and stellar mass is not necessarily made up of 100% dark matter. Baryons which did not form stars might be stored in large more or less clumpy dust and gas reservoirs in the galaxies (e.g. van Dokkum & Franx 1995). In a recent study the total dust mass of a sample of pre-selected dusty early-type galaxies was found to range from $10^{5.2}$ to $10^{7.2}$ $M_\odot$ (Kaviraj et al. 2011). This was done using a sample of 352 nearby early-type galaxies with prominent dust-lanes. It should be furthermore noted that such obviously dusty early-types represent only 4% of the early-type galaxy population with redshifts $z < 0.07$ in the SDSS GALAXY catalogue. Its stellar masses were determined to range between $10^{9.8}$ and $10^{11.2}$ $M_\odot$. In the same study the total gas fraction (gas mass over stellar mass) for the local sample was determined to be between 0.2% and 8% with a median value around 1%. Since our sample contains only two galaxies with observable dust lanes and one late-type galaxy, the dust and gas contribution to the total mass is assumed to be negligible. The exceptions will be discussed in the sample and analysis sections of Chapter 6.

Prior to subtracting pixel-by-pixel the stellar mass (Fig. 3.10) from the total lens mass (Fig. 3.2), the pixel maps are rotated to the same orientation. Due to limited computation time, the lens mass maps have pixel sizes roughly 5 to 10 times larger than the pixels of the photometry an average value for all photometric pixels is assigned to one lens mass pixel. Figure 3.11 shows the result of these efforts. The left map is the difference of total and stellar mass, whereas the right map is the stellar mass over total mass ratio. Note that there is an error attached to each pixel. However, as our analysis is based on radial mass and stellar baryon fraction profiles, which is a stellar over total mass profile. The profiles are obtained by azimuthally averaging along the isophote ellipses.

The radial scale of such profiles is determined by H-band photometry in a special manner. Regardless of the best fit parameters, e.g. R_e of the Sérsic profile, found by

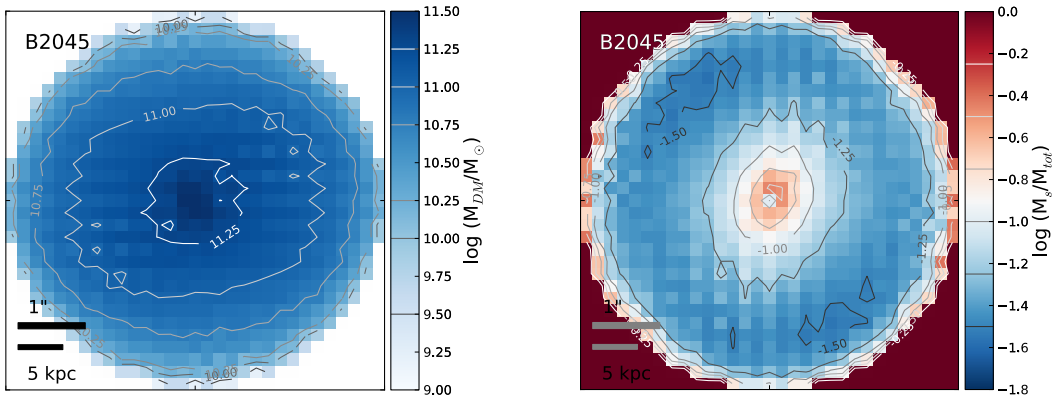

***Figure 3.11*:** As in Fig. 3.10 but for projected dark matter (left) and stellar baryon fraction (right).

GALFIT, we take the photometric model (Sec.3.2.2) in H-band (as it is the main band for the colour determination) instead to compute the Petrosian radius (Petrosian 1976). It is determined from the Petrosian ratio $\eta(r, z)$, which is simply the ratio of the mean surface brightness $I(r)$ of an annulus at radius r to the mean surface brightness within r. We have

$$\mathcal{P}(r, z) = \frac{\int_{c_1 r}^{c_2 r} 2\pi r' I(r', z)\ dr' / [\pi(c_2^2 - c_1^2) r^2]}{\int_0^r 2\pi r' I(r', z) / (\pi^2)}, \tag{3.3}$$

where c_1 and c_2 are parameters defining the radial thickness of the annulus and z denotes the redshift the flux is corrected for. Following Blanton et al. (2001), we choose $c_1 = 0.8$ and $c_2 = 1.25$. One can see that $\mathcal{P}(r, z)$ decreases nearly monotonically down to a level that depends on the background. It is common practice to define the Petrosian radius as the distance at which this ratio falls to 0.2, i.e. $\mathcal{P}(R_P, z) = 0.2$. This circularized radius is taken as the full extent of the galaxy, so that we can use it to determine the half-light radius (R_e) from the curve of growth. For the analysis of the colours, we restrict all photometric measurements within R_e. The effective radii of our lenses are given in Table C.2 in the appendix.

The introduced methods are applied to the set of gravitational lenses presented in the following Chapter.

Fig. 3.12 summarizes the stellar and total lens mass reconstruction in form of a workflow diagram. The right branch of the organization chart shows input and output of PIXELENS, which is in the focus of the following Chapter. Therein we use global light estimates to study the fundamental plane of early-type galaxies. The left branch will be used in Chapter 6, where we carry out a resolved analysis of the baryonic and dark matter distribution. Its result will be used for further analyses of halo concentrations and baryonic cooling processes in Chapter 7.

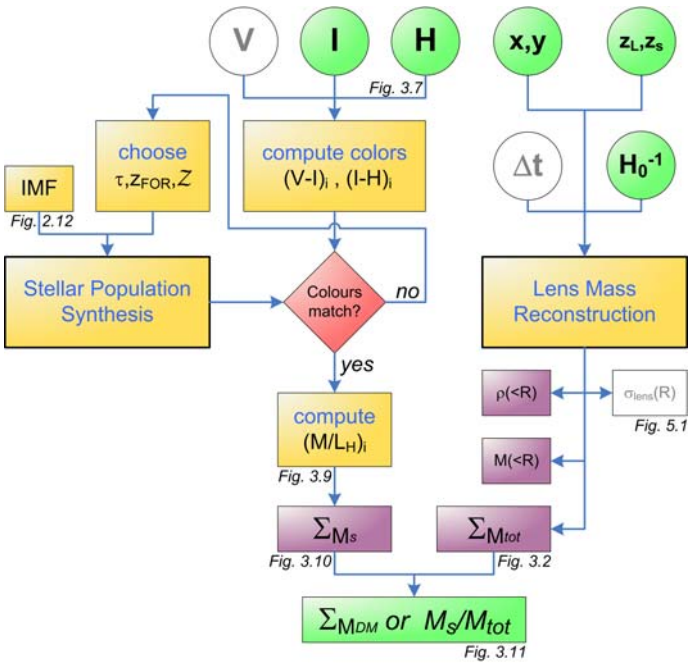

***Figure 3.12*:** The left branch of this organization chart illustrates the stellar population synthesis workflow as described in Section 3.2.3 starting with the photometric models (Section 3.2.2) as an input and ending at the stellar surface mass map Σ_{M_s} (Fig. 3.10). The right branch shows the lens mass reconstruction explained in Section 3.2.1 from input parameters (image positions (x, y), lens and source redshift (z_L, z_s), Hubble time (H_0^{-1}) and – optional – the time delays between images (Δt)) to the intermediate products, the density profile $\rho(< R)$, the enclosed total mass profile $M(< R)$, a formal velocity dispersion $\sigma_{lens}(R)$ (used only in Chapter 5) and the total surface mass map $\Sigma_{M_{tot}}$ (Fig. 3.2). Subtracting or dividing the pixelated mass maps yields the dark matter or baryon fraction map respectively. Input/output data is indicated by green colour, program routines are yellow, logical junctions red and intermediate products magenta. White components are not essential to the pipeline.

4
Lensing Galaxies

In the following we present and discuss briefly the lens sample used in the different parts of this thesis. All lens properties important for mass reconstruction and stellar population synthesis are given below. Furthermore, we provide detailed information about the lens environment, which in fact influences both the mass model and the light profile and yields important insights into the evolution of early-type galaxies.

The selection criteria for the samples are given in the respective Chapters (see Section 5.2, 6.2 and Section 7.1).

The lens sample presented in Section 4.1 is used for the studies carried out in Chapter 5. It incorporates 18 well-known early-type lensing galaxies – nine from the Sloan Lens ACS Survey[1] (SLACS), another nine from the CfA-Arizona Space Telescope LEns Survey[2] (CASTLES) – and two lensing clusters, ACO 1689 and ACO 2667. Reconstructed surface mass maps produced via `PIXELENS`[3] and corresponding input, such as lens redshift, source redshift, image positions and time delays, are shown in Figures B.1 and B.2 in the appendix. A brief tutorial on how to comprehend the input files is given at the beginning of Appendix B.

The lens sample presented in Section 4.2 is a subset of the CASTLE Survey used for the stellar and dark matter reconstruction in Chapter 6. It consists of 21 lenses subject to later analysis and another three objects used to highlight problems in photometric modeling (Section 6.2.3). Available H-band photometry is presented in Fig. 4.1 at the end of this chapter. Again a fraction of the sample, eighteen out of 21 lenses, is used for the analysis in Chapter 7.

We provide the lens parameters, references and all quantities important for (and inferred from) the studies carried out in Chapters 5, 6 and 7 in Tables C.1, C.2 and C.4 of the appendix, respectively.

Throughout this chapter we will use the terminologies *double* or *quad* to refer to lens systems with two or four lensed source images. Note that after giving the full name of the lenses we henceforth use their abbreviated identifiers only, i.e. we skip the digits indicating the declination.

[1] www.slacs.org - The full set includes about 70 lenses, but image data was only made available for a small subset.

[2] cfa-www.harvard.edu/glensdata/

[3] Available from www.qgd.uzh.ch/projects/pixelens/

4.1 Lens sample I

In this section we present the lensing systems used in Chapter 5.

Lensing systems from CASTLES

CFRS03.1077: This doubly imaged lens system was found by Crampton et al. (2002). For its lens galaxy no effective radius is known; hence it is used for the analysis in Section 5.3 but not in Section 5.4.

HST15433: The double HST15433 was discovered by Ratnatunga et al. (1999). It has a neighbouring galaxy companion, which is thought to only modestly perturb the estimated mass, according to Jiang & Kochanek (2007). Also for this lens no effective radius could be found in literature.

Q0957+561: This lensing galaxy is part of a cluster that contributes significantly to the large image separation (Garrett et al. 1992). Q0957 was the first lens discovered (Walsh et al. 1979) and is special also in other respects. First there is a doubly imaged galaxy component in addition to the famous double quasar used to calculate the projected mass map. Secondly the lens is a cD galaxy located in the centre of a cluster. The nearest cluster member lies within $10''$ East of the lens galaxy. However a simple external shear is insufficient to describe the effect of the environment on the image positions. Breaking the degeneracy between the shape of the galaxy and the cluster shear takes advantage of arc features (Keeton et al. 2000) and X-ray data as attempted by Chartas et al. (1998).

MG2016+112: This lens system was reported first by Narasimha et al. (1984). According to More et al. (2009), it exhibits quadruply imaged features of the quasar jet which can be distinguished only in the radio band. As the pixelated models evolved MG2016 is treated as a double in Chapter 5 and as a multiply imaged quasar system with three images in Chapter 6. MG2016 is known to be a giant elliptical galaxy in a cluster with 69 probable, photometrically selected members of many different galaxy types (Toft et al. 2003). Among them is a significant fraction of merging cluster galaxies, which is direct evidence for a hierarchical formation history (van Dokkum et al. 2000). Most of the neighbouring objects within $30''$ lie on an east-west axis and thus explain the major shear direction.

Q0047-2808: The quadruply imaged quasar was discovered by Warren et al. (1996). Q0047 appears to have a double component source, but this is probably not important for macro models. It is a lens with only a small shear required by lens models. However, Wong et al. (2011) find evidence for a galaxy group with 9 members.

PG1115+080: This quad was reported first by Weymann et al. (1980) and has measured time delays (e.g. Schechter et al. 1997). The environment of the quad PG1115 is thoroughly analyzed by Momcheva et al. (2006). They find 13 galaxies in a local group with elongated group emission in X-rays according to Grant et al. (2004). The brightest 4 members of the group are located on an axis with a position angle of $+60°$ (measured North through East) of the lens mass which accounts well for the shear required in our lens model.

HST14176: The lensing galaxy responsible for a quad configuration, discovered by Ratnatunga et al. (1995), is part of a cluster which is not included in the models.

B1608+656: For the complex quad system B1608 (Myers et al. 1995), the measured time delays (see Fassnacht, Pearson, Readhead et al. (1999)) are used and make a more significant difference to the lens models. The lens resides in the middle of a galaxy group with 8 other group members according to Fassnacht et al. (2006). The photometry shows an object close to the main galaxy, which constitutes a second lens galaxy. This is confirmed by the reconstructed mass map (Fig. B.3) as it predicts a conspicuously elongated mass distribution towards NE. The image (Fig. 4.1) also show a prominent dust lane between the two galaxies.

Q2237+030: The Huchra-lens Q2237, also known as the Einstein Cross, is actually the bulge of a barred spiral galaxy, which is responsible for the lensing (Huchra et al. 1985). Note that in Chapter 6 the bulge is treated as an early-type galaxy. The system shows only a mild external shear due to the disk of the spiral galaxy. For spiral galaxies the contribution of dust to the photometry is usually more significant than for early-type galaxies (the latter morphological type constitutes the majority of our lensing galaxies). The impact of dust on our analysis is discussed in Section 6.2.2.

Lensing systems from SLACS

The doubly imaged systems among the SLACS lenses are:
J0037-094, **J0912+002**, **J1330-014** and **J2303+142**.

All of them are quite typical with biases according to their observation method. The lens system J0912 takes a special position. It consists of two long arcs which are represented in this work as four doubles. Moreover, this lensing galaxy has the highest kinematic velocity dispersion $\sigma_{\rm obs}$ among all lenses of our sample. J1330 is the lens with smallest redshift ($z = 0.08$) among the SLACS lenses and shows the smallest $\sigma_{\rm obs}$.

Quadruply imaged systems among the SLACS lenses of our sample are:
J1205+491, **J1636+470** and **J2300+002**.

The mean kinematic velocity dispersion $\langle\sigma_{\rm obs}\rangle$ of our SLACS sample is 10% higher than $\langle\sigma_{\rm obs}\rangle$ of CASTLES lenses.

There are two special cases: **J0737+321** and **J0956+510**.
Both are thought to be quads, but in each of these only 3 images are used, as the astrometry of the faintest image was too uncertain. J0737 is with $z = 0.32$ the most distant in our SLACS subsample and belongs to higher z lenses in the whole catalogue.

Lensing clusters

Finally we consider the two lensing clusters ACO 1689 and ACO 2667.

ACO 1689: This galaxy cluster has a very large number of multiply imaged systems found by Broadhurst et al. (2005). In the present work this cluster is modeled by a set

of two 5-image systems, six 3-image systems and one double. The additional systems are known to affect only model details (Saha et al. 2007). Note that there are many more imaged sources, but adding those to the model does not change $M_{\rm lens}$, i.e. the mass model is tightly constrained by this set of image systems.

The kinematic line-of-sight velocity dispersion $\sigma_{\rm obs} = 1400$ km s^{-1} of galaxies within the cluster was taken from Łokas et al. (2006) for a subset of 130 galaxies in the inner region of the cluster with velocities $|v| < 3000$ km s^{-1}, which contains most likely the biggest mass fraction responsible for the lensed images. This average value applies for a radius of around 400 kpc, a region where the formal velocity dispersion seems to be sufficiently flat and in which roughly half of the projected radii of the 130 galaxies considered in Łokas et al. (2006) are to be found. Furthermore the value is not too far away from the Einstein radius or outermost image position of around 240 kpc. In order to estimate the I-band magnitude of the cluster, the 130 brightest out of 840 galaxies are taken from a cluster survey of Molinari et al. (1996) for which the Gunn g, r and i magnitudes were provided. Together with K-correction, evolution correction and galactic extinction we obtain $L_I = 2.82 \times 10^{12} L_{\odot}$.

ACO 2667: For this cluster three 3-image systems and one double were known to derive the formal mass-only related velocity dispersion curve. The kinematic velocity dispersion $\sigma_{\rm obs} = 960^{+190}_{-120}$ km s^{-1} of this lens was determined by Covone et al. (2006) from a sample of 21 galaxies in the inner region of the lensing cluster with a radius of $110 h_{70}^{-1}$ kpc, which is in the same order of magnitude as $R_{\rm lens} = 98 h_{72}^{-1}$ kpc. However, since photometric data for estimating the total flux of galaxies within the cluster was not available, ACO 2667 is not included in the mass-to-light plots of Section 5.4 and consequently there was no need to determine $R_{\rm e}$ for the mass estimate.

4.2 Lens sample II

Q0047-2808: For information on Q0047 see Section 4.1.

Q0142-100: The environments of the doubly imaged quasars Q0142 have been studied by Lehár et al. (2000), Momcheva et al. (2006) and Eigenbrod et al. (2007) and are found to have no dominant impact on the total shear beyond a cosmological (large-scale structure) contribution $\gamma_{\rm LSS}$ which is additionally confirmed by lens models. Not much is known about the close-in group environment of Q0142, although there are some galaxies near the line-of-sight, whose redshifts are mostly unknown. Surdej et al. (1987) speculate that a galaxy about $10''$ away from the lens may be a group member.

MG0414+0534: The quadruply imaged quasar MG0414 at $z = 0.960$ is the second most distant lens of our sample. Judging by its luminosity and colour, the lens is likely to be a passively evolving early-type galaxy (Tonry & Kochanek 1999). Schechter & Moore (1993) find an object close to image B visible only in I-band, which might contribute to the lensing effect. Our reconstructed mass map also shows increased surface density at the position of the object.

B0712+472: This quadruply imaged quasar was reported first by Jackson et al. (1998). Lens models found in previous studies require significant external shear, which can be attributed to 9 or more galaxies in a foreground group at $z \sim 0.3$ found by Fassnacht & Lubin (2002). Their study also shows one other galaxy at the redshift of B0712 at $\sim 100''$ from the lens.

HS0818+1227: The image separation of this doubly imaged quasar is $2.56''$. Since its discovery by Hagen & Reimers (2000) no further insights into the environmental properties of the lens have been gained. Nevertheless, Hagen & Reimers (2000) found a galaxy $5''$ north of the lens which appears to have the same redshift of $z = 0.39$, which explains the external shear required by our lens model. A chain of galaxies at a distance of $10''$ north-east could also be associated with the lens galaxy.

RXJ0911+0551: The quad lens RXJ0911, discovered by Bade et al. (1997), is located on the outskirts of a cluster (Morgan et al. 2001). *Chandra* observations of the cluster suggest a complex non-spherical cluster mass distribution at a temperature of roughly 2.3 keV.

BRI0952-0115: The environments of the doubly imaged quasar BRI0952 have been studied by Lehár et al. (2000), Momcheva et al. (2006) and Eigenbrod et al. (2007) and found to have no dominant impact on the total shear beyond a cosmological (large-scale structure) contribution $\gamma_{\rm LSS}$, which is additionally confirmed by lens models. BRI0952 was previously thought to reside in a region loosely bound to a poor group with 5 members (Momcheva et al. 2006); a later study discovered it is at higher redshift and thus not connected with the group (Eigenbrod et al. 2007).

Q0957+561: For information on Q0957 see Section 4.1.

LBQS1009-0252: This double was first reported by Hewett et al. (1994). Lehár et al. (2000) locate the lens galaxy of LBQS1009 close to quasar image B. They find that a dominant shear contribution of the host galaxy of a nearby quasar ($4.6''$ northwest of the lens — unrelated to the lensed quasar) is consistent with the derived major axis of the lens when modeled by a Singular Isothermal Ellipsoid. Using a Singular Isothermal Sphere model Claeskens et al. (2001) determine a smaller shear. Faure et al. (2004) state that there is no significant galaxy overdensity in the field. This is in agreement with the free-form lens models of this study, which do not require external shear for this lens.

B1030+071: This lens was reported by Fassnacht & Cohen (1998). It exhibits average velocity dispersions and intermediate luminosities. Observed substructures in B1030 indicate the presence of an interacting galaxy system (Jackson et al. 2000) although firm statements about the environment cannot be made (Lehár et al. 2000). However, shear is not strongly required by our mass model.

HE1104-1805: The doubly imaged quasar HE1104 features the second highest image separation of $3.19''$ and a distinct lens galaxy (the median separation is $\sim 1.5''$) (Wisotzki et al. 1993). Furthermore, the lens appears to be near the bright image, which is rather unusual and implies the presence of a group or cluster enhancing the separation (Lehár et al. 2000). Parametric as well as free-form mass models also suggest that an external

shear is mandatory to reproduce the image configuration (e.g. Wisotzki et al. 1998). The lens galaxy is unaffected by quasar light, allowing for a good fit. However, the photometric redshifts of a few neighbouring galaxies described in Faure et al. (2004) indicate that such cluster galaxies are probable companions of the lensed quasar rather than of the lens.

PG1115+080: For information on PG1115 see Section 4.1.

B1152+200: For the doubly imaged quasar B1152, whose discovery was reported by Myers et al. (1999), there is no information about the composition of the environment. Judging by the morphology of the image-source system no strong shear is expected. B1152 shows average velocity dispersions as well as intermediate luminosities.

B1422+231: The quad B1422, found by Patnaik et al. (1992), is in a poor group with 5 nearby galaxies mostly south east of the lens that cause a significant shear (Momcheva et al. 2006, Hogg & Blandford 1994). The group is visible in X-rays at $0.5-2$ keV (Momcheva et al. 2006). In recent work by Wong et al. (2011), 12 new members were found to be part of the group.

SBS1520+530: This doubly imaged quasar was discovered by Chavushyan et al. (1997). It is a member of a galaxy group with at least 4 other members as stated in Auger et al. (2008).

B1600+434: B1600, discovered by Jackson et al. (1995), is located in a denser group with at least 6 late-type galaxies which cause significant shear. It should be noted that B1600 is likely to be a late-type galaxy viewed edge-on (Auger et al. 2007). We find further evidence for this from the study of concentration parameters in Section 6.6. The absence of X-ray emission is suggestive of a not relaxed group, a conclusion strengthened by the elongated morphology of the group. Furthermore the lens galaxy appears to be almost edge-on and exhibits a prominent dust lane. B1600 shows average velocity dispersions as well as intermediate luminosities.

B1608+656: For information on B1608 see Section 4.1.

MG2016+112: For information on MG2016 see Section 4.1.

B2045+265: B2045, as found by Fassnacht et al. (1999), might be influenced by a group of galaxies west of the lens. A shear in this direction is also required by the lens model. The lens might also be affected by a close dwarf galaxy causing anomalous flux ratios (McKean et al. 2007).

HE2149-2745: The double HE2149 was discovered by Wisotzki et al. (1996). It might be a member of a cluster as inferred by Lopez et al. (1998), using a large number of red non-stellar objects in R-band images of the field around the lens. Considering recent estimates of the lens redshift from Eigenbrod et al. (2007) ($z_{\rm lens} = 0.603$) and the environment survey from Momcheva et al. (2006), HE2149 could be in a group with 3 neighbouring objects. The morphology of the lens shows no sign of strong external shear.

Q2237+030: For information on Q2237 see Section 4.1.

Special cases

The following three lenses are excluded from our analysis in Chapter 6, but used in Section 6.2.3 to highlight problems of photometric modeling.

B0218+357: B0218 is the system with the smallest known image separation (0.33″) (Patnaik et al. 1993). The projected lens mass map shows that external potentials induce a shear in B0218 that was studied in Lehár et al. (2000). They find 13 possibly perturbing galaxies inside a radius of 20″ located roughly along the axis which connects the two quasar images. It should be mentioned that according to Lehár et al. (2000), B0218 is a late-type galaxy.

RXJ0921+4529: The doubly imaged quasar RXJ0921 has the highest angular image separation (6.93″) compared to any other lens in the sample. According to Muñoz et al. (2001), it is probably a member of an X-ray cluster. From model fits of the host galaxy, Peng et al. (2006) conclude that RXJ0921 is a binary quasar rather than a gravitational lens. Also, Popović et al. (2010) find quite different spectral properties in the spectra of the two components. There are 16 objects within 20″ from the lens galaxy. Only for three of them a redshift close to that of the lens could be determined. The mass model, however, does not require any external shear. In Section 6.2.3 we find unusually low baryon fractions for this object, which can be taken as further evidence against the lens hypothesis.

B1933+503: B1933, discovered by Sykes et al. (1998), has 10 distinct images formed from a three-component source, promising an exceptionally well-constrained mass profile. As of now, there is no study of the environment of the lens, but according to the mass reconstruction, no strong shear is necessary to explain the morphology.

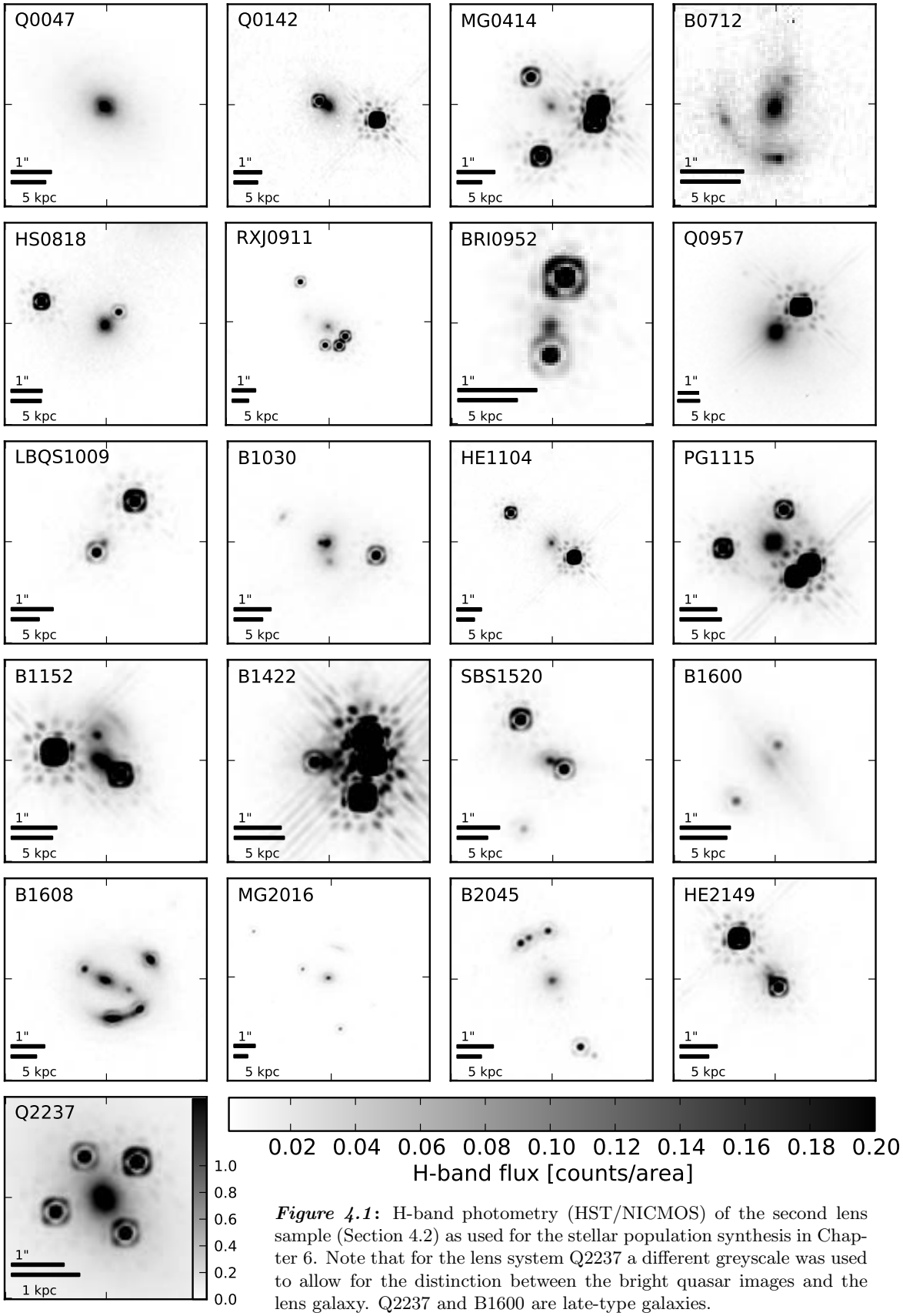

***Figure 4.1*:** H-band photometry (HST/NICMOS) of the second lens sample (Section 4.2) as used for the stellar population synthesis in Chapter 6. Note that for the lens system Q2237 a different greyscale was used to allow for the distinction between the bright quasar images and the lens galaxy. Q2237 and B1600 are late-type galaxies.

5 A Lensing View on the Fundamental Plane

The fundamental plane (FP) of early-type galaxies is an underlying regularity, which contains valuable information on how galaxies form and evolve. Understanding the origin of its departure from simple theoretical assumptions of virial equilibrium and constant mass to light ratio, as discussed in Sec. 2.6.1, will give clues on other questions concerning galaxy formation and evolution yet to be answered. The following analysis can be seen as a preparation for the studies carried out in Chapters 6 and 7. In this chapter we make use of the integrated fluxes (meaning one global luminosity quantity per lens galaxy) and give consequently global estimates of the baryonic and dark matter content. The analyses in Chapters 6 and 7 concern the resolved inner structure ($< 10kpc$) of lens galaxies.

In the following section, we introduce a formal velocity dispersion $\sigma_{\rm lens}$, based on enclosed mass and the virial theorem (Eq. 2.30). This is calculated from an ensemble of pixelated lens models, introduced in Section 3.2.1, which is found to be fairly model independent. We compare $\sigma_{\rm lens}$ with the kinematic velocity dispersion $\sigma_{\rm obs}$, which can be regarded as a test of the degree of virialization (see Section 5.3). In a second step, we calculate the I-band luminosity and the total mass content for the sample of lensing galaxies, which enables us to analyze the mass-to-light (M/L) relation $L \propto M^{\alpha}$ (Section 5.4). As galaxy clusters exhibit generally a much higher M/L ratio, they should lie on a different FP. We investigate whether this is true for lens clusters.

A sample of 18 well-known early-type lensing galaxies and two clusters, introduced in Section 4.1, is used for this analysis. It comprises 9 lensing galaxies from the Sloan Lens ACS Survey (SLACS) and another 9 from the CfA-Arizona Space Telescope LEns Survey (CASTLES) as well as the lensing clusters ACO 1689 and ACO 2667.

The results of this preparatory study are summarized in Section 5.5 and will be set in a broader context of spatially resolved studies on luminous and dark matter distributions in Chapter 8.

5.1 Introduction

With gravitational lensing as an additional, independent measure of mass one can suitably analyse the structure of the FP, as already done in different approaches. Bolton et al. (2007) linked lensing mass and virial mass, whereas Rusin, Kochanek & Keeton (2003), Treu et al. (2006), Jiang & Kochanek (2007) and Ferreras et al. (2008) analyzed the mass-to-light dependence

$$M^{\alpha} \propto L, \tag{5.1}$$

which is a representation of the FP.

By repeating the step from Equation 2.30 to 2.31 (see the introduction to fundamental plane, Section 2.6.1) for the more general definition of the mass-to-light relation in Equation 5.1, a and b in Equation 2.32 can be expressed in terms of the power index α, which is what we need to compare the results with previous FP type studies (listed in Table 2.1 in Section 2.6.1). Equating the now α-dependent exponents of σ and I yields

$$a(b) = -2(1 + 2b), \tag{5.2}$$

which only applies for a not unique mapping from (a, b) to α, assuming Equation 5.1.

In this study we combine both the virial approach and considerations including luminosities by means of lensing masses $M_{\rm lens}$ from 18 early-type lensing galaxies and 2 clusters, discussed in detail in Section 5.2. An important role is played by a formal velocity dispersion, which we define as

$$\sigma_{\rm lens}(R) = \sqrt{\frac{2}{3}\frac{GM(< R)}{\pi R}}. \tag{5.3}$$

For an isothermal sphere this is exactly equal to a line-of-sight velocity dispersion. The formal velocity dispersion $\sigma_{\rm lens}(R)$ is computed from the pixelated mass maps (Figures B.1 and B.2) as indicated in the organization chart, Fig. 3.12. A detailed description of the lens sample is provided in Section 5.2. Additional information is provided in Table C.1 in the appendix. We define $M_{\rm lens}$ and $M_{\rm vir}$ according to Eq. 2.30 as:

$$M_{\rm lens} = \frac{3\pi}{2G} R_{\rm e} \sigma^2_{\rm lens} \tag{5.4}$$

and $M_{\rm vir} = \frac{3\pi}{2G} R_{\rm e} \sigma^2_{\rm obs}$, where $R_{\rm e}$ is the effective radius. It must be emphasized that, unlike in Chapter 7, $M_{\rm vir}$ is defined here as a dynamical mass estimate rather than the mass enclosed in a sphere of radius $R_{\rm vir}$.

This in hand we can consider the following questions as a rephrased puzzle of FP:

1. Is the lensing inferred velocity dispersion $\sigma_{\rm lens}$ from non-parametric mass reconstruction equal to the kinematic velocity dispersion $\sigma_{\rm obs}$?
2. Is this applicable to cluster scale lensing objects?
3. Are the computed $M_{\rm lens}$ and $M_{\rm vir}$ consistent with the FP?
4. Does the FP relation extend to clusters?

Bearing these questions in mind we want to give a short overview of previous findings in addition to the overview on FP studies given in Section 2.6.1.
In the above mentioned approach by Bolton et al. (2007) to the FP problem, the authors find that $\sigma_{\rm lens} \approx \sigma_{\rm obs}$ without taking advantage of luminosities (see also Bolton et al. 2008). Their result is supported by our findings presented in Section 5.3. Bolton et al. (2007) take no baryonic information into account, but a different plane is introduced, which emerges from a dimensional change in the FP space from surface brightness I to surface density Σ, giving

$$R_{\rm e} \propto \sigma^{a_m} \Sigma^{b_m}.$$

In fact this scaling relation, named a more fundamental or mass plane, can be transformed into the shape $M^{-b_m}/R_{\rm e}^{-(1+2b_m)} \propto \sigma^{a_m}$ which is (for $a_m = 2$ and $b_m = -1$) consistent with our theoretical assumptions of Equation 5.3 and thus represents the virial theorem. We like to point out that the change to Σ introduces basically a redshift dependence, which comes along with a grave selection effect that reduces the significance of the scaling relation. Moreover this relation is compared to the existing FP by introducing a new parameterization of the lensing mass

$$M_L = c(G^{-1}\sigma^2_{\rm obs}(R_{\rm e}/2))^{\delta},$$

where c denotes a structure constant and δ a newly introduced power index. Bolton et al. (2007) find that by doing so "the tilt relative to the virial relation is essentially eliminated". But basically c and δ are again consistent with Equation 5.3. Upon choosing $\delta = 1$, c becomes $\log 3\pi/2$ and the new parameterization in (Bolton et al. 2007) turns into a test of the virial theorem.

Thus the decreased scatter for a mass plane is rather a natural consequence of the added fitting parameter and selection effects than a more fundamental scaling relation. Implications on structure variations are hardly possible. An appropriate treatment on the search for reasons for a tilt in the FP originating in certain structural peculiarities includes more elaborate approaches that allow for a distinction between for instance anisotropy and mass-dynamical structure.

Rusin, Kochanek & Keeton (2003) introduced a self-similar mass model for early-type galaxies consisting of two components: one concentrated component, which traces the light distribution and one more extended power-law component, which represents the dark matter. They found a strong r^{-2} dominance and therefore used the velocity dispersion σ_{iso} for an isothermal model as a surrogate in the FP yielding a mass-to-light relation of $M_{\rm lens}^{0.88^{+0.10}_{-0.11}} \propto L$, which was the first such result from strong lensing. The error of the slope already excluded a constant M/L. While substituting σ_{iso} they are effectively assuming the virial theorem.

Jiang & Kochanek (2007) constrain the average stellar mass fraction of a halo in favour of adiabatically compressed halo models by taking a sample of early-type galaxies which consists partially of lensing galaxies used in this sample. By means of a two-component model stellar and virial mass are fitted separately and an isothermal density profile is assumed. The paper takes advantage of already K-corrected B-band magnitudes and lensing masses and is, because of its common subset of gravitational lenses, directly comparable with our data. Although it is not explicitly calculated in their paper, we find $M_{\rm lens}^{0.88\pm0.12} \propto L$, based on their published data, which is in perfect agreement with the result from Rusin, Kochanek & Keeton (2003).

Switching from the lensing point of view (considering $M_{\rm lens}$) to the observational one (considering $M_{\rm vir}$) enables us to compare the FP from previous studies which were inferred from lensing with the FP based on stellar dynamics. Treu et al. (2006) analyze the FP by means of virial mass and find that the velocity dispersions for their SDSS lens sample are well approximated by σ_{iso}, which holds also for our mixed CASTLES/SLACS sample.

There are studies, e.g. from Graham & Colless (1997*b*) and Trujillo et al. (2004), which raised hope that a solution for the FP tilt is at least partially given by broken structural homology leading to strong correlations between Sérsic index n and photometric-independent galaxy properties. Graham & Colless (1997*b*) fit $R^{1/n}$ profiles and make use of the spatial velocity dispersion at spatial effective radius to show the influence of structural non-homology, whereas Trujillo et al. (2004) quantify the contribution to the tilt caused by variations of n for a wide range of B-band selected early-type galaxies. The results always show that taking account of non-homology shifts the FP parameters closer but never fully matches the virial expectations. However, by comparing the $M/L - \sigma$ relation of 25 E/S0 galaxies (see Hubble sequence, Fig. 2.9) from the SAURON sample with predictions and virial estimates Cappellari et al. (2006) find that the FP tilt is exclusively due to a real M/L-variation, while structural and orbital non-homology has a negligible effect, a result also verified in this study.

Furthermore, progress in estimating M_{tot}/M_{stel} was recently made by comparing stellar population models with the nonparametric mass profiles also used in this thesis, which allow for scanning the dark matter distribution within a galaxy (Ferreras, Saha & Williams 2005, Ferreras et al. 2008). They found that low-mass galaxies have only little dark matter content at all observed radii. On the contrary high-mass galaxies have little or no dark matter inside the effective radius but at large radii they are clearly dark matter dominated. No kinematic and virial assumptions were required.

In the following analysis, we use a combination of kinematic, photometric and lensing inferred data to address the aforementioned puzzle. The lens sample is presented in Chapter 4.1. The selection criteria and lens properties important for the understanding of following studies are discussed in Section 5.2. The comparison of $\sigma_{\rm obs}$ and $\sigma_{\rm lens}$, which is proportional to a comparison between virial mass and lens mass, is adequate for answering the above questions 1 and 2, as will be shown in Section 5.3. In Section 5.4, we compute the luminosities of the lenses, $M_{\rm lens}$ and $M_{\rm vir}$ needed for $L \propto M^{\alpha}$ and check the consistency with other FP studies in particular with data from Jiang & Kochanek (2007), who use a common subset of lens systems. Subsequently, the a-b-parameter plane is generated including a wide range of recent FP studies.

5.2 Lenses and lens models

The sample consisting of nine lensing galaxies from SLACS[1] data, nine from CASTLES[2] and two lensing clusters. We select these galaxy lenses using two criteria:

1. the lensed images were either pointlike sources or contain nearly pointlike features, and

2. the availability of $\sigma_{\rm obs}$ data.

Two cluster lenses with such properties are also included for comparison and contrast, since prior to this work FP studies were carried out for small scale and large scale objects

[1] www.slacs.org - The full set includes about 70 lenses, but image data was only made available for a small subset.

[2] cfa-www.harvard.edu/glensdata/

combined (e.g., Schaeffer et al. 1993). As an additional motivation it is worth mentioning that Zwicky (1937) originally introduced gravitational lensing as a method to estimate masses of galaxy clusters.

The analysis is done for a subsample of doubles, quads and multiple object systems of SLACS and CASTLES lenses. The CASTLES lenses turn out to be a relatively inhomogeneous sample, a consequence of the fact that they spread over a large range in redshift and effective radii as well as lens radii.

For each lens detailed information is given in Section 4.1 of the previous chapter. However, the following information on the lenses seems noteworthy here: The effective radius of CFRS03.1077 is not known; hence it is used for the analysis in Section 5.3, but not Section 5.4. Q0957 is a special case, as there is a doubly imaged galaxy component in addition to the famous double quasar. As it is part of a cluster, a position below the general trend in a mass-to-light analysis is expected. This lens is an excellent example for the consequences of possible yet unknown image systems. The considerations following in Section 5.3 for $\sigma_{\rm lens}$-$\sigma_{\rm obs}$ are carried out for two different image configurations: on the one hand the two double image system shown in Figure 5.1 and on the other a single double system. For PG1115, measured time delays were not used for the models in this study; if these are included the lens models tend to become rounder, but $\sigma_{\rm lens}$ changes only by 5% to 10%, which is insignificant for the present study. The lens Q2237 is actually the bulge of a spiral galaxy. Here the bulge is treated as an early-type galaxy. Several of the lenses in our sample have been studied individually in great detail. Different papers sometimes disagree on the slope of the profile (e.g., Treu & Koopmans 2002, Read et al. 2007, for PG1115), but agree on the enclosed mass. Hence the effect on $\sigma_{\rm lens}$ would be small.

SLACS lenses populate a redshift range from 0.05 to 0.5. Due to smaller mean effective radii and lens redshifts, as a consequence of a limited aperture ($3''$) radius of SDSS fibres, the sample of 9 SLACS lenses appears to be more clustered in mass-to-light plots than the CASTLES sample and therefore has a smaller RMS. The SLACS lenses we use are a subset of the full SLACS sample for which pointlike features are identified (Ferreras et al. 2008). The above lensing data are modeled using the `PIXELENS` program[3] (Saha & Williams 2004, Coles 2008). All the uncertainties on any parameter can be derived from this model ensemble.

For each lens, an ensemble of 100 mass maps with 21×21 pixels each has been computed, from which the mass-profile and therewith the formal velocity dispersion $\sigma_{\rm lens}$ is derived with an 90% uncertainty, as one can see e.g. for the lens Q0957 in Figure 5.1. In Leier (2009) we conduct a stability test of the `PIXELENS` output depending on the ensemble size and find that $\sigma_{\rm lens}(R)$ is not sensitive to ensemble enlargement. Thus, the number of models is fixed to 100 throughout this analysis.

Two points shall be emphasized here: Firstly, the error bars in the right panel of Figure 5.1 represent the model dependence for an ensemble of 100 models and, as one can see, it is not large. Secondly, it is sometimes stated that the enclosed mass $M(< R)$ is known for $R = R_{\rm Ein}$, the Einstein radius and unknown for any other R, but this is oversimplified. In

[3] Available from www.qgd.uzh.ch/projects/pixelens/

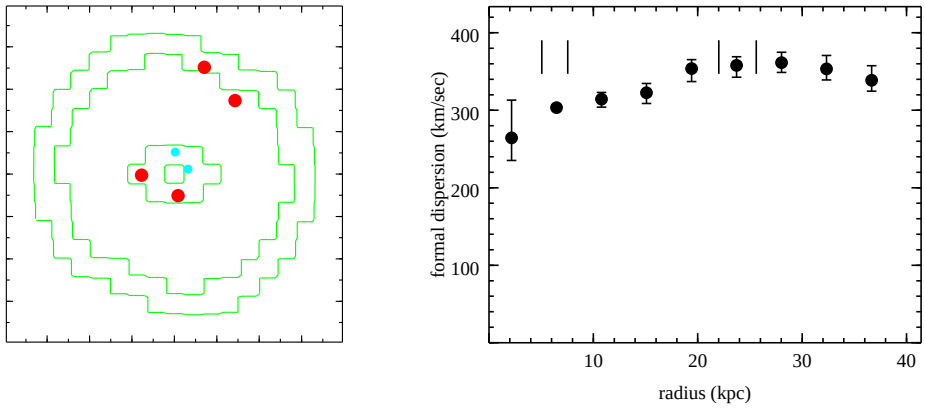

***Figure 5.1*:** Left panel: projected mass distribution of the CASTLES lens Q0957. The box size is 4×4 arcsec^2. The red dots mark two doubly imaged systems, the cyan dots their sources. Right: formal velocity dispersion $\sigma_{\rm lens}$. The vertical dashes mark the radial position of the lensed images. The same curve can be seen as second from top in Fig. 5.2.

fact $M(< R)$ has some model dependence at all R, but is minimal at $R_{\rm Ein}$. $\sigma_{\rm lens}(R \neq R_{\rm Ein})$ has a larger uncertainty than $\sigma_{\rm lens}(R_{\rm Ein})$, but is still fairly well constrained, as one can see in Figure 5.1. The velocity dispersion at the radial position of the outermost image $\sigma_{\rm lens}(R_{\rm lens})$ as a quantity, which is as well constrained as $R_{\rm Ein}$, is basic to the following analysis.

The `PIXELENS` input files, the formal velocity dispersion curves as well as the mass maps can be found in Figures B.1 and B.2 of the appendix. Note that for lensing clusters, the velocity dispersion of the galaxies on their orbit around the centre of the cluster is considered instead of the stellar velocity dispersion as in the case of lensing galaxies. The references for all the lenses and further details can be seen in Table C.1 in the appendix.

5.3 Formal versus kinematic velocity dispersion

The formal velocity dispersion curves $\sigma_{\rm lens}(R)$, such as the one illustrated in Figure 5.1 for the lens Q0957, are computed for all the lenses. Figure 5.2 shows all these curves except for the clusters, which are excluded for the sake of readability and their comparatively high $\sigma_{\rm lens}$ values.

In the following, we concentrate on the formal velocity dispersion at a radius of the outermost image position $\sigma_{\rm lens}(R_{\rm lens})$ and at the effective radius $\sigma_{\rm lens}(R_{\rm e})$. Concerning the latter, we cannot take for granted that the velocity dispersion curve at effective radii is still sufficiently flat. Because of this, when considering $\sigma_{\rm lens}(R_{\rm e})$ we exclude the lenses Q2237, HST15433, J0737, J0912, CFRS03 and J0956, for which this condition is *not* fulfilled.

In terms of absolute values the curves for CASTLES lenses extend in average to larger radii, whereas the curves of SLACS lenses are smaller due to a limited aperture of the SDSS fibres. Note that 7 SLACS lenses and 3 CASTLES lenses show a clear cuspy shape of the formal velocity dispersion curve towards inner radii as it is the case for the majority

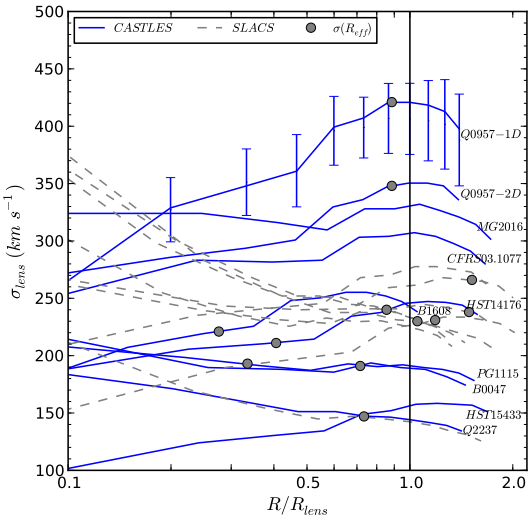

***Figure 5.2*:** Formal velocity dispersion curves. The grey dashed lines denote SLACS lenses, the blue solid lines CASTLES lenses. For readability, the error bars indicating the range of ensemble models, are shown only for one curve. The radial scale is normalized to the radius of the respective outermost image $R_{\rm lens}$, which is indicated by the horizontal solid line. Grey circles denote the effective radius provided it is located in a fairly flat region of the velocity dispersion curve. Q0957 is included twice, the model with one (two) doubly imaged source(s) is labelled -1D (-2D).

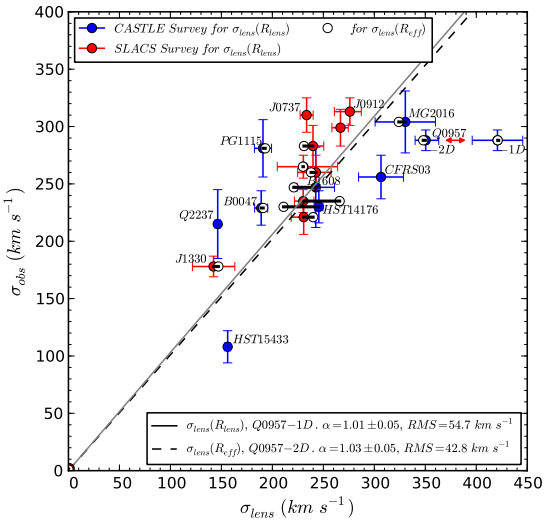

***Figure 5.3*:** $\sigma_{\rm lens}$-$\sigma_{\rm obs}$-plot for all the galaxy lenses. The filled circles refer to the formal velocity dispersions $\sigma_{\rm lens}$ measured at outermost image $R_{\rm lens}$. The open circles show $\sigma_{\rm lens}(R_{\rm e})$. Note that as in Figure 5.2 Q0957 is shown twice for different image systems. The dashed (dotted) line represents the fit for the solid (open) circles including Q0957-1D (Q0957-2D).

of early-type galaxies also in other velocity dispersion field studies (e.g., Coccato et al. 2009). However, in some cases anomalous galaxies exhibit a rising velocity dispersion profile, which might be related to the presence of a disk according to Coccato et al. (2009). Additionally, the pixelated approach causes a variety of differently shaped velocity dispersion profiles differing especially in central regions. This leads consequently to large error bars and a decreased sensitivity in the centre, rendering an interpretation of the profiles at smaller radii rather difficult.

It should be emphasized that the comparison of either $\sigma_{\rm lens}(R_{\rm lens})$ or $\sigma_{\rm lens}(R_{\rm e})$ with $\sigma_{\rm obs}$ measured within an aperture, is a proper procedure, since the $R_{\rm lens}$ is in average less than a factor of 2 different from the aperture radius where σ is measured and for most lenses $\sigma_{\rm lens}$ remains unchanged. For J0737, J1205, J1330 and J2300, the formal velocity dispersion curve ends before reaching the radius of 3 arcsec, that is, the mass does not contribute to the lensing effect, but nevertheless $\sigma_{\rm obs}$ can be taken as an indicator for the real velocity dispersion. In other words the velocity dispersion measurements at aperture radius are probably not representative since the main mass of the lens is smaller.

Comparing the curves labelled Q0957-1D and Q0957-2D in Fig. 5.2 shows the probable effect of adding formerly undiscovered image systems. As for Q0957, $\sigma_{\rm lens}(R)$ varies considerably when a formerly unseen doubly imaged system is added. This also affects

the relation between $\sigma_{\rm lens}(R_{\rm lens})$ or $\sigma_{\rm lens}(R_{\rm e})$ and the kinematic velocity dispersion $\sigma_{\rm obs}$. Both $\sigma_{\rm lens}(R_{\rm lens})$ and $\sigma_{\rm lens}(R_{\rm e})$ plotted against $\sigma_{\rm obs}$ can be seen in Figure 5.3. The comparison between the observed kinematic velocity dispersions and the mass-only related velocity dispersions reveals how virialized the lenses are, because $\sigma_{\rm lens} \approx \sigma_{\rm obs}$ is another representation of the virial theorem in Equation 5.3. We constrain the fit by fixing it to the origin, because a bias would have no physical relevance. For $\sigma_{\rm lens}$-values at the effective radius instead of the radius of the outermost image position $R_{\rm lens}$, the scatter around the best fit decreases considerably. Although all $\sigma_{\rm lens}(R_{\rm e})$ are within the error bars of $\sigma_{\rm lens}(R_{\rm lens})$, changing the radii for the determination of the $\sigma_{\rm lens}$-$\sigma_{\rm obs}$-relation might consequently be the right thing to do, since therby the relation is build on a common basis.

Furthermore, we included the two-double (2D) and the one-double (1D) system of lens Q0957 in Figure 5.3 to demonstrate the difference in $\sigma_{\rm lens}$ of the former outlier, reducing the RMS in the $\sigma_{\rm lens}$-$\sigma_{\rm obs}$-plot from 55 km s^{-1} for the $\sigma_{\rm lens}(R_{\rm lens})|_{1D}$-fit to 43 km s^{-1} for the $\sigma_{\rm lens}(R_{\rm e})|_{2D}$-fit. We conclude that generally a more complete lens system is to be favoured and henceforth we only consider Q0957-2D. The linear best fits fixed to the origin for $\sigma_{\rm lens}(R_{\rm e})$ and $\sigma_{\rm lens}(R_{\rm lens})$ yield

$$\sigma_{\rm obs} = (1.03 \pm 0.05) \times \sigma_{\rm lens}(R_{\rm e}), \tag{5.5}$$

$$\sigma_{\rm obs} = (1.04 \pm 0.04) \times \sigma_{\rm lens}(R_{\rm lens}). \tag{5.6}$$

As an aside, the y error bars plotted in Figure 5.3 are the observational errors taken from Koopmans & Treu (2003), Treu & Koopmans (2004), Tonry & Franx (1999), Tonry (1998), Ohyama et al. (2002), Koopmans et al. (2003), Koopmans & Treu (2002) and Foltz et al. (1992) for the CASTLES lenses and Bolton et al. (2006) for SLACS lenses. The x error bars represent the statistical errors of the formal velocity dispersion for an ensemble of 100 models of possible mass distributions. Thus, the rather small error bars can be understood as a relatively model independent lensing mass and formal velocity dispersion. The errors are taken from a radius closest to $R_{\rm lens}$ since the pixelated approach only allows for discrete steps in radius. One could argue about the significance of these errors, because changes in the image positions or lost information like additional image systems or mass contamination of the light path can lead to fairly different results.

However, the fits for $\sigma_{\rm obs}(\sigma_{\rm lens})$ (Equations 5.5 and 5.6) make clear that a one-to-one correlation between $M_{\rm lens}$ and $M_{\rm vir}$ of the lensing galaxy is probable. It is important to know whether our sample is dominated by a certain kind of model far from $\rho(r) \sim r^{-2}$ corresponding to a constant $\sigma_{\rm lens}$. For that we can study the correlation between the ratios $\sigma_{\rm lens}/\sigma_{\rm obs}$ and $R_{\rm lens}/R_{\rm e}$. In consideration of the virial theorem one can state:

If there is an (anti-)correlation between $\sigma_{\rm lens}/\sigma_{\rm obs}$ and $R_{\rm lens}/R_{\rm e}$ the density profile $\rho(r)$ of the lens should be (flatter) steeper than r^{-2}.

Figure 5.4 shows this relation for both $\sigma_{\rm lens}(R_{\rm lens})$ and $\sigma_{\rm lens}(R_{\rm e})$. As for the first, the best fit shows a positive trend with large error bars. For $\sigma_{\rm lens}(R_{\rm e})$ the positive trend is insignificant and the opposite result is *not* excluded by the error bars. By neglecting the outlier MG2016 with a possibly underestimated $R_{\rm e}$, as will be discussed in Section 5.4, one finds the inverse trend to be likewise significant. Nevertheless it needs to be emphasized that by excluding only one of the labelled outliers in Figure 5.4 the slope is strongly

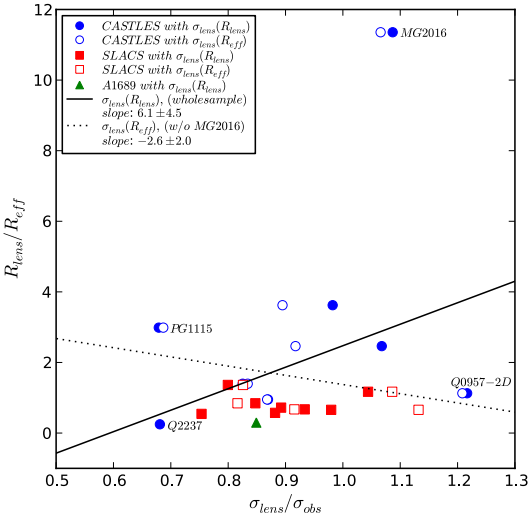

***Figure 5.4*:** Plot of $R_{\rm lens}/R_{\rm e}$ against $\sigma_{\rm lens}/\sigma_{\rm obs}$. The lines indicate extreme scenarios of formal fits for our sample of early-type galaxies which show large errors. For the $\sigma_{\rm lens}(R_{\rm e})$-fit of the whole sample the positive trend is insignificant. The trend inverts when excluding MG2016. In other words there is neither correlation nor anti-correlation, meaning that in average the density profile for all lenses is consistent with an isothermal ellipsoid.

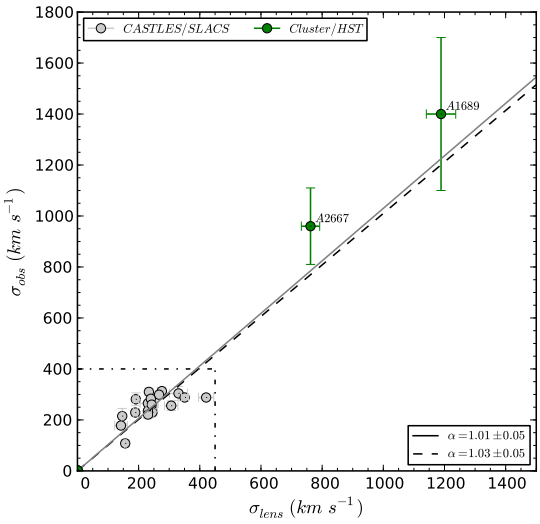

***Figure 5.5*:** Like Figure 5.3 but with the two clusters ACO 1689 and ACO 2667 included. The straight line fits do not include the clusters. The relation between $\sigma_{\rm obs}$ and $\sigma_{\rm lens}$ extends to cluster scales.

affected and can change its algebraic sign. Thus we cannot retrieve a strongly significant statement. In such exclusion scenarios we obtain slopes consistent with constant σ-ratio. Our sample of early-type lensing galaxies for $\sigma_{\rm lens}(R_{\rm lens})$ ($\sigma_{\rm lens}(R_{\rm e})$) is clustering around a mean of 1.3 ± 0.3 (1.6 ± 0.3) in $R_{\rm lens}/R_{\rm e}$ and around 0.91 ± 0.04 (0.96 ± 0.06) in $\sigma_{\rm lens}/\sigma_{\rm obs}$ excluding MG2016 because of its extraordinarily high $R_{\rm lens}/R_{\rm e}$-ratio. Since we cannot find any type of correlation throughout our sample we can summarize that $\sigma_{\rm lens}$ is model independent.

Extending the $\sigma_{\rm obs}$-$\sigma_{\rm lens}$-plot in Figure 5.3 to 100 kpc scale, as to be seen in Figure 5.5, we can find that lensing clusters fit quite well to the previously found correlations for $\sigma_{\rm obs}(\sigma_{\rm lens})$ (Equations 5.5 and 5.6).

As an aside, it must be emphasized that $\sigma_{\rm lens}$ is different from the line-of-sight velocity dispersion if the lens is not isothermal. Going from an assumed isothermal r^{-2} profile to a Hernquist profile changes the velocity dispersion of Equation 5.3 to

$$\begin{aligned}\sigma_{\rm h}^2(R_{\rm lens}) \quad \sim \quad & \frac{GM_{\rm vir}^2}{aM_{\rm lens}} \frac{(1-s^2)^2}{[(2+s^2)X(s)-3]} \Big\{ \frac{1}{2} \frac{1}{(1-s^2)^3} \\ & \times \left[-3s^2 X(s)(8s^6 - 28s^4 + 35s^2 - 20) \right. \\ & \left. -24s^6 + 68s^4 + 65s^2 + 6 \right] - 6\pi s \Big\} \end{aligned} \tag{5.7}$$

with $s = R/a$, where a denotes a scale length and

$$X(s) = \begin{cases} \frac{\operatorname{sech}^{-1} s}{\sqrt{s^2-1}} & \text{for} \quad 0 \leq s \leq 1 \\ \frac{\cos^{-1} s^{-1}}{\sqrt{s^2-1}} & \text{for} \quad 1 \leq s \leq \infty \end{cases}$$

along the lines of Hernquist (1990). This step yields a change of less than 19% of $\sigma_{\rm lens}$ for most lenses, apart from few exceptions like P1115, which turned out to be an outlier already in Figure 5.4.

Furthermore, cluster ACO 2667 shows a velocity dispersion increased by 33%. In general, central regions of galaxy clusters are best fitted by a Hernquist profile (Hernquist 1990) for the stellar component of the inner cD galaxy and a NFW model (Navarro et al. 1996) for the dark matter component, shown by e.g. Padmanabhan et al. (2004). That is why we can expect significant changes going from $\sigma_{\rm lens}$ to $\sigma_{\rm h}$ on larger scales. However, fitting the $\sigma_{\rm lens}$-$\sigma_{\rm obs}$ relation for a Hernquist profile as done before with an isothermal model for $\sigma_{\rm lens}$ reveals a slightly steepened slope compared to Equation 5.6 of (1.13 ± 0.04). The clusters still agree to this relation within the error bars.

The dynamical state of galaxy clusters is hard to determine. There are many contradictory investigations on this topic. Optical and X-ray data on the one hand indicate ongoing formation processes on substructure level (e.g., Stein 1997, Solanes et al. 1999), which should be considered in estimates of $M_{\rm vir}$. On the other hand, statistical comparisons of different mass estimates from optical and X-ray observations and weak lensing show perfect agreement on scales much greater than the core radius $R_{\rm core}$ (e.g., Wu & Fang 1997). Still, on scales of core radii there are discrepancies between X-ray and mass measurements by means of weak lensing. Allen (1998) suggests to consider substructure and line-of-sight alignments of material towards the cluster cores since they will increase the lensing masses without affecting X-ray data and to take account of the dynamical activity, which might cause the X-ray analyses to overestimate $R_{\rm core}$. Xu et al. (2000) take this apparent dichotomy as an indicator of the transition from pre-virialization to virialization. In this study however, we can probe the virialization state for the two clusters at $R_{\rm lens}$, which is in both cases not far away from $R_{\rm core}$. The core radii of the X-ray selected ACO 2667 and ACO 1689 are about (76 ± 8) kpc (Covone et al. 2006) and (80 ± 15) kpc (Allen 1998) respectively. Thus with $\sigma_{\rm lens}$ at $R_{\rm e} = 98$ kpc for ACO 2667 we already probe the core region. For ACO 1689 $R_{\rm e}$ is roughly 238 kpc, which is 3 times the given core radius. By adjusting to smaller scales $\sigma_{\rm lens}(R_{\rm core})$ becomes ~ 1000 km s^{-1} and marginally fails the relations (5.5) and (5.6). It should be emphasized that unlike the sample of lensing galaxies ACO 1689 $R_{\rm core}$ is *not* in a sufficiently flat region of $\sigma_{\rm lens}$ and thus not comparable with the relations for which this was a requirement. Since strong lensing unveils mass regardless of underlying dynamics one can summarize that also in view of findings from previous studies clusters in a wide range of radii can be regarded as virialized.

Nevertheless, the correlation between the kinematic velocity dispersion $\sigma_{\rm obs}$ and $\sigma_{\rm lens}$ is hard to decipher. First the scatter around a best fit that is smaller (larger) than the scatter around the FP in the ($R_{\rm e}$, σ, I) parameter space can be understood as a hint on a basically mass dependent (stellar dynamics dependent) $\sigma_{\rm obs}$. Of course it can also be seen as a merely statistical scatter that is influenced by a possibly biased lens sample. This allows for drawing the following conclusions:

1. The small scatter and the slope of the best fit of ~ 1 makes $\sigma_{\rm lens}$ a good surrogate for $\sigma_{\rm obs}$, which is independent of a particular density profile model.

2. The included elliptical galaxies are thus virialized and

3. the relation can be extended to larger scale objects like clusters, as we can see in Figure 5.5.

With this in hand we now want to analyze the mass-to-light relationship for the given sample and compare it to the governing FP of early-type galaxies.

5.4 Mass-to-light ratio and the fundamental plane

As a first step to a mass-to-light relation for this sample of early-type lensing galaxies we K-correct given I-band magnitudes (centred on 814 nm) and SDSS-i-band magnitudes (centred on 753 nm) in AB units to rest frame I-band since they provide the most complete set of magnitudes for our sample. These are taken from the CASTLE Survey homepage[4] and Bolton et al. (2006). In the case of the galaxy cluster ACO 1689 we obtain the overall magnitude by summing over the fluxes of the galaxy content using the catalogue of Molinari et al. (1996). Hence the K-correction is based on SDSS, HST and ESO spectral templates[5].

We carry out the K-correction from first-principles in preference to a black box program. Following Oke & Sandage (1968) we compute the K-corrected flux according to

$$K_x = 2.5 \log (1+z) + 2.5 \log \left\{ \frac{\int_0^\infty F(\lambda_0) S_x(\lambda)\ d\lambda}{\int_0^\infty F(\lambda_0/(1+z)) S_x(\lambda)\ d\lambda} \right\}, \tag{5.8}$$

where K_x denotes the K-correction for the x-Band expressed in magnitudes. The band width is smaller in the redshifted galaxy, which leads to the first term in (5.8). A source spectrum $F(\lambda)$ is redshifted through fixed spectral-response bands S_x or bandpasses respectively of the detector. The flux at an effective wavelength in the rest frame of a galaxy of redshift z, transformed from the effective wavelength λ_0 of the detector by $\lambda_0/(1+z)$, will differ from the flux of a galaxy at rest. This leads to the second term in 5.8. Figure 5.6 visualizes the denominator of the integrand in Equation 5.8, where the I-bandpass is multiplied by the redshifted flux template of an elliptical galaxy taken from Kinney et al. (1996). As an aside the apparent SDSS magnitudes are on an AB basis within 3%, which only leads to minor corrections and is therefore neglected in the following analysis. Note that the K-correction is realized with the exact template for $\lambda < 570$ nm. For higher wavelengths we assumed a constant flux for the sake of simplicity. The deviations resulting from this approximation are even in the worst case of a hardly redshifted galaxy in the upper λ-range like Q2237 of only 0.3% for L_I. This leads to negligible corrections for all following quantities. Furthermore galactic extinction corrections according to Schlegel et al. (1998) are applied to the fluxes. The luminosities are calculated in units of solar

[4] cfa-www.harvard.edu/glensdata/

[5] The spectral templates for WFPC2, SDSS ACS and ESO telescopes are taken from the STSCI homepage www-int.stsci.edu/instruments/wfpc2/Wfpc2_thru/, www.stsci.edu/hst/acs/analysis/reference_files/synphot_tables.html and filters.ls.eso.org/efs/efs_fi.htm

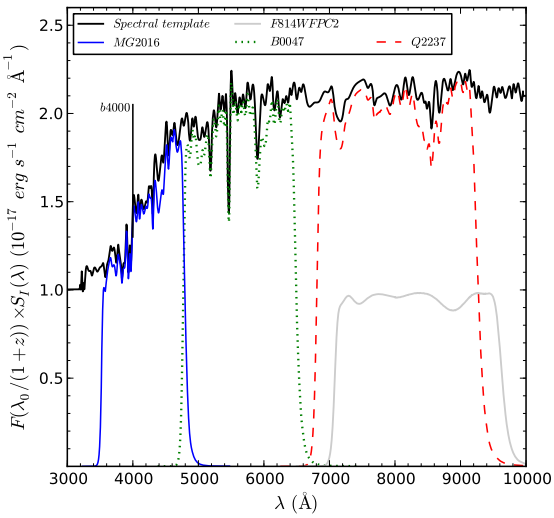

***Figure 5.6*:** Visualization of K-Correction: The black solid curve shows the flux template of an elliptical galaxy. The grey solid line represents the HST WFPC2 I-bandpass taken from www-int.stsci.edu/instruments/wfpc2/Wfpc2_thru/. The dashed curves are showing the denominator of the integrand in Equation 5.8 for 3 lenses: MG2016 ($z = 1.01$, dashed line), Q0047 ($z = 0.485$, dotted line) and Q2237 ($z = 0.04$, dash-dotted line).

luminosities according to an AB magnitude[6] $I_\odot = 4.57$ for WFPC2 data and $i_\odot = 4.48$ for SDSS data calculated along the lines of Fukugita et al. (1995). Subsequently we correct for passive M/L-evolution with a slope of

$$\frac{d \log M/L_I}{dz} = -0.397$$

inferred by stellar population synthesis models taken from Bruzual & Charlot (2003*b*).

Having the I-band luminosities L_I of all lenses in units of solar luminosities $L_\odot$ and the velocity dispersions from Section 5.3, we can analyze the underlying mass-to-light relation. Figure 5.7 shows the lensing mass $M_{\rm lens} = R_{\rm e}\sigma^2_{\rm lens}(R_{\rm lens})$ and the virial mass $M_{\rm vir} = R_{\rm e}\sigma^2_{\rm obs}$ plotted against I-band luminosity. The plot also provides a curve representing a constant M/L or according to Equation 5.1 a ($\alpha = 1$)-line respectively.

A closer look at the V-band luminosities for selected galaxies reveals that HST14176, B1608 and MG2016 emerge as outliers with mass-to-light ratios $\lesssim 1$. This can be explained by nearby groups and clusters (e.g. in the case of HST14176) or mass-contamination influencing the path of light. Another reason can be uncertainties in the effective radii, as already mentioned in Section 5.3. If we take for HST14176 (MG2016) $R_{\rm e} = 1.06$ (0.31) arcsec (Treu & Koopmans 2004) instead of the used 0.71 (0.22) arcsec (Rusin et al. 2003) then $M_{\rm lens} = R_{\rm e}\sigma^2_{\rm lens}$ would increase by a factor of ~ 1.5 (1.4), since no grave changes in σ for a flat formal velocity dispersion curve are expected. This leads for HST14176 to a lensing mass of 5.14×10^{11} $M_\odot$ instead of the former 3.43×10^{11} $M_\odot$ which is then also

[6]Listed on www.ucolick.org/~cnaw/sun.html

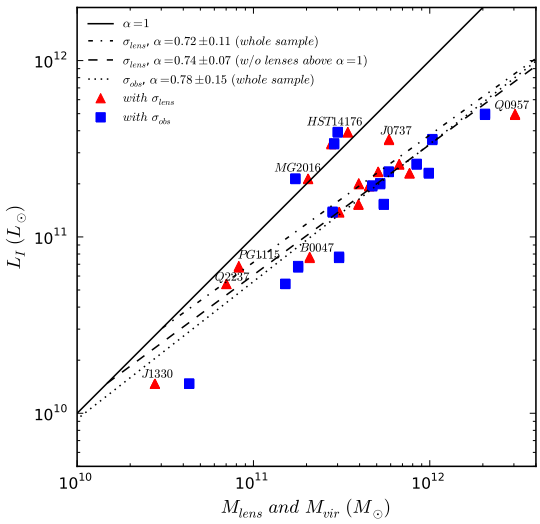

Figure 5.7: Lensing mass and virial mass against I-band luminosity for all galaxies. The triangles denote masses calculated using $\sigma_{\rm lens}$. The squares refer to masses calculated with $\sigma_{\rm obs}$. The best fits for $M^{\alpha} \propto L$ are plotted for $\sigma_{\rm lens}(R_{\rm lens})$ (dashed line) and for $\sigma_{\rm obs}$ (dotted line). The solid line refers to a constant M/L-ratio.

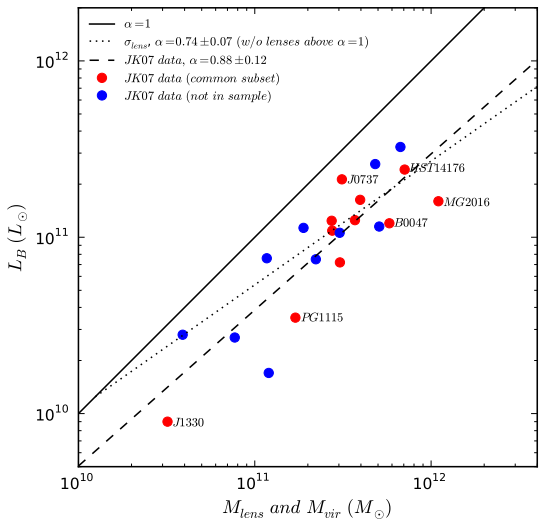

Figure 5.8: Mass-versus-light plot for data from Jiang & Kochanek (2007). The black circles denote a subset of lenses included in our lens sample. The grey circles are residual lenses. The dotted line represents the best fit for the whole dataset taken from Jiang & Kochanek (2007). The dashed line refers to the $\sigma_{\rm lens}$-fit as seen in Figure 5.7.

in the V-band clearly below the $(\alpha = 1)$-line. If such uncertainties are the true cause for comparatively high luminosities, then we also need to adjust $M_{\rm lens}$ and $M_{\rm vir}$ in Figure 5.7. However, changing $R_{\rm e}$ or excluding the problematic lenses from the fit has a negligible impact on the slope α using $M_{\rm lens}$ and only small impact using $M_{\rm vir}$, changing α from (0.80 ± 0.10) to (0.84 ± 0.10). It should be emphasized that we hold on to the dataset of Rusin et al. (2003), because it provides the effective radii computed on a common basis for the whole CASTLES subset of our lensing objects.

Both sets of data points for $\sigma_{\rm obs}$ and for $\sigma_{\rm lens}(R_{\rm lens})$ are fitted for the whole sample and reveal the slopes:

$$\begin{aligned} \alpha &= (0.70 \pm 0.08) \quad \text{for } M_{\rm lens}, \\ \alpha &= (0.80 \pm 0.14) \quad \text{for } M_{\rm vir}. \end{aligned}$$

It shows that $\alpha = 1$ is in any case clearly excluded. Figure 5.7 shows the best fit for both $M_{\rm lens}$ and $M_{\rm vir}$. Note that the fits in the plot cannot be extrapolated to lower masses, which would mean that judging by the intersection with the $(\alpha = 1)$-line the luminous mass would overtake the total mass content. The plot and therewith also the FP of nearby lenses show that more massive galaxies have a larger dark matter fraction.

In Figure 5.8 the lens sample from Jiang & Kochanek (2007) together with a best fit is shown. Their data from stellar-dynamical measurements on 22 early-type models contains a common subset with the present study. Note that the data in their paper was given in B-band luminosities, which explains the shift of the data points towards lower luminosities in most cases. The fit for their whole sample yields a slope of $\alpha = 0.88 \pm 0.12$. As in

Figure 5.7, a curve indicating a constant mass-to-light relation is included.

From these plots we can summarize, that

1. the slope of the best fit for $\sigma_{\rm obs}$ is consistent with the one for the lensing sample of Jiang & Kochanek (2007) within error bars,
2. the slope of the fit for $\sigma_{\rm lens}$ is not consistent with the fit to the data from Jiang & Kochanek (2007), although the error bars do overlap,
3. only the fit for the Jiang & Kochanek (2007) sample is consistent with $\alpha = 1$,
4. the slopes of the $\sigma_{\rm lens}$- and $\sigma_{\rm obs}$-fits (for the whole dataset and for a reduced or, due to uncertainties in $R_{\rm e}$, changed dataset) are clearly excluding $\alpha = 1$ within their error bars and thus do not agree with a constant M/L ratio.

In Figure 5.9 we extend determined mass-to-light relations to larger scales. For cluster size objects like ACO 1689, $R_{\rm e}$ is of course not defined. Nevertheless, one can still use the mass quantity $R\sigma^2$ to compare the mass-to-light behaviour of early-type galaxies and clusters. The kinematic line-of-sight velocity dispersion $\sigma_{\rm obs} = 1400$ km s^{-1} of galaxies within the cluster was taken from Łokas et al. (2006) for a subset of 130 galaxies in the inner region of the cluster with velocities $|v| < 3000$ km s^{-1}, which contains most likely the biggest mass fraction responsible for the lensed images. This average value applies for a radius of around 400 kpc, a region where the formal velocity dispersion seems to be sufficiently flat and in which roughly half of the projected radii of the 130 galaxies considered in Łokas et al. (2006) are to be found. Furthermore, the value is not too far away from the outermost image position of ~ 240 kpc. Therewith, $R_{\rm e}\sigma^2_{\rm obs}(R_{\rm e})$ and $R_{\rm e}\sigma^2_{\rm obs}(R_{\rm lens})$ are determined.

The data points for the cluster deduced from the formal velocity dispersion $\sigma_{\rm lens}$ at $R_{\rm lens}$ and $R_{\rm e}$ are included in Figure 5.9. As expected, neither the relation $M^\alpha \propto L$ with $\alpha \approx 0.70$ nor with any other slope presented above does extend to clusters. As shown by Schaeffer et al. (1993), galaxy clusters follow indeed a different FP relation. We can make up a region in the mass-to-light plot for cluster sized objects, which lies far below all previous lines and matches the findings of Schaeffer et al. (1993) for a FP consisting of 16 clusters. One should keep in mind that for early-type galaxies M/L can be a suitable dark matter versus baryon estimator because L tracks pretty much all baryons. But this is not a good approximation for clusters, whose total baryonic mass is generally believed to be made of 80% hot diffuse gas and only 20% galaxies (Fukugita et al. 1998). In order to correct for this discrepancy, one might add the missing 80% expressed in terms of luminosity. Hence the luminosity of ACO 1689 is shifted to $1.4 \times 10^{13} L_\odot$. Despite of this correction we obtain a value significantly below the given fits. Thus clusters can nonetheless be regarded as highly dark matter dominated.

We can summarize that our results are in good agreement with most of the recent FP-type studies, as one can see in Figure 5.10. In the two plots the FP parameter study results of the references listed in Table 2.1 (Section 2.6.1) are presented (left panel) together with the results of this study (right panel), summarized in Table 5.1. Recovering the FP of early-type galaxies by means of the photometric-independent $\sigma_{\rm lens}$ shows that

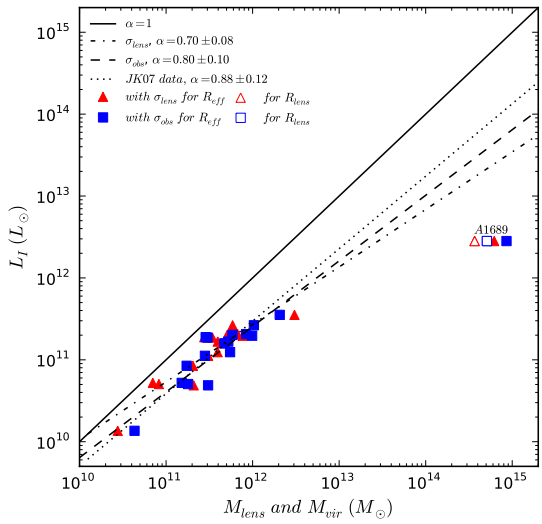

***Figure 5.9*:** Like Figure 5.7 but extended by cluster ACO 1689. As expected, clusters are not on the FP, because they have a higher mass-to-light ratio. Solid symbols denote masses calculated with $\sigma(R_\mathrm{e})$, open symbols denote masses calculated with $\sigma(R_\mathrm{lens})$.

non-homologies like structural and orbital anisotropies, which might change the photometrically determined central velocity dispersion, have small to negligible impact on the FP tilt, as also shown by Cappellari et al. (2006).

The FP parameters of our analysis are determined in consideration of the relations $a = 2\alpha(2-\alpha)^{-1}$ and $b = -(2-\alpha)^{-1}$:

$$a = 1.08, \quad b = -0.77 \quad \text{for } \sigma_\mathrm{lens},$$
$$a = 1.33, \quad b = -0.83 \quad \text{for } \sigma_\mathrm{obs},$$

corresponding to $\alpha = 0.70 \pm 0.08$ and $\alpha = 0.80 \pm 0.10$ respectively. Upper and lower limit of the σ_lens-fit are also drawn into the plot and exclude plainly the $M \propto L$ case used for Eq. 2.31.

Moreover, the FP parameters found in this study are conspicuously surrounded by the ones found in other studies (see Table 2.1). For example in recent SDSS results for nearly 9000 early-type galaxies in a redshift range of $0.01 < z < 0.3$ the parameters are determined to $a = 1.49 \pm 0.05$ and $b = -0.75 \pm 0.01$ (Bernardi et al. 2003), and

	a	b
for σ_lens	1.08	−0.77
(upper limit)	1.28	−0.82
(lower limit)	0.90	−0.72
for σ_obs	1.33	−0.83
(upper limit)	1.64	−0.91
(lower limit)	1.08	−0.77

***Table 5.1*:** Fundamental plane parameters found in this analysis. Compare with previously found FP parameters illustrated in Fig. 5.10 and listed in Table 2.1, Section 2.6.1.

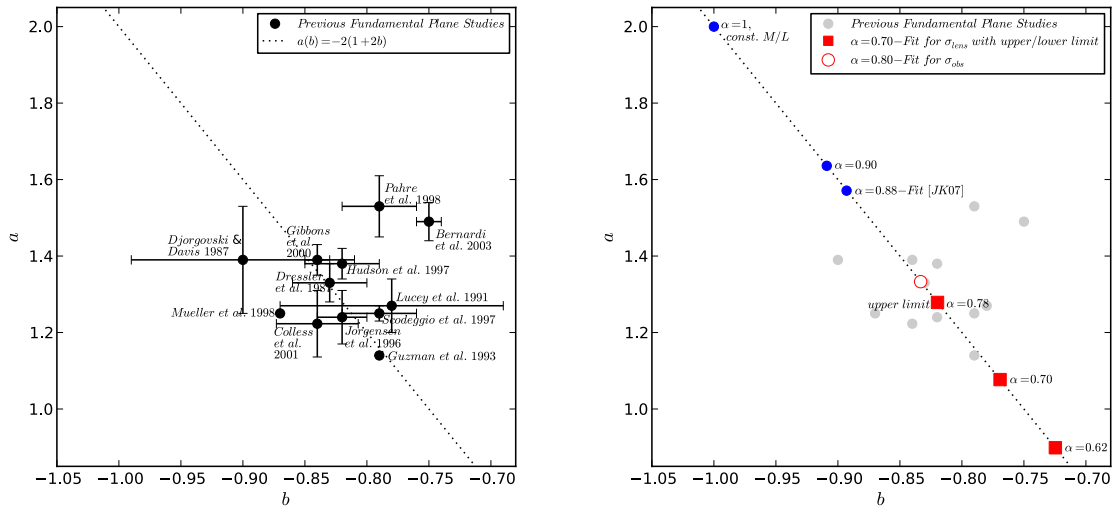

Figure 5.10: Left panel: the a-b-parameter-space according to Equation 2.32. The dashed line represents the mass-to-light power index α for related a and b according to Equation 5.2. The plot shows FP parameter from previous studies referenced in Table 2.1. The error bars are included as far as provided in the references. Right panel: like left plot but with results from this study. The squares mark upper, lower and mean value of the fit using $\sigma_{\rm lens}$ for the whole sample of early-type galaxies. The open circle denotes the fit using $\sigma_{\rm obs}$. The black filled circles denote other α-values, like e.g. the simplistic plane, Eq. 2.31, or the fit for data from Jiang & Kochanek (2007). For the sake of readability and comparison the grey filled circles corresponding to the data shown in the left panel are included.

as an aside have no common α, since Equation 5.2 does not hold. On the other hand, Dressler et al. (1987) in one of the first FP studies present parameters, which are almost perfectly in agreement with the fixed a to b relation and a common α of ~ 0.80, although measured separately. We verify the value by the mass-to-light relation found for $M_{\rm vir}$. It can be seen that (a, b) for the slope of the $\sigma_{\rm lens}$-fit is close to the results of Guzman et al. (1993), Colless et al. (2001), Jørgensen et al. (1996), Scodeggio et al. (1997), Lucey et al. (1991) and Dressler et al. (1987) in ascending order of distance in (a, b)-space. Except for Hudson et al. (1997), Pahre et al. (1998), Gibbons et al. (2000) and Bernardi et al. (2003) the errors of previous (a, b)-studies, as far as they were given, overlap with the error bars in this study. In particular the results of Jørgensen et al. (1996) and Colless et al. (2001) agree with the upper limit of α-values from the $\sigma_{\rm lens}$-fit. However, the α estimate from the dataset of Jiang & Kochanek (2007), which matches the result from Rusin et al. (2003) can be excluded. Since for all previous FP type studies kinematic velocity dispersion measurements are used, our findings suggest that the real underlying (a, b) values are even closer to the lower right corner of Figure 5.10.

5.5 Conclusion

We can summarize our findings presented in this chapter as follows:

1. Independent of the details of lens models, the lensing masses and virial masses basically agree, since $\sigma_{\rm lens} \approx \sigma_{\rm obs}$, as demonstrated in Section 5.3. This verifies the virial theorem.

2. The relation between the lensing inferred velocity dispersion $\sigma_{\rm lens}$ and the observed kinematic velocity dispersion $\sigma_{\rm obs}$ extends to cluster sized lensing objects within rather large uncertainties originating from a poorly defined scale radius $R_{\rm e}$ as shown for the two galaxy clusters ACO 1689 and ACO 2667.

3. Using the results for $\sigma_{\rm lens}$ ($\sigma_{\rm obs}$) in Section 5.4 the lensing mass (virial mass) is calculated according to $M \approx R_{\rm e}\sigma^2$. We find the mass-to-light relation $M_{\rm lens}^{0.70\pm0.08} \propto L$ for the whole sample and $M_{\rm vir}^{0.80\pm0.10} \propto L$ to be consistent with most other FP type studies. We point out that the FP defined by using $\sigma_{\rm lens}(R_{\rm lens})$ is based on lensing velocity dispersions within $R_{\rm lens}$, which is not correlated to the effective radius. In order to render the used quantities unequivocal, we analyze the change in $\sigma_{\rm lens}$-$\sigma_{\rm obs}$ switching from $R_{\rm lens}$ to $R_{\rm e}$ and find only a marginally different slope, though a reduced scatter in the $\sigma_{\rm lens}$-$\sigma_{\rm obs}$-plot can be seen. A few lenses are problematic outliers due to observational uncertainties, but excluding these does not effectively change the result. With $R \propto \sigma_{\rm lens}^{1.08} I^{-0.77}$ the FP of early-type galaxies is recovered, excluding clearly the simple plane $R \propto \sigma_{\rm lens}^2 I^{-1}$. Thus also non-homology as a reason for the FP tilt can be excluded.

4. As shown for ACO 1689, clusters are far from the FP since they have a much higher dark matter fraction than early-type galaxies.

The FP tilt discovered by Dressler et al. (1987) and recovered in this study using $\sigma_{\rm lens}$ as a surrogate is an often discussed matter (see Table 2.1) in astrophysics. Until a consensus on the explanation for the FP is found it is necessary to focus on quantities which are unequivocally related to a certain physical entity. For this purpose, we propose $\sigma_{\rm lens}$, since it fulfils the necessary condition of preserving the level of virialization for both elliptical galaxies and clusters.

The reasons for the deviation from the simple plane Eq. 2.31 are hard to resolve, because neither the mass-structure, the mass-to-light ratio nor the dark matter fraction are directly and independently observable. Certainly, dark matter is to the present day not directly traceable, but with the study presented in the next Chapter, we can resolve and visualize its spatial distribution, which is important for FP studies and other problems in galaxy formation.

6

Resolving Stellar Baryon and Dark Matter Profiles

Unlike in the previous chapter, we investigate here the radial dependence of stellar and total lens mass profiles by means of baryon fraction curves. They are defined as the ratio of enclosed stellar to total lens mass and derived using the stellar population synthesis technique and the pixel-based mass reconstruction method introduced in Chapter 3. Subject to this analysis are 21 lensing galaxies of the CfA-Arizona Space Telescope LEns Survey (CASTLES) presented in Section 4.2 (see Fig. 4.1).

In Section 6.1, we give an overview of recent studies in the field of research and point out which problems will be addressed by this analysis. The lens sample is analyzed with respect to its photometric properties and the subsequent modeling in Section 6.2. A general introduction to the analysis technique is given in Chapter 3. Additional information on the treatment of early-type galaxies, dust reddening and the choice of the initial mass function is given in Section 6.3.

Investigating the on-sky projection of stellar and dark matter surface mass maps as well as baryon fraction maps gives yet unprecedented insights in the distribution of matter in the lens galaxies (Section 6.4). Averaging these maps along mostly elliptical isophotes yields enclosed stellar mass, $M_s(< R)$ and total lens mass profiles, $M_L(< R)$ (Section 6.5). By examining the M_s and M_L dependence on the radial distance to the centre of each galaxy we find that there are pairs of lenses on small to intermediate mass scales, which approach at large radii the same values for their enclosed total mass, but exhibit very different stellar masses and stellar mass (baryon) fractions, a behaviour subsiding for the most massive lensing galaxies. We can point to a radial region common to all lenses in which the dark matter halo overtakes the stellar content.

Furthermore, we shed light on the fundamental plane puzzle, which was addressed in Chapter 5 and previous fundamental plane studies in terms of global light and mass quantities. Going from small to large radii, we show how the slope of the $M_L(< R)$-to-$M_s(< R)$ relation evolves. On basis of our findings in Chapter 5, the total-to-stellar mass relation can be considered an equivalent representation of the mass-to-light relation and a projection of the fundamental plane.

In Section 6.6 we continue with a closer examination of the stellar and total mass concentrations and define a simple model to study the energetic evolution of early-type galaxies. Novel concentration indices $c = R90/R50$ (i.e., the ratio of radii enclosing 90%

and 50% of the stellar or total mass) for stellar and total mass profiles are introduced and compared to previous concentration definitions. Moreover we investigate how the dark matter halos are influenced by the distribution of stars on resolved scales below 10 kpc.

The study of resolved baryon fraction profiles will make it possible to evaluate the validity of star formation models as well as adiabatic contraction prescriptions commonly used in simulations. The latter will be carried out in Chapter 7. Section 6.7 summarizes our findings. This analysis will be discussed in the context of other results in Chapter 8.

6.1 Introduction

Observational estimates of the stellar baryon fraction are key ingredients to the understanding of the physics driving the collapse of gas and dark matter to form galaxies (see Section 2.7). They provide important constraints on simulations, especially at length scales (sub-grid) below which grid based simulation rely on semi-analytic prescriptions of baryon physics. They also help to understand the nature of the scaling relations, such as the fundamental plane and its projections introduced in Section 2.7.

Currently, most of the studies that resolve the central regions of galaxies on scales below 10 kpc are based on dynamical models applied to the kinematics of stars (see e.g. Cappellari et al. 2006, Coccato et al. 2009). Similarly, lensing studies on galaxy scales are usually based on a parametric decomposition of the stellar and dark matter component (see e.g. Auger et al. 2010, Trott et al. 2010), with its inherent degeneracies, described in Section 3.1. Over larger scales, Guo et al. (2010) and Moster et al. (2010) match the stellar mass function of SDSS galaxies with the distribution of dark matter halos from numerical simulations to find stellar baryon fractions $f_b \sim 3-4\%$ — significantly lower than the cosmological fraction $f_b = \Omega_b/\Omega_m = 0.17$ (Dunkley et al. 2009) — with a maximum for galaxies with halo masses around $10^{12}\mathrm{M}_\odot$. However, this approach is only valid for masses enclosed within the virial radius and cannot resolve the radial dependence, which offers valuable information about how baryons build galaxies. For instance, the velocity dispersion analysis of Lintott et al. (2006) on a sample of SDSS early-type galaxies yields a baryon fraction ($f_b \sim 8\%$) within the effective radius, which is lower than the cosmological value, but twice as large as determined within the virial radius, illustrating the importance of a resolved estimate of the baryon fraction within galaxy halos. Galaxy formation models combining the evolution of the dark matter and gaseous components along with a set of sub-grid prescriptions for star formation and feedback (see e.g. Kauffmann et al. 1993, Cole et al. 1994, Croton et al. 2006) are only indirect methods with considerable uncertainties. Indeed, robust observational estimates of the baryon fraction on galaxy scales are needed to properly constrain the recipes included in these models.

Gravitational lensing opens a door to smaller scales on which baryonic processes are important. For instance, one can explore concentrations and baryon fractions to study the impact of adiabatic contraction on the mass profiles, as it is done in Chapter 7. Jiang & Kochanek (2007) analyze the relation between stellar baryon fraction and concentration in adiabatic and non-adiabatic models and find evidence of adiabatic contraction. Mandelbaum et al. (2006) present a galaxy-galaxy weak lensing analysis of a large sample of early and late-type galaxies. They obtain stellar surface masses depending on radius with

a resolution down to 10 kpc. However, their approach is also based on a halo model to describe the relation of galaxies and dark matter. To avoid the problems arising from external perturbers (see e.g. Schechter et al. (1997), in case of one component models) and degenerate multi-component modeling (non-uniqueness), as explained in Section 3.1, free-form methods are used to reconstruct the surface mass density of the lens galaxies. For the stellar component, which represents the vast majority of the baryons in the inner regions of early-type galaxies, photometric data in V, I (HST-WFPC2) and H-band (HST-NICMOS) is used to constrain a large volume of stellar population synthesis (SPS) models by means of the procedure explained in Chapter 3.

Choosing a sample of moderate redshift lenses enables us to determine the lensing profile out to a few R_e. The CASTLES sample (Section 4.2) fulfils this requirement. In the following section we focus once more on the sample properties, but now with respect to its general environmental features and the handling of the photometry. By means of three lens systems, arguably rather extreme, we illustrate the subtleties of photometric modeling and the authenticity of lenses (Section 6.2.3). The latter point refers to unlensed double quasars which mimic a lens system with a doubly imaged quasar. We will show how a real lens can be distinguished from a spurious system in our analysis. We test the reliability of our photometry-based results by comparing inferred stellar surface mass densities with equivalent results from Ferreras et al. (2009) and Shen et al. (2003).

6.2 Sample properties

In this section we compare lens samples with respect to their environment. The selection criteria for our lens sample are as follows. For the lens mass reconstruction we must have the redshifts of the source and the lens as well as accurate image positions. The stellar population synthesis analysis demands a sufficient separation between lens and quasar images in order to extract uncontaminated photometric estimates from the lens. Furthermore, NIR imaging must be available, since for the redshift of most of the lenses, the H-band maps a rest-frame region that does not change significantly for the colours found in these galaxies. Constraining the SPS models using photometry in several bands is desirable, although we note that our reference H-band is the F160W filter of HST/NICMOS.

We discuss in this section the available multiband data and respective PSFs used for the modeling of the surface brightness distribution. Finally, we discuss outliers and special cases for comparison. All information regarding lens galaxy properties, their environment and photometric modeling is given in Table C.2 and Table C.3.

6.2.1 Lens environment

To describe a lens with respect to its environment, one has to keep in mind that the lens shear required by (parametric and non-parametric) lens models can be due to physically interacting galaxies or to line-of-sight objects. Regarding the former, one could estimate how the environment of the lens galaxy evolved in its recent past, whereas any line-of-sight objects are naturally unrelated to the local region of the lens. Nevertheless, these two sources for external shear are hard to distinguish. If located in a group or cluster environment, X-ray measurements are expected to give reliable constraints on the DM content (Buote & Tsai 1995) and thus a hint about the direction and strength of the

shear. Only a few lens environments have been studied so far for CASTLES lenses (e.g. Fassnacht et al. 2006, Momcheva et al. 2006).

The environment for a sample of 70 SLACS lenses has been studied by Treu et al. (2009); they find $17 \pm 5\%$ are in overdense regions. For our sample of 21 CASTLES lenses we find that seven galaxies are located in groups and three in clusters. Four galaxies have one close galaxy or possible companion with which they may interact gravitationally. For the remaining seven, no large shear contribution is required and no close-by galaxies have been found. Thus we find that $\sim 50\%$ of our galaxies lie in overdense regions. The lower fraction found by Treu et al. (2009) is likely due to the smaller redshift range of SLACS (up to $z \approx 0.5$) and the property of the SDSS selection function to pick lenses whose Einstein radius is about the fibre-radius of the SDSS spectrograph (3 arcsec).

6.2.2 Photometric modeling

The photometry of the 21 lensing systems of our sample are subject to the PSF reduction, masking and modeling procedures described in Section 3.2.2. Subsequently, their photometric models are used to constrain a large number of SPS models, which sets constraints on the colour-to-mass relation (Section 3.2.3). For nine lensing systems all three bands were used for stellar population synthesis. Another eight lenses could be analysed in H and I-band. The remaining four lenses had suitable data in H-band only. See Table C.3 for details regarding the photometric modeling.

First, we describe the nine lenses with suitable data in all three spectral bands.
The lens system B0712 is one of the few lenses for which a *TinyTim* PSF was sufficient to remove quasar images in H-band. In V and I-band the quasar images could all be masked out. The lenses B1422, B2045, Q0047, Q2237 undergo the following treatment. In both I and V bands, *TinyTim* provided a suitable PSF. In the H-band, an isolated star taken from the same or a contemporaneous NICMOS image was used for convolution and point-source fitting if needed. For spiral galaxies the contribution of dust to the photometry is usually more significant than for early-type galaxies. However, we note that in the case of Q2237, the redshift of the lens is very low, which implies that our reference photometric band (H) maps a similar wavelength range in the *rest frame*, where dust attenuation is less severe. From the estimates of Eigenbrod et al. (2008) on VLT/FORS1 spectra of Q2237, we infer a contribution from dust in the H-band photometry of Q2237 at the level of 0.05 mag (Ferreras et al. 2010). For lenses BRI0952, Q0142 and PG1115, extensive use of the iteration method described in Section 3.2.2 was made if the quasar images could not be masked out. The lens HS0818 requires special treatment as we use an isolated quasar image of B1030 to fit the quasar image in the H-band. In the I and V-band, the quasar images are used for fitting. Iteration as it is used for enhancing PSFs of other lenses does not provide better model fits for the lens due to the large separation between images and lens. The image separation is $2.56''$. Hence the reduction process is further simplified by masking.

Next, we describe the eight lenses with suitable data in two spectral bands.
For B1608, MG2016, HE1104 and HE2149, H and I-band data could be used to isolate the lens galaxy. For all their H-band images, a sufficiently isolated star with fitted background extracted from the image of MG0414 was used to remove the quasar images with an ac-

ceptable goodness of fit. Since B1608 exhibits a prominent dust lane, we analyzed the impact of dust reddening on our results, as shown in Section 6.3.1 for B1608 and B1600. The uncertainty on $\log(M_s)$ due to dust is in both cases not larger than 0.3 dex. The lens galaxy of HE1104 is unaffected by quasar light allowing for a good fit. SBS1520 is treated like the previous lenses but with a star from the same image file in preference to other PSFs. For MG0414, RXJ0911 and Q0957 we obtain good residual maps by means of the iteration method. In the lens MG0414 Schechter & Moore (1993) find an object close to image B visible only in I-band, which might contribute to the lensing effect. Our reconstructed mass map also shows an increased surface density at the position of the object.

Finally, we describe all the lenses with suitable data in only one spectral band. B1030, B1152 and B1600 are treated similarly with regard to the fitting routine, i.e. the isolated outermost quasar image was used for subtraction and convolution. B1600 appears to be almost edge-on and exhibits a prominent dust lane. As remarked above, dust reddening changes the population synthesis input and leads to underestimated stellar content, but even for the extreme cases in our sample the effect of dust on inferred stellar masses cannot be larger than 0.3 dex (see Section 6.3.1). For the lens system LBQS1009 the star in the H-band image of MG0414 is used again as a PSF with sufficient quality for the fit.

6.2.3 Outliers and special cases

We now briefly describe three special cases, namely B0218, B1933 and RXJ0921. With the first two we want to demonstrate the impact properties like small image separations and interfering luminous structures can have on the goodness of the SPS. The third lens shows how spurious lenses, i.e. galaxies with nearby quasars which are not lensed images of the same background object, behave in this analysis. All three lenses are excluded from our analysis.

For B0218 as for ten other systems in our sample, a star was used to fit the quasar images in the H-band. Since B0218 is the system with the smallest image separation ($0.33''$) known, it is extremely difficult to separate the lens galaxy from the images of the background quasar. The system is an extreme case in several aspects and a good example for showing the impact of degeneracies between the magnitudes of overlapping objects. B0218, unlike any other lens in the sample, did not yield reasonable Sérsic profile parameters as the wings of the quasar PSFs overlap with the lens. For an unconstrained fit, the combined light from the quasar images and lens galaxy results most likely in an overestimated magnitude of the PSFs. However, after attempting to fit the lens system only by PSFs, a Sérsic profile is needed to achieve an acceptable residual map. Even though one cannot obtain zero residuals by fitting only two point sources, there are several combinations of Sérsic profile magnitudes and two PSF magnitudes that result in the same total surface brightness profile. Bearing this in mind, we use the fitting parameters with the best χ^2, which also yields an acceptable residual map, to carry out the SPS. It should be mentioned that, according to Lehár et al. (2000), B0218 is a late-type galaxy which causes the SPS to predict a different mass content.

For B1933, a star in the same H-band image was used for convolution. The resolved features of the lensed background object cannot be fitted by a PSF, but are taken out of

the fitting routine by using circular masks with a 5 pixel radius, a size chosen to cover features distinguishable from background and still show enough of the lens galaxy to allow for a reasonable fit. The trade-off between light contamination due to minimal masking and information loss due to aggressive masking is in any case problematic. In the case of B1933, almost the whole inner region is surrounded by masked regions, causing the fit parameters R_e and n to diverge. Setting a constraint on the Sérsic index ($n \leq 4$) is necessary. Despite all attempts at modeling this lens, it remained a persistent outlier, and hence is removed from the analysis.

From model fits of the host galaxy, Peng et al. (2006) conclude that RXJ0921 is a binary quasar rather than a gravitational lens. Also Popović et al. (2010) find quite different spectral properties in the spectra of the two components. For now we assume the system is a lens. Since even the smaller lens-image distance is above $3''$ and the quasar images are isolated, we obtain a high-quality fit by taking the quasar image as a PSF for both overall convolution and quasar subtraction. No constraints are necessary. In contrast to all other lenses, RXJ0921 (when treated as a lens) turns out to exhibit an unusually low stellar-mass fraction and an almost constant $M_L(< R)$ profile. The peculiar properties of RXJ0921 can be taken as further evidence against the lens hypothesis as suspected in aforementioned studies.

6.3 Analysis technique

Combining stellar mass estimates and pixel-based mass reconstruction (Section 6.3.2) yields baryon-fraction profiles for the given set of lens galaxies. In Chapter 3 we introduced the general concepts of lens mass reconstruction and population synthesis. In the following, we highlight subtleties by means of individual lenses and show how the lensing galaxies behave compared to a typical field sample of early-type galaxies.

6.3.1 Estimating stellar mass

As explained in Section 3.2.3, a pixel-based comparison of the best fits to the surface brightness of the lenses with stellar mass-to-light ratios (Υ) determined by population synthesis models is used to estimate the stellar mass. For our sample, we extract the stellar mass densities from the H-band image (NICMOS F160W). Whenever model fits of the lens were available for I or V, the colours were used on a pixel-by-pixel basis to constrain the H-band mass-to-light ratio Υ_H. Otherwise, we used integrated colours within an elliptical aperture defined by the effective radius (also half-light radius) R_e of the H-band image (see Table C.2). Note that the effective radius is computed with the Petrosian technique introduced in Section 3.2.4. The choice of the initial mass function, the presence of dust and the degeneracy between age and metallicity of the lens galaxies are prevalent issues for population synthesis, which shall be discussed in the following.

Stellar masses are less sensitive to the age-metallicity degeneracy when estimated via Υ_H (see e.g. Ferreras et al. 2008) as explained in Section 3.2.3. For comparison, we provide the total stellar mass-to-light ratio in the rest-frame V-band, M_s/L_V, in Table C.2. Colours and magnitudes are in agreement with comparable quantities in Rusin, Kochanek & Keeton (2003). The F160W band corresponds to a rest-frame wavelength between 0.8 and $1.2\mu m$ (except for Q2237, which roughly samples rest-frame H-band). Hence, for the

sample considered here, the mass-to-light ratios are not affected by the presence of young stars, an issue that becomes important when dealing with optical or near-ultraviolet indicators (see e.g. Rogers et al. 2010). From the modeling of the old stellar populations that these systems feature (except for the lenses Q2237), an uncertainty of $\Delta\Upsilon \lesssim 0.15$ dex is expected (Gallazzi & Bell 2009).

However, dust reddening can lead to underestimated stellar mass. For starburst galaxies, of which we have none in our lensing sample, large deviations can be expected. In our sample the number of lenses which exhibit dusty features (e.g. B1600) is small. In the analysis presented in the appendix of Leier et al. (2011) we show what happens when dust is included in the analysis of two lenses where the contribution of dust could be important: B1600 and B1608. In particular I. Ferreras showed in this work, that one can safely assume that the effect of dust on M_s does not exceed 20%. For simple stellar populations a comparison of the best luminosity-weighted age, stellar mass, and χ^2 as a function of the reddening parameter $E(B-V)$ shows that dust "conspires" with age such that an increase in dust is compensated by a younger age to give the same colours. This yields only a small variation of the estimated stellar mass with respect to dust reddening. Most importantly, it was shown that the value of χ^2 worsens for high amounts of reddening. The other lens from our sample that could be affected by dust, Q2237 (i.e. the bulge of a late-type galaxy) is at a very low redshift ($z = 0.039$), so that stellar masses are determined from *rest-frame* H-band, which is, as already discussed, even less sensitive to dust (Ferreras et al. 2010).

The most significant systematic error relates to the choice of the Initial Mass Function, especially the low-mass end, which does not contribute to the light, but can contribute very significantly to the total mass content. However, frequently used choices of the IMF such as Miller & Scalo (1979), Scalo (1986), Kroupa et al. (1993) or Chabrier (2003) have similar distributions at the low mass end. It is only the traditional single-power law of the Salpeter (1955*b*) IMF that gives different stellar mass predictions. Previous detailed work on the kinematics of nearby early-type galaxies (Cappellari et al. 2006) or strong lenses (Ferreras et al. 2008, 2010) shows that the low-mass end of the Salpeter IMF is ruled out as it predicts stellar mass surface densities higher than the dynamical or lensing estimates. However, even using a Salpeter IMF does not strongly affect our results, as they mainly focus on the scaling of the regions where dark matter dominates. Ferreras et al. (2010) illustrate differences between five different population synthesis models based on different prescriptions and/or stellar libraries. The predicted stellar masses – measured in the H-band – agree to within 10% (at fixed IMF), especially given the ages of these lenses.

To compare our lensing (early-type) galaxies with a typical field sample, we show in Fig. 6.1 the equivalent to the Kormendy relation (this time defined with respect to the surface stellar mass density at $1R_{\rm e}$). We show as blue dots the sample of ACS/GOODS early-type galaxies from (Ferreras et al. 2009), and our lensing galaxies as red filled circles with error bars. One can see that fourteen out of eighteen lensing galaxies are located inside a 1σ-band around the best fit of the GOODS sample. We also provide the SDSS relation from Shen et al. (2003) as a local ($z \sim 0.1$) reference. The obvious preference of the lens sample to be at larger effective radius and smaller surface mass density is due to a selection bias, which is a combination of the lensing bias and additional requirements,

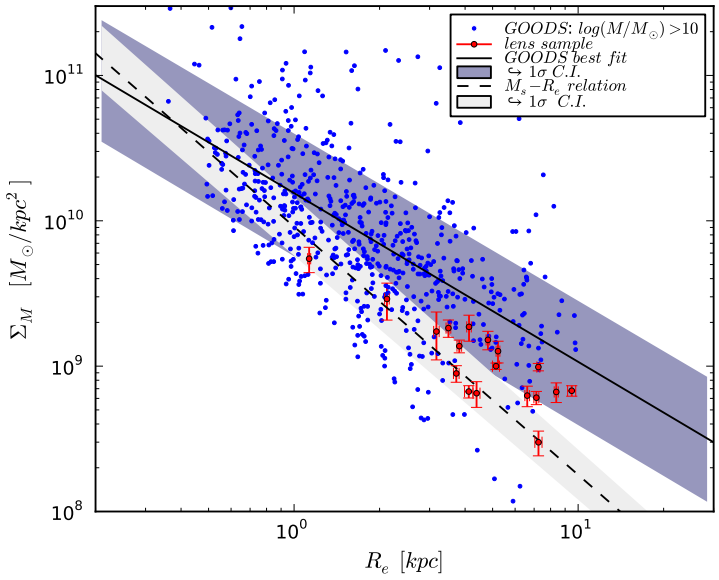

***Figure 6.1*:** Stellar surface mass density at a radius of $1R_{\rm e}$ versus effective radius. Early-type galaxies with stellar mass above $10^{10}M_{\odot}$ (blue dots) selected from the Hubble Space Telescope/Advanced Camera for Surveys images of the Great Observatories Origins Deep Survey (GOODS) are shown together with our lens sample (red filled circles). The dashed line denotes the stellar mass to size relation from SDSS which accounts for early-type galaxies at $z \sim 0.1$ (Shen et al. 2003).

such as a sufficient distinguishability from surrounding quasar images. Furthermore, as we show later in this chapter, the slope of the fundamental plane relation $M^{\eta} \sim L$ can be recovered from our data. Thus we consider the lens sample representative for early-type galaxies in general.

6.3.2 Reconstructing the total-mass profiles

For each lens, the projected total-mass distribution is reconstructed on a circular field made up of 750 square tiles or pixels, each pixel consisting of a uniform non-negative mass distribution with a mass density of a few times the critical density. We provide mass reconstruction maps of the sample in Fig. B.3 of the appendix. In Section 6.5, we will consider the circularly-averaged enclosed mass profile $M(< R)$, see e.g. Figures 6.4 and 6.5. The outermost radius to which the mass profiles are reconstructed is fixed to two times the lensing radius $R_{\rm lens}$, which is defined as the radial position of the outermost lensed image with respect to the centre of the lens. We choose $2R_{\rm lens}$ as a trade-off between uncertainty and common radial range for the sample. The uncertainties attached to $M(< R)$ are derived from the range of enclosed-mass profiles in the ensemble. The uncertainty region has a characteristic butterfly shape, as it is visible for instance in the bottom row of Fig. 6.4. That is to say, $M(< R)$ is well constrained in the image region, but becomes more uncertain farther in or out. Note that the butterfly shape is less prominent or even distorted for less symmetric lensed image configurations (see e.g. the top panel of Fig. 6.4). The steep limit of the butterfly shape is expected to be roughly $M(< R) \sim R^{1.5}$,

resulting from the minimal steepness of $R^{-0.5}$ in the projected density. The shallow limit of the butterfly shape is given by the steepest model in the ensemble. The lens models do not attempt to subtract off lensing mass outside the galaxy or, to be more precise, outside the circular pixel map. However, given that the model-ensemble technique yields conservatively large error-bars on the mass maps, we expect that external lensing mass is unlikely to be larger than the estimated uncertainties.

In the following section we focus on the two-dimensional on-sky projections of the mass distributions and come back to the azimuthally averaged mass profiles in Section 6.5.

6.4 Spatial distribution of stellar and dark matter

The stellar population synthesis routine produces projected stellar surface mass maps as demonstrated in Section 3.2.3. See also Fig. A.3 in the appendix for all stellar surface mass maps. Subtracting them from the reconstructed total mass maps (see Fig. B.3 in the appendix) yields difference mass maps which depict the distribution of dark matter in the lenses. The ratio of stellar surface mass maps and total mass maps gives, on the other hand, stellar mass fraction maps. Both dark matter (Fig. 6.2) and stellar mass fraction maps (Fig. 6.3) will be discussed in the following.

In both figures the black circles indicate the effective radius of respective lenses. The contours in the figures connect pixels with same pixel values. The enclosed pixels have thus same or higher values. It must be noted that they do not indicate the enclosed mass. Their staggered course can be explained by rounding errors of the pixel values used for the maps. The dark matter maps contain in some cases (e.g. Q0047 and Q0147) blank (white) pixels in the centres, which indicate that the stellar mass subtracted from the total mass was in fact larger than total mass. At this point it is important to note that there are error bars connected to each pixel. For the sake of simplicity of the plot these are not taken into account. Even if some pixels are actually negative their error bars are consistent with masses above zero with one exception. The central pixels of B1608 have error bars not consistent with positive mass values. B1608 is in many respects a special lens (see its description in Section 4.1) and is treated as an outlier throughout our analysis. Blank pixels in the stellar mass fraction (Fig. 6.3) arise if a region is masked out in one of the photometric bands or the total mass map was shifted or rescaled during the alignment procedure.

Most lenses exhibit elliptical stellar (Fig. A.3) and fairly elliptical total mass distributions (Fig. B.3). The structures in the dark matter and stellar mass fraction maps arise from the the elliptical distributions of stellar and dark matter not being well aligned. As a consequence, dipole-like patterns in the stellar mass fraction maps are produced as one can see e.g. for PG1115. The prominence of such dipoles is influenced by the observation angle. B1600 for instance is a lens galaxy viewed almost edge-on and has the strongest dipole shape.

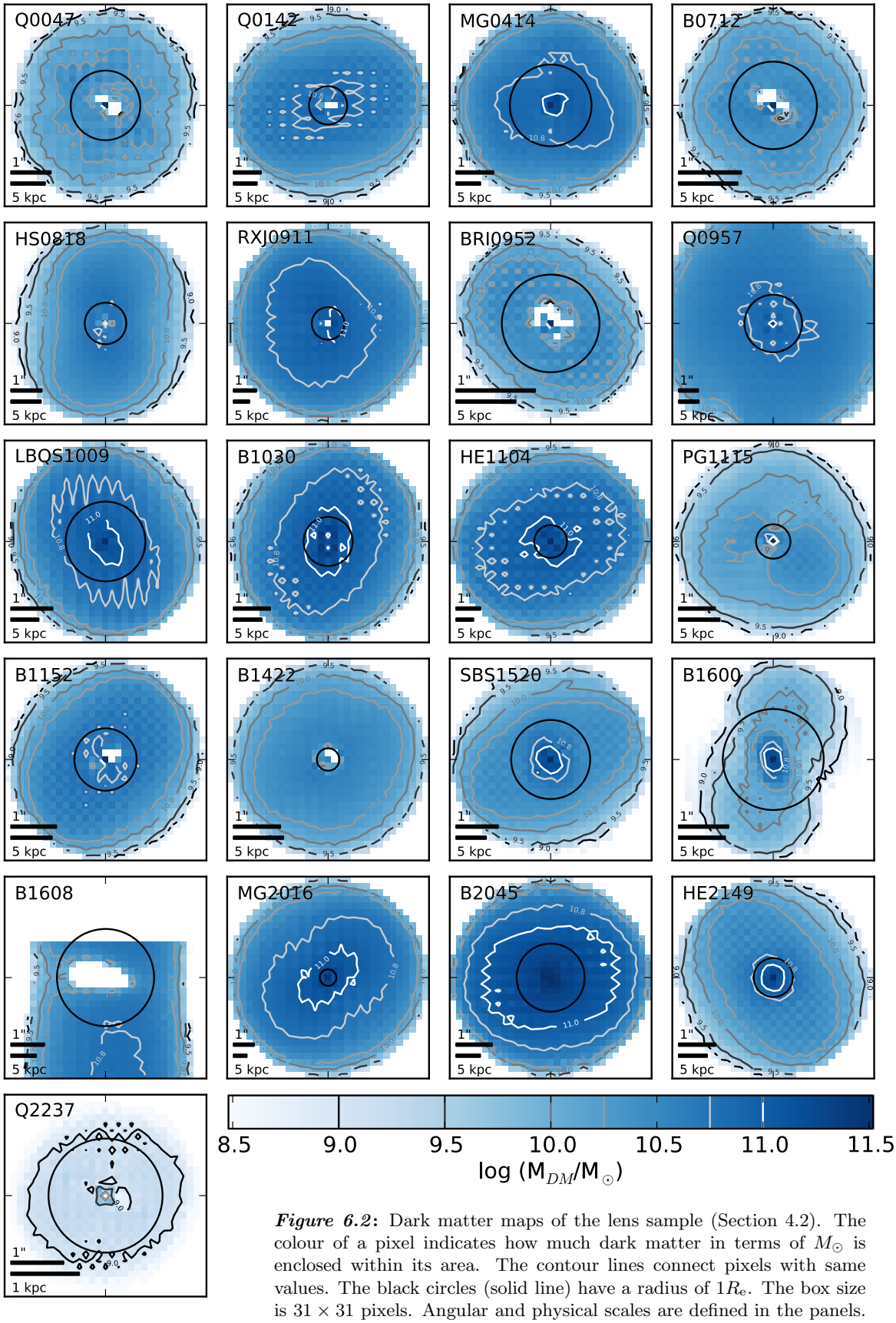

***Figure 6.2*:** Dark matter maps of the lens sample (Section 4.2). The colour of a pixel indicates how much dark matter in terms of $M_\odot$ is enclosed within its area. The contour lines connect pixels with same values. The black circles (solid line) have a radius of $1R_e$. The box size is 31×31 pixels. Angular and physical scales are defined in the panels. North is up, east is left.

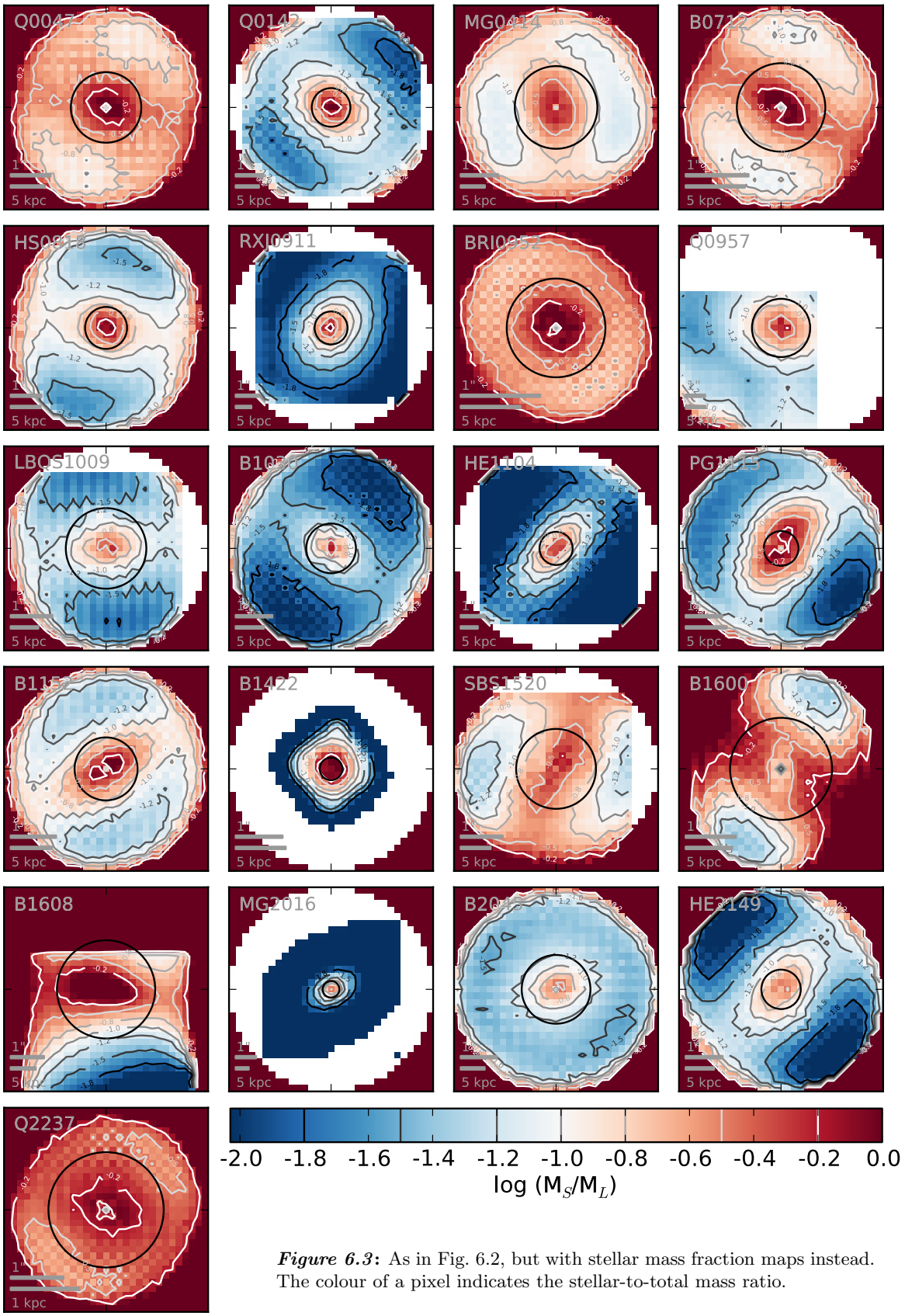

***Figure 6.3*:** As in Fig. 6.2, but with stellar mass fraction maps instead. The colour of a pixel indicates the stellar-to-total mass ratio.

Especially interesting are lenses which show significant deviations from simple elliptical shapes. PG1115 shows an extended dark matter distribution to the south-west. The corresponding stellar mass fraction map shows especially low values in this direction. Similar features can be found in Q0047, MG0414 and RXJ0911. Lenses with extended pixel regions above $10^{11} M_{\odot}$ in their dark matter map, like B2045, MG2016 and HE1104, display low (blue) stellar mass fractions and almost no dipole features. Furthermore lenses with low dark matter content (lighter blue colour in Fig. 6.2) seem to be correlated with high stellar mass fractions (redder colour in Fig. 6.3).

Analyzing the distribution and interplay of dark matter and stars in a spatially resolved manner is an intriguing perspective for future studies (see outlook in Chapter 8).

In the following sections, we simplify the study of matter distributions by looking at enclosed mass profiles only. To obtain the profiles we average azimuthally along elliptical isophotes. An ellipse is in general defined by major and minor semi-axis, i.e. two different radial measures. Because of this we simply assign their mean value to be the radius connected to $M(< R)$. These cumulative profiles have the advantage that outliers among the pixel values are marginalized. Uncertainties connected to each pixel are thus translated into more robust errors of a single mass profile.

6.5 Radial dependence of stellar versus total mass

To compare the radial dependence of stellar and total mass, it is interesting to consider pairs of lenses with matching $M_L(< R)$ or with matching $M_s(< R)$. To illustrate this, in Fig. 6.4 we show three pairs of galaxies with the following properties (see also Table C.2):

1. small mass, matching $M_L(< R)$ profiles, differing $M_s(< R)$,
2. intermediate mass, matching $M_L(< R)$ profiles, differing $M_s(< R)$,
3. high mass, differing $M_L(< R)$ profiles, matching $M_s(< R)$.

The radial scale is $R/R_{\rm Ein}$ where $R_{\rm Ein}$ has been estimated from the pixelated mass maps. For $M_s(< R)$, error bars are 68% confidence from the population-synthesis models. For $M_L(< R)$ we use error bars corresponding to 90% of the $M_L(< R)$ range of the model ensemble, as described in Section 6.3.2. Note that the errors attached to $M_s(< R)$ and $M_L(< R)$ are correlated.

The matched pairs are, of course, only rough matches. Also, the $R_{\rm Ein}$ values are not the same for the matched pairs of galaxies. The angular radial scale is proportional not only to the enclosed mass but also to $(d_{LS}/(d_L d_S))^{0.5}$ (corresponding to $(d_L d_{LS}/d_S)^{0.5}$ for the physical Einstein radius), where the d's are the angular diameter distances between observer and lens (L), observer and source (S) and lens and source (LS). Latter distance ratio must be approximately equal to identify matching profiles. To enable comparison between scales, we include $R_{\rm Ein}/R_{\rm e}$ in Table C.2. With these caveats, we point out some interesting features.

Consider first the two low-mass lenses PG1115 and Q0047 (bottom panels, Fig. 6.4). While the total mass within $2R_{\rm lens}$ is very similar, the stellar mass of PG1115 rises only

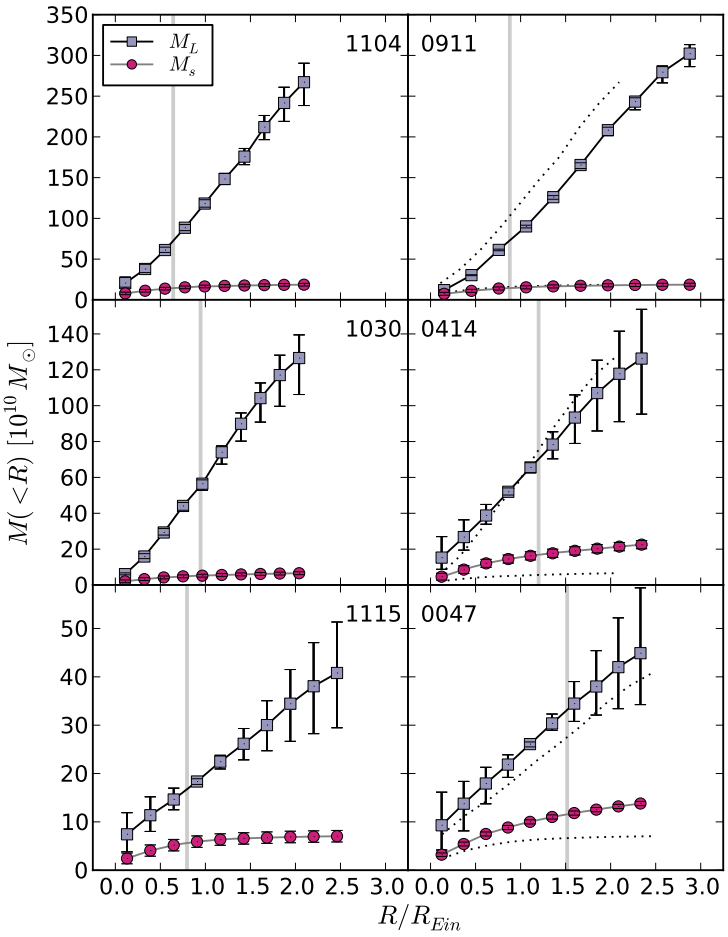

***Figure 6.4*:** Cumulative stellar mass and lens mass profiles against projected radius (in units of the Einstein radius) for three comparable pairs of lenses. PG1115 and Q0047 (bottom row) are low mass systems, B1030 and MG0414 (middle) are intermediate mass, and HE1104 and RXJ0911 (top) are high mass. The grey vertical line marks $2R_e$. To assist comparison, each right-hand panel has the profiles from the corresponding left-hand panel duplicated with thin dotted lines.

to 50% that of Q0047. The same qualitative behaviour is seen if these two galaxies are compared using R/R_e (Fig. 6.5) rather than $R/R_{\rm Ein}$ as the radial scale. Nevertheless, these two low-mass lenses belong with $f_s \equiv M_s/M_L \gtrsim 0.17$ to the range of high baryon fractions. Lenses within this range can consequently be referred to as high f_s lenses.

Comparing the two intermediate mass lenses B1030 and MG0414 in the middle panels of Fig. 6.4, we find that their cumulative total mass curves are very similar. However, the stellar mass of B1030 is just $\sim 30\%$ that of MG0414, independent of the radius. If we consider the stellar radial scale, we find that MG0414 has ~ 4 times the stellar mass of B1030. Their baryon fractions approach values from $f_s \approx 0.05$ (B1030) to $f_s \approx 0.17$ (MG0414) at the outermost radius to which we have estimates. In the intermediate mass range of our sample (roughly $5 \times 10^{11} M_\odot$ to $15 \times 10^{11} M_\odot$) MG0414 has one of largest and B1030 the lowest stellar-mass fraction. It should be noted that the opposite behaviour, namely matching stellar profiles on both $R_{\rm lens}$ and R_e scale with very different total mass

is also possible. An example for the latter would be a comparison between B1030 (middle row) and PG1115 (bottom row) of Fig. 6.4 with equal $M_s(R/R_e)$ but total mass profiles differing by a factor of 4.5 at $3R_\mathrm{e}$.

The two high mass lenses RXJ0911 and HE1104 have a total stellar mass of $\simeq 2 \times 10^{11} M_\odot$. For comparison, the total mass profiles differ slightly for radii $\lesssim 1.5R_\mathrm{e}$ and $\gtrsim 2.5R_\mathrm{e}$. But it should be noted that RXJ0911 is located at the centre of a galaxy cluster which might lead to a lens mass estimate slightly larger than the actual virial mass of the lens galaxy. At $6.5R_\mathrm{e}$, i.e., $\sim 2R_\mathrm{lens}$ HE1104 has 12% less total mass than RXJ0911. At $\sim 3R_\mathrm{e}$, i.e. R_lens the difference is still 6%. In terms of stellar-mass fraction HE1104 exhibits small values of $f_s \approx 0.07$ and RXJ0911 of $f_s \approx 0.06$. In the high mass regime ($> 15 \times 10^{10} M_\odot$) the range of possible stellar-mass fractions appears to be small compared to low and intermediate masses, and always close to 0.05. Those two lenses are thus representative for low f_s lenses.

Comparing lens profiles on R_e scales intrinsic to the luminous part of the galaxy, one can find many lenses with similar stellar mass profiles, which is not surprising. After all the enclosed mass values $M_s(< 2R_\mathrm{lens})$ cover with $\sim 10^{10}$ to $\sim 2 \times 10^{11}$ a relatively small range in contrast to a total mass range $M_L(< 2R_\mathrm{lens})$ of $\sim 2 \times 10^{10}$ to $\sim 2 \times 10^{12}$. However, pairs of lenses with matching $M_s(< R)$ and $M_L(< R)$ profiles over the whole radial range as shown in Fig. 6.5 are rare. Most lenses with matching $M_s(< R)$ profiles exhibit quite different $M_L(< R)$ profiles. The above lenses HE1104 and RXJ0911 are – apart from their data points $\gtrsim 6R_\mathrm{e}$ – matching pairs (with respect to M_s) within uncertainties on R_e scale as they are on R_lens scale, a consequence of $R_\mathrm{lens}/R_\mathrm{e}$ being equal for both objects.

In Fig. 6.5 we present the left column lenses of Fig. 6.4 now on baryonic scales, two of them have new counterparts with similar $M_s(< R)$ and $M_L(< R)$. As before we present low to high mass galaxies from the bottom up.

For the two low mass lenses PG1115 and B0712, we find that at the outermost radius probed for B0712, i.e. $\sim 2.5R_\mathrm{e}$, their baryon fraction is ~ 0.08. B1030 and LBQS1009 also match well within their error bars although the mean stellar mass profile of B1030 is consistently below the one of LBQS1009. The error region of its lens mass profile shows quite large error bars and thus make it easy to match. The baryon fraction at $2.7R_\mathrm{e}$ is approximately $f_s = 0.08$. If we compare lenses along the vertical direction of Fig. 6.5, B0712 and LBQS1009 are representative for most lenses on low to high mass scales, that is, similar $M_s(< R)$, dissimilar $M_L(< R)$ and baryon fractions.

In summary we find on both baryonic scale R_e and lensing scale R_lens:

- many pairs with the same enclosed total (lens) mass, but with different enclosed stellar mass,
- a small number of pairs (decreasing with increasing M_L) with the same enclosed total (lens) and stellar mass.

We can already conjecture an anti-correlation between enclosed lens mass and stellar-mass fraction, which will be studied in detail later on. However, one should keep in mind that our result could be influenced by the lens environment and its history. See also Table

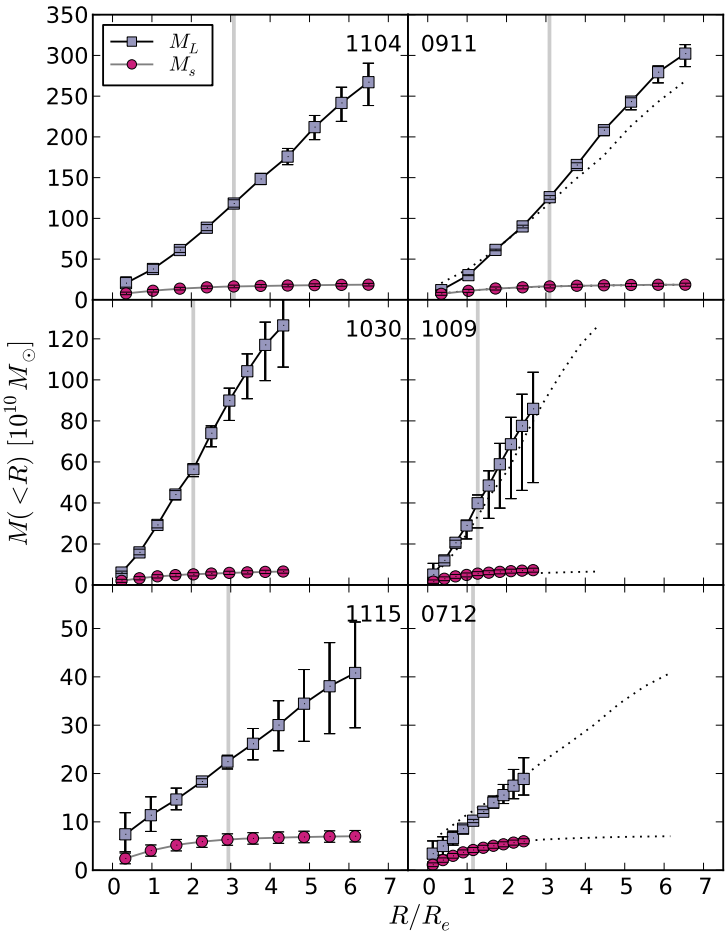

***Figure 6.5*:** As in Fig. 6.4, but with the effective radius R_e as reference scale, shown for PG1115 and B0712 (bottom), B1030 and LBQS1009 (middle), HE1104 and RXJ0911 (top). Here the grey vertical line marks $R_{\rm lens}$.

C.2, column '*Env*' and Section 6.2 for information on the local lens environment. The phenomenon of same M_L but different M_s becomes less prominent for larger total lens masses, on both $R_{\rm lens}$ and R_e scale. Nevertheless, global trends and interdependencies might be revealed by analysing the whole set of lenses, which is done below.

Using our sample of 21 lensing objects we consider the following relations to highlight the interdependencies in the (M_L,M_s,R) parameter space:

1. the enclosed total mass $M_L(< R)$ as a function of enclosed stellar mass $M_s(< R)$ at a fixed radius R,
2. the stellar-mass fraction as a function of radial distance, $f_s(R) = M_s(< R)/M_L(< R)$,
3. the stellar-mass fraction as a function of the total mass M_L,
4. the stellar-mass fraction as a function of redshift.

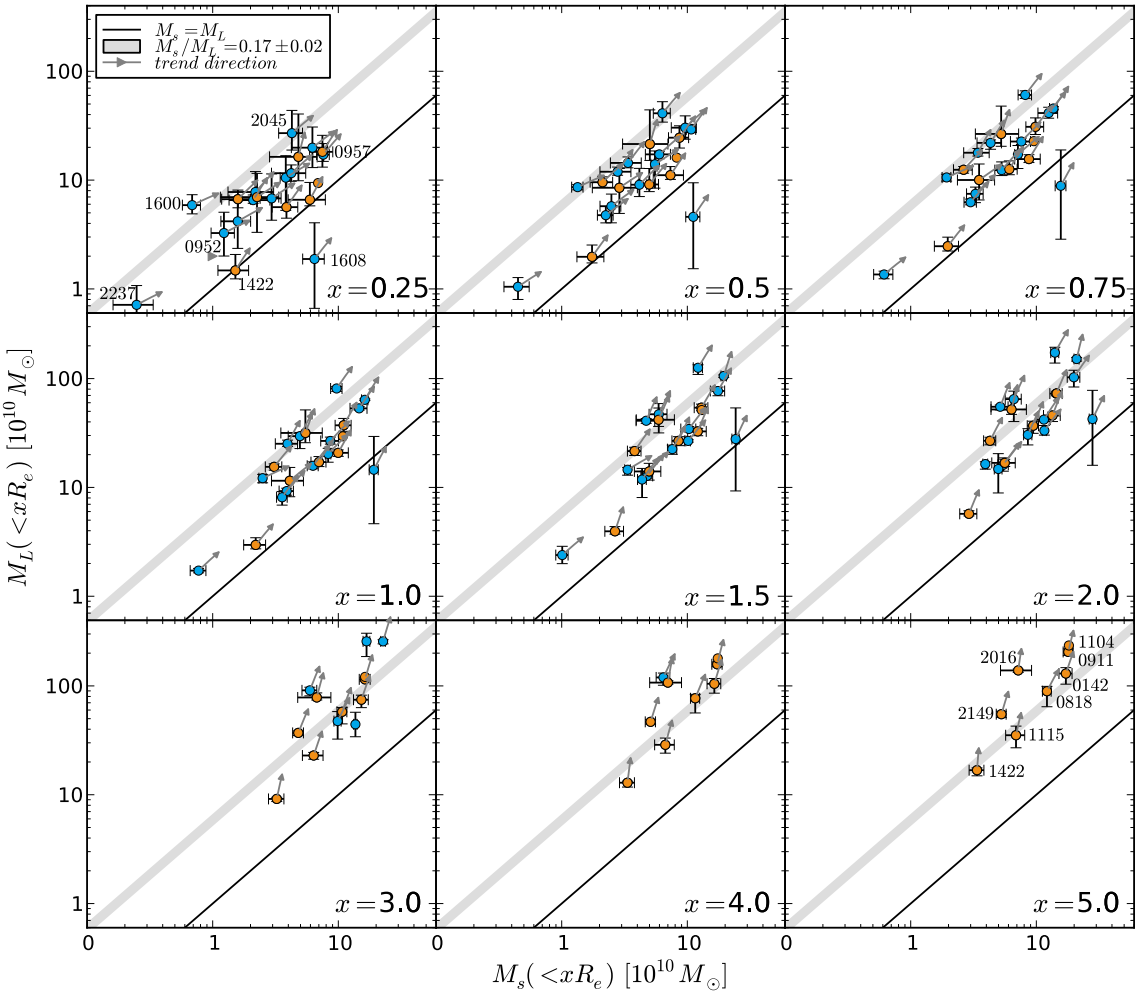

***Figure 6.6*:** The panels show the enclosed M_L against enclosed M_s plane for a number of apertures, defined by the radial distance xR_e to the centre of the lens galaxy, labelled by 'x' in the bottom-right corner of each panel. We cover a radial distance from 0.25 to $5R_\mathrm{e}$ from upper left to lower right panels in conveniently chosen steps. Orange circles highlight a subset of eight lenses which are probed out to $5R_\mathrm{e}$. Grey arrows indicate the direction in which the data points move in the next $0.25R_\mathrm{e}$ step. The solid line denotes the equality of total and stellar mass, whereas the grey band represents the uncertainty region around the global baryon fraction (Hinshaw et al. 2009).

Fig. 6.6 shows the first relation for a range of radial positions from $0.25R_\mathrm{e}$ to $5R_\mathrm{e}$, parameterized by the dimensionless quantity $x \equiv R/R_\mathrm{e}$. For reference, we list in Table C.2 of the appendix the enclosed stellar and lens mass within $2R_\mathrm{e}$ with error bars. The universal baryon fraction according to WMAP5, $f_b = \Omega_b/\Omega_m = 0.17 \pm 0.02$ (Hinshaw et al. 2009), is included as a grey band. The solid black line denotes a stellar-mass fraction of one, i.e. the total mass content consists of 100% stellar mass. The grey arrows indicate the direction in which the data point will move within the next $0.25R_\mathrm{e}$. Orange data points denote lenses with reconstructed profiles probed out to $5R_\mathrm{e}$ or farther. The distinction will be used later on. Note that the data points in Fig. 6.6 refer to baryonic matter in stars and do not account for other baryonic content like gas and dust. The gas content of our lens

sample – mostly early-type galaxies – is expected to be small. But for the Einstein Cross (Q2237), which is the bulge of a spiral galaxy, and B1600, which is likely to be a late-type galaxy viewed edge-on, one can indeed expect deviations from the obtained M_s values.

The galaxy B1608 shows an unreasonably high stellar-mass fraction for radii $\leq .75R_{\rm e}$ (e.g. left panel in top row of Fig. 6.6). To take proper account of the light distribution of B1608, we fit both the brightest galaxy and its merging companion with Sérsic profiles, but we only use the information of the light profile of the brightest galaxy for the computation of stellar mass. The enclosed mass values are thus taken with respect to the centre of the brightest galaxy. As a consequence of the degeneracy between the two Sérsic profiles, the central region of the light profile is modeled rather poorly. This causes an overestimate of the stellar content ($\lesssim 15\%$) in a region where the neighbouring galaxy, which is also responsible for light deflection, interferes with the fit. The pixels with highest total mass and highest stellar content do not match for B1608. This also causes larger deviations in the region $\lesssim 1R_{\rm e}$.

The late-type galaxies Q2237 and B1600 might be subject to dust reddening. In general, the impact of reddening on high redshift lenses is stronger due to the bluer populations observed in H-band and the higher absorption of dust at smaller wavelength. However, on the basis of the analysis shown in Section 6.3.1, we do not expect departures of more than 20% towards higher M_s. This will shift $B1600$ closer to the bulk of lenses in Fig. 6.6.

The prominent f_s curve of B1422 — starting at twice the value of most other lens galaxies — might also be caused by light contamination. This time it originates from the innermost quasar image which lies just $0.25''$ away from the galaxy centre, an extreme among the 21 lenses.

An animated version of Fig. 6.6 is provided in the ancillary material to Leier et al. (2011) (see Section A.1). The lens galaxies reveal the following properties, which are qualitatively assessable already from Fig. 6.6, but will be explained in detail later on:

1. Most lenses populate a band of $0.1 < f_s < 0.4$ within $5R_{\rm e}$.

2. The slope of the enclosed M_L-to-M_s relation of Fig. 6.6 within the shown radial range becomes gradually steeper for larger enclosed radii (an effect quantified in the following paragraph).

3. Between 2 (1.5) and $2.5R_{\rm e}$ ($2R_{\rm e}$) for most lenses with total mass below (above) $4 \times 10^{11} M_{\odot}$, the dark matter halos overtake the stellar content, that is they move primarily toward increasing total mass. The turning point thus depends on the halo mass. The dark matter halos of more massive galaxies start to dominate the matter balance at larger radii (in units of $R_{\rm e}$) than those of less massive galaxies.

Note that by 'overtake' we refer to the radius where $dM_L/dR \approx dM_s/dR$ rather than to the radius where the total stellar mass contributes 50% of the total mass. As a consequence of limited resolution, this radius can only be given with larger uncertainties ($\sim 0.5R_{\rm e}$).

Point 2 can also be illustrated by plotting the slope η determined from $M_s \propto M_L^{\eta}$ so that it represents light as a function of mass. We find that η asymptotically approaches

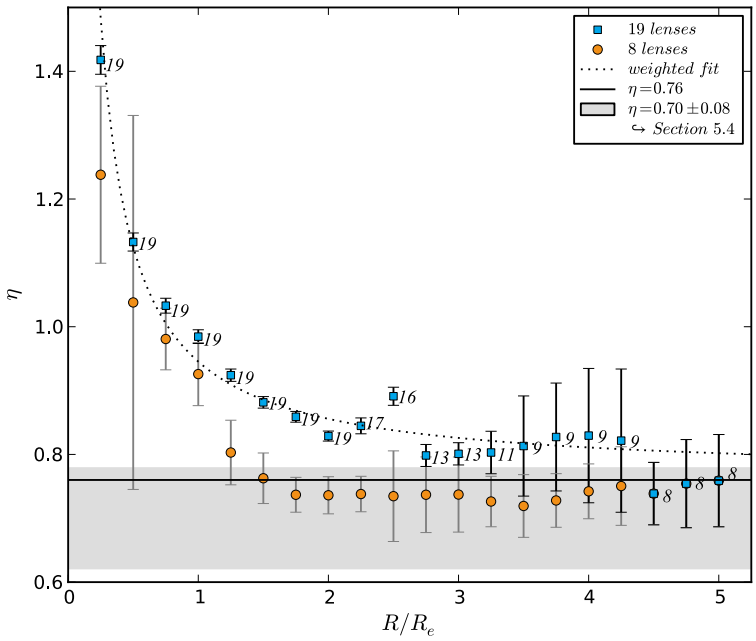

***Figure 6.7*:** Slope of the M_s-to-M_L relation taken from Fig. 6.6 plotted against the distance to the centre in terms of effective radii. The median slopes are determined via a bootstrapping fitting method with 10^4 realizations to compute meaningful standard errors for a sample of 19 lenses (blue squares) and a reduced 8 lens sample (orange circles). The numbers at the filled squares give the number of lenses probed out to the respective radius. The dotted line represents a weighted best fit of $\eta(R) \sim 1/R$+const.

0.75, as one can see in Fig. 6.7, which is in agreement with previous studies of the fundamental plane within error bars (e.g., Guzman et al. 1993, Jørgensen et al. 1996, Leier 2009). A bootstrapping method for a large and a reduced sample is used to determine the M_s-to-M_L relation and its standard errors respectively. Both runs are done with 10^4 realizations. The 19-lens sample contains all the lenses except for the outlier B1608 and the late-type galaxy Q2237. Farther out in radius, the number of lenses with profiles extending to a particular radius decreases. Because of that, Fig. 6.7 also shows the number of lenses used for each fit. As a consequence of changing sample size, discontinuities appear between 2.25 and $3.5R_e$ and at $4.5R_e$. The most extreme ones are caused by B0712 ($2.5R_e$) and B1030 ($4.5R_e$) falling out of the sample. The behaviour of the error bars in a bootstrap fit depends on the size of the drawn sample subset. To get more meaningful error bars we fixed the size of the sample subset to be 50% of the available number of lenses at each radius. The small sample instead comprises all 8 lenses being probed out to $5R_e$, which are highlighted in Fig. 6.6 by grey filled circles. From $M_s \propto M_L^{1.24\pm0.14}$ at $0.25R_e$ the reciprocal slope $\eta(R)$ declines as $1/R$ and ends up at $5R_e$ with the relation $M_s \propto M_L^{0.76\pm0.07}$. We expect only small deviations from this slope for larger radii since we run out of stars, and additional mass from the dark matter halo shifts the distribution upwards, whereas possible baryonic contributions from gas shift the whole population farther to the right of Fig. 6.6. Additionally, for the 19-lens sample a weighted best fit for $\eta(R)$ suggests that the function approaches asymptotically a constant value of 0.77 ± 0.01. Note that for the small sample $\eta(R)$ declines rapidly to reach the value of 0.76 already

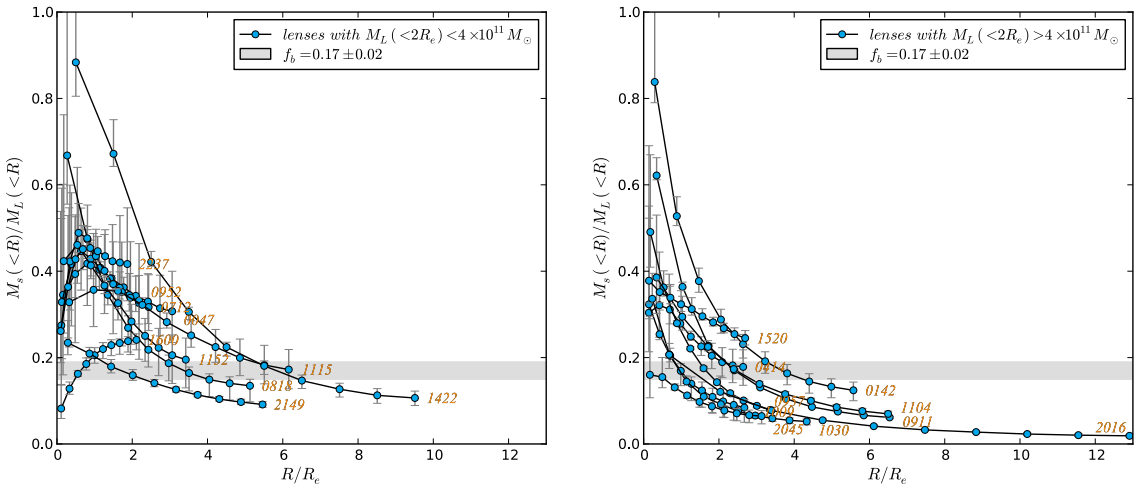

Figure 6.8: Left panel: Stellar-mass fraction against radius in effective radii for lenses with $M_L(< 2R_\mathrm{e}) < 4 \times 10^{11} M_\odot$. Right panel: Similar, but for lenses with $M_L(< 2R_\mathrm{e}) > 4 \times 10^{11} M_\odot$.

at $\sim 1.5R_\mathrm{e}$ and thereafter shows no significant departure from it. However, the change in slope from small to large radii is significant for both the 19-lens and the 8-lens sample.

All the stellar-mass fraction curves in the left and right hand panel of Fig. 6.8 turn over between 1.5 and 2.5 R_e to approach a similar stellar-mass fraction, a fact also reflected by $\eta(R)$ in Fig. 6.7. The same trend is readily identifiable from the trend arrows in Fig. 6.6. With increasing radius, the stellar-mass fractions of high mass galaxies ($M_L(< 2R_\mathrm{e}) \gtrsim 4 \times 10^{11} M_\odot$) tend towards lower values in the majority of cases, meaning $f_s \lesssim 0.2$. Low mass galaxies ($M_L(< 2R_\mathrm{e}) \lesssim 4 \times 10^{11} M_\odot$) show a larger range of possible stellar-mass fractions at high and low radii, which are in a range between 0.1 and 0.35 (see left hand panel of Fig. 6.8). This is the reason for the large scatter of enclosed stellar-to-total enclosed masses at small radii in Fig. 6.6.

Averaged over the whole lens sample we find that the stellar-mass fraction declines with increasing radius from its value $f_s(< 1R_\mathrm{e})$ enclosed in $1R_\mathrm{e}$ to only $\sim 71\%$ at $2R_\mathrm{e}$, $\sim 55\%$ at $3R_\mathrm{e}$, $\sim 39\%$ at $4R_\mathrm{e}$ and finally $\sim 33\%$ at $5R_\mathrm{e}$. Splitting the sample with respect to total mass as done before yields a different picture: For lenses with $M_L(< 2R_\mathrm{e}) \lesssim 4 \times 10^{11} M_\odot$ 79% of the stellar-mass fraction at $1R_\mathrm{e}$ remains at $2R_\mathrm{e}$, 63% at $3R_\mathrm{e}$, 47% at $4R_\mathrm{e}$ and finally 40% at $5R_\mathrm{e}$. For lenses with $M_L(< 2R_\mathrm{e}) \gtrsim 4 \times 10^{11} M_\odot$ 64% of the stellar-mass fraction at $1R_\mathrm{e}$ is found at $2R_\mathrm{e}$, 48% at $3R_\mathrm{e}$, 33% at $4R_\mathrm{e}$ and finally 27% at $5R_\mathrm{e}$. The uncertainties of stellar-mass fractions at $1R_\mathrm{e}$ for low M_L lenses are only as high as 10%. For larger radius and mass the f_s errors decline strongly to less than 1%. From this we can conclude the following.

1. Low mass galaxies show a shallower decline in their enclosed stellar-mass fraction than high mass galaxies: either their stellar content is less concentrated than in high mass galaxies or their dark matter content is more concentrated. This point becomes clearer in Section 6.6, where we calculate concentration indices of stellar and total mass profiles,

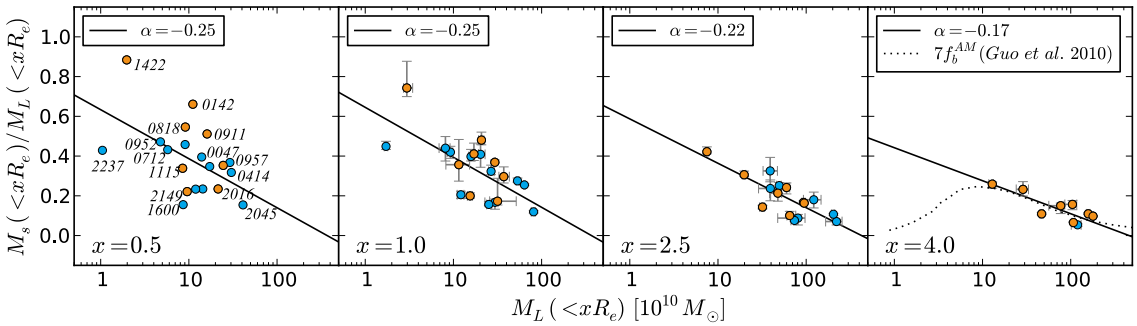

Figure 6.9: The stellar-mass fraction determined at 0.5, 1.0, 2.5 and 4.0 R_e against total mass. The best fits are found for the sample excluding lenses with mean stellar-mass fractions above 1 at R_e, which is the case only for B1608.

2. The relative stellar-mass fraction of high versus low mass galaxies is significantly offset by a constant value within $5R_\mathrm{e}$ from the centre, i.e.

$$\frac{f_s(<R)}{f_s(<1R_\mathrm{e})}\Big|_{M_L>4E11M_\odot} \approx \frac{f_s(<R)}{f_s(<1R_\mathrm{e})}\Big|_{M_L<4E11M_\odot} - 0.15 \tag{6.1}$$

for $2R_\mathrm{e} < R < 5R_\mathrm{e}$.

The latter phenomenon becomes more evident when plotting the stellar-mass fraction at fixed R/R_e against the total mass as in Fig. 6.9. From left to right the panels show the f_s–M_L relation at discrete radii of 0.5, 1.0, 2.5 and 4.0 R_e. It should be emphasized that the solid line fit does not imply a physical relation extendable to the high or low mass end of the plot. Note that the relation has a tendency to steepen gradually towards lower radii while the scatter increases. Comparing this to recent results from Guo et al. (2010), where the ratio of total enclosed stellar mass M_s and halo mass M_halo is analyzed with an abundance matching method, we find that their stellar-mass fraction curve f_b^{AM} ('AM' stands for abundance matching) shows a peak at a halo mass of around $6 \times 10^{11} M_\odot$ and decreasing fractions towards lower and higher halo masses. This is overplotted in the last panel of Fig. 6.9. The actual height of the dotted curve f_b^{AM} lies way below our results, which is why we scale f_b^{AM} by a factor chosen to make the curve match with our data. This is owing to the fact that f_b^{AM} gives the stellar-mass fraction enclosed in the virial radius. There is a significant amount of dark matter in the halo in the range from the outermost radius we probe for the lenses up to the virial radius. The latter is defined in Guo et al. (2010) as

$$R_\mathrm{vir} = \left(\frac{GM_\mathrm{halo}}{100H^2(z)}\right)^{1/3}. \tag{6.2}$$

R_vir is roughly a hundred times larger than the region probed in this study. We list R_vir values deduced from M_s of this study given their M_s-to-M_halo relation in Table C.2, which has additional implications on the lens environment, provided that the lens behaves like an SDSS-Galaxy plus simulated halo counterpart of respective stellar mass. To illustrate how the computed stellar-mass fractions change between our resolution range and the virial radius, we multiply a constant factor by the stellar-mass fraction curve f_b^{AM} from Guo et al. (2010) (Fig. 6.9) and divide its total mass by the same factor (here we use

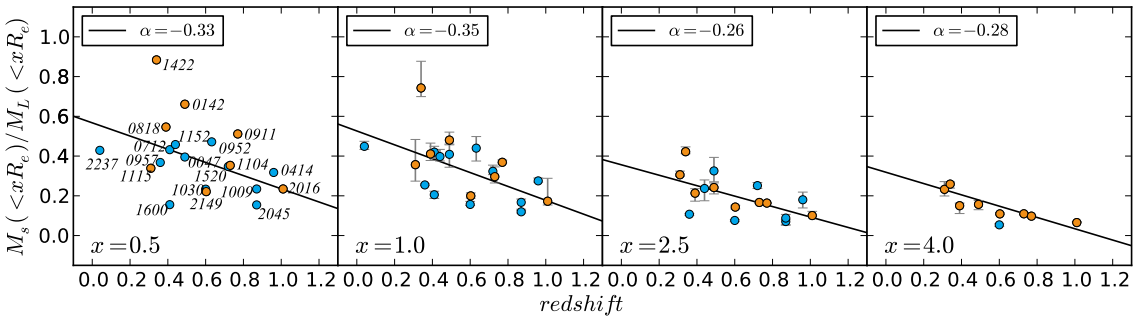

***Figure 6.10*:** The stellar-mass fraction determined at 0.5, 1.0, 2.0 and 4.0 R_e against redshift.

7). The slope of the high mass end of their curve agrees with our best fit of $M_L^{-0.16\pm0.04}$ within error bars. Scaling to lower radii makes the mismatch for lower M_L even more prominent. However, we conclude that the M_s-to-$M_{\rm halo}$ relation from Guo et al. (2010) is scalable down to a certain level. In the $5R_e$-to-$R_{\rm vir}$-range, the lower-mass lensing galaxies need to decrease their stellar-mass fractions by a larger amount than high mass galaxies in order to match with the results from Guo et al. (2010). Note that scaling our lens sample instead towards higher total masses and lower stellar-mass fractions yields the same result.

We should point out that this direct comparison of our results with Guo et al. (2010) is imperfect, since $M_{\rm halo}$ and M_L are differently defined and the spatial distribution of dark matter in a region not directly addressed in either paper is unknown. On the other hand, the steepest part of the total mass profiles is already enclosed and the cumulative mass profiles saturate, i.e. the slope of the M_L-to-f_s relation is only slowly changing beyond $5R_e$. These different trends for f_s at lower masses could be indicative of an underestimated stellar-mass fraction towards smaller halo masses or an overestimated baryonic content towards higher halo masses. If the aforementioned study of the M_L-to-f_s dependency is correct, then our findings give rise to the question of what makes the stellar-mass fraction of low mass galaxies decline less strongly within $5R_e$ than in the range from $5R_e$ up to the virial radius, in contrast to high mass galaxies. Expressed in terms of stellar mass content, we find a steeper decrease of stellar-mass fractions towards larger M_s than our results predict.

The virial radius $R_{\rm vir}$ defined in Eq. eq:rvir becomes smaller for lower stellar mass content. Low M_s galaxies reside in halos with larger f_s than high M_s galaxies, meaning the mass in the dark matter halo relative to M_s is even larger, i.e. small galaxies have more concentrated dark matter halos than larger ones (see also Section 6.6).

In order to investigate the influence of the distance/lensing-bias, we also show the redshift dependence of the stellar-mass fraction in Fig. 6.10. The ordinate might be subject to several biases. The lensing galaxies plus halo must be massive to produce an observable signature. The galaxy should not be too faint to be seen and has to obey our selection criterion of sufficient separation from the quasar images. Fig. 6.10 shows that the correlation between stellar-mass fraction and redshift becomes more pronounced with larger

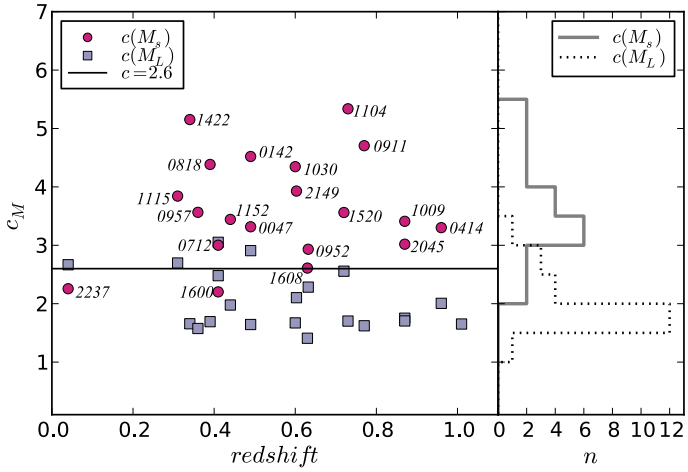

***Figure 6.11*:** Concentration index $c = R90/R50$ versus redshift, where c is the ratio of the radii enclosing 90% and 50% of the total stellar mass ($c(M_s)$, magenta circles) and lens mass ($c(M_L)$, blue squares). For MG2016 R50 cannot be calculated due to a lack of data points at small radii. The solid line indicates $c = 2.6$ separating early-type ($c > 2.6$) from late-type galaxies ($c < 2.6$). Error bars for index c can be found in Fig. 6.12.

radius. However, the strongly increasing scatter below $4R_e$ blurs the correlation and the slope shows no uniform trend.

6.6 Baryon cooling

We now consider two different measures of the stellar and total-mass profiles, with a view to gaining insights on the evolution of lens galaxies from formation to observation redshift.

6.6.1 Concentration index

Our spatially resolved stellar and total mass maps allow us to study the difference in concentration of the baryon and the total mass distribution. The concentration index as used in observations is defined by a ratio $c \equiv R90/R50$, where $R90$ and $R50$ denote the radii enclosing 90% and 50% of the Petrosian r-band luminosity (see e.g. Bershady et al. 2000). In that case a concentration index above 2.6 indicates an early-type galaxy, whereas indices below 2.6 refer to late-type galaxies (Ferreras et al. 2005). Previous studies based on the surface brightness distribution use the Petrosian radius (or a given number of Petrosian radii) to define the total brightness (see Section 3.2.4). In our case, we redefine c and take the ratio of $R90$ and $R50$ of our cumulative stellar mass and total mass profiles instead — 100% corresponding to enclosed masses at $2R_{\rm lens}$ (except for Q0957 and HS0818 where it is $1.5R_{\rm lens}$). In Fig. 6.11, we show concentration versus redshift in the left-hand panel with no obvious correlation and the frequencies per concentration bin in the right-hand panel. Note that defining the concentration values using $R_{\rm Ein}$ instead of $R_{\rm lens}$ will change the concentration values slightly, but even for $R_{\rm lens}/R_{\rm Ein} = 1.5$ we obtain changes in the lens mass concentration of less than $\sim 30\%$ and only for lenses with high concentrations.

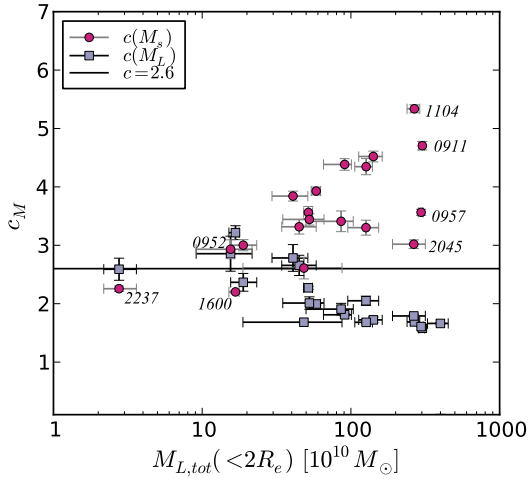

***Figure 6.12*:** As in Fig. 6.11 but plotted against the total mass $M_{L,tot}$ enclosed in $2R_e$. The y-axis error bars represent for $c(M_L)$ the standard errors for mean concentrations of 300 models. For $c(M_s)$ the error bars correspond to the uncertainties originating from a 10% error in the flux per pixel.

From Fig. 6.11 the frequency distribution of $c(M_s)$ peaks between 3.0 and 3.5, which is in agreement with most concentration studies of early-type galaxies (e.g. Yamauchi et al. 2005, Deng et al. 2010). That is, even with the redefined concentration quantities one can distinguish the lens galaxies morphologically. Evidence is given by the two late-type galaxies Q2237 and B1600, which indeed lie below 2.6. For the two merging galaxies in the lens B1608, the interfering potential (for $c(M_L)$) or light (for $c(M_s)$) causes the concentration values to be decreased, pushing $c(M_s)$ down to 2.6. For the same reason we obtain rather large error bars on the lens mass. One could check in detail now if the strong correlation between the concentration and Hubble-type is maintained for the newly defined $c(M_s)$, but this is beyond the scope of this work. If we define a concentration parameter by means of the total mass profiles we expect, as our findings in Section 6.5 already suggest, a totally different distribution, which is also plotted in Fig. 6.12. Most lenses exhibit $c(M_L)$ values in a narrow region between 1.5 and 2. However, neither in $c(M_s)$ nor in $c(M_L)$ a clear evolutionary trend can be found. Figure 6.12 shows that the concentration parameter for stellar mass $c(M_s)$ has a rising trend with total lens mass, whereas $c(M_L)$ clearly declines with lens mass.

Note that the error bars of $c(M_s)$ and $c(M_L)$ are the standard errors of the $R90/R50$ values of each model in the ensemble multiplied by student's t for a 95% confidence interval. This was done since the ensemble can be seen as being part of a normal population. The horizontal error bars are the M_L errors at the outermost radius of the reconstructed mass profile. As we can see at low total lens masses, the distributions of M_s and M_L are almost the same, which means that the M_L profile approaches the distribution of the baryonic matter. An interaction between the baryonic and dark matter distribution seems to be a reasonable explanation, since already in Section 6.5 we find that the stellar-mass fractions of less massive lenses are larger than for more massive lenses.

A possible interaction between baryons and dark matter is likely to influence the slope

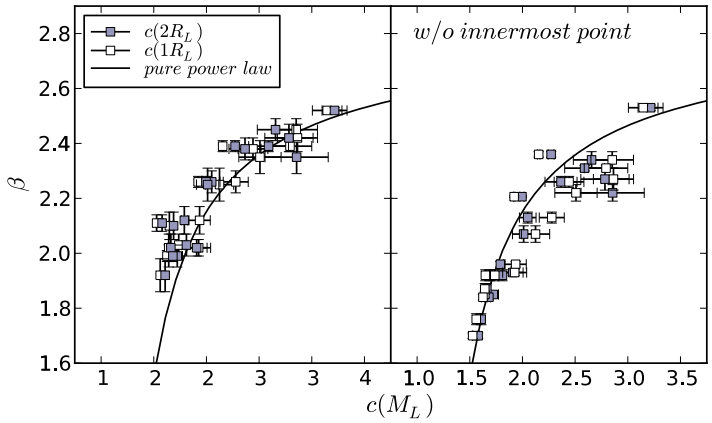

***Figure 6.13*:** Power law index β of the density profile plotted against the concentration parameter $c = (R90/R50)_{M_L}$ for the total lens mass distribution. Filled (open) squares indicate c determined for a profile extending to $2R_{\rm lens}$ ($1R_{\rm lens}$). The left panel uses power law fits to the entire radial range, whereas the right panel neglects the innermost data point. The solid black line shows the pure power law case according to Eq. 6.3.

of the total mass distribution close to the centre of galaxy. For example adiabatic contraction is thought to increase the concentration of the dark matter halo as a consequence of dissipation of gravitational energy and the feedback processes explained in Section 2.7. If we assume a density following a pure power law $\rho(r) \sim r^{-\beta}$ the enclosed mass becomes $M(< R) \sim r^{3-\beta}/(3-\beta)$. Thus the concentration c and the density slope β obey the relation

$$\beta = 3 - \frac{\ln 0.9/0.5}{\ln c}. \tag{6.3}$$

Figure 6.13 contrasts the relation between β and c based on a pure power law (solid line) and data for different radial extents. The β values represent weighted best fits to lens mass profiles with standard errors from the fit. If the mass distribution does not follow a pure power-law ($R90/R50$) might depend strongly on the radial extent of the lens ($2R_{\rm lens}$). Therefore we compare in both panels of Fig. 6.13 concentration values inferred from differently sized profiles, with a maximal radius of $1R_{\rm lens}$ and $2R_{\rm lens}$. The innermost data point has rather large uncertainties and deviates in most cases strongly from the trend at larger radius. To demonstrate its impact on the relation we contrast fits with (left panel) and without (right panel) regard of the innermost profile point. According to Eq. 6.3, we find that with increasing $M_L(< 2R_{\rm e})$ – i.e. decreasing concentration – the slope β gets shallower. It is remarkable how extraordinarily well the weighted power law fits to the data (left panel of Fig. 6.13). While neglecting the innermost point, the squares (in the right panel of Fig. 6.13) agree with the simple $\beta(c)$ model at low concentrations, but fail to do so at large concentrations, where the data is too low with respect to the pure power law relation. Higher values of β correspond to shallower M_L profiles. Including the innermost point always flattens $M_L(< R)$ fits, which explains why respective β values, although less representative for the outer part of the profiles, are in better agreement with Eq. 6.3 (see left panel of Fig. 6.13). We can conclude that

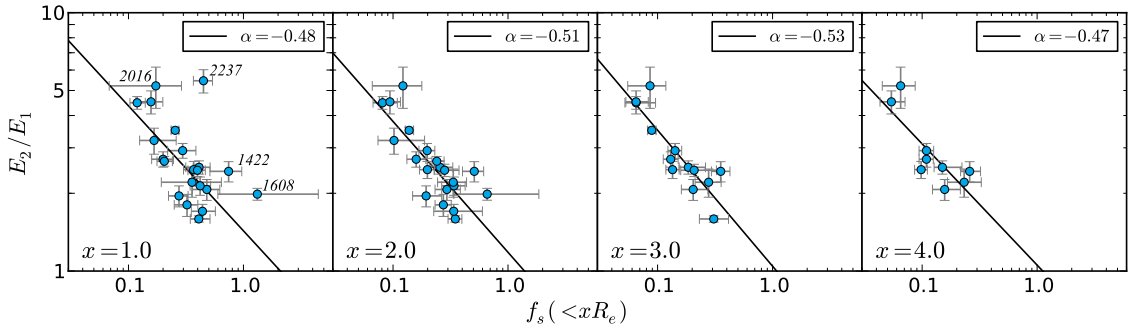

***Figure 6.14*:** The energy ratio E_2/E_1 versus stellar-mass fraction determined at 1.0, 2.0, 3.0 and 4.0 R_e. The solid line denotes the best fit of a power-law with slope α. The fits exclude Q2237 and MG2016.

1. excluding the core region of the lenses, we obtain power law indices and concentration parameters ($R90/R50$) indicative of a pure power-law behaviour for small concentrations. This notion is strengthened by only small shifts of ($R90/R50$) going from 2 to $1R_{\rm lens}$ profiles.

2. For more concentrated total mass distributions, we find evidence for a significant departure from pure power law behaviour. This is confirmed by significant shifts of ($R90/R50$) while reducing the extent of the lens from 2 to $1R_{\rm lens}$ and an increasing β error towards higher concentrations.

6.6.2 Energy ratio

By means of the stellar mass content, one can approach the subject of galaxy formation from a different viewpoint. The question is, whether it is feasible to determine a characteristic quantity which gives us the amount of energy lost between the collapse of an initial sphere of homogeneously distributed baryons and its later state as a lens galaxy. One could ask as well for a ratio of the radius of the pre-collapse sphere and an observable spatial quantity, like the effective radius. Even though this is a rough estimate, one can gain insight in the evolution process of galaxies.

At the time of collapse t_1, a region decouples from the expansion of the surrounding universe. The baryons which are assumed to be homogeneously distributed in this sphere are for now assumed to make up the entire stellar content of the later lens galaxy, neglecting any kind of active evolution such as caused by mergers, ram pressure, tidal stripping, etc. The radius r_1 of such a sphere at t_1 is

$$r_1 = \left(\frac{M_s}{\frac{4}{3}\pi \Omega_b \rho_c} \right)^{1/3} (1+z_1)^{-1}, \tag{6.4}$$

where $\Omega_b = 0.0441 \pm 0.0030$ is the baryonic energy density in terms of critical density according to Hinshaw et al. (2009) and $\rho_c \simeq 143.87 M_\odot/\mathrm{kpc}^3$. The average Newtonian energy per unit mass at t_1 consists only of the potential energy per unit mass, which is

$$E_1 = -\frac{GM_{\rm tot}}{r_1}. \tag{6.5}$$

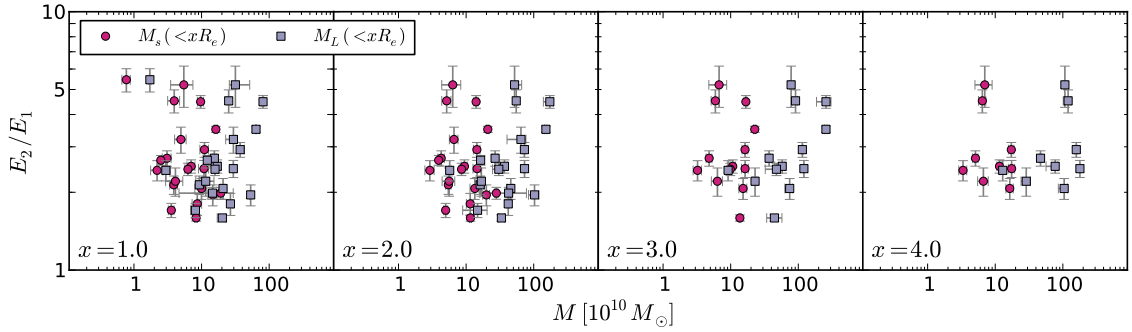

***Figure 6.15*:** The energy ratio versus enclosed stellar and enclosed total mass at 1.0, 2.0, 3.0 and 4.0 R_e.

The total mass $M_{\rm tot}$ is defined here as

$$M_{\rm tot} = \Omega_m \rho_c (1+z_1)^3 \frac{4}{3}\pi r_1^3. \tag{6.6}$$

As the collapse goes on, the baryons start to fall in to build a more tightly bound structure. At the observation redshift, i.e. at time t_2, we find mostly objects which are in virial equilibrium, that is $E = -T$, where T denotes kinetic energy. Thus we can determine the total energy per unit mass of the galaxy at t_2 to be

$$E_2 = -T_2 = -\frac{1}{2}\sigma^2_{\rm lens}, \tag{6.7}$$

where

$$\sigma_{\rm lens} \equiv \sqrt{GM_L(<R)/R} \tag{6.8}$$

is an effective velocity dispersion inferred from lensing (see Table C.2). It is computed at $R = R_{\rm lens}$ and assumed not to vary drastically with radius. This effective dispersion has been shown to be an appropriate surrogate for the observed kinematic velocity dispersion (Leier 2009). Thus,

$$\frac{E_1}{E_2} = \frac{2GM_{\rm tot}}{\sigma^2_{\rm lens} r_1} = \frac{G\Omega_m \rho_c (1+z_1)^3 \frac{8}{3}\pi r_1^2}{\sigma^2_{\rm lens}} \tag{6.9}$$

using Eq. 6.4,

$$\frac{E_2}{E_1} \propto \frac{\sigma^2_{\rm lens}}{M_s^{2/3}}. \tag{6.10}$$

Therefore we get a quantity $E_1/E_2 \propto R_{\rm lens} \times M_s^{2/3}/M_L$ or $R_{\rm lens} M_s^{-1/3} f_s$. This is reminiscent of the Kormendy relation, except that it relates to three-dimensional rather than projected densities. For definiteness, we assume a formation redshift $z_1 = 5$, but the value only implies a multiplicative constant. Plotting the energy ratio against the stellar-mass fraction we find a strong correlation (Fig. 6.14) regardless of the enclosure radius. The slope changes only marginally, but the scatter decreases with increasing radius.

However, E_2/E_1 appears to be uncorrelated with the enclosed stellar and total mass. For different radii one obtains Fig. 6.15. The fact that E_2/E_1 exhibits such a tight correlation with f_s, but no clear correlation to contributing masses, can be interpreted as

insensitivity of the star formation in early-type galaxies to active evolution processes over the time span from z_1 to $z_{\rm lens}$.

6.7 Discussion

A resolved, model-independent and thus non-degenerate (with respect to M_s and M_L for fixed f_s) estimate of stellar versus total mass within galaxy halos is crucial to constrain current galaxy formation models and prescriptions of baryon-dark matter interactions used therein. Besides dynamical methods to explore scales below 10 kpc, the combination of strong gravitational lensing and population synthesis used in this study is most promising to give robust estimates of stellar-mass fractions.

The analysis of the radial dependence of the mass profiles of 21 CASTLES lenses presented in this work allows us to draw the following conclusions. The relations between basic galaxy properties, i.e. M_L, M_s and $R_{\rm lens}$ cannot simply be scaled with their mass. The scatter in this parameter space turns out to be particularly large for galaxies of smaller size. The study of M_s versus M_L and of the stellar-mass fractions ($f_s \equiv M_s/M_L$) enables us to discriminate between lens galaxies below and above $M_L(< 2R_{\rm e}) = 4 \times 10^{11} M_\odot$. The high mass class populates a lower and narrower f_s regime (0.05 to 0.2) on scales studied here and runs out of stellar mass earlier (i.e. at lower enclosed radius) than low mass lenses. Low mass lenses ($< 4 \times 10^{11} M_\odot$) exhibit a more inhomogeneous behaviour with a wider range in f_s (0.1 to 0.5) and respective slopes.

We conclude that between 1.5 and $2.5R_{\rm e}$, dark matter halos start to dominate the matter balance depending on their total enclosed mass $M_L(< R)$. This $M_L(< R)$-dependence causes high mass galaxies to gain mass primarily in the form of dark matter already at lower radii than low mass galaxies. Therefore the slope of the mass-to-light relation, which is a projection of the fundamental plane — or our equivalent representation, $M_L^\eta \propto M_s$ — becomes shallower with increasing radius and asymptotically approaches a slope of $\eta = 0.76 \pm 0.07$. Thus, the FP tilt can be recovered as a gradually growing process with radius. Equivalently, the stellar-mass fraction shows a strong correlation with the total mass. As we contrast $f_s(M_L)$ with a comparable curve deduced by abundance matching from Guo et al. (2010) dissimilarities for low M_L galaxies become more evident the smaller the enclosed region gets. This is likely to be a result of different halo definitions, physical properties and processes, like baryon-dark matter interactions and adiabatic contraction, which is beyond the scope of the aforementioned study. However, the f_s-to-$M_{\rm halo}$ relation scaled down to $4R_{\rm e}$ agrees quite well with lenses with $M_L \sim 10^{12} M_\odot$, since the biggest part of stellar matter is still enclosed.

Another important result of this study addresses the concentration of stellar ($c(M_s)$) and total ($c(M_L)$) mass profiles. The rule-of-thumb delimiter of $c = 2.6$, which separates early-type galaxies ($c > 2.6$) from late-types $c < 2.6$), holds also for the concentration parameter ($c(M_s)$) defined by means of stellar mass instead of luminosity. In the low mass regime $M_L(< 2R_{\rm e}) \lesssim 4 \times 10^{11} M_\odot$ both, $c(M_s)$ and $c(M_L)$, tend to similar values around 2.6. This means that the total mass profile is likely to be influenced by the distribution of baryonic matter in stars. From $10^{11} M_\odot$ upwards, $c(M_s)$ and $c(M_L)$ diverge, due to a stronger confinement of stars in more massive dark matter halos. The $c(M_L)$ values above

$4 \times 10^{11} M_{\odot}$ remain around ~ 2 instead. Studying the interdependency of density slope and $c(M_L)$ we find that the reconstructed lens profiles show deviations from a pure power-law mass model, which is evidence for the sensitivity to the radial trends of the dark matter distribution. Furthermore, we analyze the evolution process of our lens galaxies considering their total kinetic and potential energy at collapse time and at their observed redshift. We find a tight correlation between the energy ratio and stellar baryon fraction, which can be interpreted as an insensitivity of star formation to active evolution, such as mergers.

The findings of this chapter are of many-faceted interest in the field of structure formation. Besides its implications on FP studies, resolved stellar and total mass profiles can be used to constrain interaction processes between dark matter and baryons. Furthermore, extrapolating obtained mass profiles to the virial radius permits to address models of structure formation by means of the concentration to virial mass relation. Both will be discussed in the next chapter.

7
Diagnostics of Baryonic Cooling

The cooling of baryons is a necessary requirement for the formation of stars. As baryonic gas falls into the potential wells of dark matter halos they interact gravitationally with the dark matter particles. The interaction is thought to lead to an increased concentration of the dark matter distribution, a process called adiabatic contraction (AC) explained in Section 2.7.

The concentration to virial mass relation states that more massive halos are less concentrated than less massive halos (see Sec. 2.6.3). Both, observations and numerical simulations agree on a power-law relation, $c \propto M_{vir}^{\alpha}$ with a negative index α. Using the enclosed mass profiles presented in the previous Chapter 6, we can extrapolate dark matter profiles probed in the range from 0.25 to 5 $R_{\rm e}$, to the virial radius. With this we produce a concentration to virial mass relation (Section 7.1) consisting of 18 lens galaxies of the CASTLES catalogue, a subset of the 21 lenses used in the previous chapter. We compare our results with abundance matching studies in Section 7.2.

Another application of our resolved stellar and total mass profiles is a test of AC prescriptions commonly used in simulations to model the baryonic content in dark matter halos in a semi-analytic manner, which is presented in Section 7.3. Moreover we investigate to what extent the c-M_{vir} relation is affected by AC. We finally summarize our findings in Section 7.4.

7.1 Virial mass and concentration

Having the enclosed total M_L (lensing) and stellar mass M_s information for 18 lens galaxies in a radial range from $0.25R_{\rm e}$ to several $R_{\rm e}$, we can safely assume

$$\Delta M(< R) = M_L(< R) - M_s(< R)$$

to consist largely of dark matter as all our lenses are early-type galaxies. Note that $\Delta M(< R)$ is computed as the difference of two profiles and not as the profile of the difference 'dark matter' map as shown Sec. 6.4. Both modes give, however, comparable results. Nevertheless, the mass difference $\Delta M(< R)$ is sufficiently close to a pure dark matter profile. We deliberately use the word "close" since the mostly elliptical density contours of the M_L- and M_s-maps do not necessarily show the same orientation. Nevertheless, larger discrepancies can be excluded, since firstly, the angle between respective orientations is rather small and secondly, the region where the surface mass contours are not matching is always far ($\gtrsim 2R_{\rm e}$) away from the centre of the lensing galaxy, that is where the dark

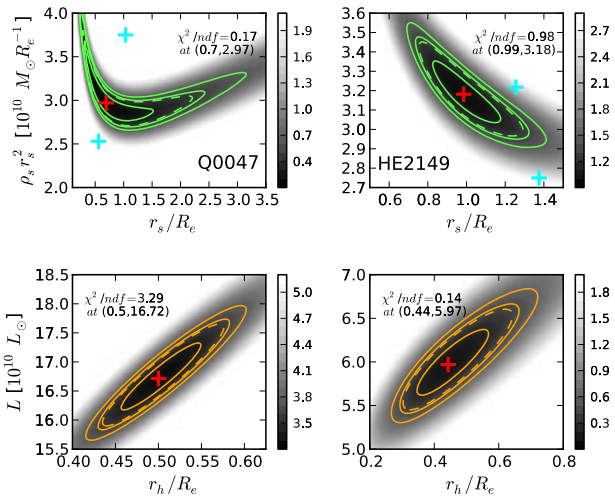

Figure 7.1: Top: χ^2 map of NFW parameter space with scale density ρ_s and scale radius r_s. Minima are indicated by red crosses. Fits to $\Delta M \pm \delta M_L$ are marked by cyan crosses. Solid contour lines indicate from centre outwards 1-3σ regions for one degree of freedom, the dashed contour a 1σ region for two degrees of freedom. Bottom: As in top panel, but for sought-after Hernquist parameters, i.e. luminosity L versus Hernquist scale radius r_h, and without cyan crosses.

matter contribution to the total mass is dominant. Furthermore, a significant contribution of baryonic matter from a gaseous component can be excluded for all lenses, since our lensing sample contains only early-type galaxies. Note that for this reason we excluded the Einstein Cross (Q2237), which is the bulge of a spiral galaxy, and B1600, which is likely to be a late-type galaxy viewed edge-on from the sample introduced in Section 4.2 used in Chapter 6. Furthermore we omit B1608 in this study due to a second merging component contributing to the lensing effect. All three excluded lenses were shown to be outliers already in Sections 6.5 and 6.6.

To find most likely NFW profiles, which agree to $\Delta M(< R)$ we use the doubly integrated NFW-profile (projected and cumulative) of Eq. 2.50 as the underlying fitting model. It gives the mass enclosed in a cylinder of radius r, depending on the scale density ρ_s and scale length r_s. Subsequently we calculate the reduced-χ^2 map of the parameter space shown exemplarily for the two lenses Q0047 and HE2149 in the top row of Figure 7.1. Note that the bottom row will be discussed in Section 7.3, but is already placed here for better comparison. The uncertainties are determined by $\sigma = \sqrt{\delta_{M_L}^2 + \sigma_{M_s}^2}$, where δ_{M_L} is half of the 90% confidence interval given by the ensemble of lens mass models and σ_{M_s} the standard deviation of stellar mass from population synthesis. The χ^2 maps for the whole lens sample are given in Fig. A.4 of the appendix.

Previous Markov-Chain Monte-Carlo (MCMC) runs[1] helped to constrain the parameter region, which shows already the isolation of the minima. Thus the possibility of several

[1] 100, 000 MC realizations each lens, with a conservative burning rate of 50% and thinning by taking every fifth trace point.

distinct minima can be excluded for physically reasonable parameters. The red crosses in Fig. 7.1 indicate the position of minimal χ^2.

Despite the ostensible disadvantage of *non*-normally distributed errors one may take advantage of the χ^2 procedure to quantify the probability distribution of parameters by means of constant $\Delta\chi^2$ contours as a boundary of the confidence region. The respective error contours for $1-3\sigma$ considering one degree of freedom are shown in Figure 7.1 as solid contours, whereas the 1σ region considering two degrees of freedom is indicated by a dashed contour. The bottom panels show respective χ^2 maps for the parameters of a projected Hernquist profile fitted to the stellar mass profiles. We will make use of latter results in Section 7.3.

To demonstrate the validity of the χ^2 error regions we include (ρ_s,r_s) values found to nicely fit the upper and lower limits of the lens mass errors within σ_{M_s}, as indicated by cyan crosses in the top panels of Fig. 7.1. Note that the ordinate of the χ^2 plots is given in terms of $\rho_s r_s^2$ and in units of $M_\odot R_e^{-1}$ to allow for conveniently probing the parameter space. Plotting ρ_s versus r_s instead gave a much thinner elongated valley in the χ^2 plane, which makes the determination of an optimal χ^2 within preferably small errors rather difficult.

In the top panels of Figure 7.2, we show corresponding original $\Delta M(<R) = M_L(<R) - M_s(<R)$ profiles (blue circles), together with best fits to the median profile (solid red line) with respective 1σ errors (grey shaded region) as well as best fits to the error limits (solid green lines). As before we neglect the bottom panels, which are placed here for comparison, but return to them later in Section 7.2. Note that the 1σ region corresponds to the dashed contour shown in Figure 7.1. The results of the parameter search can be found in Table C.4. The inflexibility of Eq. 2.50 causes the innermost data point to deviate in some cases significantly from the fit. Steeper density slopes towards the core region of halos are expected from simulations (Moore et al. 1998, Navarro et al. 2004, Diemand et al. 2005). As a result of baryon-dark matter interaction such as adiabatic contraction and their hard to quantify impact on the mass profile, latter results often tend to disagree with observations. This is suggestive of a generalized NFW (gNFW) being a more appropriate description of $\Delta M(<R)$. Cardone et al. (2011) show that under the assumption of a $c - M_{vir}$ relation a gNFW can mimic the one-parameter family of the secondary infall model, which nicely describes cored and cuspy dark matter profiles. However, as it is our aim to investigate the $c - M_{vir}$, we need to use two-parameter profiles. Since our mass profiles show only mildly steeper slopes within uncertainties, we consider NFW profiles a good description of the dark matter profile. We will address this issue later on in Section 7.2.

For now, let us assume a projected NFW depending on scale radius r_s and the normalization ρ_s to sufficiently describe the data. We extrapolate the profile to the virial radius $R_{\rm vir}$, defined as the radius for which the mean enclosed density is equal to a multiple (Δ_c) of the critical density $\rho_c(z)$, i.e. $\langle\rho(R_{\rm vir})\rangle = \Delta_c\rho_c(z)$. Hence we compute concentration values $c_{vir} = R_{\rm vir}/r_s$ and the virial mass M_{vir} (Eq. 2.38), defined as the Mass enclosed in a sphere of radius $R_{\rm vir}$, according to the procedure described in Sec. 2.6.3.

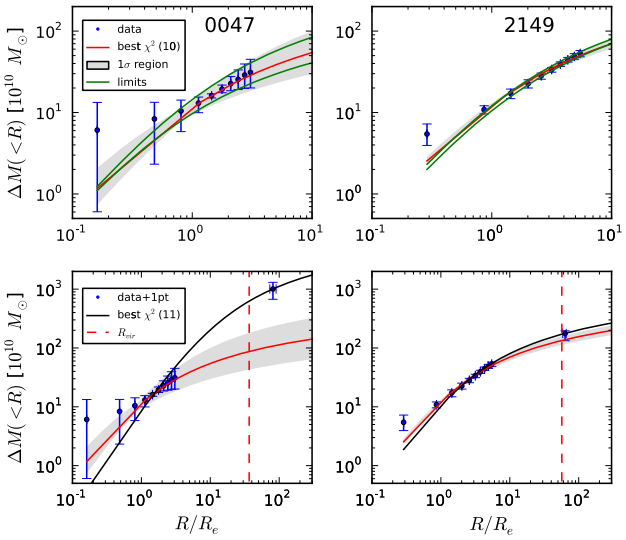

***Figure 7.2*:** Examples of disagreement and agreement with abundance matching. The grey region and the red and green curves relate to an NFW fit to the lensing region. The outermost point in each case is from abundance matching. The black curves are NFW fits that include the outermost point. The vertical dashed red line indicates $R_{\rm vir}$ as deduced from our lens data only.

Plotting c_{vir} against M_{vir} yields Figure 7.3. The red circles indicate our lens sample. The errors are calculated according to the projected 1σ regions of Figure 7.1. All quantities are given in Table C.4. There is no data yet available showing this relation to such small virial masses.

We compare our data with results from a study by Buote et al. (2007) of the X-ray $c - M_{vir}$ relation for 39 galaxy systems (grey dots in Fig. 7.3) which cover a range from 6×10^{12} to 2×10^{15} $M_\odot$. They find that a power-law fit to data using

$$c = \frac{c_{14}}{1+z}\left(\frac{M}{M_{14}}\right)^{\alpha} \tag{7.1}$$

yields a slope of $\alpha = -0.172 \pm 0.026$. The constants c_{14} and M_{14} indicate that all mass quantities are normalized to $10^{14} M_\odot$. Neglecting the $1 + z^{-1}$ term in Eq. 7.1 and consequent fitting yields $\alpha = -0.20 \pm 0.03$. Note that in some recent studies, $(1+z)^{-\beta}$ is used instead of $(1+z)^{-1}$, which introduces β as a new fit parameter (Duffy et al. 2008, Schmidt & Allen 2007). However, most studies based on observations keep $(1+z)^{-1}$ fixed or drop it if the sample is considered local. As done by Buote et al. (2007), we use a bivariate fitting method for correlated errors and intrinsic scatter (hereafter BCES) by Akritas & Bershady (1996) to see if the result is recoverable for our low-M_{vir} sample. Figure 7.3 shows that the projected 1σ contours cover a smaller region than x- and y-errors only would suggest, which means that there might be more information included accessible by appropriate tools. To contrast different approaches, we employ above BCES method (Bivariate fit for data with correlated errors and scatter) and compare its results with a bootstrapping study, sampling only in the 1σ regions. By BCES we find a slope of $\alpha = -0.40 \pm 0.06$. Normalizing by $(1+z)^{-1}$ as in Eq. 7.1 yields a marginally changed

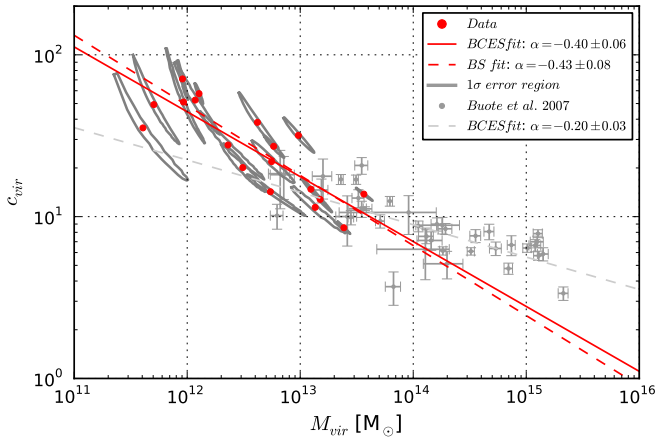

***Figure 7.3*:** Concentration versus virial mass. The red dots represent data from this study. Data from Buote et al. (2007) is marked by grey dots. The grey contours show the 1σ error region from Fig. 7.1. The red dashed line shows a bootstrapping fit to the red dots. The solid red line shows the result of a bivariate fitting method for correlated errors and intrinsic scatter (BCES) by Akritas & Bershady (1996) applied to our data (red dots) only. The same method was used by Buote et al. (2007) to obtain the dashed grey line. The result of a fit to the combined sample, i.e. red and grey dots, is presented in Table 7.1.

slope of $\alpha = -0.38 \pm 0.06$.

Our bootstrapping analysis yields $\alpha = -0.42 \pm 0.08$. We employ a piecewise analysis (fitting the relation in mass intervals) to check how the slope α of the relation evolves and to see whether fits in common mass range yield same results. Furthermore we fit a combined sample of 57 objects. The results are shown in Table 7.1.

Going from high to low M_{vir}, the slope increases from -0.103 ± 0.055 for $M_{vir} > 10^{14} M_\odot$ to -0.201 ± 0.129 for $M_{vir} < 10^{14} M_\odot$ (for data from Buote et al. (2007)) and finally -0.401 ± 0.064 for $M_{vir} < 4 \times 10^{13} M_\odot$. For the mass range between 6×10^{12} $M_\odot$ and 1×10^{14} $M_\odot$, where the two samples overlap, we do not find significant differences. However, it should be noted that the reduced sample size and considerable scatter leads to large errors for both samples. A two dimensional Kolmogorov-Smirnov test for the overlapping region gives a probability of $\sim 44\%$ that the lensing and X-ray sample are drawn from the same population. Despite this inconclusive result we use a Monte Carlo approach to draw random-subsamples of the size of the lensing sample from the X-ray sample and computing respective KS-probability shows that $\sim 90\%$ of the $100,000$ realized sub-samples would yield a probability $\lesssim 44\%$ to match the parent population.

Going back to the total virial mass range, a trend of α with virial mass was first suggested by Navarro et al. (1996) and confirmed by Bullock et al. (2001) and Eke et al. (2001) for simulations. Higher normalization factors compared to simulations are also known from a lensing study by Comerford & Natarajan (2007).

Up to now, we computed the $c - M_{vir}$ in the belief that

Sample	Size	Method	M_{vir}-range $[10^{14} M_\odot]$	α	σ_α	c_{14}	σ_{c14}
B07	39	BCES	$0.06 - 20$	-0.199	0.026	9.12	0.43
B07	22	BCES	> 1	-0.103	0.055	7.71	0.58
B07	17	BCES	< 1	-0.201	0.129	9.46	2.11
c_{vir}	18	BCES	$0.004 - 0.4$	-0.401	0.064	7.03	1.49
c_{vir}	18	BS	$0.004 - 0.4$	-0.433	0.078	6.6	$^{+33.1}_{-6.2}$
c_{vir}	9	BCES	> 0.06	-0.203	0.172	16.98	12.87
comb	57	BCES	$0.004 - 20$	-0.278	0.021	9.62	0.41
$B07_0$	39	BCES	$0.06 - 20$	-0.172	0.026	9.0	0.4
$c_{vir,0}$	18	BCES	$0.004 - 0.4$	-0.381	0.062	12.02	2.57
$CN7_0$	62	N/K	$0.4 - 100$	-0.15	0.13	10.68	5.50

***Table 7.1*:** Slope α of the $c - M_{vir}$ relation with uncertainty for different samples, sample sizes, fitting methods and mass ranges (all errors 1σ, c_{14} errors are 68% confidence interval around median). B07 denotes the sample of massive early-types in Buote et al. (2007), c_{vir} stands for the relation as in Fig. 7.3, *comb* gives the combined sample fit consisting of 39 objects of B07 and 18 lenses of the above c_{vir} sample, CN7 are results from Comerford & Natarajan (2007). The index 0 to a sample name denotes concentrations normalized with $(1+z)^{-1}$.

1. an NFW profile is a good representation of the dark matter profile beyond the radial range probed for the lens galaxies in Chapter 6,

2. the dark matter profile is well constrained by pixelated studies of stellar and total mass, meaning also that the probed radial range is sensitive to the scale radius of the NFW profile and that the given uncertainties are a fairly well estimate of suitable mass distributions.

In the next section, we compare the quantities extrapolated to the virial radius with predictions using both simulations and SDSS observations.

7.2 Comparison with abundance matching

So far, we found the scale parameters for our sample of lenses by extrapolating a best fit projected NFW to the virial radius. Abundance matching studies like Moster et al. (2010) and Guo et al. (2010) make use of cosmological simulation and galaxy surveys to determine the mass dependence of galaxies and their preferred host halos. The stellar mass enclosed in a $2R_{\rm lens}$ aperture is known from population synthesis shown in Chapter 6. Beyond $2R_{\rm lens}$, the stellar mass profiles do not change by much. Thus, we use the M_{halo}-to-M_s relation from Moster et al. (2010) to infer a virial mass and a 1σ uncertainty region. Consider the bottom panels of Fig. 7.2 showing the examples Q0047 and HE2149. As before the red line represents the best χ^2 fit to data only. In contrast to the upper panels we have one more data point which is the one inferred from abundance matching (hereafter M_{vir}^{AM}). The best fit of a projected NFW to the data plus the latter point (11 data points in total) is indicated by the black solid line. Together with the slope of the inner profile ($< r_s$), the radius of the turn-over itself increases. The virial radius of the black line is the position of M_{vir}^{AM}, whereas the previously deduced $R_{\rm vir}$ of the lensing data is indicated by the vertical dashed red line. In Fig. A.6 of the appendix, we provide Fig. 7.2 for the whole sample. As it turns out for 10 out of 18 lenses, M_{vir}^{AM} lies within the 1σ error region (grey shaded) around the extrapolated data (best $\chi^2(10)$). For the 18 lenses of our sample, $R_{\rm vir}$ changes mostly by a smaller factor than r_s. Hence adding

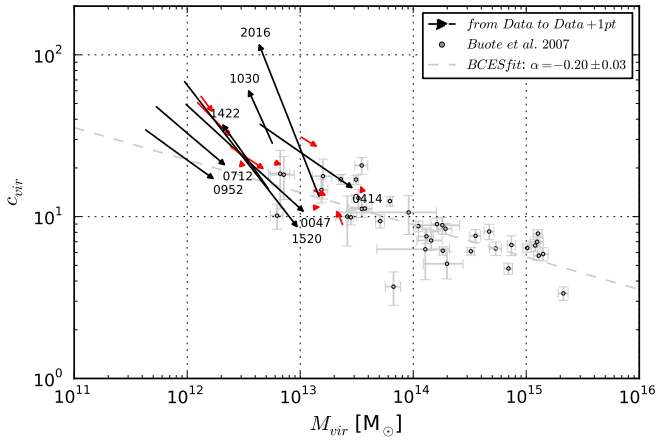

***Figure 7.4*:** Similar to Fig. 7.3, but showing how the fits change when abundance matching is included. The arrows go from the original position (red dots in Fig. 7.3) to the position for which the parameters include information on virial mass from Moster et al. (2010). Arrows highlighted in red mark lenses for which an extrapolated NFW suffices the expectations of M_{vir}.

M_{vir}^{AM} to the mass profile causes c_{vir} to decrease for most lenses. The result is illustrated in Fig. 7.4.

The arrows point from the old best fit values (M_{vir},c_{vir}) to the new ones. It should be noted that the best χ^2 fits to the profiles extended by M_{vir}^{AM} are all worse than the previous. The eight lenses with M_{vir}^{AM} that do not match the simple extrapolation exhibit the highest χ^2 from fits to the extended data. Subsequently, due to the large errors on M_{vir}^{AM}, the 1σ error region is highly extended and does not allow for one-by-one study. Nevertheless, Fig. 7.4 gives an impression of the expected overall trend if we impose constraints from abundance matching. In this plot, we highlight the ten arrows for profiles extending to the expectations from abundance matching in red and label the remaining black arrows to allow for a better comparison with Fig. A.6 in the appendix. Among the latter there are three lenses (MG2016, B1422, B1030) with a notably large upwards shift, i.e. toward higher concentrations. These are lenses for which M_{vir}^{AM} lies significantly below the extrapolation. For MG2016 M_{vir}^{AM} is even smaller than $\Delta M(< R)$ at the outermost radius. All three have reconstructed mass profiles with small uncertainties only.

So what is the reason for this discrepancy? As it appears, there is a strong correlation between the length of arrows and the environment of the lenses. MG2016 and B1422 belong to large groups or clusters with many nearby galaxies (see Table C.2 in the appendix). All eight lenses not conforming with M_{vir}^{AM} are in dense environments, whereas for six out of ten remaining conform lenses as yet no nearby objects are known.

As seen in Section 6.1, multi-component model fits yield nice agreement with the total mass content of a lens but overestimate the stellar mass if not sufficiently constraint. Thus, the dark matter content is underestimated which leads to an even more severe discrepancy in the majority of cases, even though the mismatch between abundance matching and extrapolation for the lenses MG2016, B1422 and B1030 will get slightly reduced.

The root mean square deviation ($RMSD$) with respect to the simple power-law best fit almost doubles from 0.145 (lens data only) to 0.258 (lens data + M_{vir}^{AM}). The B07 sample

gives $RMSD \simeq 0.180$. A mildly increased scatter can be found in simulations by Shaw et al. (2006) for virial masses between $\sim 3 \times 10^{13}$ and $\sim 10^{15} M_{\odot}$, which is most likely due to the indistinguishability between substructure and main halos. This, however, cannot explain the increased $RMSD$. From this we can conclude that the extrapolation to R_{vir} inferred in Section 7.1 gives a reasonable extension to the $c - M_{vir}$ relation. Given stellar mass, the $M_{halo}(M_s)$ relations of Moster et al. (2010) and Guo et al. (2010) fail to recover virial masses in agreement with expectations from $c - M_{vir}$ studies for a smaller fraction of lens galaxies. This may most likely be attributed to the simplistic halo definition and the influence of the environment (external convergence). An underestimated scatter of the abundance matching might also have a non-negligible influence.

In the following section, we want to assess to what extend the $c - M_{vir}$ relation is caused by adiabatic contraction of the halo.

7.3 Adiabatic contraction

The concentrations deduced in Section 7.1 represent the state of the halo after adiabatic contraction (AC). There are reasonable doubts that AC contributes significantly to the steepness of the density profile (Abadi et al. 2010). Hence the impact of AC on dark matter profiles might be overestimated by commonly used recipes for baryonic cooling. To analyze this issue, we make use of a halo contraction program by Gnedin et al. (2004) which computes the change of a dark matter profile caused by condensation of baryons in the centre of the halo by keeping $rM(< r)$ conserved. To take account of a wide range of orbit eccentricities, the code invokes the power-law

$$\bar{r}/R_{\rm vir} = A(r/R_{\rm vir})^w \tag{7.2}$$

to describe the mean relation between orbit-averaged $\bar{r}$ and current radius r and modifies the adiabatic invariant to $rM(< \bar{r})$. The case $A = w = 1$ corresponds to the original prescription of Blumenthal et al. (1984) where the orbits are assumed to be completely radial. This case can be understood as an upper limit to AC. The program provides the necessary resolution for comparison with our data, i.e., down to $10^{-3} R_{\rm vir}$. Input parameters are the baryon fraction f_b enclosed within $R_{\rm vir}$, the baryon scale length (e.g. Hernquist scale radius) and the concentration of the dark matter profile before contraction. We define the baryon fraction to be $M_s(< 2R_{\rm lens})/M_{vir}$, where $M_s(< 2R_{\rm lens})$ denotes the stellar mass enclosed in the total reconstructed radial range. For M_{vir}, we use the values given in Table C.4, for which Eq. 2.38 was used. For the distribution of stellar matter we assume a Hernquist profile and give r_h as an input parameter. Since population synthesis delivers the stellar mass profile (see e.g. Fig. 6.4), sought-after scale length can be determined as before by profile fits. Searching for minimal χ^2 parameters M/Υ (luminosity) and r_h (scale radius) in the projected cumulative Hernquist profile (Eq. 2.43) yields – as in the NFW case – a degenerate parameter space, shown in the bottom panels of Fig. 7.1 for Q0047 and HE2149, but this time with more concentrated probability contours. The reason for this is that the cumulative stellar mass profiles contain $\sim 100\%$ of stellar mass, whereas in case of $\Delta M(< R)$ only $\lesssim 30\%$ of the virial mass are enclosed. In other words, for the NFW-fit we use data which sparsely samples the DM profile. For a Hernquist-fit, the scale radius r_h falls well in the radial range covered by our data. It is important to note that the effective radius can be determined for any Hernquist profile using the simple relation $R_{\rm e} \approx r_h \times 1.8153$ first shown by Hernquist (1990). Nevertheless we leave r_h as a

fit parameter for several reasons. Firstly, we do not expect the Petrosian effective radius (see Section 3.2.4) to agree precisely with the half-light radius of Hernquist profiles. It is worth noting that a certain radius R corresponds to the mean of semi-minor and semi-major axes, which define the ellipse enclosing $M(< R)$. Secondly, the Hernquist profile is originally used for light profiles, but in here, we fit to mass profiles. The $r_h/R_{\rm e}$ best-fit values turn out to be mostly lower but close to 1/1.8153. The χ^2 maps for the whole lens sample are given in Fig. A.5 of the appendix.

All fit parameters and $R_{\rm vir}$ are given with 1σ errors in Table C.4. The dark matter profile before contraction is assumed to be an NFW profile with initial concentration c_{init}. We run the contraction routine for a grid of parameters (c_{init}, f_b, $r_h/R_{\rm vir}$) ranging from $(5, 0.005, 0.001)$ to $(60, 0.135, 0.015)$ in steps of $(1, 0.01, 0.002)$. The obtained adiabatically contracted halo profiles should resemble the ones probed in Chapter 6 in case the impact of baryonic cooling is not overrated. We fit Eq. 2.49 to the contracted profiles in a radial aperture between ~ 0.006 and $0.12R_{\rm vir}$ which represents an upper limit for the radial range our mass profiles are probed in. The values for $2R_{\rm lens}/R_{\rm vir}$ are given in Table C.4.

There are a number of uncertainties entering the analysis:

1. since the radial extent of a reconstructed profile is limited to two times the angular $R_{\rm lens}$ and a finite resolution, the aperture size changes from lens to lens,

2. in order to mimic the limited probed range one needs to convert the aperture size from $R_{\rm lens}$ to $R_{\rm vir}$,

3. baryon fraction as well as baryonic scale length depend on M_{vir} and $R_{\rm vir}$ which are extrapolated quantities with respective uncertainties.

To study how sensitive our results are to the radial range we discuss later on in this section the case of aperture sizes significantly reduced with respect to the one assumed for the synthetic profiles.

The top panels of Figure 7.5 show the results of the grid for AC according to Blumenthal et al. (1984) ($A = 1.0$, $w = 1.0$, i.e. no correction for anisotropic orbits). The left hand panel shows initial versus final (contracted) halo concentration. For fixed values of f_b and $r_h/R_{\rm vir}$, we provide $c_{vir,final}(c_{init})$ indicated by the solid blue line. The growing concentration towards low c_{init} is a consequence of the interplay between radial aperture and the region affected by AC. The smaller the initial concentration the larger $c_{vir,final}/c_{init}$ towards small radii for same f_b (we refer to this as the *AC-sensitive case*). As c_{init} increases, the difference between final and initial profile subsides. The farther out our radial aperture, the less affected is the fit and the extrapolation. However, for different combinations of f_b and $r_h/R_{\rm vir}$ similar curves fill the whole grey-shaded region. To enable proper differentiation with respect to the initial concentration we choose different shades of grey in all panels. The middle panel shows the final concentration versus baryon fraction. The grey shaded region consists again of our grid points which have counterparts in the left and in the right panel. If no upper limit to the grey region is shown, its $c_{vir,final}$ values exceed 120. The black dots with error bars represent our data. The right hand panel shows, as in the middle panel, the comparison between generic contracted halos and data, but depending on $r_h/R_{\rm vir}$. Middle and right panel clearly show disagreement

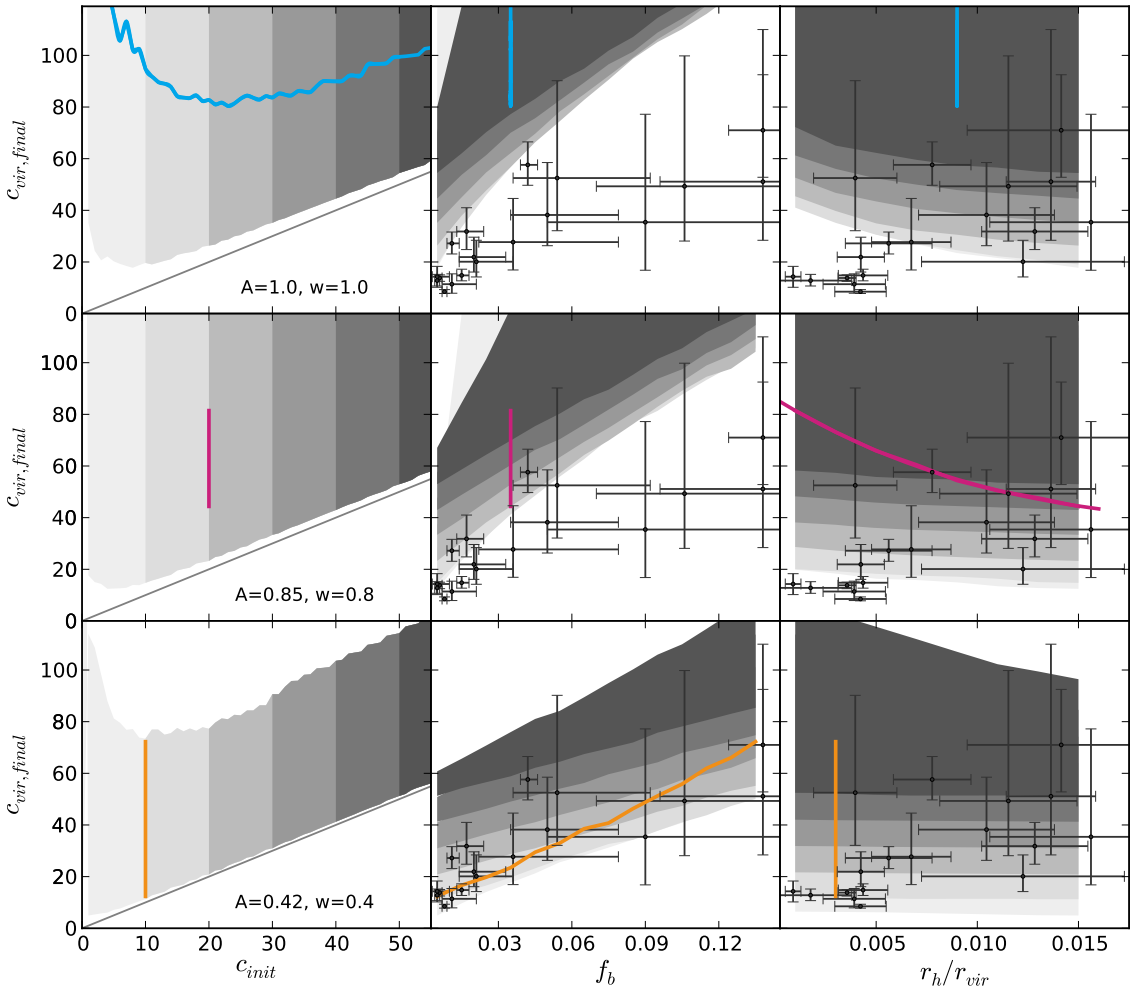

***Figure 7.5*:** Left column: final versus initial concentration for the given grid of input parameters. Different grey-shades indicate different c_{init} bins. The grey solid line indicates $c_{final} = c_{init}$. Middle column: As before the grey-shades indicate different $c_{final}(f_b)$ region according to the c_{init} bins. Our sample of lenses is indicated by black dots with error bars. Right panel: As in middle panel, but plotted against $r_h/R_{\rm vir}$. Top row: Adiabatic contraction according to Blumenthal et al. (1984). The blue line indicates all values of c_{final} with fixed $f_b = 0.035$ and $r_h/R_{\rm vir} = 0.009$. Middle row: AC according to Gnedin et al. (2004), which make use of Eq. 7.2 with $A = 0.85$ and $w = 0.8$ to take account of anisotropic orbits. The magenta line indicates all values of c_{final} with fixed $c_{init} = 20$ and $f_b = 0.035$. Bottom row: As before, but with $A = 0.42$ and $w = 0.4$ instead. The orange line indicates all values of c_{final} with fixed $c_{init} = 10$ and $r_h/R_{\rm vir} = 0.015$.

between observationally inferred and contracted profiles. Especially the low-f_b and low $r_h/R_{\rm vir}$ regions show significant departure from even lowest final concentrations of the generic halos.

The middle row of Figure 7.5 shows the AC according to Gnedin et al. (2004), which implements Eq. 7.2 with fiducial values $A = 0.85$ and $w = 0.8$ to take account of eccentric orbits. This phenomenologically motivated fudge-formula leads to much smaller concen-

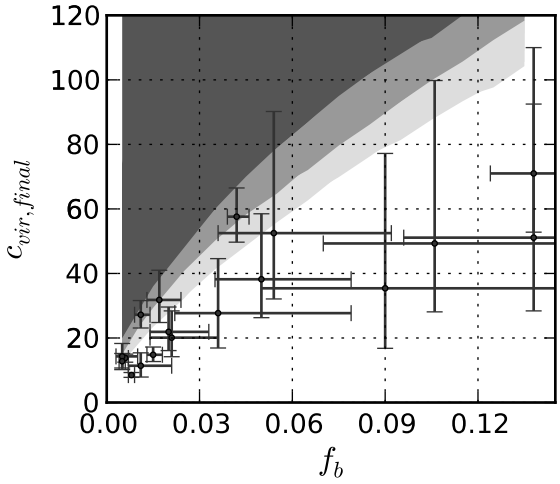

***Figure 7.6*:** Final concentration versus baryon fraction depending on size of radial window. Bright to dark grey corresponds to aperture sizes $(\sim 0.003-0.06)R_{\rm vir}$,$(\sim 0.005-0.09)R_{\rm vir}$ and $(\sim 0.006-0.12)R_{\rm vir}$. The latter range is the default case used for Fig. 7.5. The smaller the probed radial range, the less concentrated the fitted NFW profile, but even for the smallest aperture size a fraction of lenses falls significantly below the region.

trations. Still, there is significant disagreement between data and simulated contraction. The middle and right panels still show few lenses being not in agreement with any model in the investigated parameter space. The behaviour of $c_{vir,final}$ as a function of $r_h/R_{\rm vir}$ for constant $c_{vir,final}$ and f_b is indicated by the solid magenta line.

For the bottom panels of Figure 7.5, we changed the pre-defined values of A and w to 0.42 and 0.4, respectively. The orange line shows for fixed c_{init} and $r_h/R_{\rm vir}$ the final concentration as a function of f_b. These values for A and w allow even for low c_{init} between 1 and 10 good agreement with lens data. Compared to top and middle row, the range of final concentrations is much smaller, corresponding to a much shallower $c_{vir,final}$-f_b relation (middle panels). One of the intriguing results of this study is that even the simple assumption of a common mass independent initial concentration explains most of the final concentrations if (A,w) are conveniently adjusted and r_h is allowed to vary within uncertainties. There are a variety of minor results we summarize in the following.

- There is slight evidence for lenses with lower baryon fraction to require higher initial concentrations.

- Both smaller c_{init} and smaller $r_h/R_{\rm vir}$ produce steeper $c_{vir,final}(f_b)$ curves. This effect is independent of the AC-sensitive case at very low c_{init} explained above.

- As A and w are reduced, $c_{vir,final}(f_b)$ and $c_{final}(r_h)$ become flatter, i.e. the differently shaded c_{init} regions of the left panel are mapped to narrower regions in middle and right panel. Moreover, their overlap is reduced.

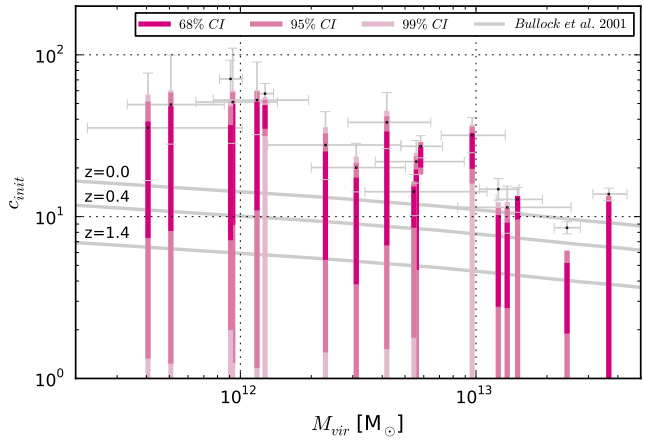

***Figure 7.7*:** As in Fig. 7.3, but with initial concentrations. The colours of the columns from dark to bright correspond to the 68%, 95% and 99% confidence intervals of a range of (c_{init}, f_b, $r_h/R_{\rm vir}$) values which produce a c_{final} in agreement with our data. For comparison we include $c_{final}(M_{vir})$.

We also study how sensitive our results are to the radial range (aperture size) chosen for the profile fits to the synthetic contracted profiles. Assuming reduced aperture sizes of $(\sim 0.005 - 0.09)R_{\rm vir}$ and $(\sim 0.003 - 0.06)R_{\rm vir}$ in Fig. 7.6, we find that even the smallest ranges do not yield agreement with our lens data. Larger radial apertures are unlikely as we chose already the largest size among our lens profiles.

If we compare the number of different (c_{init}, $r_h/R_{\rm vir}$) combinations producing final concentrations in agreement with our lens data, we can infer a c_{init}-M_{vir} plot as before, enriched by the information of the frequency distribution of initial concentrations (see Fig. 7.7). Although most of the data can be reproduced even by few initial concentrations of ~ 1, most of the (c_{init},$r_h/R_{\rm vir}$) combinations with high c_{init} produce final concentration in agreement with c_{final} and f_b. The hue of the magenta column indicates the frequency distribution of c_{init} values whereas the 68% (99%) confidence interval is highlighted by strongest (faintest) colour.

Certainly, no strong quantitative conclusions can yet be drawn from these results, but judging by the confidence regions a strongly flattened $c_{init}(M_{vir})$ relation seems likely. A flattened low-mass end of the $c-M_{vir}$ relation is expected by simulations. To show this we include $c_{init}(M, z)$ curves in Fig. 7.7 based on a toy model by Bullock et al. (2001). They find the curves to be in good agreement with results from N-body simulations. The toy model includes the free parameter K, which takes account of the contraction of the inner halo beyond that required by the top-hat formation scenario. This contraction parameter is fixed for all halos in their simulation. The difference between simulated and observed $c - M_{vir}$ is a well-known issue and matter of ongoing studies. It is however worthwhile to mention that this discrepancy is even stronger for low M_{vir}. From the comparison between c_{init}-M_{vir} found in this study and simulations which investigate the redshift-dependence we can conclude that AC alone is not enough to explain the slope of the relation.

7.4 Conclusion

We show that pixelated mass reconstruction for two component lenses yield different results for enclosed mass quantities. As a result of a model-independent mass-reconstruction approach, we are able to recover a c-M_{vir} relation by means of extrapolated NFW fits. For the majority of lenses, this relation appears to be in agreement with virial mass predictions from abundance matching studies M_{vir}^{AM} (Moster et al. 2010, Guo et al. 2010). Departures from latter predictions appear to be well-explained by environmental effects, such as external contribution to convergence, but may also be related to differing halo definitions or an underestimated error of M_{vir}^{AM}. It is, however, surprising that concentrations of profiles forced to fit M_{vir}^{AM} lead to a significantly increased scatter around the best-fit power-law for the c-M_{vir} relation and a strong disagreement with previous studies of this type. An analysis of recent prescriptions for baryonic cooling shows that the parameters (c_{final}, f_b, $r_h/R_{\rm vir}$) inferred by data fits lie significantly below even the lowest concentrations achievable with standard adiabatic cooling prescriptions. By tweaking the spherically averaged radius even stronger than intended by Gnedin et al. (2004) we find better agreement with our data. The much shallower $c_{final}(f_b)$ compared to standard AC prescriptions can be translated in a quantity indicating mass loss. Furthermore, a c-M_{vir} type study for initial concentrations leads to the conclusion that AC has a minor impact on the overall slope of the relation, but could reproduce the flattening for low virial masses.

8 Conclusion and Outlook

The findings of this work are mainly based on free-form modeling of gravitational lenses and stellar population synthesis (Section 3.2) and tackle a wide range of astrophysical problems. They give important insights in the build-up of lens galaxies and point out several misconceptions in current research. The results may also serve as benchmarks for large scale simulations, studies of the initial mass function, baryon-dark matter interactions and the modeling of strong gravitational lenses. In particular we can contribute to research in galaxy formation and evolution with our studies of the fundamental plane, stellar baryon fractions, the concentration-to-virial-mass relation and baryonic cooling using both global and resolved estimates of light and mass distributions in lens galaxies, as summarized below.

The fundamental plane puzzle

Until a consensus on the explanation for the fundamental plane is found it is necessary to focus on quantities which are unequivocally related to a certain physical entity. For this purpose we introduce a formal velocity dispersion, $\sigma_{\rm lens}$, based on the reconstructed enclosed mass. The formal velocity dispersion turns out to be a fair representation of the kinematic velocity dispersion (Chapter 5) for the sample of 18 lens galaxies and two lens clusters introduced in Section 4.1. Independent of the details of lens models, the lensing masses and virial masses basically agree, verifying the virial theorem (Section 5.3). By using $\sigma_{\rm lens}$ as a surrogate for the kinematic velocity dispersion the slope of the mass-to-light relation can be recovered (Section 5.4). Moreover we find the mass-to-light relations for both lensing mass, $M_{\rm lens}^{0.70\pm0.08} \propto L$, and virial mass, $M_{\rm vir}^{0.80\pm0.10} \propto L$. Both exclude a constant M/L, consistent with most other fundamental plane type studies. The fundamental plane of early-type galaxies can thus be reproduced as $R \propto \sigma_{\rm lens}^{1.08} I^{-0.77}$. This rules out any attempted explanation invoking kinematics, such as orbital anisotropy (see e.g. Nipoti et al. 2002). We find no evidence for structural non-homologies. The relation between formal and kinematic velocity dispersion extends to cluster sized lensing objects within rather large uncertainties due to a poorly defined scale radius $R_{\rm e}$. However, galaxy clusters are far from the FP since they have a much higher dark matter fraction than early-type galaxies. So far, these results address the FP puzzle based on estimates of the integrated flux.

Using the combination of pixelated lens mass reconstruction and stellar population synthesis, we investigate resolved stellar and total mass profiles on scales from ~ 0.5 to 10 kpc (Chapter 6) for the sample of 21 lenses presented in Section 4.2. This permits a explore the parameter space spanned by enclosed stellar, $M_s(< R)$, total lens mass,

$M_L(< R)$, and radius R. We find that the $M_L(< R)$-to-$M_s(< R)$ relation, which can be viewed as a projection of the fundamental plane, approaches the slope of the FP tilt — equivalently represented by $M_L^{0.76\pm0.07} \propto M_s$ — gradually with increasing radius. This can be interpreted as evidence against variations of the stellar mass to light ratio as a possible reason for the tilt of the FP and shows that the slope can be understood as a consequence of a non-trivial relation between stellar and dark matter in fairly virialized, i.e. dynamically relaxed, galaxy systems.

Baryon fractions and dark matter concentrations

Some early insights into the set-up of lens galaxies can be given in terms of enclosed mass ratios (Section 6.5) and concentration indices for stellar and total mass profiles (Section 6.6). In particular we investigate stellar baryon fractions and their impact on dark matter halos in the range from 0.25 to $5R_{\rm e}$ and in some cases even up to $\sim 10R_{\rm e}$. A resolved, model-independent and thus non-degenerate (with respect to M_s and M_L for fixed f_s) estimate of stellar versus total mass within galaxy halos is crucial for constraining current galaxy formation models as well as the prescriptions of baryon-dark matter interactions they employ. Other than the dynamical methods used to explore scales below 10 kpc (e.g. Cappellari et al. 2006, Coccato et al. 2009), the combination of strong gravitational lensing and population synthesis is the most promising method for producing robust estimates of stellar-mass fractions, as motivated in Chapter 3.

In light of our FP studies it becomes clear that baryon physics and interactions between luminous and dark matter with a mass dependent efficiency appear to give a typical length scale to galaxies. By examining the M_s and M_L dependence on radial distance to the centre of each galaxy (Section 6.5) we find that there are pairs of lens galaxies on small to intermediate mass scales that, at large radii, approach the same values for their enclosed total mass but exhibit very different stellar masses and stellar baryon fractions ($f_s \equiv M_s/M_L$). This peculiar behaviour is not found in the most massive lensing galaxies. All the baryon fraction profiles show that the dark matter halo becomes more massive than the stellar content at a common radial range, between 1.5 and $2.5R_{\rm e}$, depending on the enclosed total mass. This $M_L(< R)$-dependence causes high mass galaxies to enclose mass primarily in the form of dark matter at lower radii when compared to low mass galaxies. We find evidence for a stellar baryon fraction steadily declining over the full mass range.

The study of M_s versus M_L and of the stellar baryon fractions also enables us to discriminate between lens galaxies below and above $M_L(< 2R_{\rm e}) = 4 \times 10^{11} M_{\odot}$. The high mass class populates a lower and narrower f_s regime (0.05 to 0.2) on given scales and runs out of stellar mass earlier (i.e. at lower enclosed radius) than the low mass lenses. The latter exhibit a more inhomogeneous behaviour, as they populate a wider range of f_s values (0.1 to 0.5) and respective slopes. As we contrast $f_s(M_L)$ with comparable curves deduced by abundance matching (Guo et al. 2010, Moster et al. 2010) we find that their f_s-to-$M_{\rm halo}$ relation scaled down to $4R_{\rm e}$ agrees quite well with lenses with $M_L \sim 10^{12} M_{\odot}$, since most of the stellar matter is still enclosed. This can be taken as evidence for the accuracy of our data at large enclosure radii.

In Section 6.6 we introduce a novel concentration index, $c = R90/R50$, for stellar ($c(M_s)$) and total *mass* profiles (c_{M_L}). Following the definition of light concentrations

(e.g. Bershady et al. 2000, Ferreras et al. 2005), we define the ratio of radii enclosing 90% and 50% of the stellar or total mass. The rule-of-thumb delimiter of $c = 2.6$ which separates early-type galaxies ($c > 2.6$) from late-types $c < 2.6$) also holds for $c(M_s)$ defined by means of stellar mass instead of luminosity. In the low mass regime, $M_L(< 2R_e) \lesssim 4 \times 10^{11} M_\odot$, both c_{M_s} and c_{M_L} approach similar values around 2.6. From $10^{11} M_\odot$ upwards $c(M_s)$ and $c(M_L)$ diverge, due to a stronger confinement of stars in more massive dark matter halos. The $c(M_L)$ values above $4 \times 10^{11} M_\odot$ stay around ~ 2, while $c(M_s)$ becomes roughly twice as large. Thus we conclude that in particular less massive dark matter halos are influenced by the distribution of stellar matter. In other words we observe central total matter concentrations increasing with stellar baryon fraction similar to the results from observations of extended cores in the density profile of low surface brightness galaxies and cuspy profile features in early-type galaxies (e.g. de Blok 2010, Li & Chen 2009). It must be noted, however, that our lensing galaxies are much different from low surface brightness galaxies.

Furthermore we present projected two-dimensional maps of dark matter surface densities and baryon fractions for the large sample of lens galaxies discussed in Section 6.4. These maps will aid studies of the matter distributions in terms of smoothness and the occurrence of substructures.

Baryonic cooling

Previous studies have found evidence for an inverse proportionality between concentration and virial mass (e.g. Buote et al. 2007, Comerford & Natarajan 2007). From our analysis of the relation between lens mass and the *central* concentration we see that such a trend is true for enclosed masses even on scales far below the virial radius, more precisely in a range from 10^{-3} to $0.1 R_{\rm vir}$. Using NFW profile fits we are able to extrapolate the reconstructed dark matter profiles to the virial radius, recovering a c-M_{vir} relation for lens galaxies that extends to unprecedentedly low virial masses (Section 7.1). The inferred slope, $\alpha = -0.40 \pm 0.06$, of the relation is in agreement with recent studies of X-ray and weak lensing clusters (Schmidt & Allen 2007, Okabe et al. 2010) which probe the high-mass end of the c-M_{vir} relation.

For the majority of lenses the relation appears to be in agreement with virial mass predictions from abundance matching studies M_{vir}^{AM} (Moster et al. 2010, Guo et al. 2010), as shown in Section 7.2. Departures from the latter predictions appear to be well-explained by environmental effects, such as external contribution to convergence, but may also be related to differing halo definitions or an underestimated error of M_{vir}^{AM}. It is surprising, however, that concentrations of profiles forced to fit M_{vir}^{AM} lead to a significantly increased scatter around the best-fit power-law for the c-M_{vir} relation, in strong disagreement with previous studies of this type.

In view of the fact that the central stellar concentration, $c(M_s)$, does not follow the trend of the global $c - M_{vir}$ relation and in light of the inverse relation between total mass and baryon fraction, one is tempted to ask how the dark matter distribution is affected by the presence of stars. Feedback processes, such as super novae winds (Larson 1974) and outflows from AGN (Di Matteo et al. 2005), might impede star formation and redistribute matter in galaxy centres such that strong density cusps, as predicted by N-body simulations (Diemand et al. 2005), hardly form. The gravitationally interacting dark

matter is believed to respond to such changes in the potential. In opposition to feedback mechanisms, baryonic cooling might be responsible for a gradual steepening of the inner dark matter profiles during adiabatic contraction (Blumenthal et al. 1984). Focusing on the latter, our analysis of recent prescriptions for baryonic cooling (Section 7.3) shows that the parameters (c_{final}, f_b, $r_{hern}/R_{\rm vir}$) inferred by our data fits lie significantly below even the lowest concentrations achievable with standard adiabatic cooling prescriptions (Gnedin et al. 2004, Blumenthal et al. 1984). Adiabatic contraction as implemented in these prescriptions is hence too strong.

Adiabatic contraction is based on preserving angular momentum by keeping $rM(<r)$ constant. By tweaking the spherically averaged radius r – a strategy used in a weaker form by Gnedin et al. (2004) – we find better agreement with our data. The much shallower $c_{final}(f_b)$ compared to the standard AC prescriptions can be translated in a quantity indicating mass loss. Furthermore a c-M_{vir}-type study for concentrations freed from the effect of adiabatic contraction leads us to the conclusion that AC has at most a minor impact on the overall slope of the relation but could reproduce the flattening of the $c-M_{vir}$ relation for low virial masses found in simulations (Bullock et al. 2001, Macciò et al. 2008, Hennawi et al. 2007).

Outlook

With the discovery of more and more gravitational lenses at high resolution, one can think of a manifold of applications of stellar population synthesis and lens mass reconstruction that will permit exploration of the distribution of dark matter on radial scales of $\lesssim 0.1$ kpc, a region where interactions between dark matter and baryons should be most efficient and where stellar populations give hints on the star formation history of the galaxy.

- Uncertainties on individual lens profiles are hard to improve, but analyzing a much larger sample of lenses in a quasi-automatized way will boost the statistical significance of our findings and enable new questions to be posed. This is of course also true for studies on the fundamental plane and the c-M_{vir} relation. For example the scatter in the c-M_{vir} (Section 7.1) relation constrains the CDM model. If galaxies form early the scatter in the relation is small in contrast to late formation scenarios.

- Sub-classes of lenses which show signs of recent gravitational interaction, such as tidal streams or merging galaxies acting as one lens, are particularly intriguing study subjects. Structural features, can be modeled by new fitting algorithms (e.g. Peng et al. 2010). This allows for extending presented studies to lens galaxies in a larger range of morphological types. Furthermore, resolved dark matter and baryon fraction maps, as shown in Sec. 6.4, will give new insights about the interplay between luminous and dark matter.

- Lens galaxies can be used to constrain the stellar initial mass function below 1 $M_\odot$. Using the light and the reconstructed mass profile, an upper limit to the stellar mass-to-light ratio is obtained. The maximal stellar mass can then be compared to the output of the population synthesis, which is based on an adjustable IMF, for example, by making the slope of the low-mass end of the IMF a free parameter (Ferreras et al. 2010).

- The baryon-fraction maps (Fig. 6.3) can be used in combination with microlensing models of lensed quasars. The convergence κ_{tot} and shear γ inferred by `PIXELENS` and the stellar convergence κ_* inferred from stellar population synthesis can be input to microlensing codes that compute the probability distribution of magnifications and hence make statistical predictions about flux ratios for optical quasars. Previous work in this area (e.g., Pooley et al. 2011) has treated the stellar-mass fraction as a free parameter. A comparison with latter studies permits furthermore to investigate how smooth or clumpy dark matter distributions in lensing galaxies are.

A

Photometry, Mass Maps and Profiles

In the following we provide material necessary for a detailed study of individual lensing galaxies of sample II (Section 4.2). Figures A.1 and A.2 are used for the photometric modeling (Sections 3.2.2 and 6.2.2). Figure A.3 shows the output of the stellar population synthesis (Sections 3.2.3 and 6.3.1).

The results of the best-χ^2 search for NFW and Hernquist parameters, carried out in Sections 7.1 and 7.3, is presented in Figures A.4 and A.5, respectively. Figure A.6 shows cumulative dark matter profiles and a comparison with abundance matching studies (Section 7.2). Finally, in Section A.1 of this appendix, we explain the animated version of Fig. 6.6 available online.

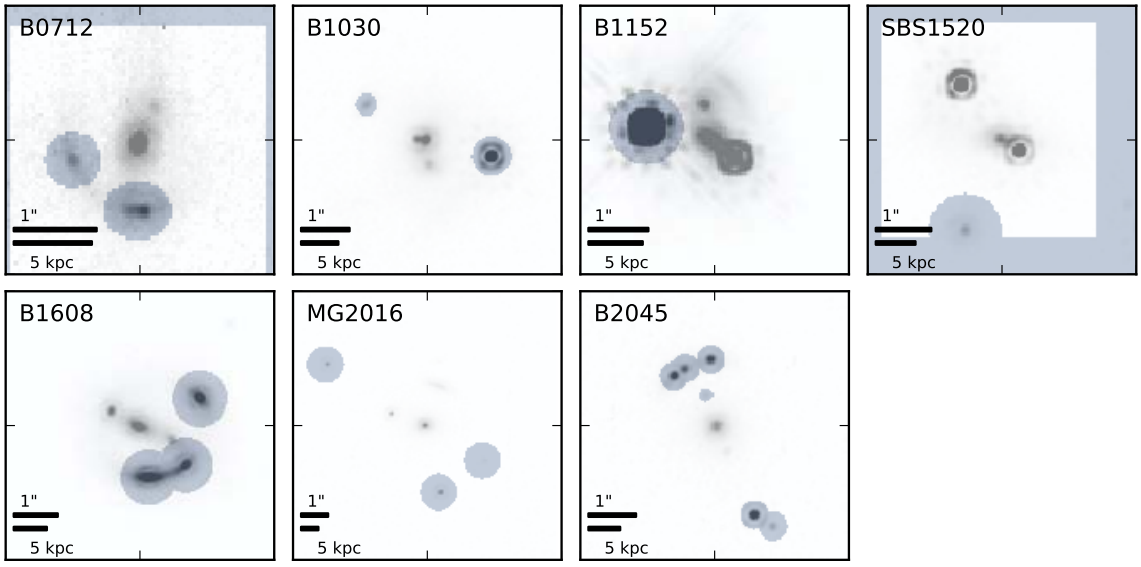

Figure A.1: Overview of lenses in H-band photometry subject to masking during photometric modeling. The blue-shaded area is ignored by GALFIT.

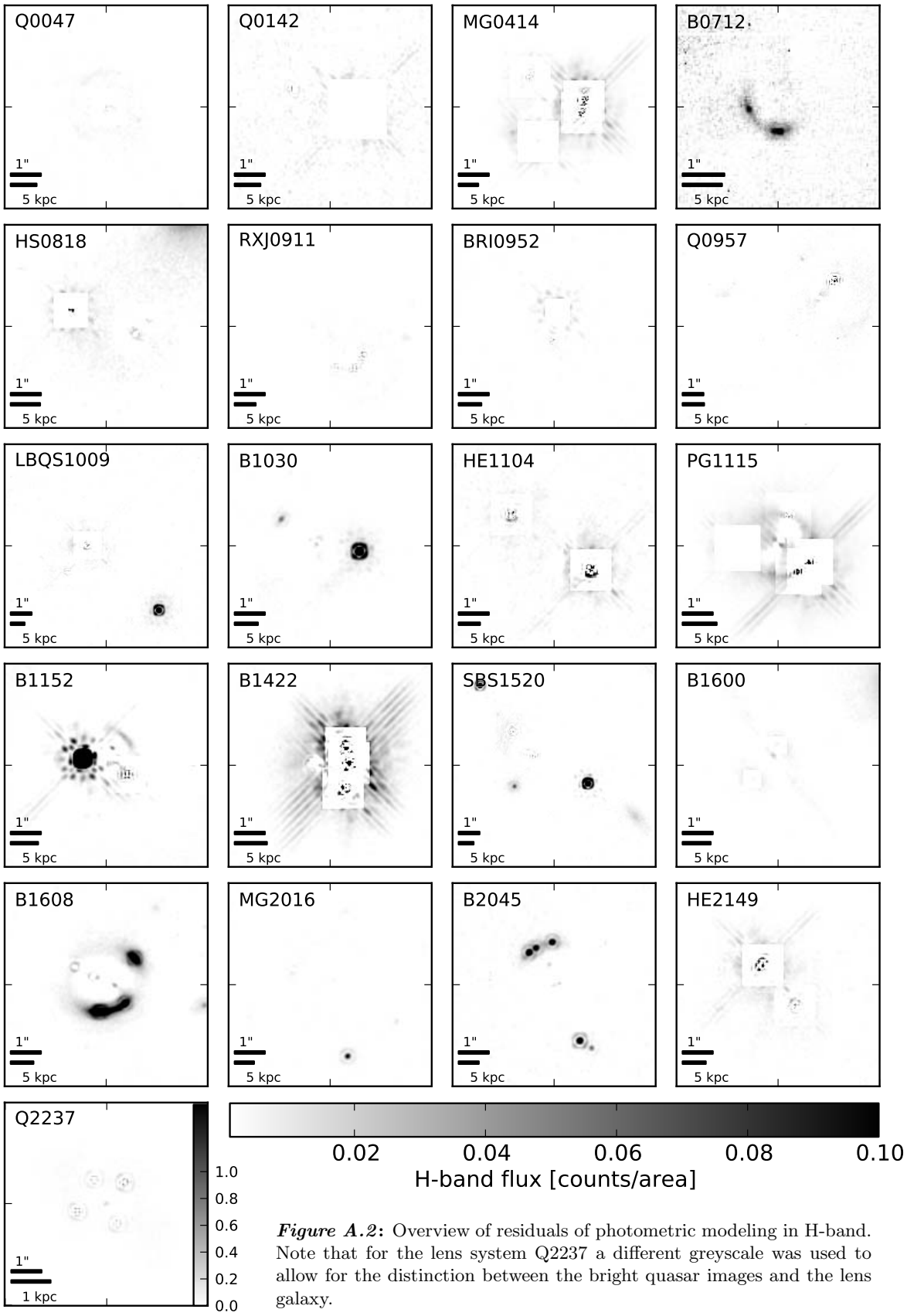

***Figure A.2*:** Overview of residuals of photometric modeling in H-band. Note that for the lens system Q2237 a different greyscale was used to allow for the distinction between the bright quasar images and the lens galaxy.

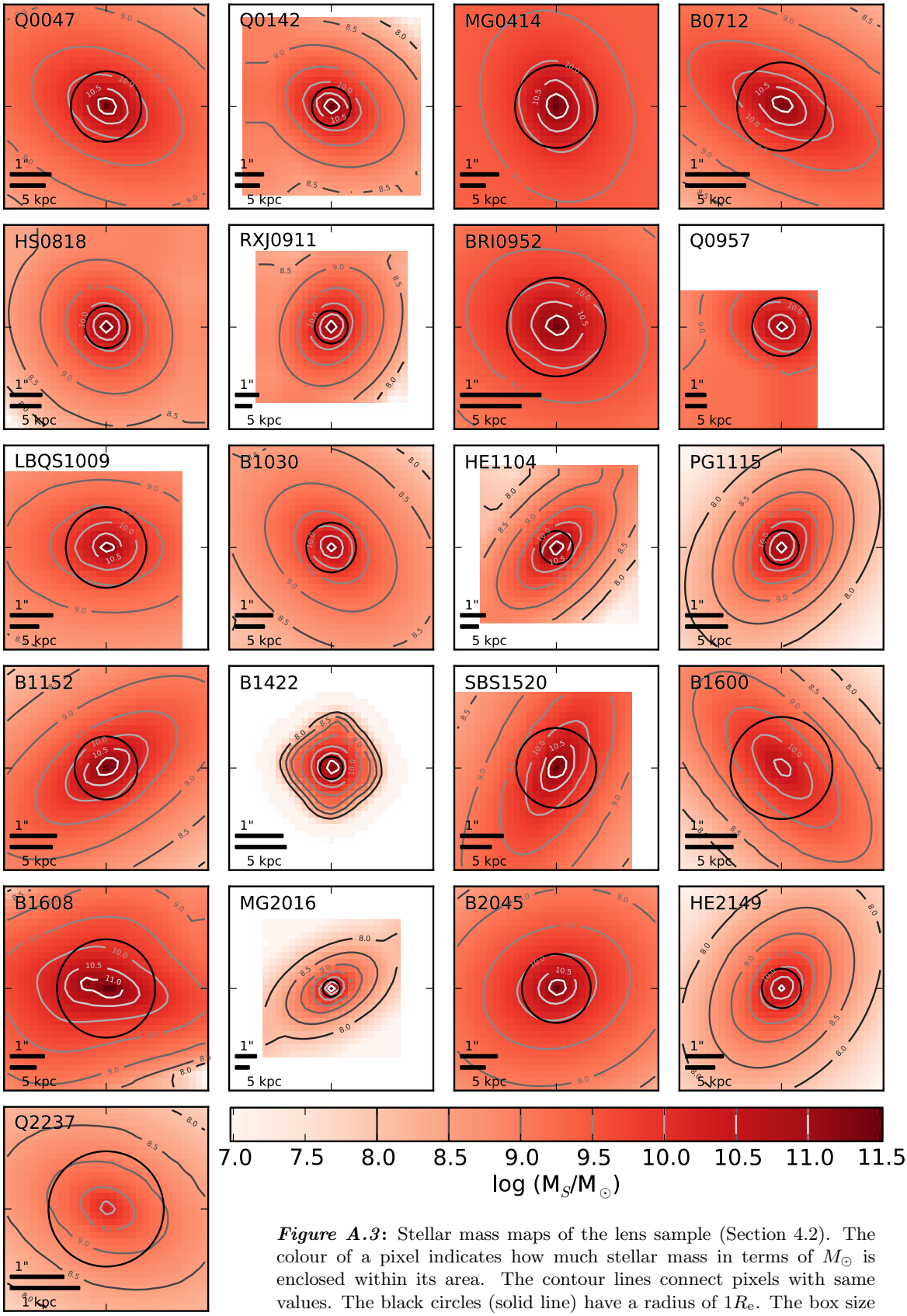

Figure A.3: Stellar mass maps of the lens sample (Section 4.2). The colour of a pixel indicates how much stellar mass in terms of $M_\odot$ is enclosed within its area. The contour lines connect pixels with same values. The black circles (solid line) have a radius of $1R_e$. The box size is 31×31 pixels. Angular and physical scales are defined in the panels. North is up, east is left.

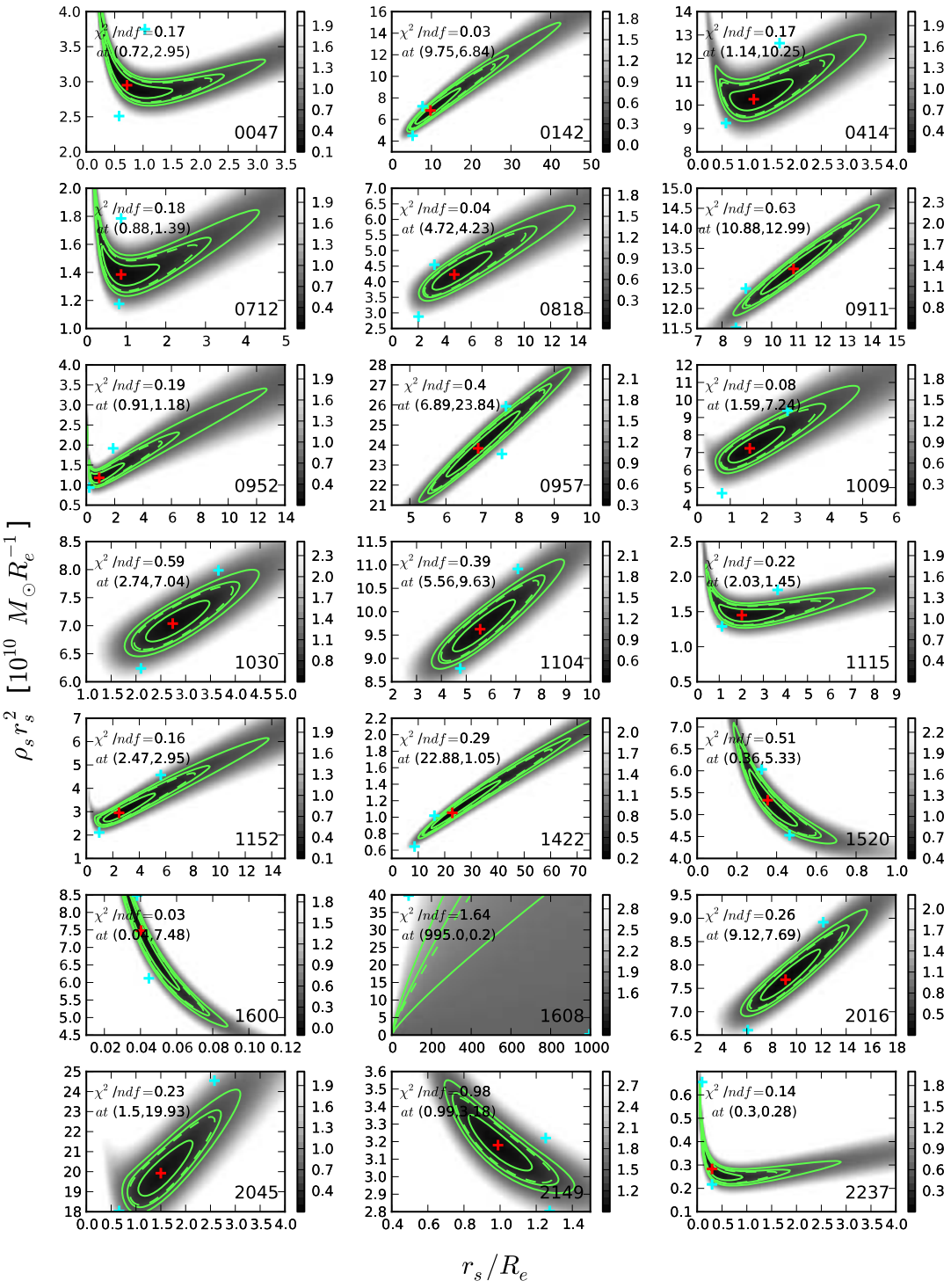

Figure A.4: χ^2 map of NFW profile parameter space. Minima are indicated by red crosses. Fits to $\Delta M \pm \delta M_L$ are marked by cyan crosses. Solid contour lines indicate from center outwards 1-3σ regions for one degree of freedom, the dashed contour a 1σ region for two degrees of freedom.

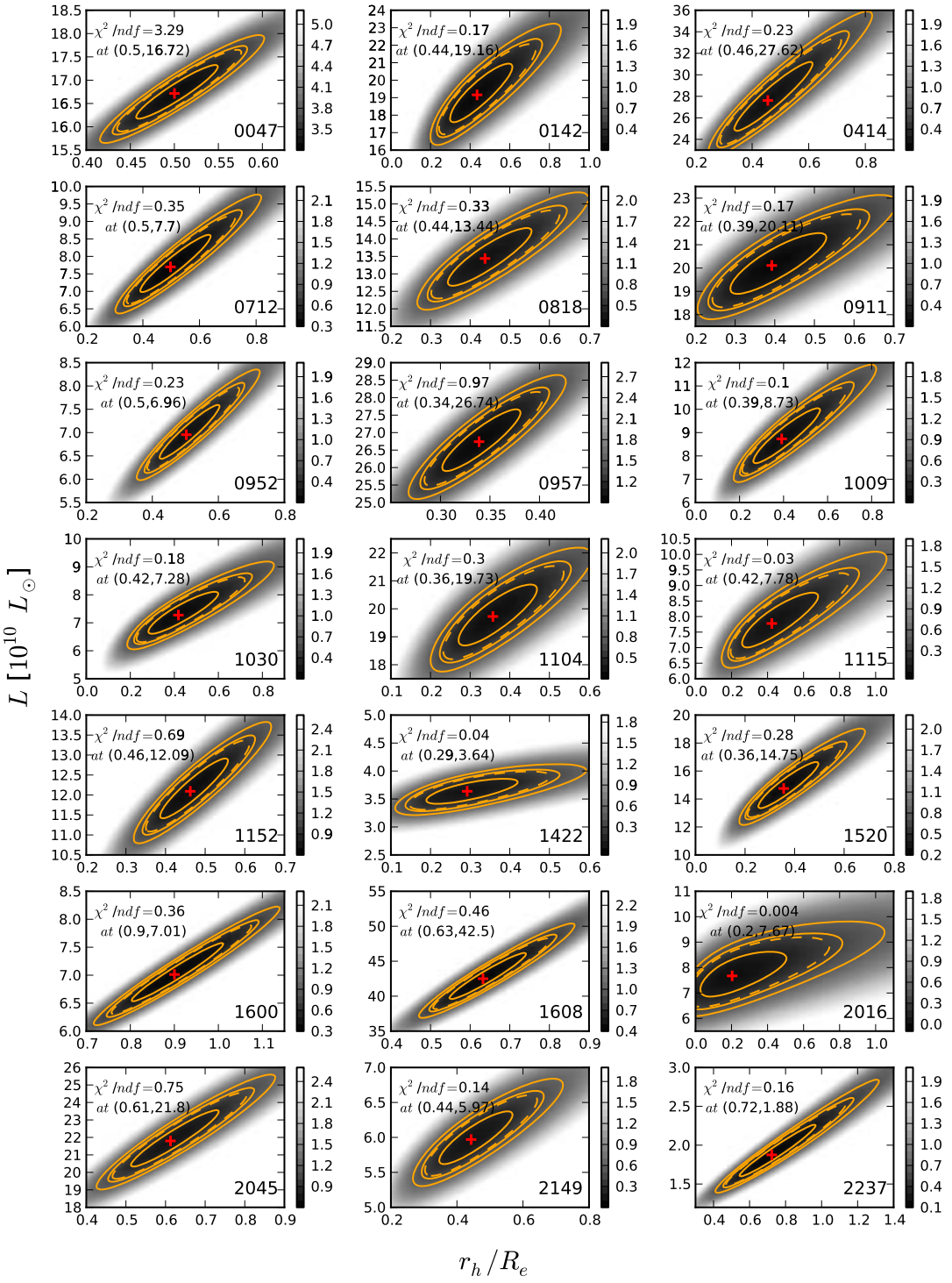

Figure A.5: As in Fig. A.4 but for Hernquist profile parameters.

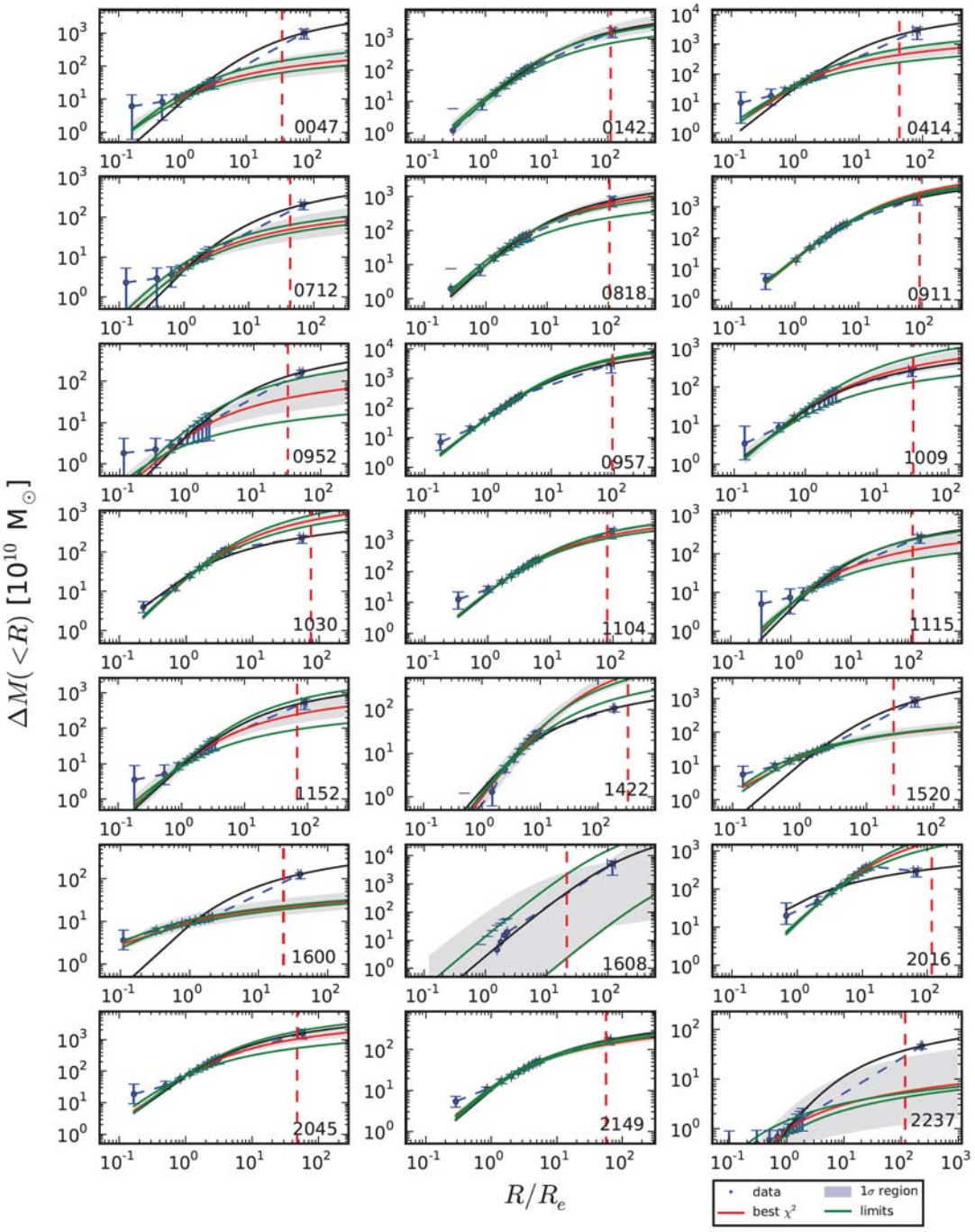

***Figure A.6*:** Extrapolation of mass profiles. The grey shaded area indicates the 1σ region around the best (NFW) fit (red line) to the lens data (inner 10 blue dots). The green curves relate to the fits to the upper and lower error limits. The outermost point in each case is from abundance matching. The black curves are NFW fits that include the outer point, i.e., 11 data points in total.

A.1 Animated results

An animated version of Fig. 6.6 is provided as online material under

`arxiv.org/src/1102.3433v2/anc/bfilg.mov`.

The movie contains three panels. The left panel shows the enclosed M_L against enclosed M_s plane depending on the size of the aperture, defined by the radial distance $xR_{\rm e}$ to the centre of the lens galaxy. The solid black line denotes the equality of total and stellar mass, whereas the dashed lines represent the upper and lower limit of the global baryon fraction (Hinshaw et al. 2009). The upper right panel shows the lens PG1115 which is highlighted by a red label in the left panel. The lower right panel shows stellar baryon fraction versus radius as in Fig. 6.8. The solid black line denotes the baryon fraction curve of PG1115. With each time step of the movie the enclosure radius increases indicated by the factor x in the legend of the left panel and the red lines in the two right-hand panels. We cover a radial distance from 0.125 $R_{\rm e}$ to 5 $R_{\rm e}$ in 40 time steps.

B
Mass Reconstruction Data

The PIXELENS input format can be read as follows. The option symm allows only symmetric models, reducing the amount of equations by one half. The numbers after redshift are lens (z_L) and source redshift (z_s). To account for external gravity from nearby objects, the shear direction can be entered as a position angle (counted counterclockwise from positiv x-axis). The commands double, quad and multi refer to the number of images listed below them. After multi the number of images and z_s must be given. Also, zlens must be separatly defined in the header. The image positions are given as x- and y-coordinate. For quads and doubles the time-delay between two consecutive images is given as a third number right after the image position, starting in the row with the second image. For multi the number following the image positions indicates the image parity, i.e. 1 for a minimum, 2 for a saddle point and 3 for a maximum. The mininum steepness is defined by minsteep with a default value of 0.5, i.e. the mass profile is $R^{0.5}$ or steeper. maxsteep is similarly defined. Further information on the functionality of PIXELENS can be found on www.qgd.uzh.ch/projects/pixelens/.

The following pages contain the PIXELENS input/output for the lensing sample I (Section 4.1) and II (Section 4.2).

***Figure B.1*:** Lens sample I: CASTLES lenses used in Chapter 5. First column includes the `PIXELENS` input files, the second column shows the formal velocity dispersion curves and in the third column the projected mass distributions (red dots mark image positions, cyan dots mark source position, green lines are logarithmic contours in terms of critical density) are presented. IMPORTANT NOTE: The y-axes of the velocity dispersion plots need to be multiplied by $\sqrt{2/\pi} \approx 0.8$ to yield the true $\sigma_{\rm lens}$ values.

```
object Q0047-2808
symm
redshifts 0.485 3.6
quad
 1.270   0.105
-0.630 -0.995   0
 0.520 -1.045   0
-0.730   0.705   0
```

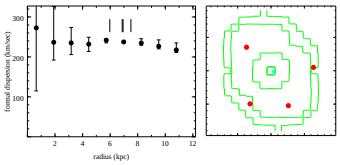

```
object CFRS03.1077
redshifts 0.938 2.941
quad
-2.085 0.383
-1.979 -0.521 0
-1.415 -1.213 0
0.713 0.340 0
```

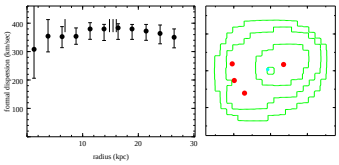

```
object Q0957+561 (2D)
symm
redshifts 0.356  1.41
shear -30
double
1.408   5.034
0.182 -1.018   423
double
2.860   3.470
-1.540 -0.050 0
```

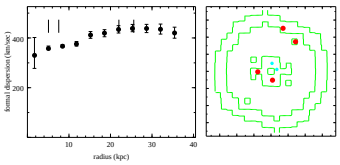

```
object PG1115+080
redshifts 0.31 1.72
quad
0.381 1.344
-0.947 -0.690   0
-1.096 -0.232    0
0.722 -0.617   0
```

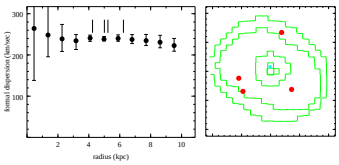

```
object HST14176+5226
redshifts 0.81 3.4
quad
 -1.288 -1.175
-0.880 0.879 0
0.792 1.332 0
0.808 -0.794 0
```

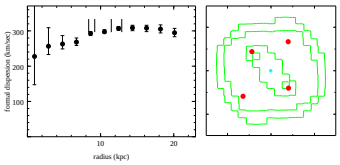

```
object HST15433+5352
redshifts 0.497 2.092
quad
0.590 0.200
-0.110   -0.770   0
0.360   -0.450    0
-0.330 0.100   0
```

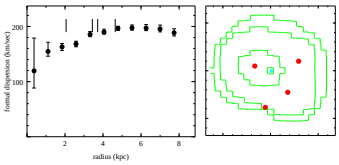

```
object B1608+656
redshifts 0.630 1.394
quad
-1.300 -0.800
-0.560   1.160   31
-1.310   0.700    5
 0.570 -0.080   40
```

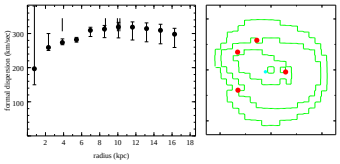

```
object MG2016+112
redshifts 1.01 3.27
double
-1.735   1.778
1.269   0.274 0
```

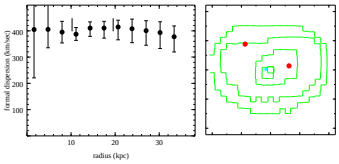

```
object Q2237+030
redshifts 0.04 1.69
quad
0.598 0.758
-0.075 -0.939 0
0.791 -0.411 0
-0.710 0.271 0
```

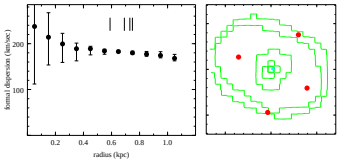

***Figure B.2*:** Lens sample I: As in Fig. B.1, but for SLACS lenses and clusters used in Chapter 5. IMPORTANT NOTE: The y-axes of the velocity dispersion plots need to be multiplied by $\sqrt{2/\pi} \approx 0.8$ to yield the true $\sigma_{\rm lens}$ values.

```
object J0037-094
redshifts 0.1954
          0.6322
double
1.920 -0.730
-0.730 0.730 0
```

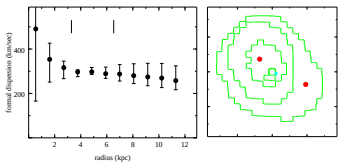

```
object J0737+321
zlens 0.3223
multi 3 0.5812
-0.08 1.17   1
0.52  -0.77  2
-0.68 -0.57  2
```

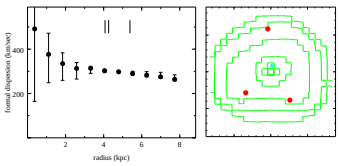

```
object J0912
redshifts 0.1642
          0.3239
double -1.275 1.025
0.375  -0.825 0
double -0.425 1.675
0.225  -0.975 0
double 0.975  1.575
-0.425 -1.075 0
double 1.475  1.225
-0.625 -0.575 0
```

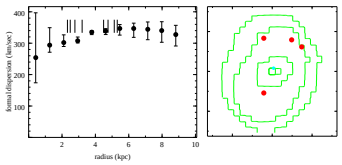

```
object J0956+510
zlens 0.2405
multi 3 0.47
-1.67 0.170 1
-0.220 -1.270 2
0.730 0.620 2
```

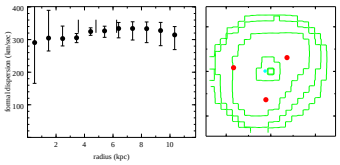

```
object J1205+491
redshifts 0.2150
          0.4808
quad
1.480 -0.320
-0.88 0.570 0
-0.520 0.930 0
-0.820 -0.470 0
```

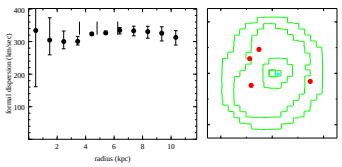

```
object J1330-014
symm
redshifts 0.0808
          0.7115
double
1.020 -0.520
-0.43 0.080 0
```

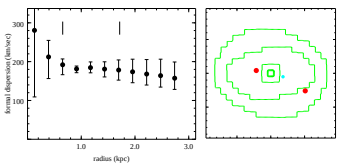

```
object J1636+470
redshifts 0.2282
          0.6745
quad
-0.080 1.730
0.88  -0.620 0
1.080  -0.280 0
-0.770 -0.430 0
```

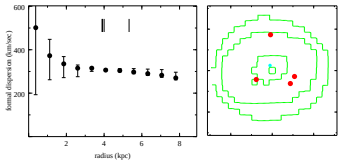

```
object J2300+002
symm
redshifts 0.2285
          0.4635
quad
-0.120  1.480
-0.28  -1.080 0
-0.570 -0.930 0
0.120  -1.080 0
```

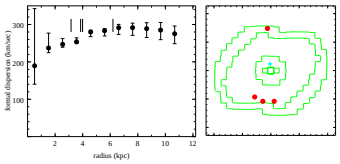

```
object J2303+142
redshifts 0.1553
          0.517
double
-1.270 -1.580
-0.28 1.170 0
```

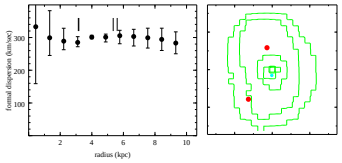

```
object ACO 1689
pixrad 18
maprad 95
minsteep 0
shear 0
g 13.7
models 100
zlens 0.183
```

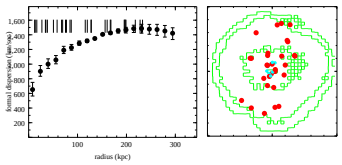

```
object ACO 2667
pixrad 10
minsteep 0
zlens 0.233
g 13.7
```

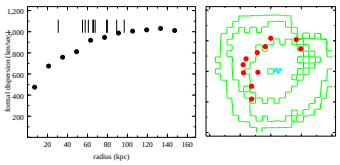

```
ACO 1689 - continued -
multi 5 2.54
 10.38 -54.35  1
 24.18  45.85  1
 34.48  24.60  2
-32.58  20.25  2
 -8.03   9.85  3
multi 3 1.99
  7.88  71.90  1
  2.38 -24.90  2
 -1.43  -3.85  3
multi 3 1.98
-24.98  59.80  1
 18.43  -5.75  2
  4.42  -0.35  3
multi 2 4.53
 27.58  72.15  1
-12.88 -10.80  2
multi 3 1.74
-32.33 -56.70  1
 14.78  23.80  2
 -0.18  11.35  3
multi 5 2.99
  4.48 -55.60  1
 23.08  48.00  1
 35.27  23.60  2
-34.12  20.40  2
 -7.33   9.10  3
multi 3 4.92
-47.53 -45.00  1
 20.08   9.80  2
  4.73   2.90  3
multi 3 2.01
 14.38  74.20  1
 -7.38 -21.85  2
 -4.38  -7.85  3
multi 3 1.78
-11.98 -64.90  1
 -6.53  28.15  2
 -7.03  24.65  3
```

```
ACO 2667 - continued -
multi 3 1.033
-17.94  -0.84 1
-3.60 16.33 1
-8.81 12.28  2
multi 3 1.20
16.59 20.77 1
-12.54 -9.71 2
-8.42 -0.58 3
multi 3 1.578
-0.13 21.74 1
-18.07 4.37 1
-16.14 8.23 2
multi 2 3.0
19.55 14.79 1
-12.54 -18.01 2
```

***Figure B.3*:** Lens sample II: PIXELENS input data and projected mass distribution for the lens sample 2 (Sec. 4.2). The black dots mark the multiple images. All maps have a radius of 15 pixels. All mass maps have a radius of 2 $R_{\rm lens}$, which corresponds roughly to 2 $R_{\rm Ein}$. All lens properties as well as respective length specifications are in Table C.2.

```
object B0712+472
redshifts 0.41 1.34
shear -45
quad
-0.013 -0.804
 0.795 -0.156 0
 0.747 -0.292 0
-0.391  0.307 0
```

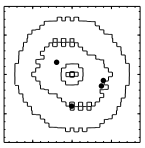

```
object 1030+071
redshifts 0.600 1.540
shear +45
double
 0.846  1.097
-0.085 -0.156 0
```

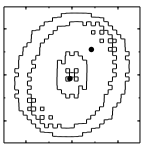

```
object B1152+200
redshifts 0.439 1.019
shear +30
double
 0.549  0.978
-0.387 -0.268 0
```

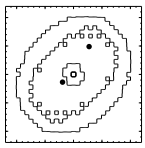

```
object B1422+231
redshifts 0.337 3.620
shear +45
quad
 1.079 -0.095
 0.357  0.973 0
 0.742  0.656 0
-0.205 -0.147 0
```

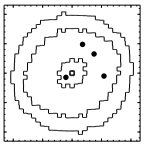

```
object B1600+434
redshifts 0.42 1.59
shear +60
double
 0.610  0.814
-0.110 -0.369 51
```

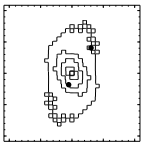

```
object B1608+656
redshifts 0.630 1.394
shear -30
quad
-1.300 -0.800
-0.560  1.160  31
-1.310  0.700   5
 0.570 -0.080  40
```

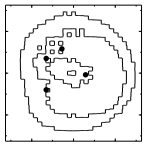

```
object B2045+265
redshifts 0.870 1.280
shear +30
quad
 1.121  0.824
 1.409  0.035 0
 1.255  0.576 0
-0.507 -0.183 0
```

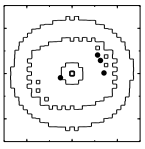

```
object BRI0952-012
redshifts 0.632 4.500
shear -45
double
-0.396  0.506
 0.300 -0.203 0
```

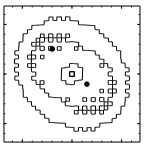

```
object HE1104-181
redshifts 0.730 2.320
shear +30
double
-1.927 -0.822
 0.974  0.510 161
```

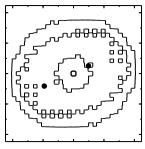

```
object HE2149-275
redshifts 0.603  2.03
shear +45
double
 0.736 -1.161
-0.173  0.284 103
```

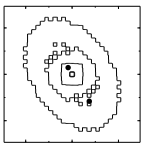

```
object HS0818+123
redshifts 0.390 3.115
ptmass -2 2 2 10
double
-1.657 -1.475
-0.152  0.592 0
```

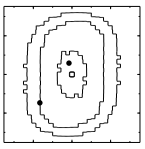

```
object LBQS1009-025
redshifts 0.880 2.740
shear +90
double
-0.537  1.097
 0.133 -0.286 0
```

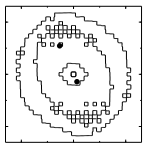

```
object MG0414+053
redshifts 0.960 2.640
shear -30
- 3 quads -
```

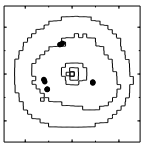

```
object MG2016+112
zlens 1.01
shear +45
- 3 ptmasses -
multi 3 3.27
-1.735  1.778 1
 0.317 -1.470 1
 1.269  0.274 2
```

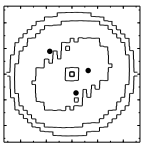

```
object PG1115+080
redshifts 0.311 1.722
shear -30
quad
 0.3550  1.3220
-0.9090 -0.7140 13.3
-1.0930 -0.2600 0
 0.7170 -0.6270 11.7
```

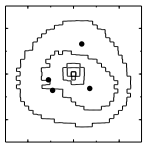

```
object Q0047-281
redshifts 0.485 3.6
quad
 1.270  0.105
-0.630 -0.995  0
 0.520 -1.045  0
-0.730  0.705  0
```

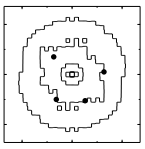

```
object Q0142-100
redshifts 0.490 2.720
shear 0
double
 1.764  0.574
-0.381 -0.039 0
```

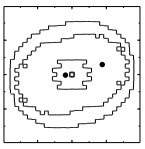

```
object Q0957+561
redshifts 0.356  1.41
shear 0
double
 1.408  5.034
 0.182 -1.018 423
double
 2.860  3.470
-1.540 -0.050 0
```

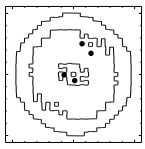

```
object Q2237+030
redshifts 0.039 1.69
shear -45
maxsteep 3
quad
 0.598  0.758
-0.075 -0.939 0
 0.791 -0.411 0
-0.710  0.271 0
```

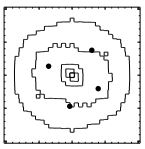

```
object RXJ0911+055
redshifts 0.769  2.80
shear +90
quad
 2.226  0.278
-0.968 -0.105  146
-0.709 -0.507    0
-0.696  0.439    0
```

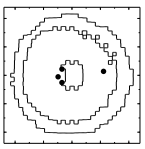

```
object SBS1520+530
redshifts 0.71 1.855
shear +45
double
 1.141   0.395
-0.288  -0.257 130
```

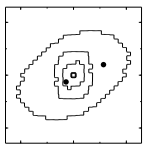

C Tables

This part of the appendix contains all tables essential to the Chapters 5, 6 and 7.

Lens	z_L	σ_{obs} [km s^{-1}]	σ_{lens} [km s^{-1}]	R_e [kpc]	R_{lens} [kpc]	M_{lens} [$10^{11} \times M_\odot$]	M_{vir} [$10^{11} \times M_\odot$]	L_I [$10^{11} \times L_\odot$]	M_{lens}/L_I [$M_\odot/L_\odot$]	Ref.
B0047-2808	0.4850	229 ± 15	189.0 ± 6.4	5.324	7.440	2.084 ± 0.141	3.059 ± 0.401	0.760	2.74	①②①
CFRS03.1077	0.9380	256 ± 19	306.6 ± 22.0	-	15.905	-	-	-	-	①③①
Q0957 (2D)	0.3600	288 ± 9	$351.6^{+12.8}_{-10.4}$	22.64	25.529	$30.458^{+2.477}_{-1.583}$	20.58 ± 1.29	4.922	6.19	①④⑩
PG1115+080	0.3100	281 ± 25	190.8 ± 8.4	2.072	6.188	0.826 ± 0.073	1.792 ± 0.319	0.671	1.23	①⑤①
HST14176	0.8100	230 ± 14	245.6 ± 4.0	5.190	12.780	3.430 ± 0.112	3.008 ± 0.366	3.910	0.88	①⑥①
HST15433	0.4970	108 ± 14	156.2 ± 2.8	-	4.601	-	-	-	-	①③①
B1608+656	0.6300	247 ± 35	242.6 ± 18.4	4.291	15.542	2.766 ± 0.420	2.868 ± 0.813	3.354	0.82	①⑦①
MG2016+112	1.0100	304 ± 27	330.4 ± 29.6	1.707	19.388	2.041 ± 0.366	1.729 ± 0.307	2.128	0.96	①⑧①
Q2237+030	0.0400	215 ± 30	146.4 ± 2.8	2.993	0.743	0.703 ± 0.027	1.516 ± 0.423	0.542	1.30	①⑨①
J0037-094	0.1954	265 ± 10	$230.4^{+33.6}_{-36.0}$	6.804	6.470	$3.956^{+1.239}_{-1.139}$	5.234 ± 0.395	1.990	1.99	❶
J0737+321	0.3223	310 ± 15	233.6 ± 6.4	9.823	5.333	5.874 ± 0.322	10.34 ± 1.00	3.544	1.66	❶
J0912+002	0.1642	313 ± 12	$276.0^{+11.2}_{-15.2}$	9.203	5.271	$7.679^{+0.637}_{-0.821}$	9.877 ± 0.757	2.289	3.35	❶
J0956+510	0.2405	299 ± 16	$266.8^{+7.6}_{-8.4}$	8.607	6.201	$6.710^{+0.390}_{-0.414}$	8.430 ± 0.902	2.572	2.61	❶
J1205+491	0.2150	235 ± 10	$230.2^{+10.6}_{-8.6}$	7.805	5.138	$4.531^{+0.427}_{-0.332}$	4.722 ± 0.402	1.936	2.34	❶
J1330-014	0.0808	178 ± 9	$142.3^{+20.9}_{-20.7}$	1.244	1.696	$0.276^{+0.087}_{-0.074}$	0.432 ± 0.044	0.147	1.88	❶
J1636+470	0.2282	221 ± 15	$230.7^{+9.3}_{-12.3}$	5.256	6.150	$3.065^{+0.252}_{-0.318}$	2.812 ± 0.382	1.376	2.23	❶
J2300+002	0.2285	283 ± 18	$239.8^{+10.6}_{-7.8}$	6.256	5.278	$3.942^{+0.355}_{-0.253}$	5.489 ± 0.698	1.522	2.59	❶
J2303+142	0.1553	260 ± 15	$242.7^{+14.9}_{-17.9}$	7.901	5.303	$5.098^{+0.646}_{-0.724}$	5.851 ± 0.675	2.333	2.19	❶
ACO 1689	0.1830	1400 ± 300	$1188.7^{+40.0}_{-56.0}$	400.0	237.6	6192^{+424}_{-570}	8589 ± 2187	33.48	185	❷
ACO 2667	0.2330	960^{+190}_{-120}	$762.0^{+7.2}_{-8.0}$	-	98.01	-	-	-	-	❸

***Table C.1*:** For Chapter 5: Full set of gravitational lenses used for this analysis. The first 9 lenses are from CASTLES, the following 9 from SLACS and the last two are clusters. The image positions and flux data have been taken from HST data (www.cfa.harvard.edu/glensdata/), Bolton et al. (2006) and Covone et al. (2006). The symbols mark the references for the data in the columns z_L, σ_{obs} and R_e and refer to the following publications: ① (Rusin et al. 2003), ② (Koopmans & Treu 2003), ③ (Treu & Koopmans 2004), ④ (Tonry & Franx 1999), ⑤ (Tonry 1998), ⑥ (Ohyama et al. 2002), ⑦ (Koopmans et al. 2003), ⑧ (Koopmans & Treu 2002), ⑨ (Foltz et al. 1992), ⑩ (Keeton et al. 1998), ❶ (Bolton et al. 2006), ❷ (Łokas et al. 2006) and ❸ (Covone et al. 2006). Note that σ_{obs} is the kinematic central velocity dispersion, which is in the case of SLACS lenses the line of sight stellar velocity dispersion measured by the 3″ diameter SDSS spectroscopic fibre. The σ_{lens} values are determined for the projected distance R_{lens} from the outermost lensing image to the central lensing mass. The effective radii given in arcseconds in Rusin et al. (2003) and Bolton et al. (2006) have been transformed into kpc. The virial mass M_{vir} is computed via $M_{vir} = \frac{3\pi}{2G} R_e \sigma^2_{obs}$ and is thus a dynamical mass estimate rather than the mass enclosed in a sphere with radius R_{vir}. All quantities in the table assume $H_0 = 72$ km s^{-1} Mpc^{-1}, $\Omega_m = 0.3$ and $\Omega_\Lambda = 0.7$.

Lens	z_L	z_s	$\Delta\theta$ [″]	$\Delta\theta$ [kpc]	R_e [″]	R_{lens}/R_e	$M_L(<2R_e)$ [$10^{10} M_\odot$]	$M_s(<2R_e)$ [$10^{10} M_\odot$]	M_s/L_V [$M_\odot/L_\odot$]	σ_{lens} [km s^{-1}]	R_{vir} [kpc]	*Env*
Q0047	0.485	3.60	2.20	12.82	0.880 ± 0.025	1.45 ± 0.04	$33.27^{+3.80}_{-3.03}$	11.58 ± 0.43	$5.04^{+1.09}_{-0.89}$	$189.2^{+5.7}_{-4.8}$	538.4	Gr(9)
Q0142	0.490	2.72	2.23	13.10	0.703 ± 0.013	2.64 ± 0.05	$45.81^{+3.31}_{-5.50}$	13.45 ± 2.05	$2.92^{+0.90}_{-0.69}$	$245.8^{+16.8}_{-46.8}$	666.5	-
MG0414	0.960	2.64	2.08	16.01	0.734 ± 0.018	1.85 ± 0.05	$102.76^{+16.55}_{-19.04}$	19.90 ± 2.29	$5.62^{+2.27}_{-1.62}$	$247.0^{+9.93}_{-12.9}$	635.0	1
B0712	0.410	1.34	1.29	6.82	0.702 ± 0.016	1.15 ± 0.03	$16.13^{+2.55}_{-2.04}$	5.46 ± 0.52	$3.27^{+0.62}_{-0.52}$	$164.1^{+6.73}_{-6.78}$	295.8	1
HS0818	0.390	3.21	2.56	13.15	0.679 ± 0.013	3.27 ± 0.06	$36.88^{+3.69}_{-5.48}$	9.44 ± 0.97	$5.42^{+1.11}_{-0.92}$	$245.8^{+16.9}_{-41.8}$	517.8	1
RXJ0911	0.769	2.8	3.22	23.16	0.725 ± 0.011	3.09 ± 0.05	$73.04^{+1.15}_{-1.36}$	14.52 ± 1.87	$2.99^{+1.00}_{-0.75}$	$278.6^{+3.9}_{-6.0}$	590.4	Cl
BRI0952	0.632	4.5	0.99	5.27	0.619 ± 0.021	1.04 ± 0.04	$14.76^{+5.67}_{-5.87}$	4.98 ± 0.35	$2.78^{+0.64}_{-0.52}$	$140.0^{+15.8}_{-20.6}$	233.5	Gr(5)
Q0957	0.356	1.41	6.17	29.98	1.491 ± 0.018	3.51 ± 0.04	$151.29^{+5.17}_{-6.58}$	20.92 ± 0.96	$2.52^{+0.62}_{-0.50}$	$374.6^{+11.9}_{-14.0}$	950.0	Cl
LBQS1009	0.880	2.74	1.54	11.56	0.963 ± 0.028	1.27 ± 0.04	$64.73^{+11.97}_{-24.46}$	6.62 ± 0.96	$2.14^{+0.86}_{-0.61}$	$220.9^{+17.8}_{-65.6}$	252.1	-
B1030	0.600	1.54	1.32	8.60	0.675 ± 0.019	2.05 ± 0.06	$55.09^{+2.11}_{-3.52}$	5.16 ± 0.80	$1.12^{+0.32}_{-0.25}$	$256.8^{+9.9}_{-17.9}$	277.2	1
HE1104	0.730	2.32	3.19	22.54	0.681 ± 0.010	3.08 ± 0.05	$72.80^{+3.68}_{-3.22}$	14.43 ± 1.62	$3.50^{+1.04}_{-0.80}$	$302.9^{+11.9}_{-11.0}$	604.5	-
PG1115	0.310	1.72	2.43	10.76	0.478 ± 0.009	2.94 ± 0.06	$16.80^{+1.31}_{-1.23}$	5.61 ± 1.19	$3.68^{+1.23}_{-0.92}$	$191.6^{+11.7}_{-12.9}$	354.0	Gr(13)
B1152	0.439	1.02	1.56	8.60	0.691 ± 0.013	1.62 ± 0.03	$30.43^{+4.23}_{-5.86}$	8.57 ± 0.65	$2.84^{+0.61}_{-0.50}$	$216.9^{+22.8}_{-37.6}$	431.4	-
B1422	0.337	3.62	1.29	6.02	0.241 ± 0.003	4.49 ± 0.06	$5.72^{+0.39}_{-0.24}$	2.91 ± 0.45	$6.40^{+1.21}_{-1.02}$	$162.9^{+4.9}_{-11.9}$	231.3	Gr(17)
SBS1520	0.710	1.86	1.57	10.97	0.947 ± 0.018	1.28 ± 0.02	$41.98^{+1.49}_{-1.82}$	11.49 ± 1.41	$2.63^{+1.14}_{-0.79}$	$198.3^{+7.2}_{-9.1}$	434.3	Gr(4)
B1600	0.420	1.59	1.38	7.45	1.015 ± 0.007	1.00 ± 0.01	$16.38^{+0.82}_{-1.67}$	3.93 ± 0.17	$6.37^{+1.86}_{-1.44}$	$154.4^{+6.1}_{-12.1}$	236.0	Gr(6)
B1608	0.630	1.39	2.10	13.92	0.839 ± 0.047	1.82 ± 0.01	$42.49^{+35.50}_{-26.52}$	27.99 ± 1.63	$2.44^{+0.55}_{-0.45}$	$266.8^{+6.0}_{-14.9}$	972.9	Gr(8)
MG2016	1.010	3.3	3.36	26.22	0.406 ± 0.009	6.12 ± 0.14	$52.05^{+14.23}_{-5.13}$	6.34 ± 1.99	$0.89^{+0.40}_{-0.28}$	$308.6^{+9.9}_{-26.5}$	242.6	Cl(69)
B2045	0.870	1.28	1.93	14.46	0.950 ± 0.019	1.48 ± 0.03	$173.07^{+21.02}_{-34.20}$	14.05 ± 1.03	$2.47^{+0.62}_{-0.50}$	$338.8^{+16.6}_{-40.2}$	517.2	-
HE2149	0.603	2.03	1.71	10.02	0.531 ± 0.008	2.59 ± 0.04	$26.82^{+2.07}_{-2.19}$	4.28 ± 0.47	$0.79^{+0.20}_{-0.16}$	$191.2^{+7.1}_{-9.1}$	242.6	-
Q2237	0.039	1.7	1.83	1.40	1.090 ± 0.014	0.89 ± 0.01	$2.76^{+0.85}_{-0.58}$	1.15 ± 0.12	$4.39^{+1.76}_{-1.26}$	$145.2^{+3.8}_{-3.9}$	212.4	-

***Table C.2*:** For Chapter 6: Full set of gravitational lenses used for this analysis. All quantities in the table assume $H_0 = 72$ km s^{-1} Mpc^{-1}, $\Omega_m = 0.3$ and $\Omega_\Lambda = 0.7$. The underlined values show maximum and minimum. $\Delta\theta$ is the image separation. For systems with more than two images the maximal image separation between two images is given. Columns R_e and R_{lens}/R_e contain Petrosian radii determined in the observed H-band with 1σ error bars. The total and stellar masses enclosed within $2R_e$ are given in the following two columns. The stellar mass-to-light ratios in the rest-frame V-band are median values of all models. σ_{lens} denotes the velocity dispersion at R_{lens}. Column R_{vir} gives the virial radius calculated using Eq. 6.2 and our stellar mass values in combination with the M_s-to-M_{halo} relation from Guo et al. (2010). The column labelled *Env* contains environmental information. "Cl" denotes a cluster environment, "Gr" a group environment and "1" a lens with only one known companion. If known the number of group members is given in parentheses. References for given values are mentioned in Section 6.2. Colours and magnitudes are in agreement with comparable quantities in Rusin et al. (2003).

Lens	Im.	Bands			PSF			fitting			masking			constraints		
		I	V	H	I	V	H	I	V	H	I	V	H	I	V	H
Q0047	4	✓	✓	✓	tt	tt	A(1030)	-	-	-	-	4P	-	-	-	-
Q0142	2	✓	✓	✓	it	tt	it	2P	1P	2P	-	1P	-	-	n	-
MG0414	4	✓		✓	tt		it	-		4P	4P		-	-		m
B0712	4	✓	✓	✓	tt	tt	tt	-	-	1P	4P	4P	3P	R_e	R_e	-
HS0818	2	✓	✓	✓	A	A	A(1030)	1P	1P	2P	B	B	-	-	PA	-
RXJ0911	4	✓		✓	it		it	4P		4P1S	-		-	n,S		xy
BRI0952	2	✓	✓	✓	it	it	it	2P	2P	2P	-	-	-	b/a	-	b/a
Q0957	2+2	✓		✓	it		it	1P		2P	A		-	-		-
LBQS1009	2			✓			*(0414)			2P			-			n
B1030	2			✓			A			1P1S			1P			n
HE1104	2	✓		✓	A		*(0414)	1P		2P	-		-	b/a,PA		xy
PG1115	4	✓	✓	✓	tt	it	it	-	-	4P	4P	4P	-	-	n	R_e
B1152	2			✓			A			1P1S			1P			-
B1422	4	✓	✓	✓	tt	tt	*(0414)	1P	1P	4P	3P	3P	-	R_e	$R_e, b/a$	b/a
SBS1520	2	✓		✓	it		*(1520)	2P		2P	1*		1*	R_e		S
B1600	2			✓			A			2P			-			-
B1608	4	✓		✓	tt		*(0414)	1P1S		1P1S	3P		3P	R_e,S		n, R_e,S,xy
MG2016	2+4	✓		✓	tt		*(0414)	-		1P1S	2P		1P2*	b/a		-
B2045	4	✓	✓	✓	tt	tt	*(2045)	-	-	1P	3P1b	3P	3P1b2*	-	-	n
HE2149	2	✓		✓	it		*(0414)	2P		2P	-		-	-		-
Q2237	4	✓	✓	✓	tt	tt	*(1654)	-	-	4P	4P	4P	-	S	PA,S	S

***Table C.3*:** For Chapter 6: List of lens systems and how they were treated to obtain surface brightness profiles of the lens galaxies. From left to right the Lens-ID, the number of lensed images, the bands for which fitting was feasible, the PSF picking method, fitted and masked objects and necessary constraints are given. The column *PSF* includes the abbreviations *tt* for a PSF created with *TinyTim*, *A* for the outermost and thus fairly isolated quasar image, **(0414)* for an isolated star close to lens MG0414, *it* for the iteration method applied to the most isolated image and *A(1030)* for an isolated quasar image taken from lens B1030 used for subtracting quasar images and for the convolution of the whole image. In column *fitting* we summarize the number of objects, not significantly contributing to the lens mass, which are fitted with previously picked PSFs (P) and Sérsic profiles (S). In column *masking* xP refers to a number of x masked out point sources, mostly quasar images, b denotes resolved but indistinct objects which are not necessarily connected to the lens mass and henceforth excluded from each fit. Point sources like foreground stars indicated by * are also masked out. A,B refer to quasar images which could be masked out given their separation from the lens galaxy. The last column states the type of constraint used if necessary to prevent each fit from diverging. The constrained parameters are: effective radius R_e, Sérsic index n, axis ratio b/a, magnitude *mag*, position angle PA, sky background S and position of the Sérsic profile xy. Parameters fixed at a certain value are underlined.

Lens	z_L	r_s [kpc]	ρ_s [10^8 $\frac{M_\odot}{kpc^3}$]	R_{vir} [kpc]	$\frac{2R_{lens}}{R_{vir}}$	r_h [kpc]	$\frac{M}{\Upsilon}$ [10^{10} $L_\odot$]	M_{vir} [10^{12} $M_\odot$]	c_{vir}	$\frac{M_s}{M_{vir}}$
Q0047	0.485	$3.69^{+3.96}_{-2.16}$	$4.22^{+8.67}_{-3.28}$	$188.43^{+29.56}_{-21.33}$	0.079	$2.57^{+0.24}_{-0.22}$	$16.7^{+0.6}_{-0.5}$	$0.93^{+0.51}_{-0.28}$	$51.1^{+58.9}_{-22.7}$	$0.138^{+0.075}_{-0.042}$
Q0142	0.49	$40.3^{+31.0}_{-14.5}$	$0.10^{+0.11}_{-0.05}$	$459.55^{+106.30}_{-68.40}$	0.047	$1.80^{+0.70}_{-0.54}$	$19.16^{+1.76}_{-1.52}$	$13.57^{+1.18}_{-5.20}$	$11.4^{+4.0}_{-3.5}$	$0.011^{+0.01}_{-0.004}$
MG0414	0.96	$6.45^{+4.30}_{-2.72}$	$4.35^{+8.84}_{-2.63}$	$246.78^{+37.97}_{-29.38}$	0.085	$2.58^{+0.87}_{-0.63}$	$27.62^{+3.51}_{-2.73}$	$4.18^{+2.24}_{-1.32}$	$38.2^{+20.3}_{-11.9}$	$0.05^{+0.029}_{-0.015}$
B0712	0.41	$3.26^{+3.53}_{-1.86}$	$3.98^{+13.49}_{-2.64}$	$160.37^{+30.50}_{-21.20}$	0.054	$1.85^{+0.52}_{-0.39}$	$7.70^{+0.88}_{-0.72}$	$0.51^{+0.35}_{-0.18}$	$49.3^{+50.5}_{-21.2}$	$0.106^{+0.075}_{-0.036}$
HS0818	0.39	$16.5^{+9.4}_{-5.8}$	$0.44^{+0.51}_{-0.24}$	$360.73^{+60.90}_{-45.20}$	0.063	$1.53^{+0.40}_{-0.31}$	$13.44^{+0.84}_{-0.76}$	$5.58^{+3.33}_{-1.85}$	$21.9^{+7.7}_{-5.8}$	$0.02^{+0.013}_{-0.006}$
RXJ0911	0.769	$56.8^{+7.9}_{-6.7}$	$0.08^{+0.01}_{-0.01}$	$485.04^{+21.35}_{-19.89}$	0.067	$2.05^{+0.70}_{-0.52}$	$20.11^{+1.38}_{-1.20}$	$24.34^{+3.36}_{-2.87}$	$8.5^{+0.8}_{-0.7}$	$0.008^{+0.001}_{-0.001}$
BRI0952	0.632	$3.75^{+6.92}_{-2.31}$	$2.04^{+2.51}_{-1.73}$	$132.54^{+47.55}_{-23.73}$	0.065	$2.07^{+0.40}_{-0.32}$	$6.96^{+0.63}_{-0.51}$	$0.41^{+0.61}_{-0.18}$	$35.4^{+41.8}_{-18.6}$	$0.09^{+0.139}_{-0.04}$
Q0957	0.356	$49.9^{+8.36}_{-6.37}$	$0.13^{+0.04}_{-0.02}$	$687.73^{+42.13}_{-34.61}$	0.074	$2.45^{+0.29}_{-0.26}$	$26.74^{+0.92}_{-0.84}$	$36.59^{+7.15}_{-5.25}$	$13.8^{+1.2}_{-1.3}$	$0.006^{+0.001}_{-0.001}$
LBQS1009	0.88	$11.5^{+7.4}_{-4.4}$	$0.75^{+0.97}_{-0.54}$	$231.71^{+40.24}_{-31.54}$	0.079	$2.84^{+1.24}_{-0.91}$	$8.73^{+1.26}_{-1.02}$	$3.10^{+1.91}_{-1.10}$	$20.1^{+8.3}_{-5.9}$	$0.021^{+0.015}_{-0.007}$
B1030	0.6	$12.0^{+3.2}_{-2.3}$	$1.11^{+0.53}_{-0.35}$	$327.36^{+24.32}_{-20.46}$	0.055	$1.84^{+0.79}_{-0.59}$	$7.28^{+0.80}_{-0.65}$	$5.82^{+1.40}_{-1.02}$	$27.2^{+4.4}_{-4.1}$	$0.011^{+0.003}_{-0.002}$
HE1104	0.73	$26.7^{+6.5}_{-5.0}$	$0.28^{+0.12}_{-0.08}$	$395.14^{+27.71}_{-23.76}$	0.075	$1.72^{+0.53}_{-0.41}$	$19.73^{+1.10}_{-1.00}$	$12.43^{+2.80}_{-2.11}$	$14.8^{+2.4}_{-2.1}$	$0.015^{+0.003}_{-0.002}$
PG1115	0.31	$4.27^{+3.99}_{-2.09}$	$3.76^{+12.04}_{-2.65}$	$224.36^{+41.10}_{-29.80}$	0.055	$0.89^{+0.53}_{-0.35}$	$7.78^{+0.99}_{-0.77}$	$1.18^{+0.77}_{-0.41}$	$52.5^{+37.7}_{-20.4}$	$0.054^{+0.038}_{-0.018}$
B1152	0.439	$9.43^{+10.29}_{-4.57}$	$0.87^{+2.11}_{-0.55}$	$261.25^{+72.93}_{-44.80}$	0.047	$1.76^{+0.36}_{-0.29}$	$12.09^{+0.81}_{-0.67}$	$2.30^{+2.51}_{-0.99}$	$27.7^{+16.9}_{-10.8}$	$0.036^{+0.043}_{-0.014}$
B1422	0.337	$25.9^{+20.3}_{-8.5}$	$0.14^{+0.13}_{-0.04}$	$368.43^{+99.18}_{-54.28}$	0.028	$0.33^{+0.14}_{-0.11}$	$3.63^{+0.20}_{-0.20}$	$5.45^{+5.69}_{-2.07}$	$14.3^{+4.0}_{-4.1}$	$0.005^{+0.005}_{-0.002}$
SBS1520	0.71	$2.35^{+0.93}_{-0.60}$	$14.57^{+3.22}_{-7.67}$	$166.82^{+6.69}_{-5.89}$	0.101	$2.36^{+0.90}_{-0.64}$	$14.75^{+1.80}_{-1.40}$	$0.91^{+0.11}_{-0.09}$	$71.0^{+21.5}_{-18.2}$	$0.138^{+0.017}_{-0.014}$
MG2016	1.01	$28.9^{+8.6}_{-6.1}$	$0.29^{+0.15}_{-0.10}$	$369.53^{+31.19}_{-24.92}$	0.105	$0.65^{+0.94}_{-0.56}$	$7.67^{+0.94}_{-0.77}$	$15.01^{+4.13}_{-2.84}$	$12.8^{+2.4}_{-2.1}$	$0.005^{+0.001}_{-0.001}$
B2045	0.87	$10.7^{+4.6}_{-3.1}$	$2.45^{+2.32}_{-1.10}$	$339.55^{+38.59}_{-32.61}$	0.062	$4.36^{+0.85}_{-0.68}$	$21.80^{+1.76}_{-1.44}$	$9.63^{+3.67}_{-2.52}$	$31.8^{+9.2}_{-7.0}$	$0.017^{+0.007}_{-0.004}$
HE2149	0.603	$3.42^{+0.65}_{-0.53}$	$7.86^{+3.72}_{-2.53}$	$196.91^{+5.53}_{-5.54}$	0.091	$1.53^{+0.42}_{-0.33}$	$5.97^{+0.40}_{-0.34}$	$1.27^{+0.11}_{-0.10}$	$57.6^{+8.9}_{-7.9}$	$0.042^{+0.004}_{-0.003}$

***Table C.4*:** For Chapter 7: Lens, redshift of the lens z_L, NFW scale radius r_s, NFW scale density ρ_s, inferred virial radius $R_{\rm vir}$, outermost radius of the mass profiles in terms of virial radius $2R_{\rm lens}/R_{\rm vir}$ (for the innermost radius multiply by 1/19), Hernquist scale radius r_h, Hernquist scale luminosity M/Υ, the virial mass M_{vir} as defined in Equation 2.38, the concentration c_{vir} as defined in Equation 2.35, total enclosed stellar mass fraction M_s/M_{vir}.

List of Figures

List of Tables

List of Publications

List of publications during doctoral studies:

[1] **D. Leier**, I. Ferreras, and P. Saha, "Diagnostics of baryonic cooling", submitted to Month. Not. Roy. Astr. Soc., Sep. 2011.

[2] **D. Leier**, I. Ferreras, P. Saha, and E. E. Falco, "Resolving the baryon-fraction profile in lensing galaxies", accepted by Astrophys. J., ArXiv e-prints, Feb. 2011.

[3] I. Ferreras, P. Saha, **D. Leier**, F. Courbin, and E. E. Falco, "Constraining the low-mass end of the initial mass function with gravitational lensing" Month. Not. Roy. Astr. Soc., vol. 409, pp. L30-L34, Nov. 2010.

[4] **D. Leier**, "A lensing view on the Fundamental Plane" Month. Not. Roy. Astr. Soc., vol. 400, pp. 875-886, Dec. 2009.

Bibliography

Abadi, M. G., Navarro, J. F., Fardal, M. et al. (2010), *Month. Not. Roy. Astr. Soc.* **407**, 435–446.

Akritas, M. G. & Bershady, M. A. (1996), *Astrophys. J.* **470**, 706–+.

Allen, S. W. (1998), *Month. Not. Roy. Astr. Soc.* **296**, 392–406.

Auger, M. W., Fassnacht, C. D., Abrahamse, A. L. et al. (2007), *Astron. J.* **134**, 668–679.

Auger, M. W., Fassnacht, C. D., Wong, K. C. et al. (2008), *Astrophys. J.* **673**, 778–786.

Auger, M. W., Treu, T., Bolton, A. S. et al. (2010), *Astrophys. J.* **724**, 511–525.

Bade, N., Siebert, J., Lopez, S. et al. (1997), *Astron. & Astrophys.* **317**, L13–L16.

Bastian, N., Covey, K. R. & Meyer, M. R. (2010), *Ann. Rev. Astron. Astrophys.* **48**, 339–389.

Bate, N. F., Floyd, D. J. E., Webster, R. L. et al. (2011), *Astrophys. J.* **731**, 71–+.

Bell, E. F., Phleps, S., Somerville, R. S. et al. (2006), *Astrophys. J.* **652**, 270–276.

Bernardi, M. et al. (2003), *Astron. J.* **125**, 1866–1881.

Bershady, M. A., Jangren, A. & Conselice, C. J. (2000), *Astron. J.* **119**, 2645–2663.

Bertin, E. & Arnouts, S. (1996), *Astronomy and Astrophysics Supplement* **117**, 393–404.

Blandford, R. & Narayan, R. (1986), *Astrophys. J.* **310**, 568–582.

Blanton, M. R. et al. (2001), *Astron. J.* **121**, 2358–2380.

Blumenthal, G. R., Faber, S. M., Primack, J. R. et al. (1984), *Nature* **311**, 517–525.

Bolton, A. S., Burles, S., Treu, T. et al. (2007), *Astrophys. J. Let.* **665**, L105–L108.

Bolton, A. S. et al. (2006), *Astrophys. J.* **638**, 703–724.

Bolton, A. S. et al. (2008), *Astrophys. J.* **684**, 248–259.

Borgeest, U. (1983), *Astron. & Astrophys.* **128**, 162–164.

Borriello, A., Salucci, P. & Danese, L. (2003), *Month. Not. Roy. Astr. Soc.* **341**, 1109–1120.

Bosma, A. (1978), PhD thesis, PhD Thesis, Groningen Univ., (1978).

Bouwens, R. J., Illingworth, G. D., Labbe, I. et al. (2011), *Nature* **469**, 504–507.

Bower, R. G., Benson, A. J., Malbon, R. et al. (2006), *Month. Not. Roy. Astr. Soc.* **370**, 645–655.

Boylan-Kolchin, M., Ma, C.-P. & Quataert, E. (2008), *Month. Not. Roy. Astr. Soc.* **383**, 93–101.

Bradač, M., Allen, S. W., Treu, T. et al. (2008), *Astrophys. J.* **687**, 959–967.

Broadhurst, T. et al. (2005), *Astrophys. J.* **621**, 53–88.

Brooks, A. M., Governato, F., Booth, C. M. et al. (2007), *Astrophys. J. Let.* **655**, L17–L20.

Bruzual, G. (1983), *Astrophys. J.* **273**, 105–127.

Bruzual, G. & Charlot, S. (2003*a*), *Month. Not. Roy. Astr. Soc.* **344**, 1000–1028.

Bruzual, G. & Charlot, S. (2003*b*), *Month. Not. Roy. Astr. Soc.* **344**, 1000–1028.

Bryan, G. L. & Norman, M. L. (1998), *Astrophys. J.* **495**, 80–+.

Bullock, J. S., Kolatt, T. S., Sigad, Y. et al. (2001), *Month. Not. Roy. Astr. Soc.* **321**, 559–575.

Buote, D. A. (2004), Vol. 220 of *IAU Symposium*, pp. 149–+.

Buote, D. A., Gastaldello, F., Humphrey, P. J. et al. (2007), *Astrophys. J.* **664**, 123–134.

Buote, D. A. & Tsai, J. C. (1995), *Astrophys. J.* **439**, 29–41.

Busarello, G., Capaccioli, M., Capozziello, S. et al. (1997), *Astron. & Astrophys.* **320**, 415–420.

Cappellari, M. et al. (2006), *Month. Not. Roy. Astr. Soc.* **366**, 1126–1150.

Cardone, V. F., Del Popolo, A., Tortora, C. et al. (2011), *Month. Not. Roy. Astr. Soc.* pp. 1234–+.

Chabrier, G. (2003), *The Publications of the Astronomical Society of the Pacific* **115**, 763–795.

Chandrasekhar, S. (1943), *Astrophys. J.* **97**, 255–+.

Chartas, G., Chuss, D., Forman, W. et al. (1998), *Astrophys. J.* **504**, 661–+.

Chavushyan, V. H., Vlasyuk, V. V., Stepanian, J. A. et al. (1997), *Astron. & Astrophys.* **318**, L67–L70.

Chen, D.-M. (2003), *Astrophys. J. Let.* **587**, L55–L58.

Chiosi, C. & Carraro, G. (2002), *Month. Not. Roy. Astr. Soc.* **335**, 335–357.

Chwolson, O. (1924), *Astronomische Nachrichten* **221**, 329–+.

Claeskens, J., Khmil, S. V., Lee, D. W. et al. (2001), *Astron. & Astrophys.* **367**, 748–758.

Clowe, D., Bradač, M., Gonzalez, A. H. et al. (2006), *Astrophys. J. Let.* **648**, L109–L113.

Coccato, L. et al. (2009), *Month. Not. Roy. Astr. Soc.* **394**, 1249–1283.

Coe, D. (2010), *ArXiv e-prints* .

Cole, S., Aragon-Salamanca, A., Frenk, C. S. et al. (1994), *Month. Not. Roy. Astr. Soc.* **271**, 781–+.

Coles, J. (2008), *Astrophys. J.* **679**, 17–24.

Colless, M. et al. (2001), *Month. Not. Roy. Astr. Soc.* **321**, 277–305.

Comerford, J. M. & Natarajan, P. (2007), *Month. Not. Roy. Astr. Soc.* **379**, 190–200.

Cooke, J. H. & Kantowski, R. (1975), *Astrophys. J. Let.* **195**, L11+.

Covone, G., Kneib, J.-P., Soucail, G. et al. (2006), *Astron. & Astrophys.* **456**, 409–420.

Crampton, D., Schade, D., Hammer, F. et al. (2002), *Astrophys. J.* **570**, 86–91.

Croton, D. J. et al. (2006), *Month. Not. Roy. Astr. Soc.* **365**, 11–28.

de Blok, W. J. G. (2010), *Advances in Astronomy* **2010**.

Dekel, A. & Silk, J. (1986), *Astrophys. J.* **303**, 39–55.

Delgado-Serrano, R., Hammer, F., Yang, Y. B. et al. (2010), *Astron. & Astrophys.* **509**, A78+.

Deng, X., Bei, Y., He, J. et al. (2010), *Astrophys. J.* **708**, 101–108.

Di Matteo, T., Springel, V. & Hernquist, L. (2005), *Nature* **433**, 604–607.

Diemand, J., Zemp, M., Moore, B. et al. (2005), *Month. Not. Roy. Astr. Soc.* **364**, 665–673.

Djorgovski, S. & Davis, M. (1987), *Astrophys. J.* **313**, 59–68.

Dressler, A., Lynden-Bell, D., Burstein, D. et al. (1987), *Astrophys. J.* **313**, 42–58.

Duffy, A. R., Schaye, J., Kay, S. T. et al. (2008), *Month. Not. Roy. Astr. Soc.* **390**, L64–L68.

Dunkley, J. et al. (2009), *Astrophys. J. Sup. S.* **180**, 306–329.

Dyer, C. C. & Roeder, R. C. (1980), *Astrophys. J. Let.* **238**, L67–L70.

Eggen, O. J., Lynden-Bell, D. & Sandage, A. R. (1962), *Astrophys. J.* **136**, 748–+.

Eigenbrod, A., Courbin, F. & Meylan, G. (2007), *Astron. & Astrophys.* **465**, 51–56.

Eigenbrod, A., Courbin, F., Meylan, G. et al. (2008), *Astron. & Astrophys.* **490**, 933–943.

Einstein, A. (1936), *Science* **84**, 506–507.

Eke, V. R., Navarro, J. F. & Steinmetz, M. (2001), *Astrophys. J.* **554**, 114–125.

Evans, N. W. & Wilkinson, M. I. (1998), *Month. Not. Roy. Astr. Soc.* **296**, 800–812.

Faber, S. M. (1972), *Astron. & Astrophys.* **20**, 361–374.

Falco, E. E., Gorenstein, M. V. & Shapiro, I. I. (1985*a*), *Astrophys. J. Let.* **289**, L1–L4.

Falco, E. E., Gorenstein, M. V. & Shapiro, I. I. (1985*b*), *Astrophys. J. Let.* **289**, L1–L4.

Fassnacht, C. D. & Cohen, J. G. (1998), *Astron. J.* **115**, 377–+.

Fassnacht, C. D., Gal, R. R., Lubin, L. M., McKean, J. P. et al. (2006), *Astrophys. J.* **642**, 30–38.

Fassnacht, C. D. & Lubin, L. M. (2002), *Astron. J.* **123**, 627–636.

Fassnacht, C. D., Pearson, T. J., Readhead, A. C. S. et al. (1999), *Astrophys. J.* **527**, 498–512.

Fassnacht, C. D. et al. (1999), *Astron. J.* **117**, 658–670.

Faure, C., Alloin, D., Kneib, J. P. et al. (2004), *Astron. & Astrophys.* **428**, 741–755.

Ferguson, H. C. & Binggeli, B. (1994), *Astronomy and Astrophysics Review* **6**, 67–122.

Ferreras, I., Lisker, T., Pasquali, A. et al. (2009), *Month. Not. Roy. Astr. Soc.* **396**, 1573–1578.

Ferreras, I., Saha, P. & Burles, S. (2008), *Month. Not. Roy. Astr. Soc.* **383**, 857–863.

Ferreras, I., Saha, P., Leier, D. et al. (2010), *Month. Not. Roy. Astr. Soc.* **409**, L30–L34.

Ferreras, I., Saha, P. & Williams, L. L. R. (2005), *Astrophys. J. Let.* **623**, L5–L8.

Ferreras, I. & Silk, J. (2000), *Month. Not. Roy. Astr. Soc.* **316**, 786–794.

Ferreras, I. et al. (2005), *Astrophys. J.* **635**, 243–259.

Flores, R. A. & Primack, J. R. (1994), *Astrophys. J. Let.* **427**, L1–L4.

Foltz, C. B. et al. (1992), *Astrophys. J. Let.* **386**, L43–L45.

Fukugita, M., Hogan, C. J. & Peebles, P. J. E. (1998), *Astrophys. J.* **503**, 518–+.

Fukugita, M., Shimasaku, K. & Ichikawa, T. (1995), *The Publications of the Astronomical Society of the Pacific* **107**, 945–+.

Gallazzi, A. & Bell, E. F. (2009), *Astrophys. J. Sup. S.* **185**, 253–272.

Gao, L., Loeb, A., Peebles, P. J. E. et al. (2004), *Astrophys. J.* **614**, 17–25.

Garrett, M. A., Walsh, D. & Carswell, R. F. (1992), *Month. Not. Roy. Astr. Soc.* **254**, 27P–31P.

Gibbons, R. A. et al. (2000), *in* 'Cosmic Flows Workshop', Vol. 201 of *Astronomical Society of the Pacific Conference Series*, pp. 92–+.

Gilmore, G., Zucker, D., Wilkinson, M. et al. (2008), *in* T. Kodama, T. Yamada, & K. Aoki, ed., 'Panoramic Views of Galaxy Formation and Evolution', Vol. 399 of *Astronomical Society of the Pacific Conference Series*, pp. 453–+.

Gnedin, O. Y., Kravtsov, A. V., Klypin, A. A. et al. (2004), *Astrophys. J.* **616**, 16–26.

Gorenstein, M. V., Shapiro, I. I. & Falco, E. E. (1988), *Astrophys. J.* **327**, 693–711.

Graham, A. & Colless, M. (1997*a*), *Month. Not. Roy. Astr. Soc.* **287**, 221–239.

Graham, A. & Colless, M. (1997*b*), *Month. Not. Roy. Astr. Soc.* **287**, 221–239.

Grant, C. E., Bautz, M. W., Chartas, G. et al. (2004), *Astrophys. J.* **610**, 686–690.

Guo, Q., White, S., Li, C. et al. (2010), *Month. Not. Roy. Astr. Soc.* pp. 367–+.

Guzman, R., Lucey, J. R. & Bower, R. G. (1993), *Month. Not. Roy. Astr. Soc.* **265**, 731–+.

Hagen, H. & Reimers, D. (2000), *Astron. & Astrophys.* **357**, L29–L31.

Hamabe, M. & Kormendy, J. (1987), *in* P. T. de Zeeuw, ed., 'Structure and Dynamics of Elliptical Galaxies', Vol. 127 of *IAU Symposium*, pp. 379–+.

Häussler, B. et al. (2007), *Astrophys. J. Sup. S.* **172**, 615–633.

Hennawi, J. F., Dalal, N., Bode, P. et al. (2007), *Astrophys. J.* **654**, 714–730.

Hernquist, L. (1990), *Astrophys. J.* **356**, 359–364.

Hewett, P. C., Irwin, M. J., Foltz, C. B. et al. (1994), *Astron. J.* **108**, 1534–1541.

Hinshaw, G. et al. (2009), *Astrophys. J. Sup. S.* **180**, 225–245.

Hjorth, J. & Madsen, J. (1995), *Astrophys. J.* **445**, 55–61.

Hoessel, J. G., Oegerle, W. R. & Schneider, D. P. (1987), *Astron. J.* **94**, 1111–1115.

Hogg, D. W. (1999), *ArXiv Astrophysics e-prints* .

Hogg, D. W. & Blandford, R. D. (1994), *Month. Not. Roy. Astr. Soc.* **268**, 889–+.

Hopkins, A. M. & Beacom, J. F. (2006), *Astrophys. J.* **651**, 142–154.

Hubble, E. P. (1926), *Astrophys. J.* **63**, 236–274.

Huchra, J., Gorenstein, M., Kent, S. et al. (1985), *Astron. J.* **90**, 691–696.

Hudson, M. J. et al. (1997), *Month. Not. Roy. Astr. Soc.* **291**, 488–+.

Hughes, J. P. (1989), *Astrophys. J.* **337**, 21–33.

Ilbert, O., Lauger, S., Tresse, L. et al. (2006), *Astron. & Astrophys.* **453**, 809–815.

Jackson, N., de Bruyn, A. G., Myers, S. et al. (1995), *Month. Not. Roy. Astr. Soc.* **274**, L25–L29.

Jackson, N., Nair, S., Browne, I. W. A. et al. (1998), *Month. Not. Roy. Astr. Soc.* **296**, 483–490.

Jackson, N., Xanthopoulos, E. & Browne, I. W. A. (2000), *Month. Not. Roy. Astr. Soc.* **311**, 389–396.

Jiang, G. & Kochanek, C. S. (2007), *Astrophys. J.* **671**, 1568–1578.

Jog, C. J. & Maybhate, A. (2006), *Month. Not. Roy. Astr. Soc.* **370**, 891–901.

Johnston, D. E., Sheldon, E. S., Wechsler, R. H. et al. (2007), *ArXiv e-prints* .

Jørgensen, I. (1999), *Month. Not. Roy. Astr. Soc.* **306**, 607–636.

Jørgensen, I., Franx, M. & Kjaergaard, P. (1996), *Month. Not. Roy. Astr. Soc.* **280**, 167–185.

Kauffmann, G., White, S. D. M. & Guiderdoni, B. (1993), *Month. Not. Roy. Astr. Soc.* **264**, 201–+.

Kaviraj, S., Ting, Y. S., Bureau, M. et al. (2011), *ArXiv e-prints* .

Kayser, R. & Refsdal, S. (1983), *Astron. & Astrophys.* **128**, 156–161.

Keeton, C. R. (2001*a*), *ArXiv Astrophysics e-prints* .

Keeton, C. R. (2001*b*), *ArXiv Astrophysics e-prints* .

Keeton, C. R. & Kochanek, C. S. (1997), *Astrophys. J.* **487**, 42–+.

Keeton, C. R., Kochanek, C. S. & Falco, E. E. (1998), *Astrophys. J.* **509**, 561–578.

Keeton, C. R. et al. (2000), *Astrophys. J.* **542**, 74–93.

Kinney, A. L. et al. (1996), *Astrophys. J.* **467**, 38–+.

Komatsu, E., Smith, K. M., Dunkley, J. et al. (2011), *Astrophys. J. Sup. S.* **192**, 18–+.

Koopmans, L. V. E. & Treu, T. (2002), *Astrophys. J. Let.* **568**, L5–L8.

Koopmans, L. V. E. & Treu, T. (2003), *Astrophys. J.* **583**, 606–615.

Koopmans, L. V. E. et al. (2003), *Astrophys. J.* **599**, 70–85.

Kormann, R., Schneider, P. & Bartelmann, M. (1994), *Astron. & Astrophys.* **284**, 285–299.

Kormendy, J. (1977), *Astrophys. J.* **218**, 333–346.

Krist, J. (1993), *in* R. J. Hanisch, R. J. V. Brissenden, & J. Barnes, ed., 'Astronomical Data Analysis Software and Systems II', Vol. 52 of *Astronomical Society of the Pacific Conference Series*, pp. 536–+.

Kroupa, P. (2001), *Month. Not. Roy. Astr. Soc.* **322**, 231–246.

Kroupa, P. (2008), *in* G. Israelian & G. Meynet, ed., 'The Metal-Rich Universe', pp. 227–+.

Kroupa, P., Tout, C. A. & Gilmore, G. (1993), *Month. Not. Roy. Astr. Soc.* **262**, 545–587.

Kuzio de Naray, R., McGaugh, S. S. & Mihos, J. C. (2009), *Astrophys. J.* **692**, 1321–1332.

La Barbera, F., de Carvalho, R. R., de La Rosa, I. G. et al. (2010), *Month. Not. Roy. Astr. Soc.* **408**, 1335–1360.

Larson, R. B. (1974), *Month. Not. Roy. Astr. Soc.* **169**, 229–246.

Larson, R. B. (2006), Vol. 26 of *Revista Mexicana de Astronomia y Astrofisica, vol. 27*, pp. 55–59.

Lehár, J. et al. (2000), *Astrophys. J.* **536**, 584–605.

Leier, D. (2009), *Month. Not. Roy. Astr. Soc.* **400**, 875–886.

Leier, D., Ferreras, I., Saha, P. & Falco, E. E. (2011), *ArXiv e-prints* .

Lewis, A. D., Buote, D. A. & Stocke, J. T. (2003), *Astrophys. J.* **586**, 135–142.

Li, N. & Chen, D.-M. (2009), *Research in Astronomy and Astrophysics* **9**, 1173–1184.

Li, Y., Klessen, R. S. & Mac Low, M.-M. (2003), *Astrophys. J.* **592**, 975–985.

Liesenborgs, J., de Rijcke, S., Dejonghe, H. & Bekaert, P. (2008), *Month. Not. Roy. Astr. Soc.* **386**, 307–312.

Lintott, C. J., Ferreras, I. & Lahav, O. (2006), *Astrophys. J.* **648**, 826–834.

Łokas, E. L. et al. (2006), *Month. Not. Roy. Astr. Soc.* **366**, L26–L30.

Lopez, S., Wucknitz, O. & Wisotzki, L. (1998), *Astron. & Astrophys.* **339**, L13–L16.

Lucey, J. R., Bower, R. G. & Ellis, R. S. (1991), *Month. Not. Roy. Astr. Soc.* **249**, 755–762.

Macciò, A. V., Dutton, A. A. & van den Bosch, F. C. (2008), *Month. Not. Roy. Astr. Soc.* **391**, 1940–1954.

Mandelbaum, R., Seljak, U., Kauffmann, G. et al. (2006), *Month. Not. Roy. Astr. Soc.* **368**, 715–731.

McKean, J. P., Koopmans, L. V. E., Flack, C. E. et al. (2007), *Month. Not. Roy. Astr. Soc.* **378**, 109–118.

Miller, G. E. & Scalo, J. M. (1979), *Astrophys. J. Sup. S.* **41**, 513–547.

Molinari, E., Buzzoni, A. & Chincarini, G. (1996), *Astronomy and Astrophysics Supplement* **119**, 391–401.

Momcheva, I., Williams, K., Keeton, C. et al. (2006), *Astrophys. J.* **641**, 169–189.

Moore, B., Governato, F., Quinn, T. et al. (1998), *Astrophys. J. Let.* **499**, L5+.

More, A., McKean, J. P., More, S. et al. (2009), *Month. Not. Roy. Astr. Soc.* **394**, 174–190.

Morgan, N. D., Chartas, G., Malm, M. et al. (2001), *Astrophys. J.* **555**, 1–6.

Moster, B. P., Somerville, R. S., Maulbetsch, C. et al. (2010), *Astrophys. J.* **710**, 903–923.

Muñoz, J. A. et al. (2001), *Astrophys. J.* **546**, 769–774.

Müller, K. R. et al. (1998), *Astrophys. J. Let.* **507**, L105–L108.

Myers, S. T. et al. (1995), *Astrophys. J. Let.* **447**, L5+.

Myers, S. T. et al. (1999), *Astron. J.* **117**, 2565–2572.

Narasimha, D., Subramanian, K. & Chitre, S. M. (1984), *Astrophys. J.* **283**, 512–514.

Narasimha, D., Subramanian, K. & Chitre, S. M. (1986), *Nature* **321**, 45–+.

Navarro, J. F., Frenk, C. S. & White, S. D. M. (1996), *Astrophys. J.* **462**, 563–+.

Navarro, J. F., Hayashi, E., Power, C. et al. (2004), *Month. Not. Roy. Astr. Soc.* **349**, 1039–1051.

Nigoche-Netro, A., Ruelas-Mayorga, A. & Franco-Balderas, A. (2008), *Astron. & Astrophys.* **491**, 731–738.

Nipoti, C., Londrillo, P. & Ciotti, L. (2002), *Month. Not. Roy. Astr. Soc.* **332**, 901–914.

Odewahn, S. C., Burstein, D. & Windhorst, R. A. (1997), *Astron. J.* **114**, 2219–+.

Oguri, M., Ofek, E. O., Inada, N. et al. (2008), *Astrophys. J. Let.* **676**, L1–L4.

Ohyama, Y. et al. (2002), *Astron. J.* **123**, 2903–2912.

Okabe, N., Takada, M., Umetsu, K. et al. (2010), *The Publications of the Astronomical Society of Japan* **62**, 811–.

Oke, J. B. & Sandage, A. (1968), *Astrophys. J.* **154**, 21–+.

Oort, J. H. (1932), *Bull. Astr. Inst. Netherlands* **6**, 249–+.

Padmanabhan, N. et al. (2004), *New Astronomy* **9**, 329–342.

Pahre, M. A., Djorgovski, S. G. & de Carvalho, R. R. (1998), *Astron. J.* **116**, 1591–1605.

Patnaik, A. R., Browne, I. W. A., King, L. J. et al. (1993), *Month. Not. Roy. Astr. Soc.* **261**, 435–444.

Patnaik, A. R., Browne, I. W. A., Walsh, D. et al. (1992), *Month. Not. Roy. Astr. Soc.* **259**, 1P–4P.

Peebles, P. J. E. (1980), Princeton University Press.

Peirani, S., Kay, S. & Silk, J. (2008), *Astron. & Astrophys.* **479**, 123–129.

Peng, C. Y., Ho, L. C., Impey, C. D. & Rix, H. (2002), *Astron. J.* **124**, 266–293.

Peng, C. Y., Ho, L. C., Impey, C. D. & Rix, H.-W. (2010), *Astron. J.* **139**, 2097–2129.

Peng, C. Y., Impey, C. D., Rix, H., Kochanek, C. S., Keeton, C. R., Falco, E. E., Lehár, J. & McLeod, B. A. (2006), *Astrophys. J.* **649**, 616–634.

Petrosian, V. (1976), *Astrophys. J. Let.* **209**, L1–L5.

Pooley, D., Rappaport, S., Blackburne, J. A. et al. (2011), *ArXiv e-prints* .

Pooley, D., Rappaport, S., Blackburne, J. et al. (2009), *Astrophys. J.* **697**, 1892–1900.

Popović, L. Č., Moiseev, A. V., Mediavilla, E. et al. (2010), *Astrophys. J. Let.* **721**, L139–L142.

Primack, J. R. (2009), *New Journal of Physics* **11**(10), 105029–+.

Prugniel, P. & Simien, F. (1997), *Astron. & Astrophys.* **321**, 111–122.

Ratnatunga, K. U., Griffiths, R. E. & Ostrander, E. J. (1999), *Astron. J.* **117**, 2010–2023.

Ratnatunga, K. U., Ostrander, E. J., Griffiths, R. E. & Im, M. (1995), *Astrophys. J. Let.* **453**, L5+.

Read, J. I., Saha, P. & Macciò, A. V. (2007), *Astrophys. J.* **667**, 645–654.

Renzini, A. & Ciotti, L. (1993), *Astrophys. J. Let.* **416**, L49+.

Rich, J. (2001), Springer-Verlag Heidelberg.

Rix, H.-W., Schneider, D. P. & Bahcall, J. N. (1992), *Astron. J.* **104**, 959–967.

Robertson, B., Yoshida, N., Springel, V. et al. (2004), *Astrophys. J.* **606**, 32–45.

Rogers, B., Ferreras, I., Peletier, R. et al. (2010), *Month. Not. Roy. Astr. Soc.* **402**, 447–460.

Romano-Díaz, E., Shlosman, I., Hoffman, Y. et al. (2008), *Astrophys. J. Let.* **685**, L105–L108.

Rubin, V. C. & Ford, Jr., W. K. (1970), *Astrophys. J.* **159**, 379–+.

Rusin, D., Kochanek, C. S. & Keeton, C. R. (2003), *Astrophys. J.* **595**, 29–42.

Rusin, D. et al. (2003), *Astrophys. J.* **587**, 143–159.

Saha, P. (2000*a*), *Astron. J.* **120**, 1654–1659.

Saha, P. (2000*b*), *Astron. J.* **120**, 1654–1659.

Saha, P. & Williams, L. L. R. (1997), *Month. Not. Roy. Astr. Soc.* **292**, 148–+.

Saha, P. & Williams, L. L. R. (2001), *Astron. J.* **122**, 585–590.

Saha, P. & Williams, L. L. R. (2003), *Astron. J.* **125**, 2769–2782.

Saha, P. & Williams, L. L. R. (2004), *Astron. J.* **127**, 2604–2616.

Saha, P., Williams, L. L. R. & Ferreras, I. (2007), *Astrophys. J.* **663**, 29–37.

Salpeter, E. E. (1955*a*), *Astrophys. J.* **121**, 161–+.

Salpeter, E. E. (1955*b*), *Astrophys. J.* **121**, 161–+.

Sanders, D. B. & Mirabel, I. F. (1996), *Ann. Rev. Astron. Astrophys.* **34**, 749–+.

Sarazin, C. L. (1988), Cambridge University Press.

Scalo, J. M. (1986), *Fundamentals of Cosmic Physics* **11**, 1–278.

Schaeffer, R. et al. (1993), *Month. Not. Roy. Astr. Soc.* **263**, L21+.

Schechter, P. L. & Moore, C. B. (1993), *Astron. J.* **105**, 1–6.

Schechter, P. L. & Wambsganss, J. (2002), *Astrophys. J.* **580**, 685–695.

Schechter, P. L. et al. (1997), *Astrophys. J. Let.* **475**, L85+.

Schlegel, D. J., Finkbeiner, D. P. & Davis, M. (1998), *Astrophys. J.* **500**, 525–+.

Schmidt, M. (1959), *Astrophys. J.* **129**, 243–+.

Schmidt, R. W. & Allen, S. W. (2007), *Month. Not. Roy. Astr. Soc.* **379**, 209–221.

Schneider, P., Kochanek, C. S. & Wambsganss, J. (2006), Springer-Verlag Heidelberg.

Schweizer, F. & Seitzer, P. (2007), *Astron. J.* **133**, 2132–2155.

Scodeggio, M., Giovanelli, R. & Haynes, M. P. (1997), *Astron. J.* **113**, 2087–2093.

Sérsic, J. L. (1963), *Boletin de la Asociacion Argentina de Astronomia La Plata Argentina* **6**, 41–+.

Shaw, L. D., Weller, J., Ostriker, J. P. et al. (2006), *Astrophys. J.* **646**, 815–833.

Shen, S., Mo, H. J., White, S. D. M. et al. (2003), *Month. Not. Roy. Astr. Soc.* **343**, 978–994.

Sijacki, D., Springel, V., Di Matteo, T. et al. (2007), *Month. Not. Roy. Astr. Soc.* **380**, 877–900.

Solanes, J. M., Salvador-Solé, E. & González-Casado, G. (1999), *Astron. & Astrophys.* **343**, 733–739.

Spinrad, H. & Taylor, B. J. (1971), *Astrophys. J. Sup. S.* **22**, 445–+.

Springel, V., White, S. D. M., Jenkins, A. et al. (2005), *Nature* **435**, 629–636.

Stein, P. (1997), *Astron. & Astrophys.* **317**, 670–675.

Surdej, J. et al. (1987), *Nature* **329**, 695–+.

Sykes, C. M. et al. (1998), *Month. Not. Roy. Astr. Soc.* **301**, 310–314.

Tabor, G. & Binney, J. (1993), *Month. Not. Roy. Astr. Soc.* **263**, 323–+.

Tinsley, B. M. (1978), *Astrophys. J.* **222**, 14–22.

Toft, S., Soucail, G. & Hjorth, J. (2003), *Month. Not. Roy. Astr. Soc.* **344**, 337–346.

Tonry, J. L. (1998), *Astron. J.* **115**, 1–+.

Tonry, J. L. & Franx, M. (1999), *Astrophys. J.* **515**, 512–517.

Tonry, J. L. & Kochanek, C. S. (1999), *Astron. J.* **117**, 2034–2038.

Toomre, A. & Toomre, J. (1972), *Astrophys. J.* **178**, 623–666.

Trager, S. C., Faber, S. M., Worthey, G. et al. (2000), *Astron. J.* **119**, 1645–1676.

Tremonti, C. A. et al. (2004), *Astrophys. J.* **613**, 898–913.

Treu, T., Gavazzi, R., Gorecki, A. et al. (2009), *Astrophys. J.* **690**, 670–682.

Treu, T. & Koopmans, L. V. E. (2002), *Month. Not. Roy. Astr. Soc.* **337**, L6–L10.

Treu, T. & Koopmans, L. V. E. (2004), *Astrophys. J.* **611**, 739–760.

Treu, T. et al. (2006), *Astrophys. J.* **640**, 662–672.

Trott, C. M., Treu, T., Koopmans, L. V. E. et al. (2010), *Month. Not. Roy. Astr. Soc.* **401**, 1540–1551.

Trujillo, I., Burkert, A. & Bell, E. F. (2004), *Astrophys. J. Let.* **600**, L39–L42.

van Dokkum, P. G. & Franx, M. (1995), *Astron. J.* **110**, 2027–+.

van Dokkum, P. G., Franx, M., Fabricant, D. et al. (2000), *Astrophys. J.* **541**, 95–111.

Volders, L. M. J. S. (1959), *Bull. Astr. Inst. Netherlands* **14**, 323–+.

von Hoerner, S. (1960), *Z. Astrophys.* **50**, 184–214.

Walsh, D., Carswell, R. F. & Weymann, R. J. (1979), *Nature* **279**, 381–384.

Warren, S. J., Hewett, P. C., Lewis, G. F. et al. (1996), *Month. Not. Roy. Astr. Soc.* **278**, 139–145.

Weymann, R. J., Latham, D., Roger, J. et al. (1980), *Nature* **285**, 641–643.

Wisotzki, L., Koehler, T., Kayser, R. et al. (1993), *Astron. & Astrophys.* **278**, L15–L18.

Wisotzki, L., Koehler, T., Lopez, S. et al. (1996), *Astron. & Astrophys.* **315**, L405+.

Wisotzki, L., Wucknitz, O., Lopez, S. et al. (1998), *Astron. & Astrophys.* **339**, L73–L76.

Witt, H. J. & Mao, S. (1997), *Month. Not. Roy. Astr. Soc.* **291**, 211–218.

Wong, K. C., Keeton, C. R., Williams, K. A. et al. (2011), *Astrophys. J.* **726**, 84–+.

Wu, X.-P. & Fang, L.-Z. (1997), *Astrophys. J.* **483**, 62–+.

Xu, W., Fang, L.-Z. & Wu, X.-P. (2000), *Astrophys. J.* **532**, 728–739.

Yamauchi, C. et al. (2005), *Astron. J.* **130**, 1545–1557.

Yoo, J., Kochanek, C. S., Falco, E. E. et al. (2006), *Astrophys. J.* **642**, 22–29.

Young, P., Gunn, J. E., Oke, J. B. et al. (1981), *Astrophys. J.* **244**, 736–755.

Ziegler, B. L., Saglia, R. P., Bender, R. et al. (1999), *Astron. & Astrophys.* **346**, 13–32.

Zwicky, F. (1937), *Astrophys. J.* **86**, 217–+.

Acknowledgements

First of all I would like to express my gratitude and appreciation for my supervisor Prof. Joachim Wambsganß, for the opportunity to continue my PhD in Heidelberg, for the confidence in my work, all helpful advice and also the financial support. Many thanks also to Prof. Eva Grebel for filling financial gaps and for all the good advice that has been given.

I want to express my deep gratitude to my thesis advisor Dr. Prasenjit Saha, in whom I found a sincere mentor and guide, for all the help I received in Zurich and in Heidelberg, for patiently answering my many lensing questions and for always having an open ear.

I would like to extend my sincere thanks and gratitude to Dr. Ignacio Ferreras for many insightful conversations, his many, indispensable contributions to our papers, the good cooperation, the opportunity to visit him at MSSL and the frequent pep talks.

I am thankful for the opportunity to collaborate with Dr. Emilio Falco, who provided the reduced photometric data used in this thesis.

Furthermore, I would like to thank Prof. Johanna Stachel and Prof. Eva Grebel, who kindly agreed to join my examination committee.

Special thanks to all my proofreaders, in particular Ingo Berentzen, Markus Bieletzki, Jonathan Downing, Sonia Duffau, Janine Fohlmeister, Sebastian Maetje, Robert Schmidt, Frederik Schönebeck and Dominique Sluse. Without their accuracy and diligence my thesis would not have been what it is.

I am also grateful to many lensing group members and other co-workers at ARI. For interesting scientific discussions and good advice, I would like to extend my thanks to Robert Schmidt, Dominique Sluse and Anna Pasquali. Special thanks go to Janine Fohlmeister for the encouragement on the home stretch. For a pleasant atmosphere, chats and laughs, I would like to thank Timo Anguita, Tobias Brandt, Federica Capranico, Arnaud Cassan, Alex Büdenbender, Thomas Gerner, Alessandra Grassi, Christine Liebig, Svea Proft, Gabriel Stöckle, Fabian Zimmer and Martha Zub. Special thanks go to Fazeel Khan for many scientific and non-scientific chats and for being a great office mate.

During all these years my family has been of vital importance to me. I am thankful for all their support and love. Also, I am thankful for my good friends, Markus und Alice Bieletzki, who believed in me and helped me in dire straits. Finally, but most importantly, I want to thank Sebastian Maetje: I'm so grateful for your presence in my life. I wouldn't have made it without you!

Statement of Authorship - Selbständigkeitserklärung

Ich, Dominik Leier, erkläre hiermit, dass ich die vorgelegte Dissertation selbst verfasst und mich dabei keiner anderen als der von mir ausdrücklich bezeichneten Quellen und Hilfen bedient habe.